ΕΘΝΙΚΟ ΜΕΤΣΟΒΙΟ ΠΟΛΥΤΕΧΝΕΙΟ
ΣΧΟΛΗ ΜΗΧΑΝΟΛΟΓΩΝ ΜΗΧ.
ΤΟΜΕΑΣ ΡΕΥΣΤΩΝ
Ηρώων Πολυτεχνείου 9
15773, Ζωγράφου,
Αθήνα, Ελλάδα

NATIONAL TECHNICAL UNIVERSITY OF ATHENS
SCHOOL OF MECHANICAL ENGINEERING
FLUIDS SECTOR
9 Heroon Polytechniou Str., 15773 Zografou,
Athens, Greece

Experimental and computational study of three-dimensional separation and its control using passive vortex generators

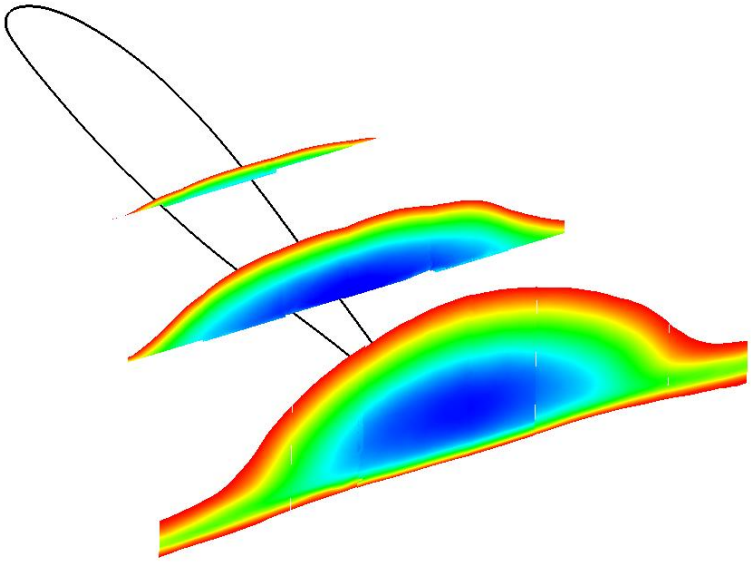

by

Marinos Manolesos

Dissertation submitted to the National Technical University of Athens in partial fulfilment of the requirements for the degree of Doctor of Philosophy in Mechanical Engineering

Athens, September 2013

Examining committee members

Prof.	Manolis Gavaises, City University, London	
Prof.	Kyriakos Giannakoglou, NTUA	
Assoc. Prof.	Mathioulakis Dimitrios, NTUA	Member of the Advisory Committee
Lect.	Riziotis Vassilis, NTUA	
Prof.	Tzabiras George, NTUA	
Assoc. Prof.	Voutsinas Spyros, NTUA	Thesis Supervisor
Prof.	Zervos Arthouros, NTUA	Member of the Advisory Committee

Contents

Abstract

The present thesis deals with the issue of three-dimensional separation of the Stall Cell type on rectangular unswept wings and also the control of Stall Cells using passive vortex generators. The problem was approached experimentally and computationally. Flow visualization tests, pressure measurements and Stereo Particle Image Velocimetry (PIV) experiments were conducted at the small test section of the National Technical University of Athens wind tunnel. On the computational side, an in-house solver of the unsteady Reynolds Averaged Navier-Stokes equations was used.

The dynamic nature of Stall Cells was confirmed by the tuft flow visualization experiments and it was found that the inherent instability can be suppressed by means of a large enough spanwise disturbance. Computational data revealed the complex vortical structure inside a Stall Cell which was confirmed by the experimental results. A Stall Cell consists of three different types of vortices which strongly interact with each other: a) The counter rotating Stall Cell vortices that start normal to the wing surface within the separation line and extend downstream; b) The Separation Line Vortex that runs along the wing span; c) The Trailing Edge Line Vortex that also runs parallel to the wing trailing edge, but has vorticity of opposite sign compared to the Separation Line Vortex. The study of the turbulence characteristics of the flow reveals a highly anisotropic flow. Finally, based on the combined results a SC generation mechanism is suggested.

As far as separation control is concerned, it was found that Stall Cell formation can be suppressed by means of passive vortex generators in the form of triangular vanes. Depending on the vortex generators position and the wing angle of attack, flow instability or bifurcation can appear. It was also shown that results from a computational approach that cannot predict Stall Cell formation (e.g. very small aspect ratio simulations) should be treated with caution. The Stereo PIV study of the vortex generator induced flow revealed that turbulent interaction between the vortex generator vortices and the underlying flow is strong closer to the generators while further downstream diffusion becomes the main mechanism that governs the flow.

The present investigation comes in support of previous studies that highlighted the need to be cautious when using wind tunnel data, especially in the post stall region. The widely used assumption of two-dimensional flow over a two-dimensional airfoil set up is not valid when Stall Cells form. For the correct interpretation of experimental data it is vital to know how the tests were carried and what state of the flow was actually measured. Furthermore, the three-dimensionality of the flow should be taken into account when it comes to separation control.

Acknowledgements

I would like to express my deepest gratitude to Assoc. Professor Spyros Voutsinas, my thesis supervisor, for guiding me throughout the four years of this project. Spyros was always happy to share his great knowledge and experience, while being open to different views. His patience and calmness were also of great help. His overall support classifies as invaluable. I would also like to express my appreciation to Dr. Dimitris Mathioulakis, member of the advisory committee, for his willingness to spend his time answering my various questions.

Papis, AKA Georgios Papadakis, is the best collaborator I could ask for. Extremely knowledgeable and hardworking, he raises the standards in the lab, not just for the programmers. I am indebted to him. I am also particularly grateful for the assistance given by Dr. Stamatios Pothos, whose help and guidance through the experimental part of this thesis was vital. Sotiris Mavrakis had the magic touch that made all machines work in time, especially the wind tunnel motor. His skill and enthusiasm is also very much appreciated.

Aris Kapelonis is gratefully acknowledged for his scientific advice and practical guidance through walks around the campus along with Ivi Tsantili. Dimitris Manolas is acknowledged for the great cooperation we had both at work and on the football pitch. All members of the Aerodynamics Lab are acknowledged for their help during the past four years.

Through the past four years various researchers from different labs were of great help. Asst. Professors E. Lamprou and G. Pantazis are acknowledged for the survey campaign in the wind tunnel test section. Dr. Kaisarlis was of great help when the model surface had to be digitally measured. Finally, Titos Giannakakis and Nikos Kontolaths are acknowledged for the fences construction.

I would like to extend my thanks to all the students who did their graduate theses or placements at the wind tunnel during the past four years. I would like to thank George Metanides for introducing me to the NTUA lab and showing me how things work. Giannis Vasiliades' help with the tufts was crucial. Giannis Lyberopoulos was great at setting up the PIV experiment which came to its final form with the help of Antoine Dumez. Manos Nanos helped me learn a lot about vortex flow, while the assistance of Etienne Lopion and Clement Lepers in the final stages of this project is also appreciated.

I am also grateful to the Onassis Foundation for their financial support to this PhD project through the G ZF 032 / 2009-2010 scholarship grant.

On a more personal note, I would like to express my sincerest appreciation to the Squirrels around the world. I believe they deserve a prize for their achievements of a life time. Spitimouspitisouhkaikapouallou also know that the past four years would not be as fruitful as they were, had it not been for them. Friends without a group tag and my family were of great support, too. Finally, Daphne Giannoulatou, probably the only person to read this thesis without having to, is gratefully acknowledged. Thank you for this and more.

List of Symbols

Lower case Greek symbols

α	Angle of attack
a_{RES}	Ratio of probe size to vortex core radius
α_{SC}	Angle of attack at which a Stall Cell is initially formed
β	Vortex generator angle to the free stream flow
δ	Boundary layer height
λ_2	Vortex detection criterion
ρ	Density
ω	Vorticity
ω_{max}	Maximum Vorticity
ω_x	Vorticity along the x-axis
ω_z	Vorticity along the z-axis

Upper case Greek symbols

Δx	Distance from the VG trailing edge
Δt	Pulse separation time

Lower case Latin symbols

$\hat{b}$	Unit vector along the vortex generator span
c	Chord
c_{VG}	Empirical BAY model constant subject to calibration
e	Error
d	Spanwise distance between the leading edge of two VGs of the same pair
dCl	Difference in lift coefficient
dU	Velocity deficit
dU_{centre}	Velocity deficit at the wing centre
dU_{tip}	Velocity deficit at the wing tip
dx_{sep}	Difference in separation location between the wing centre and tip
h	Laser sheet thickness (Eqn. (1) in Chapter 2)
h	VG height
l	VG length
$\hat{l}$	Unit vector in the direction of the lifting force acting on the flow
$\hat{n}$	Unit vector normal to the VG surface
r_c	Vortex radius
rms	Root mean square

$\hat{t}$	Unit vector tangent to the vortex generator chord
$\hat{u}$	Unit vector in the direction of the local flow
$\vec{u}$	Local velocity vector
$u_i(y,z,t)$	Total instantaneous velocity field on a chordwise plane
$u_i'(y,z,t)$	Fluctuating velocity field on a chordwise plane
$\overline{u_i'u_j'}$	Reynolds stress tensor
$u_{PIV}(y,z)$	Time average of the total velocity field
x	Flow main direction / chordwise position
x_{centre}	Separation location at the wing centre
x_{tip}	Separation location at the wing tip
X_{VG}	Chordwise location of the vortex generator trailing edge
y	Vertical direction
z	Spanwise direction

Upper case Latin symbols

$A_{0.5}$	Vortex area where vorticity is higher than half the peak vorticity
Cd	Drag coefficient
Cl	Lift coefficient
Cl_{max}	Maximum lift coefficient
Cp	Pressure coefficient
Cp_{min}	Suction peak
Cl_{2D}	Lift coefficient of a two dimensional airfoil
Cl_{3D}	Lift coefficient at section of the three-dimensional wing
EV_SSA	Evaluated shear stress angle
L/D	Lift to drag ratio
D	Spanwise distance between two consecutive VG pairs
$\vec{L_i}$	Lift force source term
N	Node
N'	Half-node
L_m	Interrogation area length
$P_{u_iu_j}$	Reynolds stress production term
Q	Vortex detection criterion
$R_{0.5}$	Vortex "half-life" radius
S	Saddle point
S'	Half-saddle point

S_A	Saddle point of separation
S_S	Saddle point of attachment
S_{VG}	Vortex generator planform area
$SC_{\text{actual area}}$	Stall Cell area
$SC_{\text{relative area}}$	Stall Cell relative area
$SC_{Rel.Growth}$	Stall Cell relative growth
SSA	Shear stress angle
U	Streamwise velocity
U_d	Velocity corresponding to a displacement of one pixel
$U_i(y)$	Mean velocity field on a chordwise plane
U_{inf}	Free stream velocity
U_{max}	Velocity at the suction peak location
U_{max_2D}	Velocity at the suction peak of a two dimensional airfoil
U_{max_3D}	Velocity at the suction peak at a section of the three-dimensional wing
U_{rms}	Root-mean-square of the velocity
$U_x(y)$	Spanwise average of the streamwise velocity
U_∞	Free stream velocity
V	Velocity in the vertical direction
V_i	Grid cell volume
$V_i(y,z)$	Vortex velocity field on a chordwise plane
V_R	Volume retention
W	Spanwise velocity
$Wing_{\text{planform area}}$	Wing planform area
$2D$	Two-dimensional
$3D$	Three-dimensional

List of Abbreviations

ARNE	Adverse Reynolds Number Effect
AR	Aspect Ratio
BAY	Bender, Anderson and Yagle
BL	Boundary Layer
CFD	Computational Fluid Dynamics
LE	Leading Edge
NTUA	National Technical University of Athens
PIV	Particle Image Velocimetry
RANS	Reynolds Averaged Navier-Stokes
SC	Stall Cell
TE	Trailing Edge
TKE	Turbulent Kinetic Energy
VG	Vortex Generator
ZZ	Zigzag

List of Tables

List of Figures

Part I.

Introduction and Tools of Investigation

1 Introduction

1.1 Motivation

Stall Cells

Wind tunnel testing of rectangular wing models has been the main way to create airfoil polar curves for decades. The common practice is to deduce the lift coefficient from pressure measurements around the airfoil. The measurements are performed at the centre of the wing span using staggered pressure taps. The drag force is usually measured using a wake rake at one or more spanwise stations. The main assumption is that the flow at the centre of the wing is two-dimensional even under separated flow conditions as long as the wing aspect ratio is large enough. The resulting force coefficients are used in wind turbine blade design along with steady Computational Fluid Dynamics (CFD) calculations and panel codes that include strong viscous-inviscid interaction coupling methods. Therefore the confidence in the design strongly depends on the quality of the experimental sectional polars. In fact the accuracy of aerofoil data is regarded as the greatest potential source of error in wind turbine performance prediction (Tangler, 2002).

Aiming at smooth lift development with respect to the effective angle of attack and adequate thickness for load resistance, wind turbine blades are often designed on the basis of profiles with flat-top pressure distributions. Airfoils of this type exhibit Trailing Edge (TE) separation which renders them prone to the formation of the so called *Stall Cells* (SCs) as concluded in the extensive airfoil profile investigation of (Broeren & Bragg, 2001). SCs are highly three-dimensional (3D) coherent structures of separated flow that consist of two counter rotating vortices.

SCs have been encountered in various aerodynamic applications. Examples include the separated flow region behind flat plates, circular cylinders, shock induced separation and finite wings (Winkelmann, 1982). (Lockman & Seegmiller, 1983; Flynn et al., 2001) mention the formation of SCs on swept cantilevered wings and (Murri & Jordan, 1987; Ross & Perkins, 1994; Supamusdisukul, 2008) observed SCs on airplane wings. Experimental data of (Hahn et al., 2010) show SCs on the suction side of the flap of a two-element high lift wing. Interestingly, computational results (Dropkin et al., 2012) show that SCs are also formed on a wing with a NACA 63_4 - 021 profile, which resembles the cross-section of a whale flipper (Fish & Battle, 1995).

Even though they are broadly encountered, SCs are perhaps of special interest for the wind energy industry for one additional reason. Computational results (Sørensen & Schreck, 2012) suggest that SCs are formed on wind turbine blades at standstill, a condition of particular interest in designing wind turbine blades because of its connection to structural stability. In addition, SCs have been linked to wing buffeting (Flynn et al., 2001). In both aspects a deeper understanding of the phenomenon is necessary in order to correctly predict the loads on blades.

The formation of 3D structures on two-dimensional (2D) set ups had raised questions on the validity of 2D wing tests under separated flow conditions from early on (Gregory et al.,

1971). Until recently, models that exhibited SCs were either "avoided" (Fuglsang & Bove, 2008) or only studied up to their 2D flow limit (Gleyzes & Capbern, 2003). This comes to show that despite the fact that SCs are known for a long time our understanding about their behaviour, structure and formation mechanisms remains limited. It is towards this aim that the first part of the present investigation was conducted in connection to wing model wind tunnel experiments and in relevance to wind turbine blade design.

Vortex Generators

In many practical aerodynamic applications flow separation is encountered at least to a certain extent. Separation occurs when the boundary layer close to the wall becomes detached from the object surface. For streamlined objects this happens due to excessive momentum loss in the boundary layer as the flow moves against an adverse pressure gradient. The amount and location of separation plays a crucial role in the aerodynamic forces on an object, both lift and drag. Increasing lift and minimizing drag can lead to improved energy efficiency as well as to weight and volume saving. This is why separation control is vital for many applications in fluid mechanics (Chang, 1976; Gad-el-Hak & Bushnell, 1991).

One of the simplest and most effective ways to control boundary layer separation is the use of passive Vortex Generators (VGs). Passive VGs are solid devices located inside a boundary layer. Their ease of construction and implementation, robustness and light weight have made them very popular in different industries. Examples of improved performance with use of passive VGs include but are not limited to internal flows (Wendt et al., 1995), airfoils (Ashill et al., 2001; Seshagiri et al., 2009), highly swept wings (Langan & Samuels, 1995), bluff bodies (Aider et al., 2009), wind turbines (Øye, 1995) and noise reduction (Holmes et al., 1987).

Passive VGs come in various shapes (e.g. vanes, wishbones, doublets etc (Lin, 2002; Lu et al., 2011) and all share the same operating principle: they create streamwise vortices which bring high energy flow from outside the boundary layer into the region close to the wall and thus delay or even completely suppress separation. Although the general description of their effect is known, details of the mechanism that prevents separation remain to be understood. The second part of the present investigation deals with the effect of solid VGs on three-dimensional separation and more specifically SCs. The ability of VGs to delay SC formation was examined and the phenomenon was quantitatively described.

1.2 Objective

The objective of this PhD project was to perform experiments and simulations that would deepen our understanding of SCs and to examine the possibility of three-dimensional separation control using VGs. Important milestones in the course of the investigation were:

- *The examination of the SC dynamic nature.*

  The tuft flow visualization technique was used. Unlike the oil flow visualization technique which represents the average flow, tufts follow the unsteady flow. SCs were found to be highly unstable, but easily stabilized by means of a localized disturbance.

- *The validation of simulation results against the experimental data.*

  Computational results were validated against pressure measurements from the wing surface and wake. The agreement was found to be good and thus CFD data were deemed trustworthy of a qualitative analysis of the SC structure

- *The experimental study of a SC.*

  A Stereo Particle Image Velocimetry (PIV) experiment was designed based on the CFD derived model of the SC vortical structure. A SC was studied for the first time using this technique. The mean flow and turbulence characteristics are discussed.

- *The optimization of the VG configuration.*

  A CFD parametric study was performed to find the optimum VG configuration for the airfoil in question. The results were tested in the wind tunnel and possible limitations of the technique were highlighted. Separation is successfully controlled up to $\alpha = 16°$.

- *The experimental study of the VG vortices*.

  The vortex flow was studied by means of a Stereo PIV investigation. The vortex behaviour downstream of the VGs is discussed along with the turbulence characteristics of the flow.

1.3 Previous Work

1.3.1 Stall Cells

Experiments

Table 1, in page 11, lists some of the most significant experimental studies that detected three-dimensional cellular patterns of separated flow in nominally two-dimensional configurations. There is a wide variety of airfoil shapes, airfoil thickness values, Aspect Ratio (AR) values and operating Reynolds (Re) numbers.

Most researchers have found that SCs are dynamic structures. (Yon & Katz, 1998) using tufts, found that at a Reynolds (Re) number of 0.6×10^6 (turbulence intensity 1%) SCs moved in the spanwise direction. Earlier, but at higher Re numbers ($Re > 0.75 \times 10^6$) (Gregory & O'Reilly, 1970; Gregory et al., 1971) reported "intermittent flicking between the un-stalled and the stalled patterns" and "arbitrary change in the number of SCs formed". (Zarutskaya & Arieli, 2005) also found lateral irregular motion of the SCs on their NACA 0012 model at a chord Re number of 0.39×10^6. On the contrary in their tests at lower Re (0.3×10^6), (Broeren & Bragg, 2001) did not report any SC movement as such but reported non-symmetrical separation in the spanwise direction. Worth noting is that in Broeren and Bragg's experiments the turbulence intensity was less than 0.1%. No such information is given in the other tests.

With regard to the effect of the angle of attack, α, (Winkelmann & Barlow, 1980) report that by increasing α (at $Re < 0.4 \times 10^6$) fewer, but wider cells were created. Also, (Schewe, 2001) in his wide Re number range study found that for a specific angle of attack the SC structures would appear only after a certain Re number.

In various studies (Winkelmann & Barlow, 1980; Schewe, 2001) the number of SCs was found to increase as the span of the model increased, for fixed Re number and angle of attack. (Gregory et al., 1971) observed that SCs would not form if the wing AR was lower than a specific value.

Multiple reports state that the formation of Stall Cells is not caused by a tip effect. (Gregory et al., 1971) report that for a wall to wall model suction at the tip region did not prevent the formation of SCs. (Winkelmann & Barlow, 1980) found that for a Clark Y 14% thick airfoil the number of SCs increased when the AR increased from 3 to 12. (Yon & Katz, 1998) came to the same conclusion for a NACA 0015 airfoil and AR values from 2 to 6, by increasing the model span and therefore the AR for a fixed Re number. Yon & Katz also suggest that the number of SCs on a wing equipped with tip plates is greater than that on a wing with free tips. Finally, (Schewe, 2001) found that SCs are not restricted to the wall region when the aspect ratio of a 27% thick airfoil was raised from 4 to 6 and suggested that the width of a single SC remains intact as the AR grows. (Wokoeck et al., 2006) also mentions that mushroom-shaped structures were "resistant" to various sidewall treatments. The conclusion from the above references is that no tip condition (wall to wall with or without suction, free tips or endplates) can prevent the formation of SCs.

As regards boundary layer tripping, in an early report by (Moss & Murdin, 1971), tripping on the suction side of the airfoil led to the creation of Stall Cells at lower angle of attack. (Wokoeck et al., 2006) mentions that SCs are "resistant" to turbulators, whereas, (Swalwell et al., 2004) found that increasing free stream turbulence up to 5% altered the lift characteristics of a NACA 4421 wing during stall. A laminar separation bubble (LSB) is also formed on the specific airfoil at the test Re number ($Re = 2.85x10^5$).

To date no reference of a SC on a rotating (wind turbine or helicopter) blade has been made and it is still unknown how a SC would behave under radial pressure gradients. Coherent three-dimensional structures on rotating blades have been mentioned (DiOttavio et al., 2008; Komerath et al., 2009; Raghav et al., 2009; Mulleners et al., 2012) which could be linked to the SCs studied in the present investigation. In any case, before dealing with the rotating case the fixed one should be better understood.

Simulations

While some extensive experimental studies regarding SCs have been published in the past, to the author's knowledge, only a limited number of computational investigations on SCs exist. To confuse matters a bit more, multiple terms are used when referring to SCs, e.g. *mushroom-shaped* or *owl's eyes structures* or simply *three-dimensional separation*. As result studies basically dealing with the same phenomenon do not gain from all the available knowledge.

(Zarutskaya & Arieli, 2005) used Reynolds Averaged Navier-Stokes (RANS) simulations and examined SCs on a NACA 0012 and a supercritical NASA SC2 airfoil at Reynolds (Re) number of $0.39x10^6$ and $4.6x10^6$. In (Zarutskaya & Arieli, 2005) two different eddy viscosity models were used, namely the Spalart - Allmaras one equation model (Spalart & Allmaras, 1992) and Menter's k-ω SST model (Menter, 1993). It was found that the Spalart - Allmaras model predicts stall with delay, i.e. at a greater angle of attack than expected.

(Bertagnolio et al., 2005; Bertagnolio et al., 2006) refer to three-dimensional chaotic structures present at high angles of attack for the flow past four different airfoils (RISØ-B1-18, NACA 63-430, S809 and DU 83-W-210) in a study that compared 2D RANS, 3D RANS and 3D Detached Eddy Simulation data with experimental results. Although the structures they describe are not named as SCs, they do look similar and it is probably correct to assume that they are. It was found that in the stall region 3D RANS computations do not capture the full turbulent wake structure, although, they usually give sensible results as far as averaged values are concerned.

(Wokoeck et al., 2006) analysed "mushroom-shaped" structures on an airfoil with combined Leading Edge (LE) - TE stall type. In this combined study the computational results failed to reproduce the experimentally observed SCs.

Relevant is also the work of (Rodríguez & Theofilis, 2010) who, based on global stability analysis, attribute the onset of SCs to spanwise instabilities, albeit at a very low Re number of 200.

Regarding turbulence modelling it is accepted (Rubinstein et al., 2001) that eddy viscosity models in general are not sufficient for modelling three-dimensional turbulent vortical flows as they erroneously produce eddy viscosity in the vicinity of free vortices, which causes the vortices to be excessively diffused over and above the effects of insufficient grid resolution. In this sense, the choice amongst various eddy viscosity models is not regarded essential in view of the qualitative analysis targeted in this work.

Although the aforementioned works present skin friction flow lines, pressure measurements and wake contours, the complex vortex structures involved in three-dimensional separation are not discussed. One question raised by (Bertagnolio et al., 2005; Bertagnolio et al., 2006) regards the validity of the measurements used as a reference, since all data were obtained assuming 2D flow over the wing.

Stall Cell formation mechanism and structure

Theoretical results suggest that SCs could be the result of spanwise flow instability. At low Re number (Re = 200) and for an airfoil in deep (laminar) stall, (Rodríguez & Theofilis, 2010) via a BiGlobal stability analysis (Theofilis et al., 2000) attributed the generation of SCs to the amplification of spanwise instability. Recently, (Elimelech et al., 2012) showed on the basis of measurements at low Re numbers that the amplification of a two-dimensional perturbation cannot justify the formation of structures of such a large scale as the SCs and that SCs could be explained as result of a spanwise 3D perturbation.

In deep stall, the separation bubble is formed by two intense shear layers, one originating from the TE and the other from the separation point releasing vorticity of opposite sign into the flow. Under these conditions, a spanwise perturbation can trigger the development of a Crow like instability (Crow, 1970), as (Weihs & Katz, 1983) first suggested.

The computational study of (Taira & Colonius, 2009) for the flat plate case, showed that a small wing of AR = 1.0 does not give SCs, unlike wings of higher AR (AR = 2-4) indicating that

a minimum span (or equivalently a lower bound in wave length) is needed. Beyond that level, multiple SCs can be formed.

Various models regarding the structure of the vortices that form a SC have been proposed in the past. Initially (Winkelmann & Barlow, 1980) proposed a "*tentative flow model*" according to which a *loop vortex* connects the two nodes on the wing surface and a secondary vortex of opposite vorticity runs along the wing TE. Next (Yon & Katz, 1998) based on pressure measurements supported that no loop vortex exists and that two counter rotating vortices start from the surface nodes and then extend downstream aligned with the flow. (Yon & Katz, 1998) also claimed that no spanwise vortex exist other than the TE vortex. As it will be shown next, the present investigation indicates that inside the SC three different kinds of 3D vortices exist in the time averaged flow inside a SC:

a. The two counter rotating SC vortices that start normal to the wing surface and extend downstream, as suggested by (Yon & Katz, 1998)
b. The Separation Line Vortex (SLV) that runs above and parallel to the wing TE. This vortex has vorticity of the same sign as the one suggested by (Winkelmann & Barlow, 1980), but does not end on the surface nodes.
c. The Trailing Edge Line Vortex (TELV) that is also parallel to the wing TE but has vorticity of opposite sign.

1.3.2 Vortex Generators

Unlike SCs which have received limited attention, significant amount of research has been focused on VGs since their first application on a wing (McCurdy, 1948). VGs favourably affect a separating Boundary Layer (BL) by inducing streamwise vortices which transfer high energy fluid from the free stream towards the near wall region. This mechanism has been described by various researchers, e.g. (Rao & Kariya, 1988; Pauley & Eaton, 1988; Lin et al., 1991; Lin, 1999; Lu et al., 2011).

Various studies have provided optimization guidelines, e.g. (Taylor, 1950; Schubauer & Spangenberg, 1959; Pearcey, 1961; Lin, 2002; Wendt, 2004; Godard & Stanislas, 2006) under various flow conditions. It is generally accepted that vane type VGs are more effective than other passive flow control devices, such as wishbones, doublets, grooves etc (Lin, 2002). Of these, low-profile vortex generators are considered preferable as they can be as effective as normal VGs but have less induced drag (Rao & Kariya, 1988). A flow control device is called *low-profile* if its height (h) is less than the local BL height (δ).

Low-profile VGs remain effective despite their limited height as they take advantage of a full turbulent boundary layer profile. However, compared to conventional VGs they create weaker vortices and must be placed fairly close to the separation location. This means that in cases where separation is not fixed, e.g. for an airfoil under varying flow conditions, higher VGs (O(δ)) might be the way to go. In fact, in some cases (Janiszewska, 2004) low profile VGs had little or no effect. In any case, it has been found (Lin, 2002) that, in general, conventional and low-profile VGs follow the same guidelines as established by (Pearcey, 1961).

Regarding specific VG configurations, (Godard & Stanislas, 2006) for a 2D bump found that triangular vanes are more effective than rectangular ones, as is the counter rotating configuration compared to the co-rotating one. (Ashill et al., 2001) also for a 2D bump, found that counter rotating triangular vanes spaced by a gap equal to their height are the more effective in reducing flow-separation control, compared to other low profile devices. According to (Lin, 2002) increasing the gap between the counter rotating vanes reduces the device drag. Finally, in previous experimental studies of VGs on airfoils used on wind turbine blades (Fuglsang & Bove, 2008; Velte & Hansen, 2012) counter rotating triangular vanes were used with significant improvement in lift and lift to drag ratio.

Airfoil applications

Given the fact that various generic review studies have been published in the literature (Lin, 1999; Lu et al., 2011), in the present document the focus will be on the applications of VGs on airfoils with or without SCs. Table 2 in page 12 summarizes the relevant published works and below a short description is given.

The first and only documented successful attempt to delay SC formation using VGs was done by (Moss & Murdin, 1971) on a NACA 0012 airfoil, at a Re number of 0.9×10^6 and 1.7×10^6. More than four decades later (Velte & Hansen, 2012) mentioned SCs at high angles of attack for a DU 91-W2-250 profile with VGs, also at a Re number of 0.9×10^6.

At the same Re number (Bragg & Gregorek, 1987) suggested triangular vane VGs as an aerodynamic fix for the canard airfoil issue of the Voyager aircraft, which made the first nonstop, unrefueled flight around the Earth in December 1986.

(Storms & Jang, 1994) showed that VGs can be used on a NACA 4412 profile combined with a TE Gurney flap to further increase maximum lift ($Re = 2.0 \times 10^6$). It is possible that this was another application of VGs on an airfoil on which SCs form. Interestingly, (Coles & Wadcock, 1979) report three-dimensional separation on the same airfoil at a similar Re number ($Re = 1.5 \times 10^6$).

As far as low Re numbers applications are concerned, VGs are used to control the formation of a laminar separation bubble (LSB) (Kerho et al., 1993). VGs can prevent or delay LSB formation and have even be reported to "slice the laminar separation bubble into segments" (Seshagiri et al., 2009).

VGs are currently used in most wind turbine designs. Multiple studies have proven their effectiveness on airfoils designed for or used on wind turbine blades (Fuglsang et al., 1998; Timmer & Van Rooij, 2003; Fuglsang et al., 2003).

Even earlier than these studies, the application of VGs on multi element high lift wings was proven (Lin et al., 1994; Lin, 1999) at a relatively high Re number of 9×10^6. In such cases VGs can be located on the flap suction side and remain hidden during cruise, thus causing no drag penalty.

(Ashill et al., 2001) showed significant increase in lift for a RAE 5243 transonic airfoil, at a Mach number of 0.68. Counter-rotating vanes spaced VG height apart delayed trailing-edge separation leading to an increase in the maximum lift by about 20%.

It is true that VGs are sometimes used on various applications as a "band aid" tool, i.e. applied on e.g. a blade after its construction and once undesirable flow characteristics have been observed. (Kerho et al., 2003) developed an airfoil design method which incorporates VGs right from the start. This design led to 8% drag reduction in a natural laminar flow profile.

With regard to their effect on dynamic stall (Janiszewska, 2004) showed that application of VGs reduced hysteresis loop and increased Cl max in the Re number range 0.75 - 1.25x10^6.

Finally a recent application of VGs is that of (Heine et al., 2011) where LE finite thickness VGs (or disturbance generators) successfully delayed stall while also changing its characteristics. VGs were used on a OA209 airfoil resulting in an alleviation of the airfoil's leading-edge stall characteristics while trailing-edge separation was promoted. Using very short vane VGs at the wing LE (Pape et al., 2012) also achieved the same effect on the airfoil's characteristics.

Computation of flow past vortex generators

Fully resolving VG geometry is computationally very expensive mainly due to the VG small size. In an attempt to reduce computational cost efforts were made from early on to model the presence of the VG in the flow. In general VG models can be classified in three categories, (a) modelling the effect of the VG shape on the flow (Smith, 1994; Bender et al., 1999; Jirasek, 2005), (b) modelling the profile of the vortex shed by the VG (Kunik, 1986; Wendt, 1996; May, 2001; Zhang et al., 2011; Dudek, 2011; Velte, 2013) and (c) statistically modelling the effect of the shed vortex (Nikolaou et al., 2005; Stillfried et al., 2012).

The fact that research on VG modelling has been so active for almost three decades is indicative of the need for an effective VG model and proves that no clear winner has emerged so far. In the present study the BAY model was used, which was designed for infinitely thin VGs by (Bender et al., 1999). This model has been found to produce results that compare very well with the fully gridded VG cases, but at a fraction of computational cost (Waithe, 2004b; Jirasek, 2005; Dudek, 2011).

Up to date no eddy-viscosity turbulence model has been found to correctly predict the flow downstream of a VG. (Dudek, 2006), who compared experimental data with CFD results using the Spalart - Allmaras (Spalart & Allmaras, 1992) and the k-w SST model (Menter, 1993) for a flow inside a duct with VGs, found that the rate of vorticity decay is significantly greater in CFD than in the experiment. Regarding the turbulence model comparison, it was found that the Spalart - Allmaras model produces higher turbulent viscosity in the vortex core, but downstream enough from the VGs both CFD results agree well with each other and the experimental data.

In fact RANS simulations of the flow past a VG, using either of the aforementioned turbulence models, tend to over-predict vortex size and under-predict peak vorticity downstream of the VG, although vortex circulation is predicted correctly. In other words the vortex strength is computed well, however, computational vortices are more diffused than the measured ones. This is not related to grid resolution, but to the numerical scheme and the turbulence model, e.g (Lin, 2002; Yao et al., 2002; Allan et al., 2002; Dudek, 2011).

Study	Airfoil	AR	Re [x10^6]	c [m]	Wind tunnel cross section [m x m]	Height to chord ratio (h/c)	Width to chord ratio (w/c)	Sidewall treatment	Visualization Technique
(Moss & Murdin, 1971)	NACA 0012	5	0.86, 1.68	0.305	3.96x2.74	8.98	12.98	Side to side (False walls)	Oil surface flow
(Gregory et al., 1971)	NACA 0012	1.4 - 2.8	1.7 - 0.85	0.254 - 0.127	0.91x0.36	1.42 - 0.71	3.53 - 1.76	Side to side	Oil drops
	NACA 0012	6	0.76	0.203	3.96x2.74	13.5	19.51	Side to side / Endplates	Oil drops
	NPL9619	3.59	2.88	0.76		3.61	5.21		
		3.29	3.14	0.83		3.3	4.77		
(Winkelmann & Barlow, 1980)	Clark Y	3.5	0.245	0.089	0.46x1.17	13.1	5.16	Free tips	Oil surface flow
		2.86							
		3, 6, 9	0.26		0.38x0.38	4.27	4.27		
			0.385		2.36x3.35	37.68	26.55		
(Yon & Katz, 1998)	NACA 0015	2-6	0.62	0.152	0.81x1.14	5.32	7.5	Endplates	Tufts
(Broeren & Bragg, 2001)	Ultra Sport, NACA 2414	2.8	0.3	0.305 - vertical	1.22x0.8542	4.00	2.8	Side to side	Mini-tufts
(Schewe, 2001)	FX-77-W270	4 - 6	0.32 - 10.0	0.15 - 0.1	0.6x0.6	4 - 6	4 - 6	Side to side	Oil flow
(Wokoeck et al., 2006)	HGR-01	3.2	0.35, 0.7, 1.4	0.4	1.3x1.3	3.25	3.25	Various	Tufts, Oil Flow
(Elimelech et al., 2012)	NACA 0009	2.5, 5	0.02	1.2, 0.6	0.5x0.5	0.4, 0.8	0.4, 0.8	Sidewalls	-
Present study	NTUA t18	1.5, 2.0	0.5 - 1.5	0.60 - vertical	1.8x1.4	3.0	2.3	Endplates	Tufts, Oil Flow

Table 1: Experimentally observed Stall Cells in the literature.

Study	Airfoil	Re [x10^6]	VG type	VG height	VG position (x/c)	Method	Stall Cells?
(Moss & Murdin, 1971)	NACA 0012	0.86, 1.68	Vanes	0.016c	10% airfoil chord	Pressure measurements	Yes
(Bragg & Gregorek, 1987)	Canard airfoil from the Voyager aircraft	0.9	Vane (delta and trapezoid)	0.018c - 0.022c	17-45% airfoil chord	Pressure measurements	No
(Kerho et al., 1993)	Liebeck LA2573A	0.2 - 0.6	Wishbones, ramp cones	0.3δ - 0.4δ	22% airfoil chord	Hot Wire Anemometry	No
(Storms & Jang, 1994)	NACA 4412	2.0	Wishbones	~3.5δ	12% airfoil chord	Pressure measurements	3D effects are mentioned, but not examined further.
(Lin et al., 1991; Lin et al., 1994)	Three-element high lift airfoil	5, 9	Vane (delta and trapezoid)	0.2δ	25% flap chord	Pressure measurements	No
(Fuglsang et al., 1998)	FFA-W3-241, FFA-W3-301, NACA 63-430	1.6	Vanes	O(δ)	10-30% airfoil chord	Pressure measurements	No
(Klausmeyer et al., 1996)	Three-element high lift airfoil	1.3	Vanes	0.2δ	20% flap chord	Laser Doppler Anemometry, Pressure measurements	No
(Ashill et al., 2001)	RAE 5243 transonic airfoil	19	Vanes, Forward wedges	O(δ)	46.5% airfoil chord	Pressure measurements	No
(Kerho et al., 2003)	Modified NLF(1)-1015	0.5 - 2.0	Vanes	0.5δ	75% airfoil chord	Pressure measurements	No
(Fuglsang et al., 2003)	Risø-B1-18 Risø-B1-24	1.6	Vanes	O(δ)	20% airfoil chord	Pressure measurements	No
(Timmer & Van Rooij, 2003)	DU 91-W2-250, DU 93-W-210, DU 96-W-180, DU 97-W-300	1-3	Vanes	O(δ)	20% to 30% airfoil chord	Pressure measurements	No
(Janiszewska, 2004)	LS(1)-0417 MOD	0.75 - 1.25	Vanes	O(δ)	7% to 15% chord	Pressure measurements	No
(Seshagiri et al., 2009)	LS(1)-0417 GA(W)-1	0.08 - 0.16	Vanes	0.1c	20% airfoil chord	Force measurements	No
(Heine et al., 2011)	OA209	1.8	Finite thickness cylinders and wedges	0.108 - 0.18c	Airfoil LE	Time resolved PIV, Pressure measurements	No
(Velte & Hansen, 2012)	DU 91-W2-250	0.9	Vanes	0.5δ	0.3% airfoil chord	Stereo PIV	SCs mentioned at post stall, but not examined further.

Table 2: Applications of VGs on airfoils in the published literature.

1.4 Thesis Outline

The thesis consists of four main parts, each divided into several chapters as outlined below:

I. Introduction
   - Chapter 1 - Introduction
   - Chapter 2 - Experimental procedures
   - Chapter 3 - Computational modelling

II. Three-dimensional separation
   - Chapter 4 - Geometrical characterization of Stall Cells
   - Chapter 5 - Stall Cell structure analysis
   - Chapter 6 - Stereo PIV study of a Stall Cell
   - Chapter 7 - Reynolds number effect

III. Separation Control
   - Chapter 8 - Vortex generator configuration optimization
   - Chapter 9 - Experimental study of the vortex generator induced flow

IV. Conclusions
   - Chapter 10 - Conclusions and suggestions for future work

V. Appendices
   - Appendix A – Tuft Flow Visualization
   - Appendix B – Trip tape height computation

Chapter 2 reports on the experimental procedures followed during the course of the present investigation. The wind tunnel and measuring equipment is presented. The procedures followed for flow visualization (tufts and oil flow), pressure recording and Stereo PIV measurements are described. Stereo PIV measurements being more challenging, they receive greater focus.

Chapter 3 presents the computational tool used for the present study. The in-house code MaPflow was developed by Georgios Papadakis, and a detailed description can be found in (Papadakis, 2011). Hence, the description given here is limited to its basic features.

In Chapter 4 the dynamic behaviour of SCs formed on a stalled wing is confirmed using tufts. It is found that the inherently unstable SCs can be stabilized by applying a large enough local disturbance to the flow. The overall characteristics of the resulting flow are not affected by the disturbance. The effects of Re number, AR and angle of attack on the stabilized flow are discussed.

Chapter 5 combines experimental and computational data and examines the SC structure. CFD results appear in good qualitative agreement with pressure measurements and are hence used for a qualitative analysis of the time averaged flow inside a SC. Three different types of vortices are observed: a) the SC vortices, b) the Separation Line Vortex and c) the TE line vortex.

The Stereo PIV measurements of a SC are given in Chapter 6. Experimental data confirm the SC vortical structure suggested by CFD simulations. Time averaged data and turbulence statistics are presented. According to the hypothesis made at the end of the chapter, SCs are the result of a Crow like instability between the Separation Line Vortex and the the TE line

vortex. The perturbed vortices lead to three-dimensional separation on the wing suction surface and hence to spanwise flow. As a result the separation shear layer is folded and the SC vortices are formed.

The unexpected lift reduction as Re increases from $0.5x10^6$ to $1.0x10^6$, also observed by (Yoshida & Noguchi, 2000), is investigated computationally in Chapter 7. This adverse Re number effect is linked to the SCs and SC vortex strength.

As no single VG configuration can be expected to perform best for all aerodynamic applications, an optimization study was performed, described in Chapter 8. The presence of the VGs was modelled using the BAY model (Bender et al., 1999). The best performing set ups were tested experimentally and the optimal one was chosen for further investigation.

Chapter 9 reports on the experimental tests of the wing with and without VGs. A Stereo PIV investigation was performed and the vortex size, path and strength are examined for the case of $\alpha = 10°$, at a Re number of $0.87x10^6$. Stereo PIV data are used to investigate the correlation between Re stresses and their production to mean flow gradients.

The thesis ends with Chapter 10, where the final conclusions are presented along with some recommendations regarding future work.

In Appendix A photos from the tuft flow visualization experiments are given, highlighting the effect of angle of attack, Re number and AR on SC size. In Appendix B the trip tape height computation is described in greater detail, for completeness.

2 Experimental procedures

2.1 Wind tunnel Facility

All experiments were carried out at the small test section (1.4mx1.8m) of the National Technical University of Athens (NTUA) wind tunnel. The wind tunnel is of the closed single-return type with a total circuit length of 68.81 m. The circuit has a contraction ratio of 6.45 to 1. The free-stream turbulence level in the 3.75 m long octagonal test section is 0.2% with a maximum test section velocity of about 60 m/s. Energy to the flow is given by a 2.67 m diameter eight-bladed fan driven by a 300 kW DC motor.

2.2 Wing Model

The investigation refers to an 18% thick airfoil profile designed at the NTUA (Mourikis et al., 2005). The specific profile is optimized for use on variable pitch and variable speed multi MW wind turbine rotors. Shape optimization was based on evolutionary algorithms and use of XFOIL (Drela, 1989) as flow solver. The profile belongs to the flat-top type experiencing TE separation leading to a gradual built-up of the lift and smooth post stall behaviour. The profile coordinates are given in Appendix C.

The wing model had a chord of 0.6m and spanned the test section vertically in order to minimize blockage. The solid blockage of the model was 6.9% of the tunnel section at 12° angle of attack and reached a maximum of 9.2 % at the highest measured angle, 16°, still below the usual upper bound of 10%, see (Barlow et al., 1999).

In order to minimize the effect of the wind tunnel boundary layer, side fences were used (Figure 1, left). Figure 1, right, shows a schematic side view of the test set up. The fences were made of Plexiglas and could move along the model span so the aspect ratio (AR) of the model could vary. Figure 2 shows a close up of the top and lower fences as they were positioned on the wing model. Figure 3 shows the wing model in the test section as seen from inside the contraction. The wake rake and the traverse mechanism can be seen in the background.

The model surface has been measured in order to quantify the deviation from the nominal profile. Figure 4 present the surface deviations from the mean profile for the suction and the pressure side respectively. The mean profile was defined from the mean values of the 12455 points that were measured on the wing. It can be seen that the deviations on the suction side are within 0.8mm whereas this figure grows to 1.5mm for the pressure side.

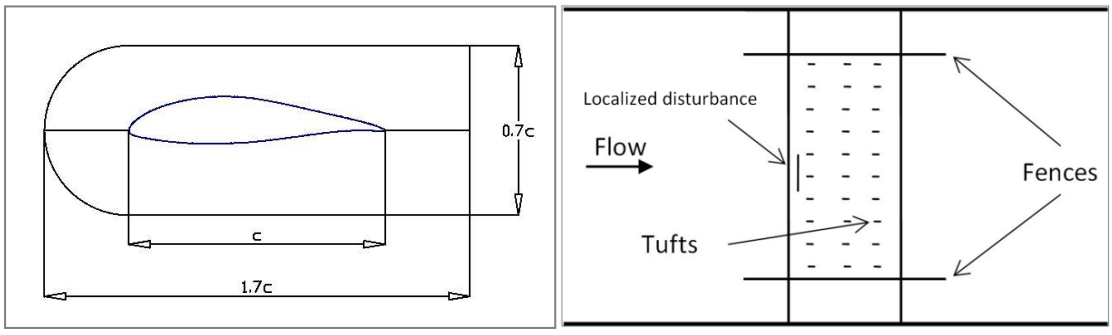

Figure 1: Fences shape and dimensions (left) and side view of the test set up (right).

Figure 2: Top (left) and lower fence (right) close-up.

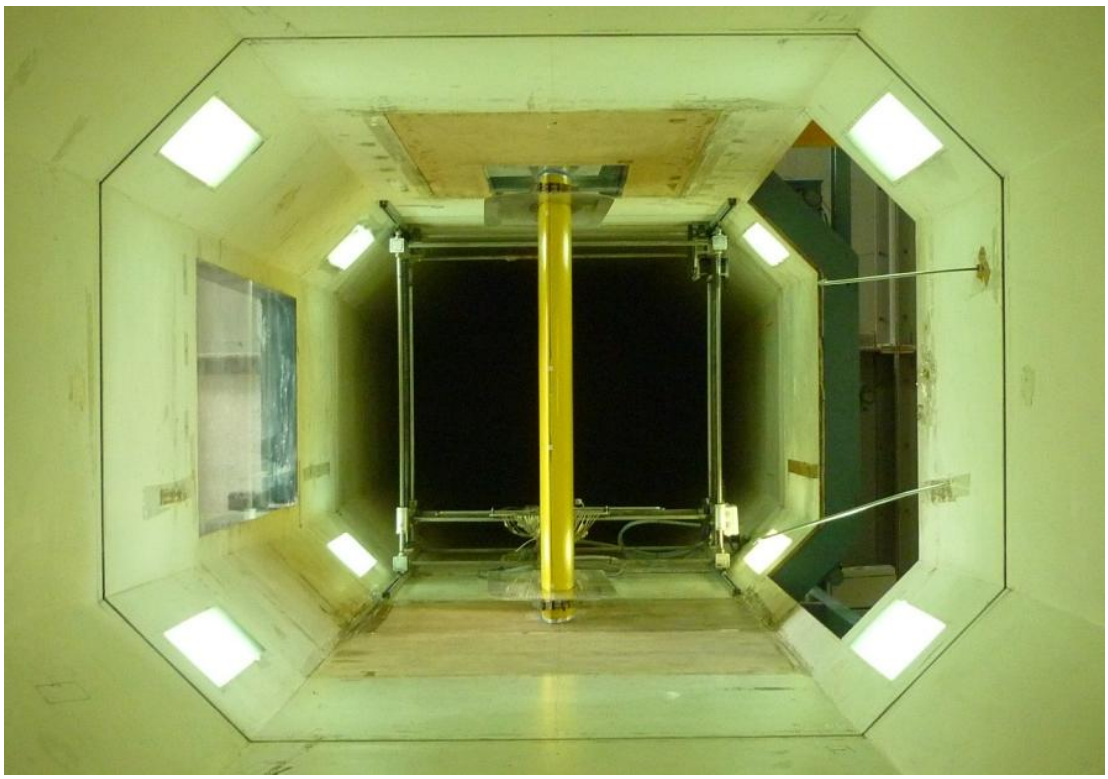

Figure 3: View of the test section from upstream, from inside the contraction. The traverse mechanism and the wake rake are also visible.

The wing surface was originally yellow but was later on painted black in order to minimize the reflections during the PIV experiments. The model was first spray-painted black and the finish was done with mat varnish mixed with Rhodamine 6G. Rhodamine 6G shifts the wavelength of the impeding laser light through absorption and re-emission, e.g. see (Kubin & Fletcher, 1982). By applying suitable band-pass filters on the camera lenses it is possible to prevent the reflections from reaching the CCD sensors. Thus measurements closer to the surface can be performed. The technique was also used in (Velte & Hansen, 2012). The model's final colour is shown in Figure 5.

The VGs were constructed by a 0.2mm thick aluminium strip that was located on wing suction surface. The strip thickness was chosen so that the VGs would have adequate rigidity and impose minimum distortion to the boundary layer. The metal band acted like a step amounting to 1/30 of the BL thickness at the position of VGs (δ=6mm) which is regarded small.

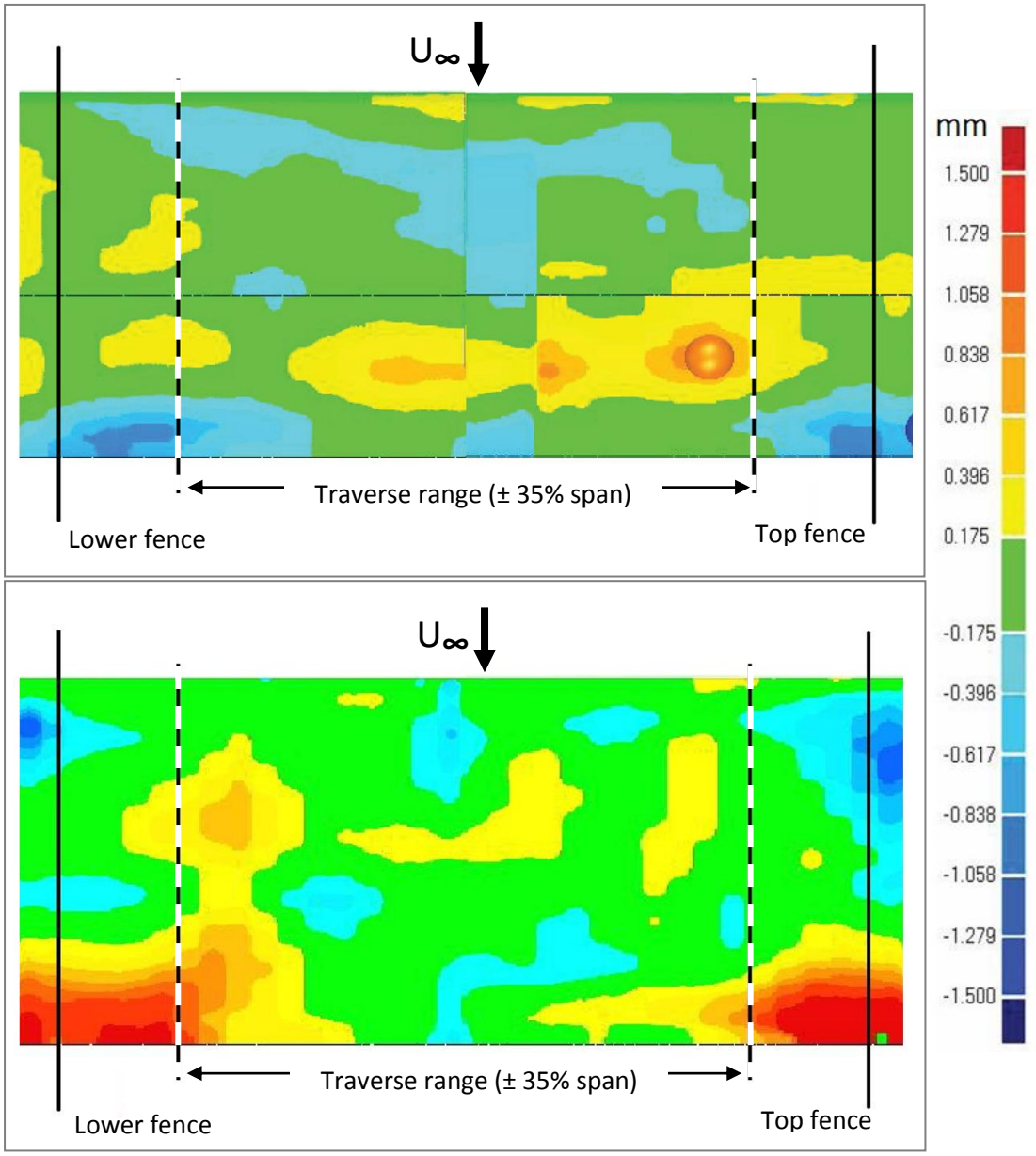

Figure 4: Wing model surface deviation from mean profile. (Top) suction side and (bottom) pressure side. Dashed lines show the traverse spanwise range and solid lines show the fences position for the AR = 2.0 case. Highest deviation point on the suction side is shown with a sphere.

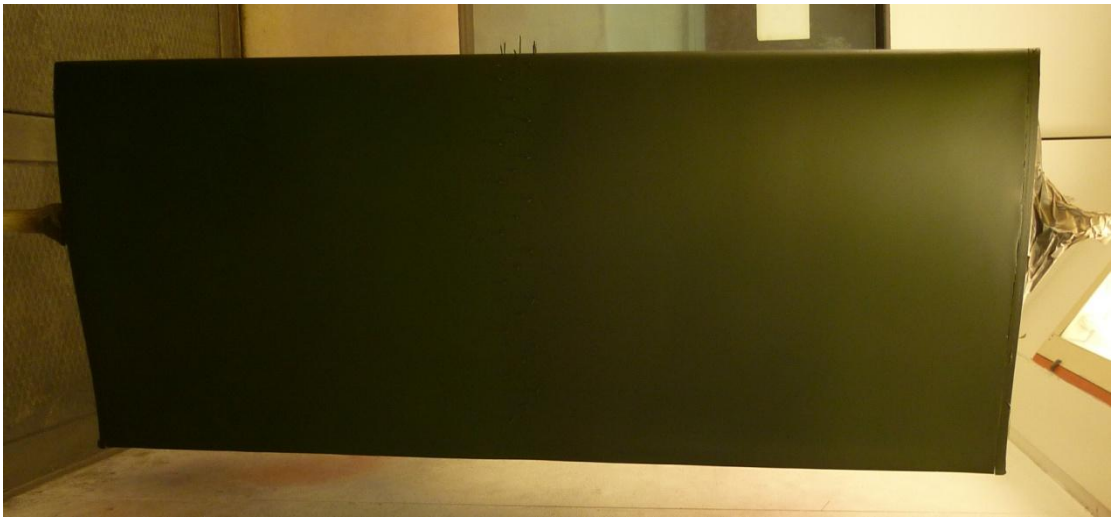

Figure 5: The wing model after being painted with a mat black dye with Rhodamine 6G. View of the pressure side.

2.3 Flow visualization

2.3.1 Tuft flow visualization

For the tuft visualization experiments, No 60 sewing threads were fitted over the suction side of the model in chordwise rows with 4cm spacing between them in the spanwise direction. The chordwise position of the tufts is shown in Figure 6. Every single tuft was individually taped on the model surface in order to minimize their interference to the boundary layer.

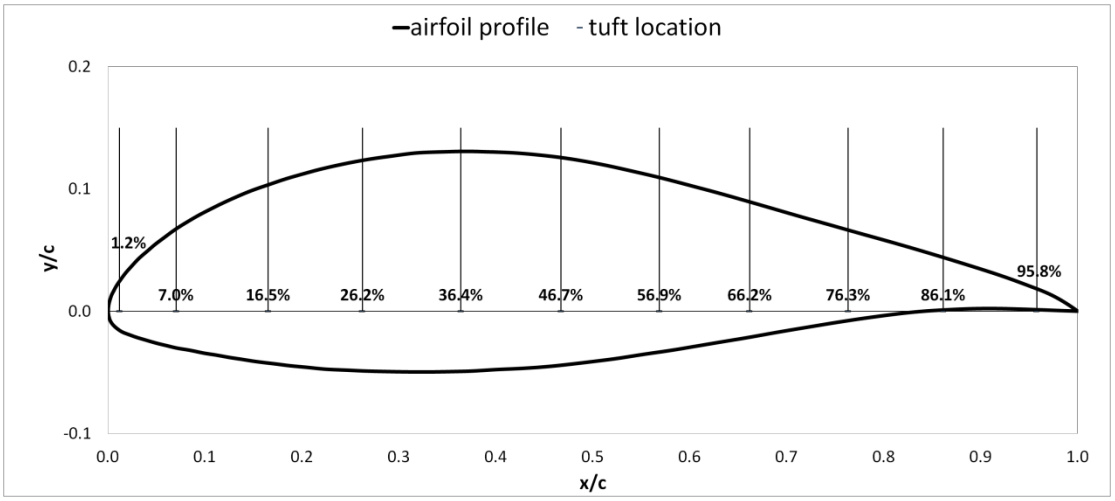

Figure 6: The airfoil profile and chordwise location of tufts.

In order to check whether the tufts correctly follow the flow even at the lowest Re number, the tuft data were compared with pressure data in Figure 7. The earliest separation point at the wing mid-plan for the AR = 2.0, Re number 0.5×10^6 case with zigzag (ZZ) tape is plotted against angle of attack for both the tuft and the pressure data. The agreement is very good and therefore the tuft data are trustworthy even at the lowest free stream velocity.

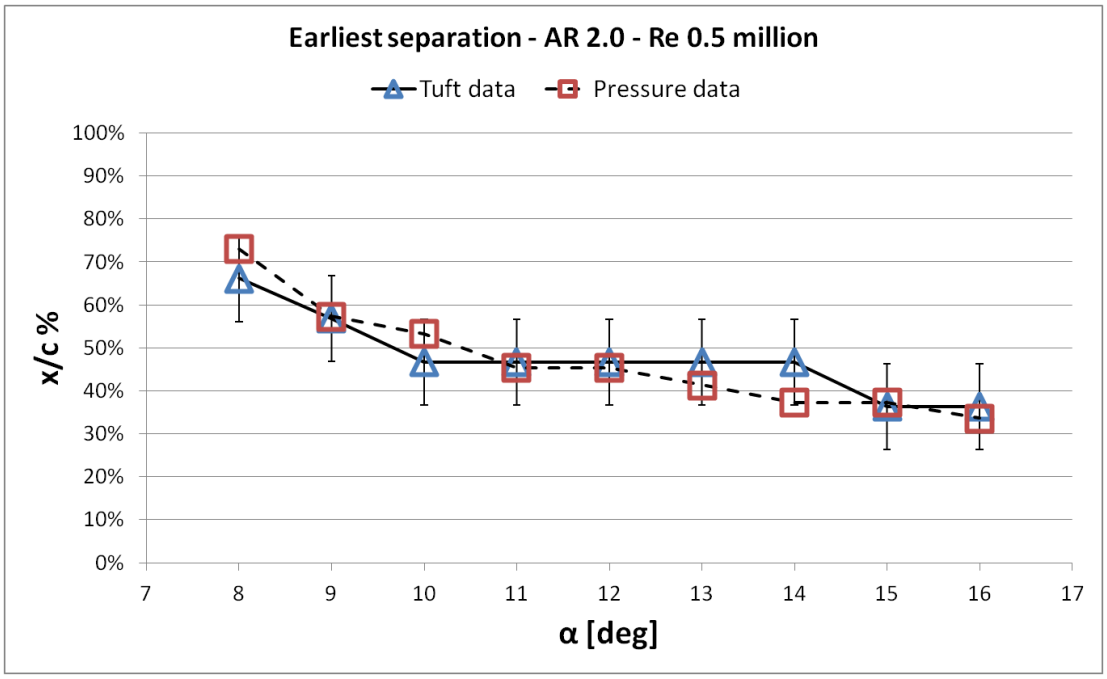

Figure 7: Earliest point of separation as found by tuft and pressure data for Re = 0.5x10^6, AR = 2.0, with a localised disturbance using a ZZ tape. The two sets agree well and so trustworthy conclusions can be drawn from the tuft data.

2.3.2 Oil surface flow visualization

Various coloured powders mixed with kerosene were used for surface flow visualization. Kerosene was preferred over other lubricant oils as it dried on the wing surface and allowed for photographs to be taken after the tunnel was shut down. Other oils on the other hand would move in the vertical direction due to gravity and distort the surface flow pattern.

2.4 Pressure Measurements

2.4.1 Instrumentation

The model had 62 pressure taps located at the centre of the wing span. Chordwise they extended from the LE to 88.8% of the chord. All chord pressure channels were fed through a pressure scanner (model FCS421, Furness Controls Ltd) to either a Furness Manometer (FCO16, ±2000 Pa or a Scanivalve pressure transducer (Model J - 500PSI). The wake rake was 39.1cm wide and consisted of 45 total pressure tubes (of which 44 were used) and two static pressure tubes, located on a different plane from that of the rake. All the tubes were directly connected to the Scanivalve sensor and then through a 16 bit A/D card (National Instruments - USB6251) to the lab computer.

The wake rake was positioned on the traverse table at 0.8c and 1.06c downstream of the wing TE for the cases without and with the VGs, respectively. The wake rake could travel both in the spanwise and the normal to the chord directions. When the wake was wider than the rake width a second measurement would be taken after the rake was moved normal to the chord with sufficient overlapping. The rake travel region was 84cm and covered ±35% span.

2.4.2 Procedure

For each set of measurements first the targeted free stream velocity was reached and then the model would be set at the desired angle of attack. The wing pressure measurements were then followed by the wake pressure measurements. All measurements were taken at 200Hz for 5 seconds. A constant misalignment of the model with the flow by 0.2^{o} is allowed for in the results.

2.4.3 Force Coefficients

The lift coefficient (Cl) was computed from the pressure distribution around the airfoil. Since the pressure taps only covered up to 88.8% of the chord, the values reported in the present study are not the full Cl of the profile. Accordingly when CFD data are compared with experimental data, then the computational lift coefficient is also computed by integrating up to 88.8%c for a fair comparison.

For attached flow conditions the drag coefficient (Cd) was computed from the wake pressure distribution according to (Barlow et al., 1999). For separated flow conditions the pressure drag was used instead. In order to estimate the pressure drag an approximation had to be used for the part of the chord that had no pressure taps (x > 88.8%c). It was assumed that the pressure on the suction side remained constant through the separated flow region up to the TE. Then a second order approximation for the pressure on the pressure side was used. No such approximation was used for the Cl computation.

For the case with VGs the drag varied significantly even under attached flow conditions due to the presence of the streamwise vortices shed by the actuators, as expected (Timmer & Van Rooij, 2003). The drag was hence measured in four positions downstream of a VG pair and the average value is reported here. The central VG pair was selected, which was downstream of the ZZ tape. The four drag measurement positions are shown in Figure 8, and were the following: Position 0 was between the two VGs of the central VG pair, Position 3 was between two consecutive VG pairs and Positions 1 and 2 were in equal distance between Positions 0 and 3. Although the wake rake method has been used by other researchers in the past (Fuglsang et al., 1998), in order to measure drag of an airfoil equipped with VGs, it should be noted that it might over predict Cd since rotational losses are also included in the measured drag (Barlow et al., 1999).

As a convention the force coefficients at the centre of the wing will be referred to as the *wing Cl and Cd*, even though this is not literally true, due to the three dimensionality of the flow.

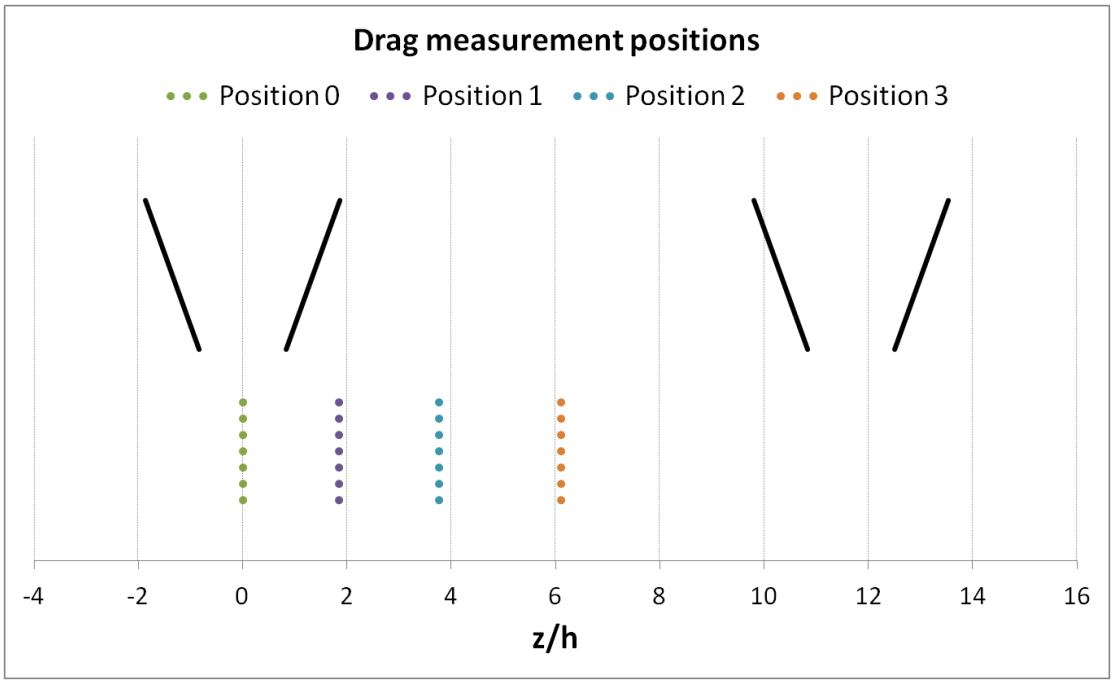

Figure 8: Drag measurement positions.

2.4.4 Wind tunnel corrections

Wind tunnel corrections were applied to the measured data according to (Barlow et al., 1999) for the case of a wing spanning the tunnel height. In particular the corrections allowed for the model's solid blockage, the wake blockage and the tunnel walls. The horizontal buoyancy is considered insignificant for 2D airfoil models.

However, these corrections have been developed with the assumption of a two-dimensional flow. Even though the effect of the corrections is small, it has to be mentioned that their application in the present study is somewhat problematic since, as shown latter on, when a SC is formed the wake becomes highly three-dimensional.

It's worth noting that the wake rake position did not affect the measured Cl value at the centre of the wing, i.e. the measured values were always within ± 0.5% regardless of the rake position. It did however affect the static pressure measurements at the lowest positions due to increased blockage. The affected measurements were not used and an average pressure drop along the wind tunnel axis was used for all span positions.

2.5 Stereo Particle Image Velocimetry

2.5.1 Experimental Set-up

Measurement Equipment

Two different TSI Nd:YAG PIV lasers with dual cavities were used depending on availability. For the uncontrolled case a 30mJ laser produced a 2.5mm thick light sheet, whereas a 200mJ laser was used for the VG tests which produced a 1.8mm thick laser sheet at the measurement position. The flow was seeded with oil droplets of mean 1µm diameter created by a commercial generator (TSI model 9307). Two TSI Powerview Plus™ 4MP Cameras were used, located inside the test section 1.2c downstream of the TE. The camera set up can be seen in Figure 9. Depending on the size of the desired field of view, three

different pairs of lenses, one Nikkon 50mm f/1.8 and one Tamron 90mm f/2.8 and one Sigma 150mm f/2.8, were used. For the uncontrolled case, the lenses were always set at the largest aperture to allow the maximum amount of light to reach the CCD sensor.

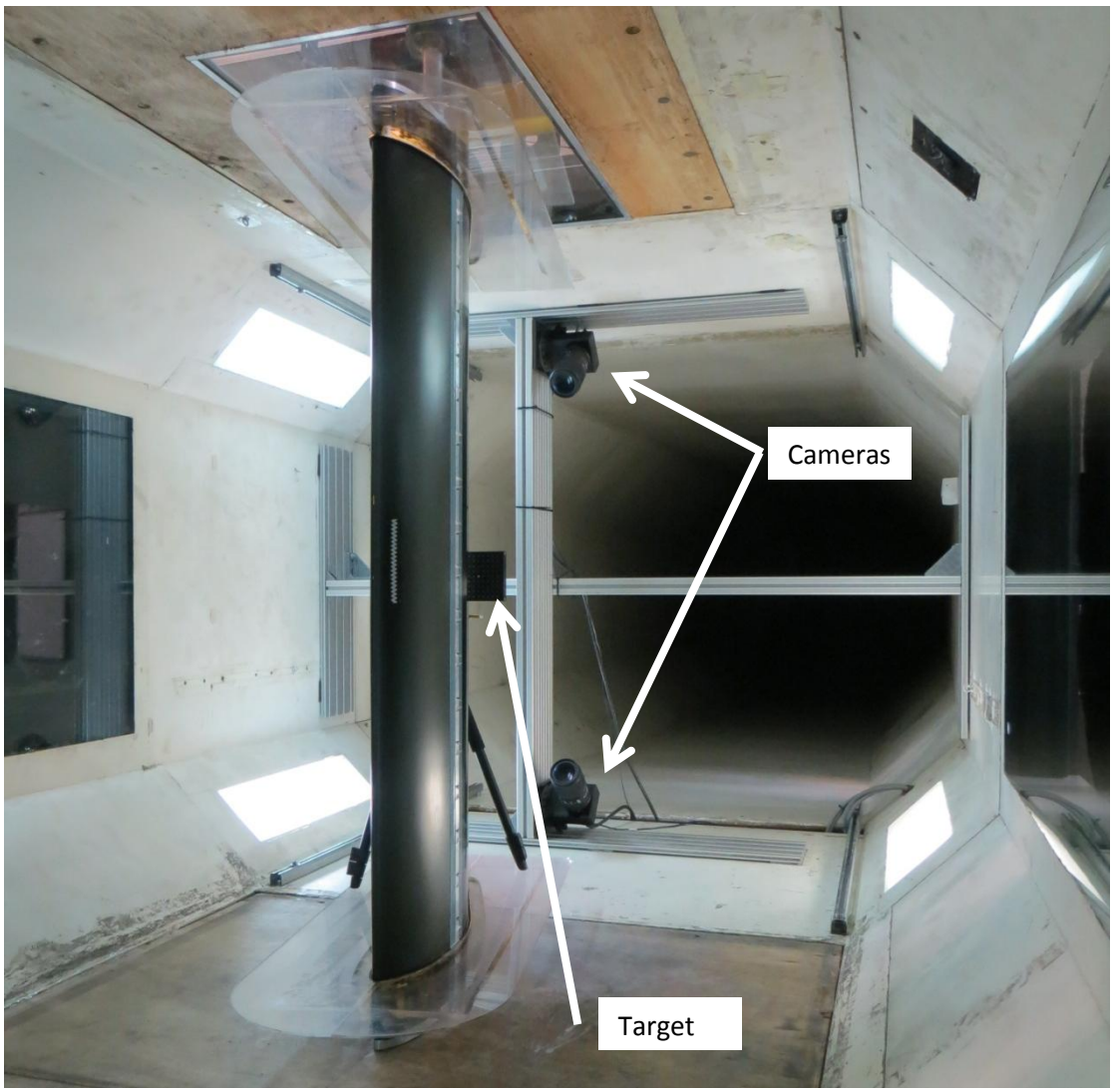

Figure 9: View of the camera set up inside the test section. The target positioning for a plane normal to the free stream span can also be seen.

Pulse separation time

A small pulse separation time is preferable when it comes to reducing the errors associated with flow acceleration and curvature effects (M. Ramasamy & Leishman, 2006). Also, when the velocity normal to the measurement plane is high a small pulse delay is required to reduce the number of particles that go out of the measurement window. However, reducing the pulse delay reduces the measurement dynamic range, so a compromise is necessary.

Volume retention (V_R, eqn (1)), as defined in (Waldman & Breuer, 2012), describes the percentage of particles present in both images of a PIV measurement for a plane normal to the flow.

$$V_R = \frac{h - U_\infty * \Delta t}{h + U_\infty * \Delta t} = 1 - \frac{2}{\frac{h}{U_\infty * \Delta t} + 1} \quad (1)$$

where h is the laser sheet thickness, U_∞ is the free stream velocity and Δt is the pulse separation time. It is apparent that a large sheet thickness and a small pulse separation time are required in cases where the free stream velocity is high. For the uncontrolled case (Chapter 6) a pulse separation time of 20μsec was used, that resulted in a V_R value of 70%. For the case with the VGs (Chapter 9) the pulse separation time as 12μsec and V_R was 73%. For all measured planes the number of spurious vectors was always below 5% and the particle displacement was in all cases less than 1/4 of the 32x32 final interrogation area.

Given the number of parameters involved estimating the uncertainty in a PIV system is not trivial (Willert, 1997). Under optimal conditions the minimum displacement that can be accurately estimated is 0.1px (Westerweel, 2000; Foucaut et al., 2004). The corresponding minimum estimated velocity according to the relevant pulse separation time is given for each measurement plane in the relevant chapter. Any velocity value below the minimum estimated velocity for each plane is not reliable.

Reflection reduction

Due to the vicinity of the measurement planes to the wing surface, reflections were significant. To deal with this issue a background reflection image was subtracted from the measurement images prior to processing, removing most of the unwanted reflections. Areas where this was not achieved have been masked out in the results shown this thesis.

Stereo PIV calibration

Two different targets (one 100x100 mm and one 200x200 mm) were used for the calibration of the Stereo PIV experiments, depending on the size of the measurement plane. They were both dual plane double sided allowing the computation of the calibration coefficients without traversing the target in the out-of-plane direction. As a result the velocity component normal to the plane is first order accurate (M. Ramasamy & Leishman, 2006).

The side of the targets was fitted with a plate that had two mirrors, one aligned with the centreline of the target and other aligned with the centreline between the two planes of one side of the target. The former mirror was used to align the laser sheet with the target when the cameras were located at both sides of the light sheet (i.e. for planes parallel to the flow) and the latter was used when the cameras were located at the same side of the light sheet (i.e. for planes normal to the flow). In all cases the optical path of the reflected sheet was made co-planar with the incident sheet to ensure the best possible alignment of the laser sheet with the calibration target. Using the stereo-automapping module of the insight 4G software the average misalignment of the light sheet with the calibration target was found to be lower than 0.2°.

For some frames the camera field of view (FOV) was larger than the available 20cm x 20cm target (e.g. 10° case, plane at x/c = 1.06). On these occasions, the target was first positioned at one end of the FOV and then at the other as shown in Figure 10. In this way two separate perspective calibrations were performed one for each end of the image. Then the images

were analysed twice, once for each side, using the corresponding calibration and mask. At the end, the two set of vectors were brought together based on the initial target positioning. Agreement in the overlapping regions was found to be excellent.

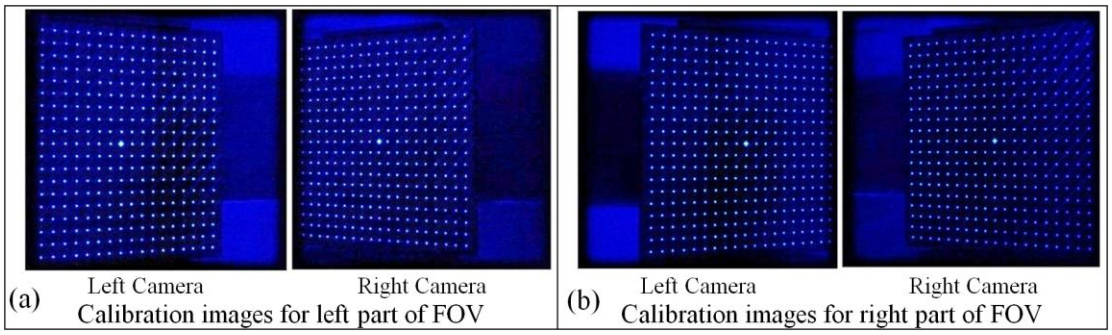

Figure 10: Left and Right camera images used for perspective calibration. (a) Images used for the left part of the field of view. (b) Images used for the right part of the field of view.

Post processing

All image post processing was done using TSI Insight 4G software. The overlap between interrogation areas was set to 50% and a Gaussian peak estimator was used. Velocity derivatives were computed using the least squares method which is second order accurate and cancels out the effect of oversampling and produces smoother results (Raffel et al. 1998).

When a standard deviation filter was used to locate outliers, it was found that valid vectors would erroneously be considered as spurious. This was attributed to the fact that the velocity field in each measurement window did not follow a normal distribution (see e.g. Figure 13 and Figure 14), since apart from the undisturbed flow (high above the airfoil) it included regions of separated flow (for the SC study case) or highly vortical flow (for the VG study case). It was hence decided to omit the standard deviation filter. Given the fact that 2000 snapshots were used to generate the average flow statistics, the random error introduced by a few outliers not excluded was insignificant. A double correlation filter was used to locally examine the validity of the processed vectors. Spurious vectors were replaced using a 3x3 local mean.

Spatial resolution

Stereo-PIV is a very popular technique for measuring vortex flows (M. Ramasamy & Leishman, 2006; Godard & Stanislas, 2006; Manikandan Ramasamy et al., 2011; Velte & Hansen, 2012) since, apart from being non-intrusive, has the advantage of providing instantaneous realizations of all three velocity components in a plane. However, spatial resolution can be an issue, especially for flows with steep spatial gradients. (Martin et al., 2000) found that to sufficiently resolve a vortex flow the ratio of probe size to vortex core radius, α_{RES}, should be

$$a_{RES} = \frac{L_m}{r_c} < 0.1 \qquad (2)$$

where L_m is the length of the interrogation area and r_c is the vortex radius.

In the present set of experiments this was particularly challenging given the small size of the VGs, the resulting vortices and the distance of the cameras from the measurement planes. For plane A, where distance from cameras is the greatest and vortex size is the smallest, the vortex radius, defined as the distance between the two vorticity peaks, was found to be 7.4mm. The desired resolution was achieved by using Macro lenses (150mm), high resolution cameras (4Mpixel) and image deformation, as described in (M. Ramasamy & Leishman, 2006), in post-processing.

Sample size effect

The effect of sample size on the measured mean velocities was investigated on two different points, Point A, inside the SC, and Point B, outside of it. Figure 11 and Figure 12 show the results for the streamwise component (U) for the point inside and outside the SC, respectively. The behaviour of the other components was similar so they are not presented here. The mean streamwise velocity at each point based on the maximum sample size, 2000, is drawn as a straight solid line and the 95% confidence interval is given with a dashed line. Mean values computed from groups of 100, 250, 500, and 1000 samples are also plotted in the graphs. As expected the data variation is a lot higher for Point A, inside the SC. 2000 samples were taken for all measurement planes. For this number of samples the average velocity components are measured with a 95% confidence interval of at most ±0.23m/s or ±0.9% of the free stream. For the rms quantities the corresponding confidence interval is 6.0%.

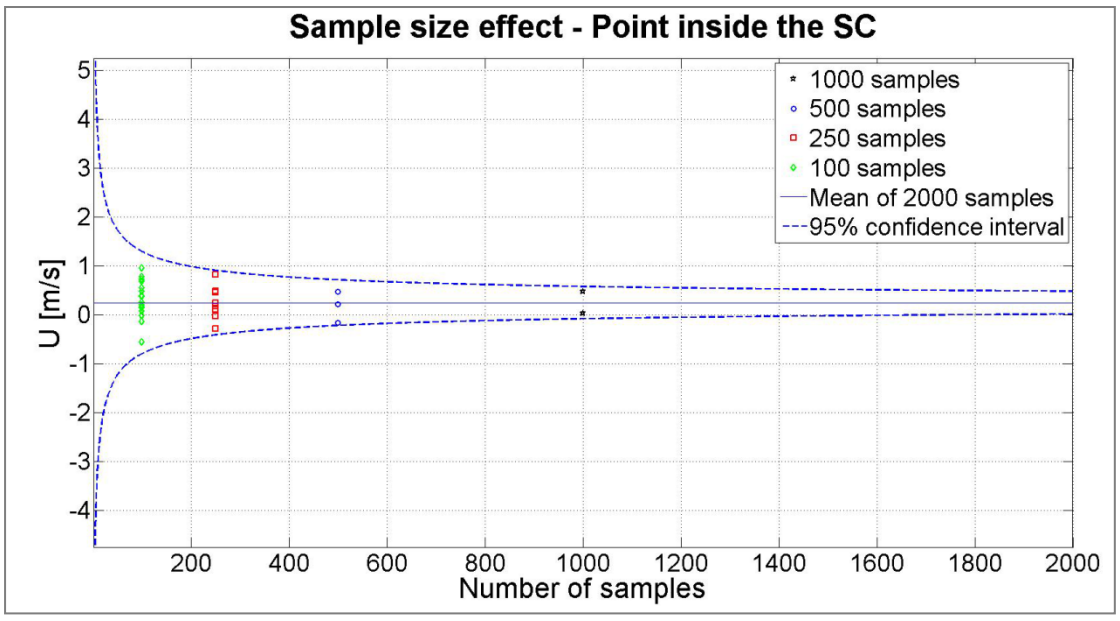

Figure 11: Sample size effect for the streamwise velocity component (U) at Point A, inside the SC. Data from plane C, normal to the flow at x/c = 1.06, 10° case.

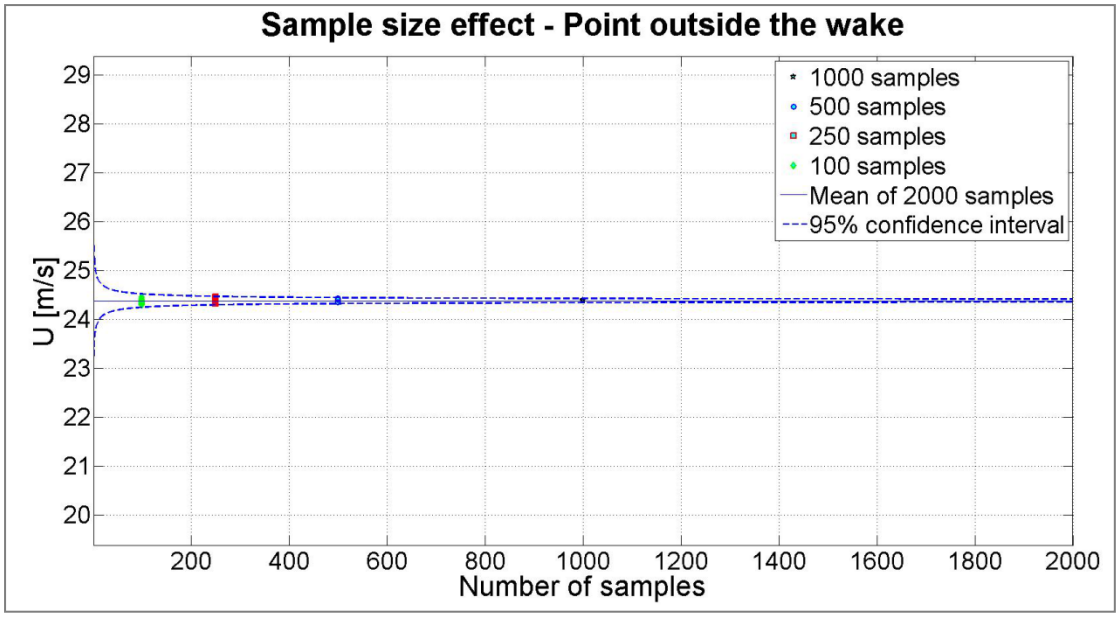

Figure 12: Sample size effect for the streamwise velocity component (U) at Point B, outside the SC. Data from plane C, normal to the flow at x/c = 1.06, 10° case.

Peak-locking effect

Peak locking is a discretisation effect that occurs when the size of the particle image is small, i.e. comparable to the size of the CCD pixel. When peak-locking exists in the measurements displacement estimation is biased towards integer pixel values. This has no effect on the averaged quantities but can affect the turbulence statistics, especially if the fluctuating displacements are less than 0.5px (Christensen, 2004). (Angele & Muhammad-Klingmann, 2005) found that when the ratio $U_d/U_{rms} < 2.0$ where U_d is the velocity corresponding to a displacement of one pixel and U_{rms} is the root-mean-square velocity, then the errors introduced due to peak-locking are not significant (e < 1%).

As an example Figure 13 and Figure 14 show the displacement histogram for a plane at x/c = 0.8 for the uncontrolled and the controlled case respectively. There is limited, if at all, peak locking effect in the data. Also, only a small portion of the measured displacements (d) is in the region -0.5px < d < 0.5px since displacement probability distribution is distributed over at least a few pixels. Finally, the U_d/U_{rms} ratio was found to be lower than 2.0. Based on the above facts it was concluded that peak-locking should have a negligible effect on the statistics presented in the present report. Displacement histograms for the other measurement places were similar and are not displayed here.

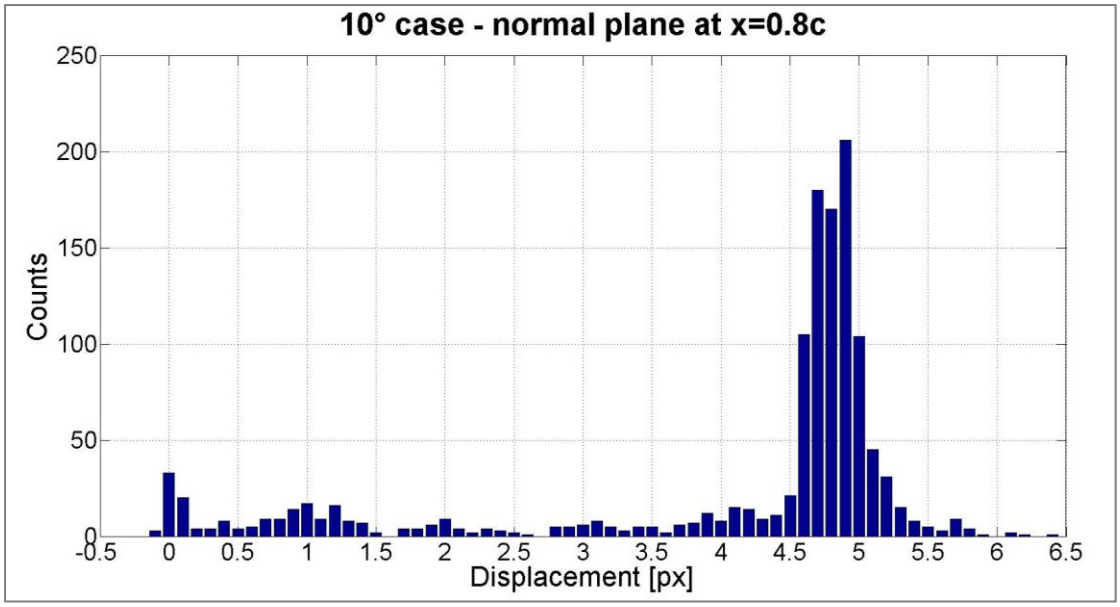

Figure 13: Displacement histogram for plane normal to the flow at x/c = 0.8, 10° case, no VGs.

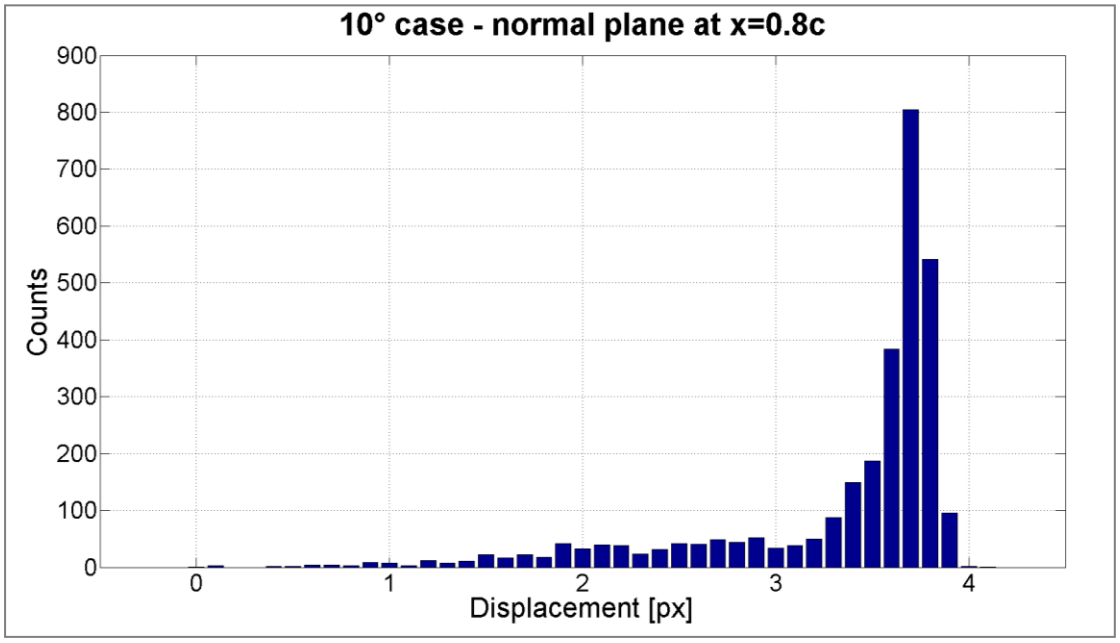

Figure 14: Displacement histogram for plane normal to the flow at x/c = 0.8, 10° case, case with VGs.

2.5.2 Camera vibration analysis

The cameras were located inside the test section, 1.2c downstream of the wing TE. The camera base was secured on elastic anti-vibrating pads and both cameras were mounted on reinforced Scheimpflug angle adjustable mountings. Since the cameras where located inside the test section two issues needed to be addressed.

1. Determine whether and how the camera base affected the flow over the wing model.
2. Determine whether the cameras vibrated and if so, quantify the effect of this vibration on the results.

As regards the first issue, pressure measurements with and without the cameras in the test section where practically identical so it was concluded that the cameras and the camera base did not affect the flow on the wing, see Figure 15.

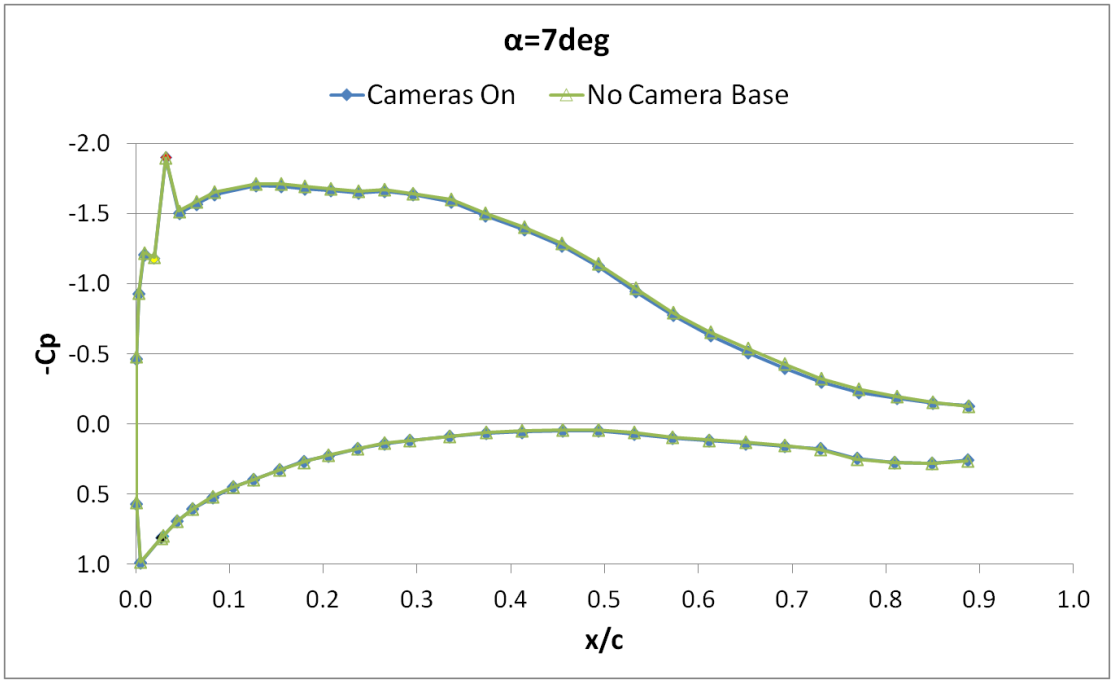

Figure 15: Pressure coefficient distribution around the wing with and without the Cameras in the test section.

The issue of camera vibration has been encountered in the past by various researchers. Some apply a frame by frame correction to the measurements (Bremner et al., 2005; Bian et al., 2009), whereas others simply attribute *non-physical* variation of the measured rms data to camera vibration (Krothapalli et al., 2003; Kang et al., 2008).

In the present case camera vibration was examined using a procedure similar to that of (Bremner et al., 2005; Bian et al., 2009), who applied a frame by frame correction using a fixed point in the camera FOV as a reference. In the present case the wing TE position was used for the same reason. However, during the actual measurements the wing TE was out of focus so a frame by frame correction could not be applied. Instead the error introduced by the camera vibration was quantified before the measurements and as it will be shown it was found to be acceptably small.

In more detail, initially a series of photos was taken with the cameras focused at the wing TE. The TE position could be directly extracted from the PIV images as it was a clear step in the image light intensity. One such PIV image is shown in Figure 16 (left). For all the image columns, one of which is highlighted in Figure 16 (left), the light intensity had a distribution similar to the one shown with blue circles in Figure 16 (right). A 3rd order curve was fitted through the light intensity data of each photo to allow the identification of the TE location with sub-pixel accuracy, as suggested by (Bian et al., 2009). The TE was defined as the location where the intensity derivative had a maximum value.

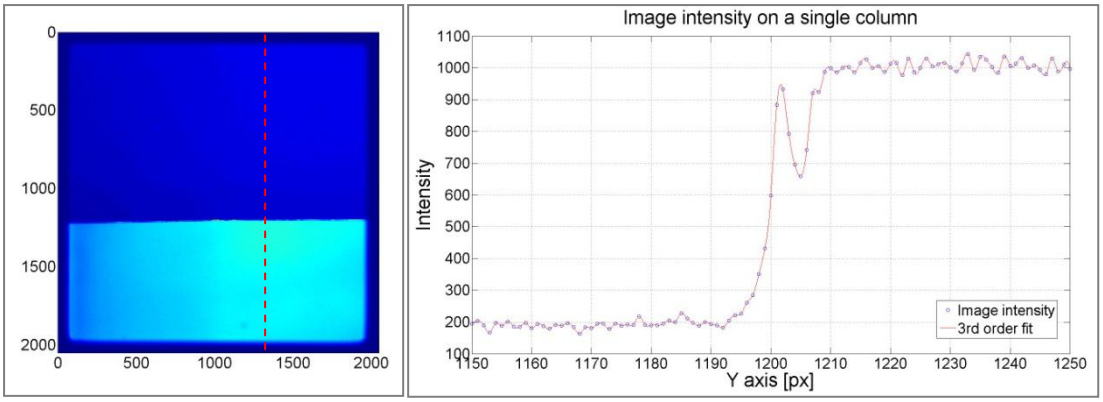

Figure 16: In the left part of the figure an image from the α = 7° vibration test case is shown, axes in pixels. One column is highlighted with red dashed line. Image intensity along the highlighted column is given in the right part of the figure.

In Stereo PIV a single snapshot consists of two images (Image A and Image B) for each camera (left and right) which are taken consecutively, with a time distance equal to the pulse separation time. The pulse separation time is usually at the order of a few μsec, whereas the time distance between two snapshots can be at the order of a few seconds. Given the large difference in scales, camera displacement was examined both between Image A and Image B of a single snapshot and between snapshots.

As Figure 17 and Figure 18 show, the camera displacement from Image A to Image B of a single snapshot and the camera displacement from Image A of one snapshot to Image A of the next snapshot are similar. They both follow an almost normal distribution (see Figure 19 and Figure 20) with a mean value of 0.0px and a standard deviation of 0.2px, or 12.7μm. It is also observed that both cameras (left and right) have similar behaviour. The above set of data refers to the α = 7° case, when a 90mm lens was used.

The camera displacement from Image A of one image pair to Image A of the next image pair for the 10° case is given in Figure 21 and the corresponding PDF in Figure 22. The distribution is again almost normal with a mean value of 0.0px and a standard deviation of 0.1px, or 12.3μm. It is observed that although the displacement standard deviation is smaller for the 10° case (50mm lens) when expressed in px, it is very similar to the α = 7° when computed in μm. Equivalently when the magnification factor is taken into account the camera displacement is not affected by the lens being used, or the wing angle of attack. This suggests that it is purely mechanical.

Based on the above findings it was concluded that the cameras were vibrating with zero time-mean and small amplitude. As a result the averaged data should not be affected by it.

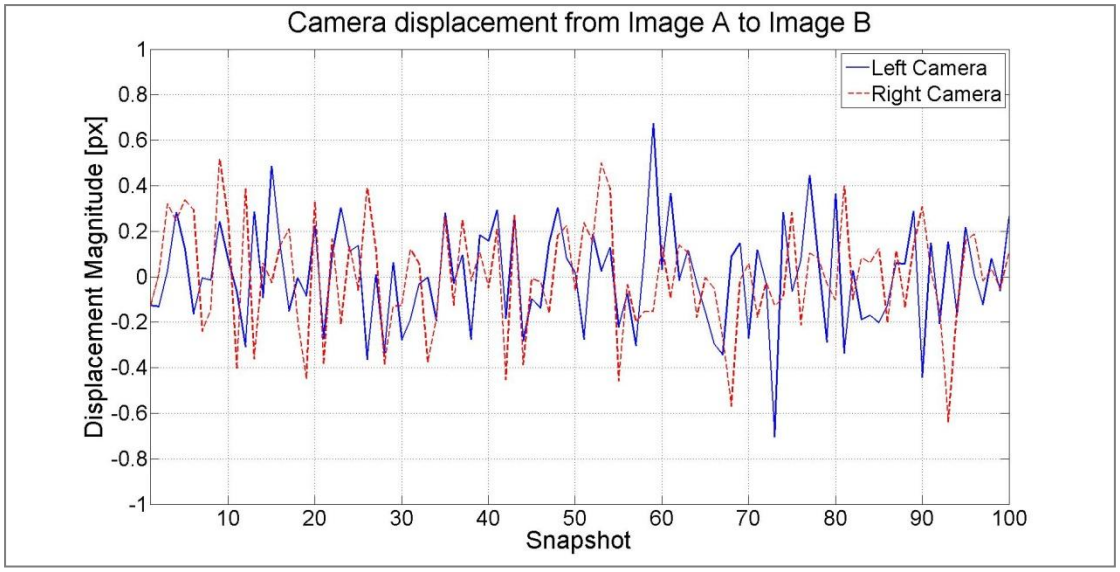

Figure 17: Camera displacement from image A to Image B of an image pair. α = 7°, Re = 0.87x10^6, 90mm lenses, Magnification ≈ 63.5µm/px.

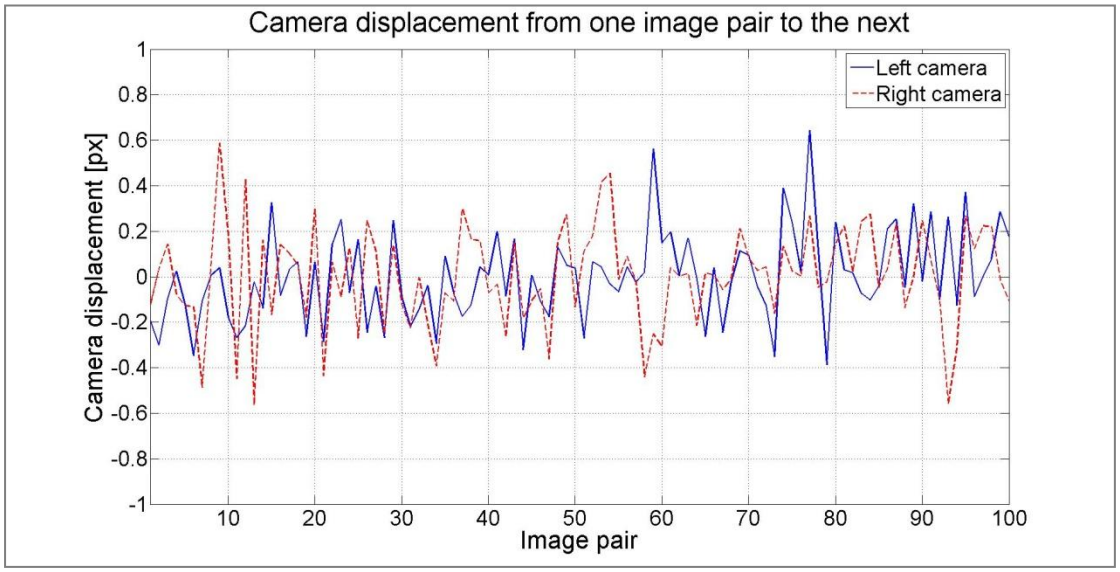

Figure 18: Camera displacement from image A of one image pair to Image A of the next image pair. α = 7°, Re = 0.87x10^6, 90mm lenses, Magnification ≈ 63.5µm/px.

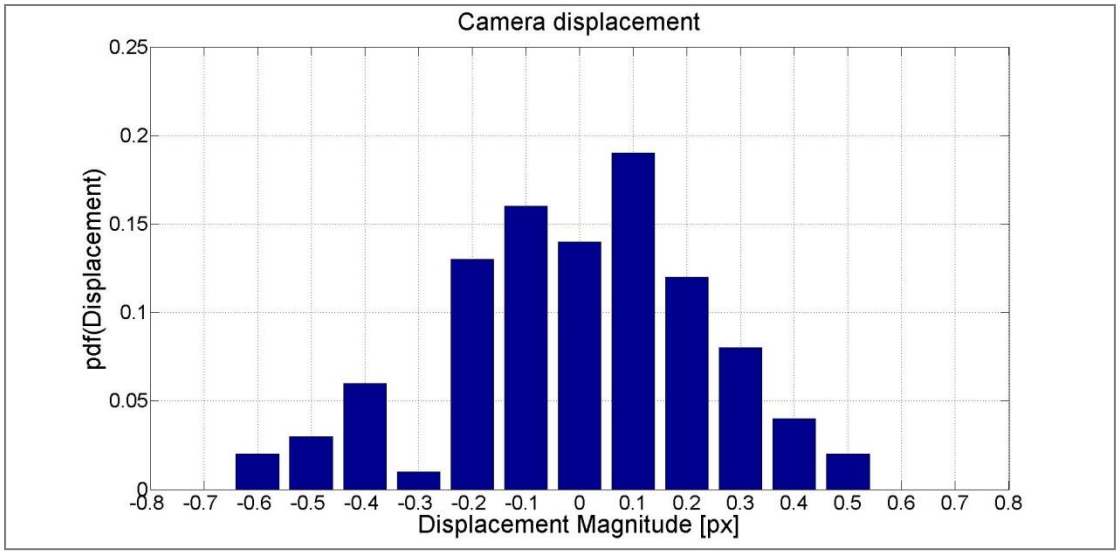

Figure 19: Camera displacement from image A to Image B of an image pair. α = 7°, Re = 0.87x10^6, 90mm lenses, Magnification ≈ 63.5µm/px. Right camera.

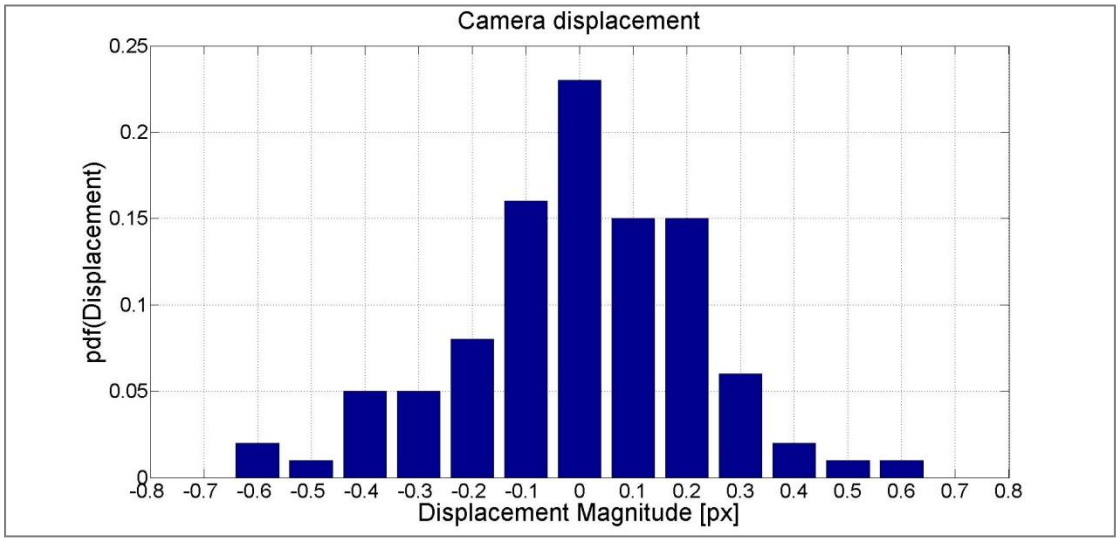

Figure 20: Camera displacement from one image pair to the next. α = 7°, Re = 0.87x10^6, 90mm lenses, Magnification ≈ 63.5µm/px. Right camera.

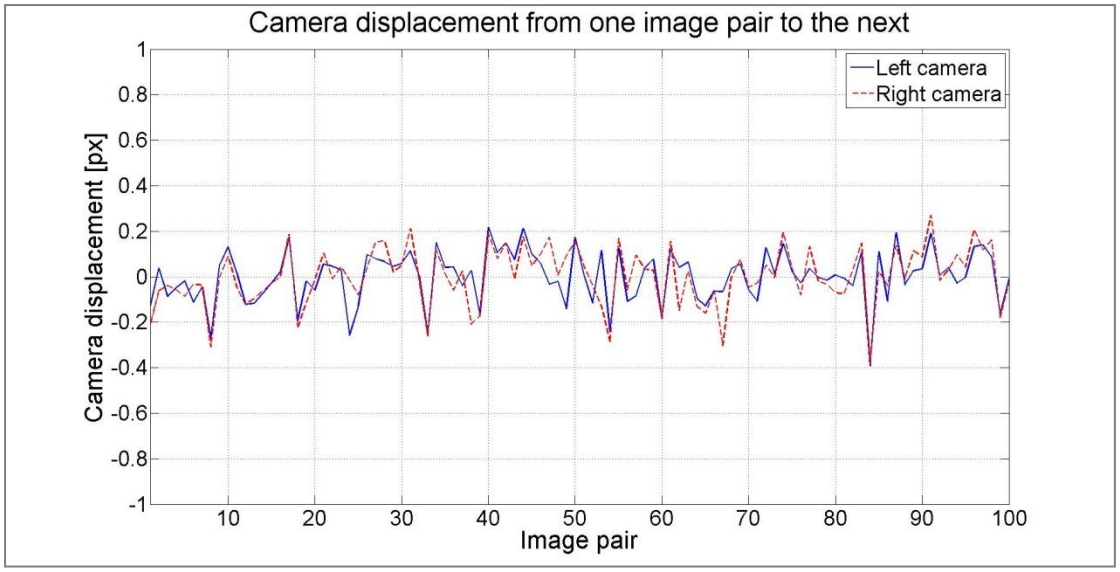

Figure 21: Camera displacement from one image pair to the next. 10°, Re = 0.87x10^6, 50mm lenses, Magnification ≈ 123.5µm/px.

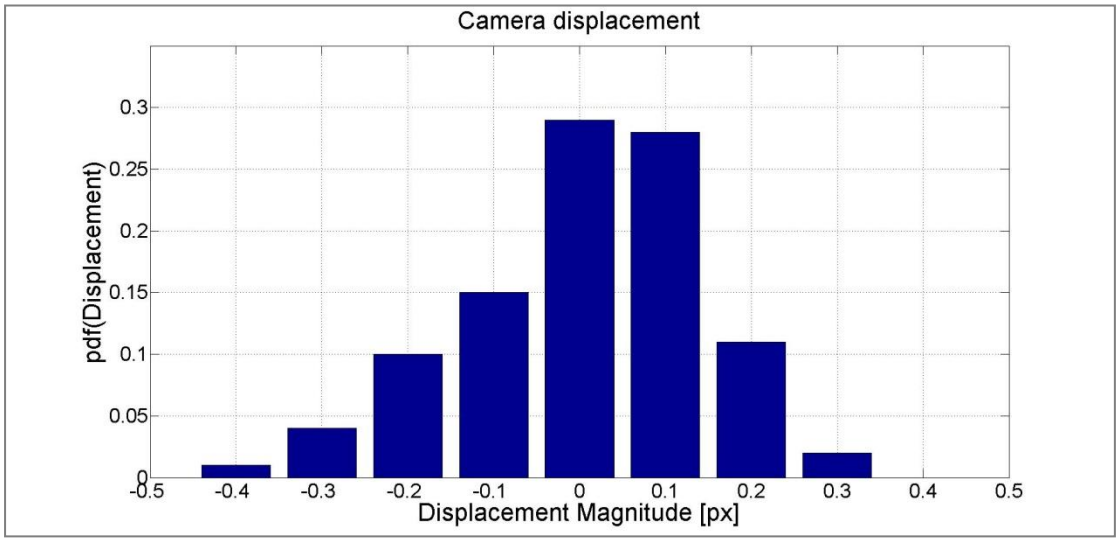

Figure 22: Camera displacement from one image pair to the next. 10°, Re = 0.87x10^6, 90mm lenses, Magnification ≈ 123.5µm/px. Left camera.

3 Computational modelling

3.1 Solver

The in-house solver MaPflow (Papadakis, 2011) was used in the present investigation. MaPflow is an unsteady RANS MPI parallelised, multi-block finite volume compressible code applied to mixed structured/unstructured grids. The code is equipped with pre-conditioning for low Mach flow conditions and uses the Spalart - Allmaras turbulence model. The discretisation is 2nd order accurate in time and space while dual time stepping is introduced in order to facilitate convergence.

3.2 Computational mesh

To create the necessary computational meshes either an in-house code (GFOIL) was used or the commercial software ICEM CFD. Details of typical grids around the airfoil are shown in Figure 23 and Figure 24, for the case with and without VGs. Grid dependence studies were performed for all applications and the results are given in the relevant chapters.

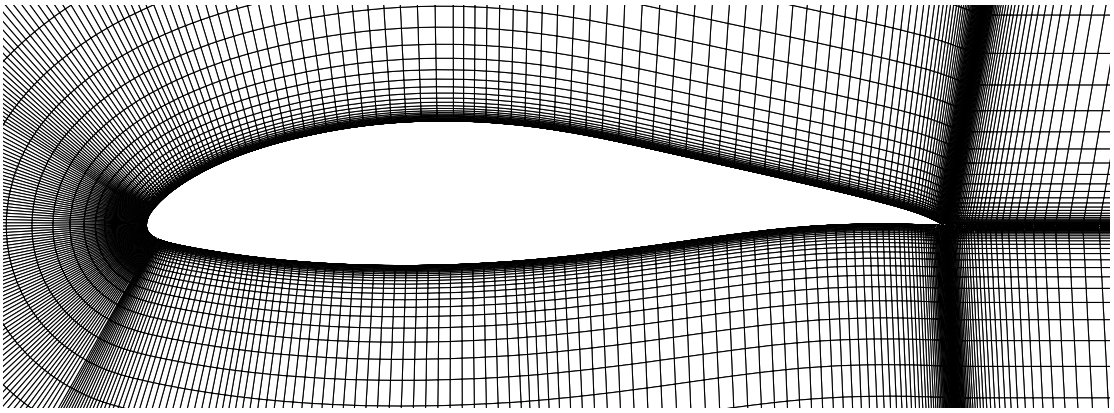

Figure 23: Detail of a typical grid around the airfoil. Case without VGs.

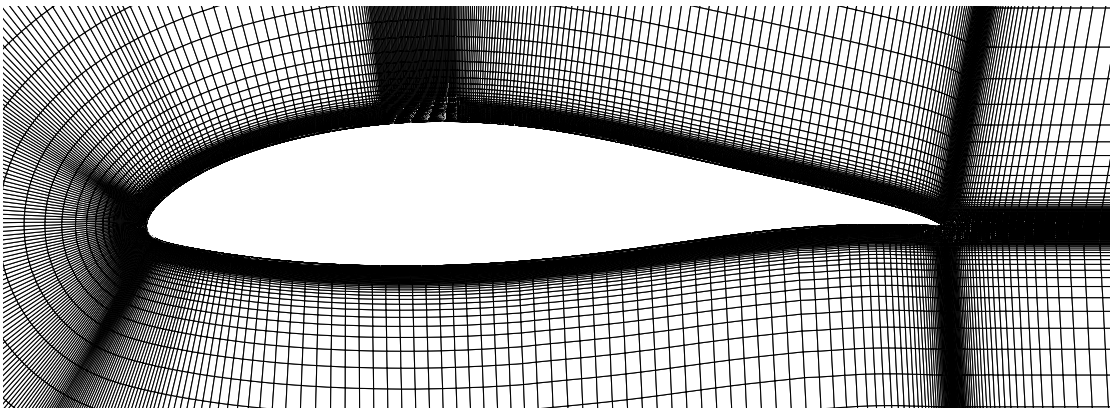

Figure 24: Detail of a typical grid around the airfoil. Case with VGs.

3.3 BAY Model

The vortex generators and the zigzag tape used in the experiments were not fully resolved in the simulations because of their prohibitively high computational cost. Therefore a more engineering approach has been followed. The BAY model, introduced by (Bender et al., 1999), was implemented. The model assumes that the presence of a zero thickness vane VG

can be represented as a source term in the momentum and energy equations. The source term simulates the lift force introduced by the VG in the flowfield. This term aligns the flow with the VG direction. The derivation of the source term as written originally by (Bender et al., 1999), is repeated here for completeness.

The momentum and energy equations become:

$$V_i \frac{\Delta(\rho\vec{u})_i}{\Delta t} = \sum_j \vec{F}_{M_j} S_j + \vec{L}_i \tag{3}$$

$$V_i \frac{\Delta(\rho E)_i}{\Delta t} = \sum_j F_{E_j} S_j + \vec{u} * \vec{L}_i \tag{4}$$

where

$$\vec{L}_i = c_{VG} S_{VG} \frac{V_i}{\sum V_i} \beta\rho|\vec{u}|^2 \hat{l} \tag{5}$$

and

$\hat{l}$ is a unit vector in the direction of the lifting force acting on the flow

$\vec{u}$ is the local velocity,

ρ is the local density,

β is the angle of incidence of the vane with the primary flow,

V_i is the volume of the grid cell,

$\sum V_i$ is the sum of the volumes of all of the cells over which the model is being applied,

S_{VG} is the VG planform area, and

c_{VG} is an empirical constant subject to calibration.

The vane VG surface is described by three unit vectors, namely $\hat{t}$ that is tangent to the VG chord, $\hat{b}$ that is along the VG span and $\hat{n}$ that is normal to the VG surface and the other two unit vectors. The unit vector $\hat{l}$ is assumed to be normal to the local velocity vector and the unit vector $\hat{b}$, see Figure 25.

$$\hat{l} = \frac{\hat{u}}{|\vec{u}|} \text{ x } \hat{b} \equiv \hat{u} \text{ x } \hat{b} \tag{6}$$

where $\hat{u}$ is a unit vector in the direction of the local flow. Using the small angle approximation the angle α is:

$$\beta \approx \sin\beta = \cos\left(\frac{\pi}{2} - \beta\right) = \hat{u} \cdot \hat{n} \tag{7}$$

To approximate the loss of side force at higher angles of attack (of the VG with respect to the free stream) the lift force source term is also multiplied by a factor of $\hat{u} \cdot \hat{t}$. The equation for the lift force source term is:

$$\vec{L}_i = c_{VG} S_{VG} \frac{V_i}{\sum V_i} \rho |\vec{u}|^2 (\hat{u} \cdot \hat{n}) \left(\hat{u} \times \hat{b}\right) (\hat{u} \cdot \hat{t}) \qquad (8)$$

The c_{VG} constant defines the intensity with which the local velocity is aligned with the flow. If c_{VG} is too low then the VG is not modelled correctly, whereas results reach an asymptotic behaviour for large values of c_{VG} (Waithe, 2004a). In the latter study a value of c_{VG} = 10 was used, whereas (Bender et al., 1999) suggest c_{VG} > 5 and (Jirasek, 2005) c_{VG} = 7. In the present case the greatest value c_{VG} = 10 was selected for the solution to be constant independent.

The model was applied in its jBAY variation (Jirasek, 2005) in which the VG is replaced by a surface with zero thickness. The cells, to which the source term is added, are the cells that intersect this VG surface, see Figure 25 centre and right, where a schematic representation is given.

Various researchers (Waithe, 2004a; Jirasek, 2005; Dudek, 2011) have shown that simulations using the BAY model produce results similar to simulations of fully resolved VGs at a significantly lower computational cost. Naturally, the BAY model has some inherent shortcomings, such as its inability to predict vortices produced by finite thickness VGs (Joubert et al., 2011) or reversed flow on the VG surface. Still it remains one of the most popular VG models mainly due to the quality of the produced results, its limited empiricism and its ease of use and implementation.

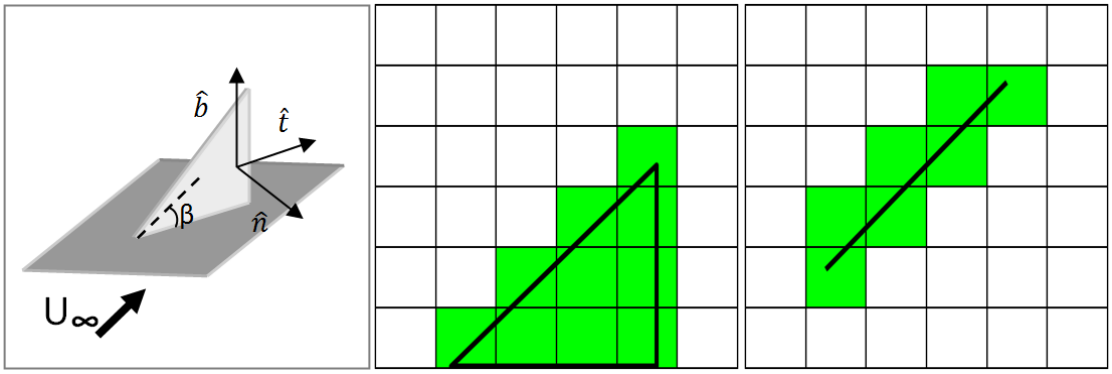

Figure 25: Unit vectors for the VG geometry. (Centre) Side and (right) top view of the cells on which the BAY model is applied.

Part II.

Three-dimensional separation

4 Geometrical characterization of Stall Cells

In this chapter the tuft flow visualization data are presented. The tuft set up is described in Chapter 2. The dynamic nature of SCs is described and a way to suppress it is proposed. The geometrical features of the stabilized SC and their dependence on Re, angle of attack and AR are discussed.

4.1 Metrics

The examined experimental parameters (Re, AR, α, zigzag tape) and their range of values are given in Table 3, in page 40. At each setting a video of at least 30 sec was filmed and analysed according to the following rule: a tuft would be considered "belonging to a SC" if it would deviate from the chordwise direction most of the time during a run. Based on the number of tufts belonging to a SC the following geometrical metrics were introduced, all defined in Figure 26:

a) The SC width as % of the span (SC width = z/S)
b) The most upstream x/c location of the SC boundary (earliest separation point)
c) The SC area as % of the wing planform area

$$\mathrm{SC}_{\text{relative area}} = \frac{\mathrm{SC}_{\text{actual area}}}{\mathrm{Wing}_{\text{planform area}}} \tag{9}$$

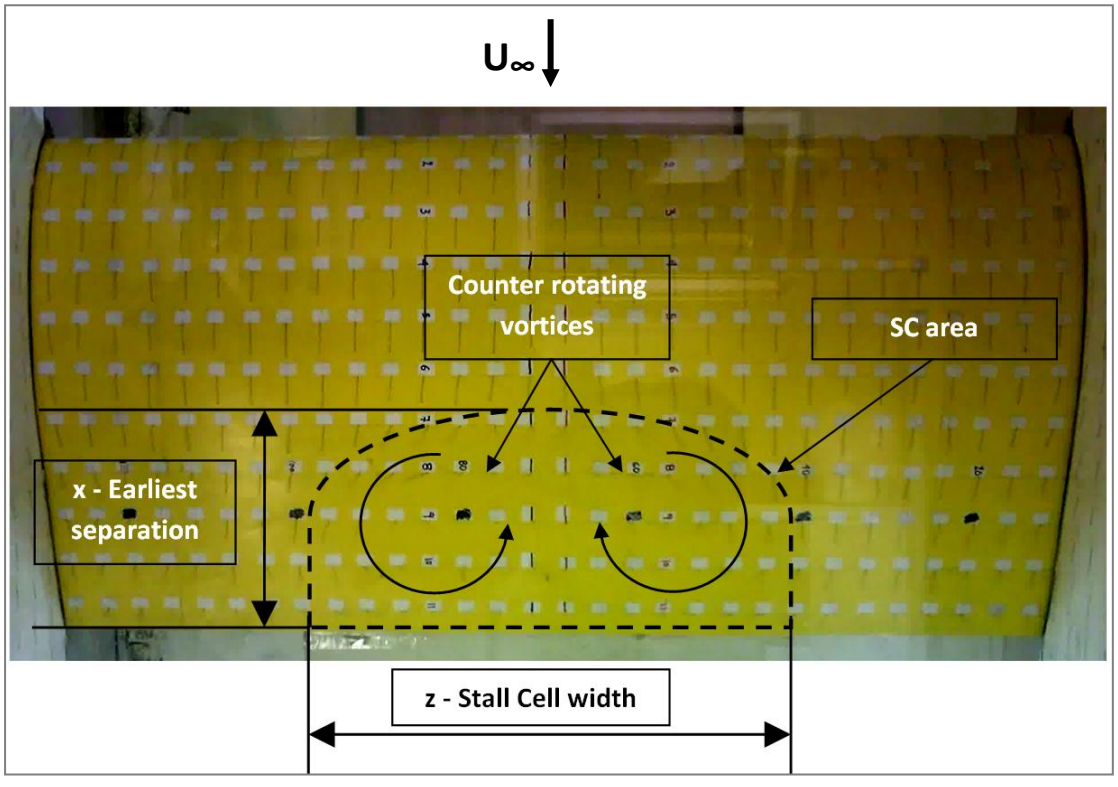

Figure 26: Schematic view of a SC for AR = 2.0, Re = 1.0x10^6, α = 8.0°, with local disturbance at the wing span centre. The direction of the flow is from top to bottom.

These metrics were chosen to examine the SC size and shape which clearly affects the wing performance. For example it is common practice for wind tunnel wing models to have

pressure taps only at a single spanwise location, usually at the mid span. In the case of a single SC the earliest separation point would crucially affect the measured pressure distribution.

For each of the spanwise series of tufts that a SC would occupy, the uncertainty would be +/- 2 tufts, i.e. one tuft on each end of the tuft series. Therefore the uncertainty in the measurement of the SC width is +/-6.7% and +/-9.1% for AR = 2.0 and 1.5, respectively. Similarly, the chordwise uncertainty for the SC boundary line is approximately +/-10%. Finally the uncertainty for the SC area ranged from +/-1.6% (smallest SC) to +/-3.5% (largest SC) of the wing area for the AR = 2.0 case and from +/-1.2% to +/-4.7% for the AR = 1.5 case. The error bars in the following graphs are drawn based on the maximum values.

Parameter	Re number [x10^6]	AR	α	ZZ tape
Range	0.5, 1.0, 1.5	1.5, 2.0	6°-16°	Yes - No

Table 3: Experimental parameters for the tuft experiments and their values.

4.2 Stall Cell stabilization

The first series of tests were conducted without any extra flow perturbation apart from what the tufts themselves induce, aiming at exploring the possible dynamic behaviour of SCs at higher Re numbers as compared to the findings of previous works (Gregory et al., 1971; Yon & Katz, 1998).

Patterns with one, one and a half or two SCs were observed indicating the existence of multiple modes. On occasions, even a "half SC" would form at the wing tips, i.e. only one vortex structure next to the fence forming a "full SC" together with its mirror vortex with respect to the fence wall. Similar oil flow visualization results have been reported (Velte & Hansen, 2012), at Re 0.9x10^6, and earlier by (Gregory et al., 1971), at Re 3.14x10^6.

In certain cases, the pattern switched from one state to another, in others a single SC would move in the spanwise direction while in yet others there were one or several SCs that appeared and disappeared in a seemingly random manner. In this first series of tests longer videos were filmed (even longer than 60 sec) to allow for the different states of the flow to be documented. In the particular configuration a single SC was always formed at the onset of three-dimensional separation. Formation of a second (half or full) SC would occur at higher angle of attack for a specific Re number. However, clear correlation with any of the basic flow parameters (Re number or angle of attack) was not concluded.

Next a zigzag (ZZ) tape was fitted all along the span at the LE of the model that did not cancel the dynamic character of the SCs suggesting that the dynamic nature of SCs is not linked to transition.

Assuming, in accordance to the theoretical analysis by (Rodríguez & Theofilis, 2010), that SCs result from large enough self-excited and self-sustained spanwise perturbations, it was decided to force the flow to select one such mode by introducing a spanwise disturbance and therefore render the further investigation possible. A 0.4mm thick zigzag tape with 60^o angle(shown in Figure 27) was added at mid-span covering 10% of the span. The tape was

placed at x = 0.02c so that it would always be at or prior to natural transition. The specific position is the natural transition point that XFOIL (Drela, 1989) predicts for the highest Re number ($1.5x10^6$) and angle of attack (16deg) tested. No ZZ tape was added on the pressure side. Of course, a ZZ tape of sufficient height would also locally trip the flow, apart from introducing a localized disturbance. However this was not the purpose in the present case. It was decided to use an oversized ZZ tape even for the lowest Re number ($0.5x10^6$) so that the trip tape would be oversized throughout the range of Re numbers considered.

In order to only trip the boundary layer at this chord position (0.02c) for the lowest Re number in this test ($0.5x10^6$), a grit roughness height of about 0.88 mm would be sufficient, as calculated by the method of (Braslow & Knox, 1958). ZZ tapes, however, are more effective in tripping the flow than grit roughness as (Timmer & Van Rooij, 2003) suggest and according to their approach a ZZ tape of 0.29 mm height would be high enough to trip the flow. For Re number of $1.0x10^6$ and $1.5x10^6$ the corresponding tape heights are 0.14mm and 0.09mm, respectively. The estimation of the appropriate ZZ height is described in detail in Appendix B. Clearly the effect of the specific tape is not entirely the same, given the Re number and angle of attack range; however, in all conditions considered the ZZ tape is met by laminar flow and exceeds height requirements for transition and therefore acts as a disturbance.

Indeed the presence of the specific ZZ tape led to the creation of a fixed, single SC, positioned at the centre of the wing span. In order to examine the effect of the ZZ tape in comparison with the undisturbed case, the variation of the relative SC area with respect to the angle of attack at Re = $1.5x10^6$ and for AR = 2.0 is shown in Figure 28 with and without the ZZ tape. Except for a limited difference at $\alpha < 9^o$, the overall agreement is found to be very good. The same was observed for the SC earliest separation point and width throughout the Re numbers and AR range. This suggests that the limited span ZZ tape of the specific height causes an earlier formation of a SC, in agreement with (Moss & Murdin, 1971), and locks in a single stable SC mode without affecting the amount of separated flow on the wing suction surface for $\alpha \geq 9°$. Unless otherwise stated it is the stabilized SC that is studied in the present investigation.

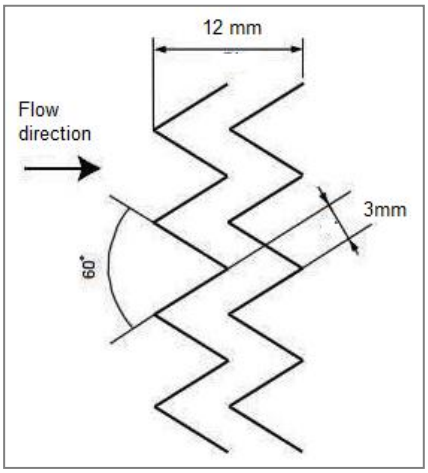

Figure 27: Geometry of the zigzag tape used for tripping the flow.

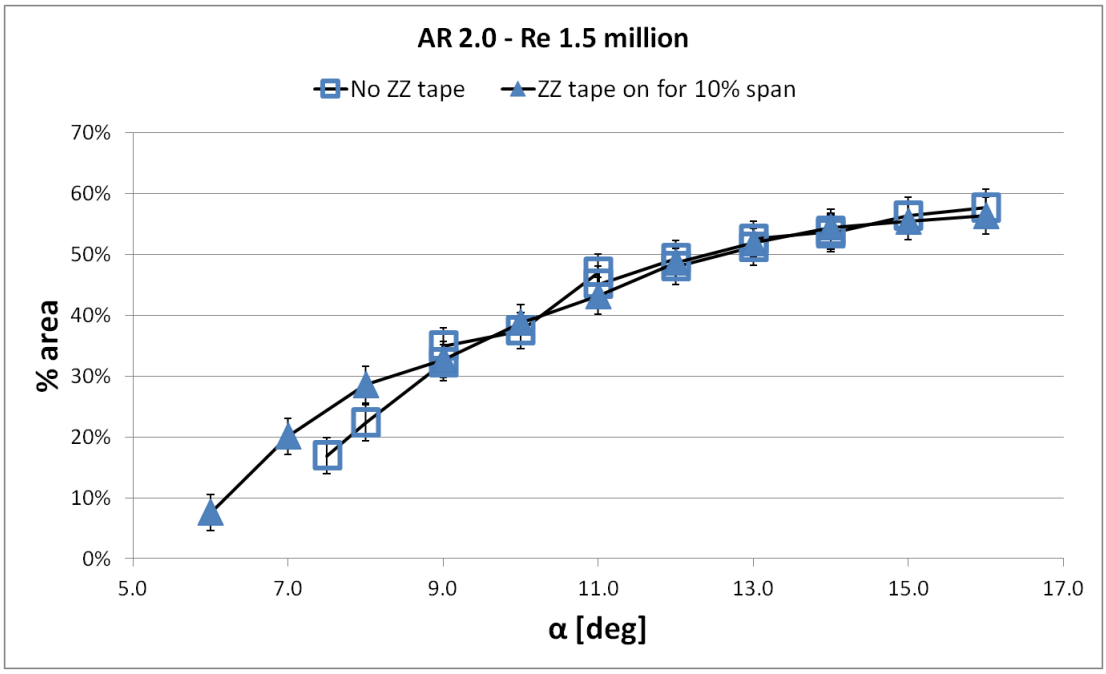

Figure 28: Relative SC area vs. angle of attack, Re = 1.5x10^6, AR = 2.0 with and without the ZZ tape. There is good agreement especially at angles of attack higher than 9° suggesting the addition of the ZZ tape does not affect the size of the SC. Multiple points on the "no ZZ tape" curve correspond to different flow states (e.g. a single SC alternating with two SCs) for a specific test set up.

4.3 Geometrical characterization of Stall Cells

The vortical structures were identifiable only when the SC was at least 3 tufts long in the chordwise direction and therefore the separation line was at x/c < 77%. This is in agreement with (Gregory et al., 1971), who found that three-dimensionality of the separated flow begins when the chordwise extent of the separated flow region exceeds about 20% of the chord and shows up as a curved separation line

In this section the metrics listed below are used in order to geometrically characterize the SC and its behaviour. They are given in terms of Re and angle of attack for two AR values (or wing spans), namely AR = 2.0 and 1.5.

- the relative SC width (z/span %) (Figure 29 and Figure 30),
- the actual SC area (Figure 31),
- the relative SC area (Figure 32 and Figure 33),
- the relative SC growth (Figure 34),
- the maximum chordwise length (Figure 35) and
- the angle at which a SC is first formed (Figure 36)

The relative SC width is increasing with Re number and angle of attack regardless of the AR, as Figure 29 shows for AR = 2.0. As this happens the two vortices move toward the wing tips and are elongated in the spanwise direction. For the smaller AR case and for all Re numbers tested, the SC reaches the full wing span a lot earlier than for the greater AR, see Figure 30 where the relative SC width is plotted against the angle of attack for Re number 1.5x10^6 and AR = 1.5 and 2.0. As an example, the growth of a SC for an increase of 1^o in angle of attack can be seen in Figure 137 (in page 164) and Figure 138 (in page 165), where snapshots from

the AR = 2.0, Re = $1.0x10^6$, case with ZZ tape are shown for α=8.0 and 9.0°, respectively. Figure 139 (in page 166) shows details from these snapshots where the growth of the SC vortex can be seen more clearly.

Until the SC covers the full span for the low AR case (at α=9.0° for Re = $1.5x10^6$), the growth of the actual SC area is very similar for both ARs, see Figure 31. This suggests that while sufficiently small, the SC grows unaffected by the proximity of the fences for a wing of fixed chord (and therefore Re). Beyond that stage, the SC is forced to grow in the chordwise direction for AR = 1.5 whereas it can still expand in both directions for the AR = 2.0 case, hence the greater area for AR = 2.0 at higher angles of attack. The fact that at an early stage the SC size is not affected by the wing span is shown in Figure 140 (in page 167) and Figure 141 (in page 168) in Appendix A, where snapshots are presented from the Re = $0.5x10^6$, 11.0°, case with ZZ tape for AR = 1.5 and AR = 2.0, respectively.

In all cases the relative SC area appears to increase asymptotically with angle of attack as Figure 32 shows for the highest Re number case. The maximum relative SC area depends on the Re number but not on AR, see Figure 33 where the SC area is plotted against angle of attack for AR = 1.5 and the three Re numbers tested. Actually after the SC area gets larger than 95% of its highest value at $\alpha = 16^o$, there is no difference between the two AR cases. This happens for $\alpha > 13^o$ when Re = $1.5x10^6$ and Re = $1.0x10^6$ and for $\alpha > 14^o$ when Re = $0.5x10^6$.

However, the SC relative area is not the same throughout the polar. The initial rate of increase is considerably higher for AR = 1.5 than for AR = 2.0 leading to higher relative SC area values for the smaller AR case at intermediate angles of attack. This is explained by the fact that, at low angles of attack the actual SC area is the same for the two ARs, whereas the total area is not. For higher angles of attack the rate of increase is gradually reduced for AR = 1.5 until the SC reaches the same relative size at the end of the polar in both cases, as mentioned.

As far as the SC relative area is concerned, it is found that it increases with Re number, albeit with a decreasing rate for a given angle of attack (e.g. Figure 33). This suggests that the maximum SC relative area is not expected to grow significantly at higher Re numbers. Snapshots for the AR = 2.0, $\alpha = 14^o$ case are given in Appendix A (Figure 142, Figure 143 and Figure 144, in pages 169 to 171) for the three Re numbers considered.

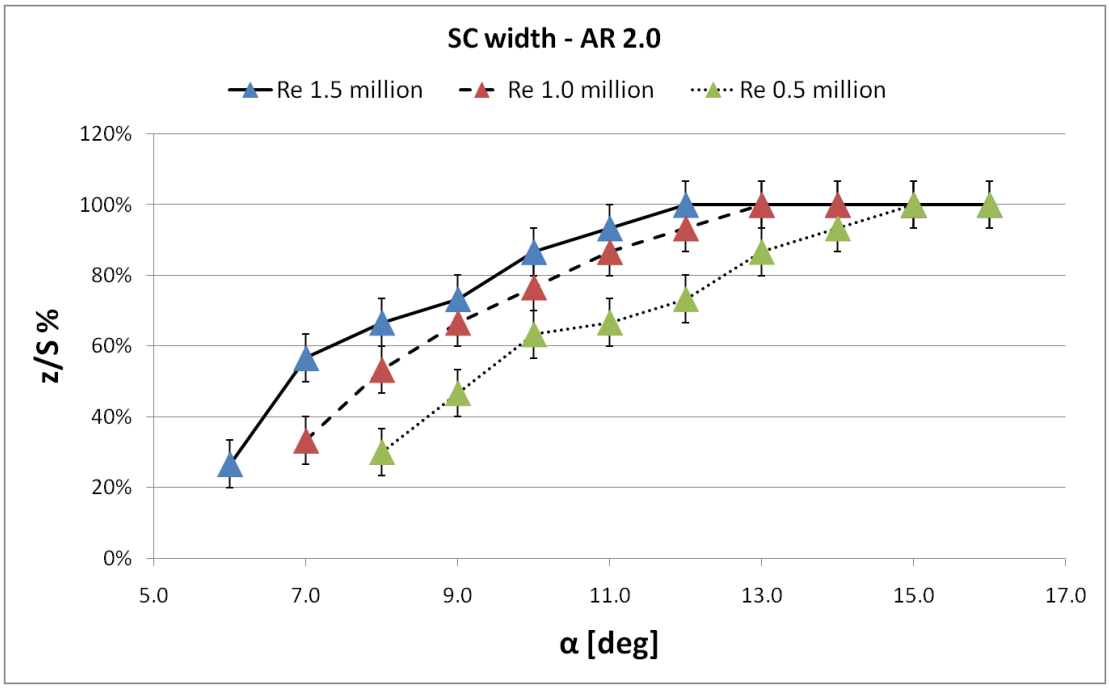

Figure 29: SC width vs. angle of attack, AR = 2.0 for the three Re numbers considered. The SC width increases with Re number and angle of attack.

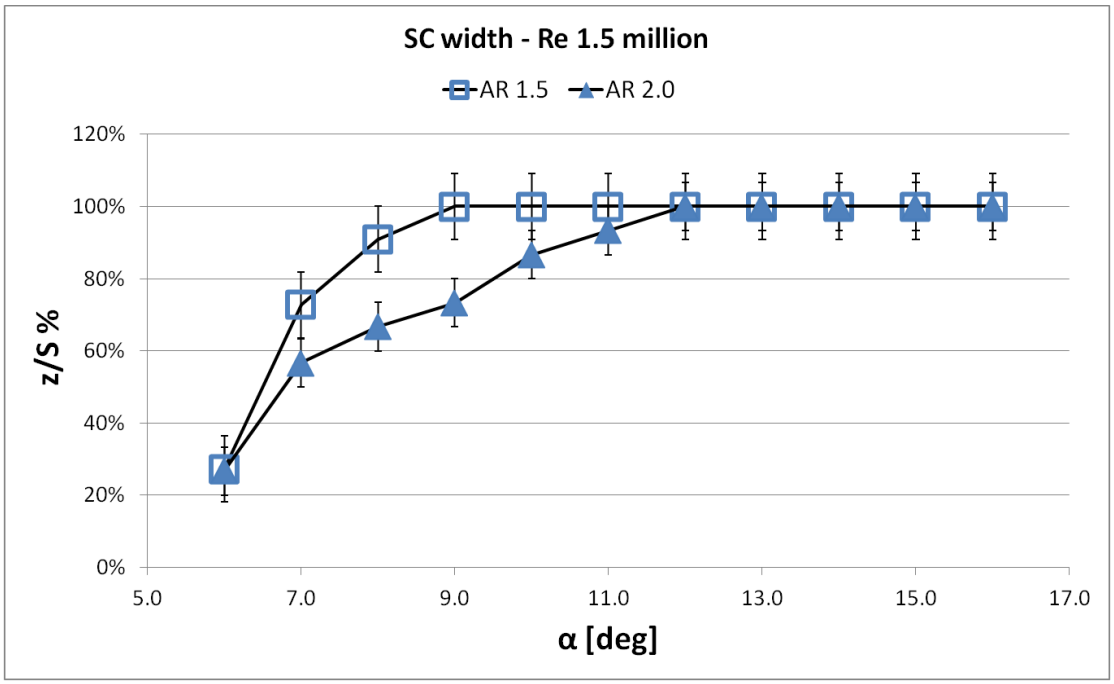

Figure 30: SC width vs. angle of attack for AR = 1.5 and 2.0 at Re = 1.5×10^6. The SC reaches the wing full width earlier for the lower AR case.

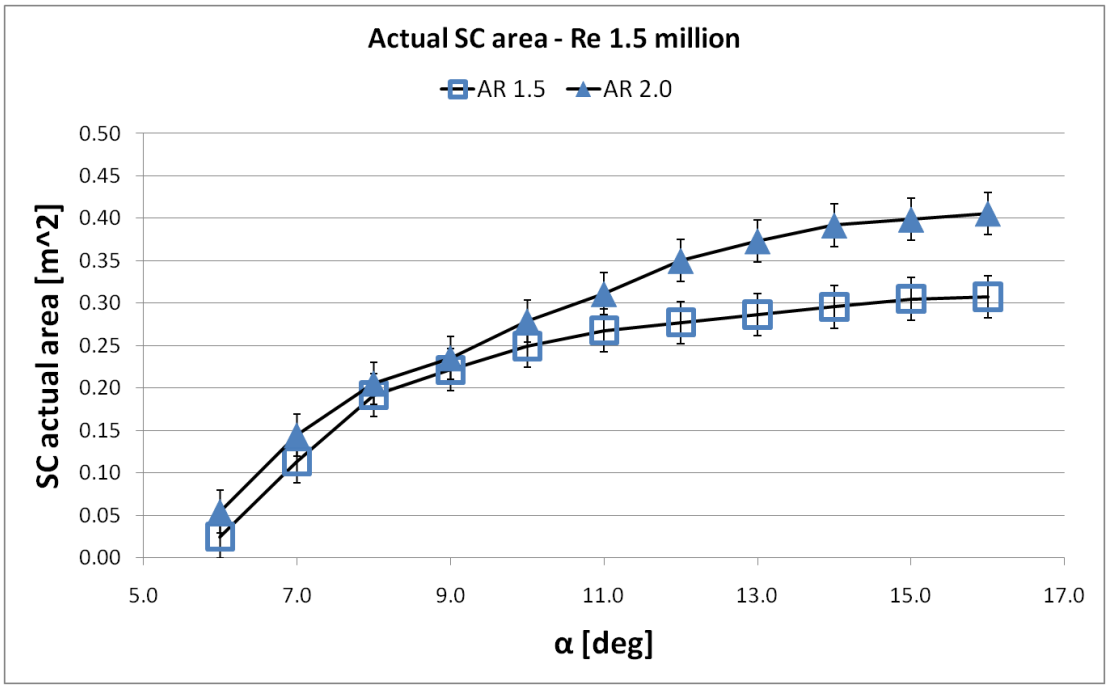

Figure 31: Actual SC area vs. angle of attack, for AR = 1.5 and 2.0 at Re = 1.5x10^6. Until the SC covers the entire wind span (α < 10deg) the SC is unaffected by the end walls.

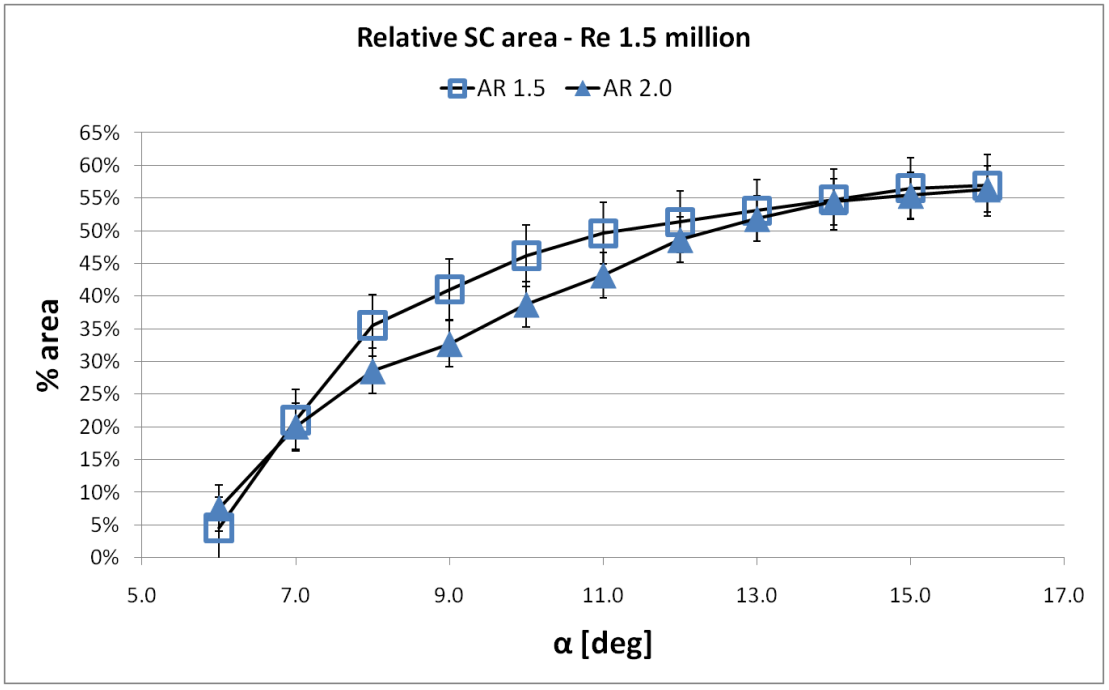

Figure 32: Relative SC area vs. angle of attack, for AR = 1.5 and 2.0 at Re = 1.5x10^6. The Relative SC area grows asymptotically with angle of attack to a maximum value that is independent of the AR. At intermediate angles of attack the relative SC area is higher for the lower AR wing.

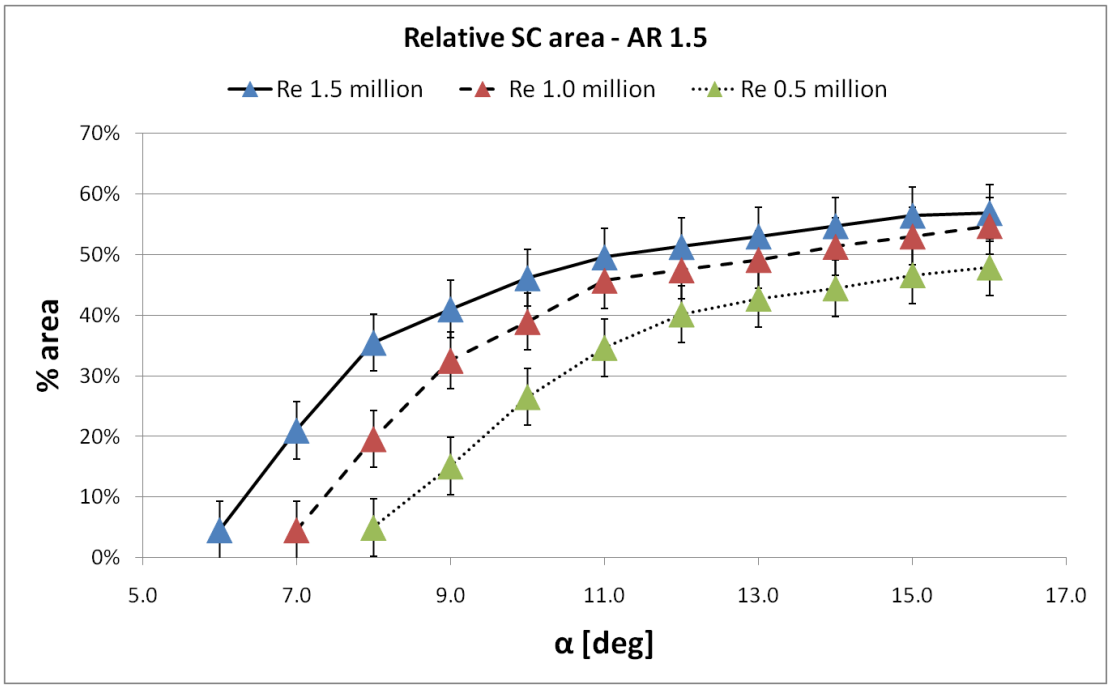

Figure 33: Relative SC area vs. angle of attack, AR = 1.5 for the three Re numbers considered. The relative SC area maximum value grows with Re number.

In order to better understand the dependence of the SC relative size growth on Re number, the relative SC growth is plotted against the SC relative area for all the cases tested in Figure 34. The relative SC growth ($SC_{Rel.Growth}$) is defined as the ratio of the SC relative area growth for a rise in Re number of 0.5x10^6 over the SC relative area at the final Re number, as shown below. It is interesting to see that the data for the relative SC growth from Re 0.5 to Re = 1.0x10^6 and from Re 1.0 to Re = 1.5x10^6 collapse on a single curve for each AR case. This suggests that for a specific increase in Re number, the relevant growth of the SC area is independent of the initial Reynolds number. Also, for relative SC area greater than 40%, i.e. for "big" SCs, the relevant growth seems to be independent of AR and approaches zero, also suggesting that maximum SC relative area is not expected to grow significantly at higher Re numbers.

$$SC_{Rel.Growth} = \frac{\text{SC relative area @ Re}_{x+0.5x10^6} - \text{SC relative area @ Re}_x}{\text{SC relative area @ Re}_{x+0.5x10^6}} \qquad (10)$$

In all cases the maximum chordwise length of a SC as determined by the earliest separation point, appeared at the centre of the SC between the two counter rotating vortices (e.g. see Figure 26) and no change in behaviour was observed even for the cases without the ZZ tape. As the angle of attack increases, the earliest separation point quickly moves upstream until it reaches x/c=46.7% (tuft column #6 in Figure 6); then remains at this level for at least a couple of degrees in all cases, before moving to x/c=36.4%, which is right before the maximum thickness location (x/c=35.1%). This behaviour is described in Figure 35 where the variation of the earliest separation location with angle of attack and Re number is given for AR = 2. Although this behaviour is profile specific, a qualitatively similar behaviour could be expected for other profiles as well, see also (Moss & Murdin, 1971).

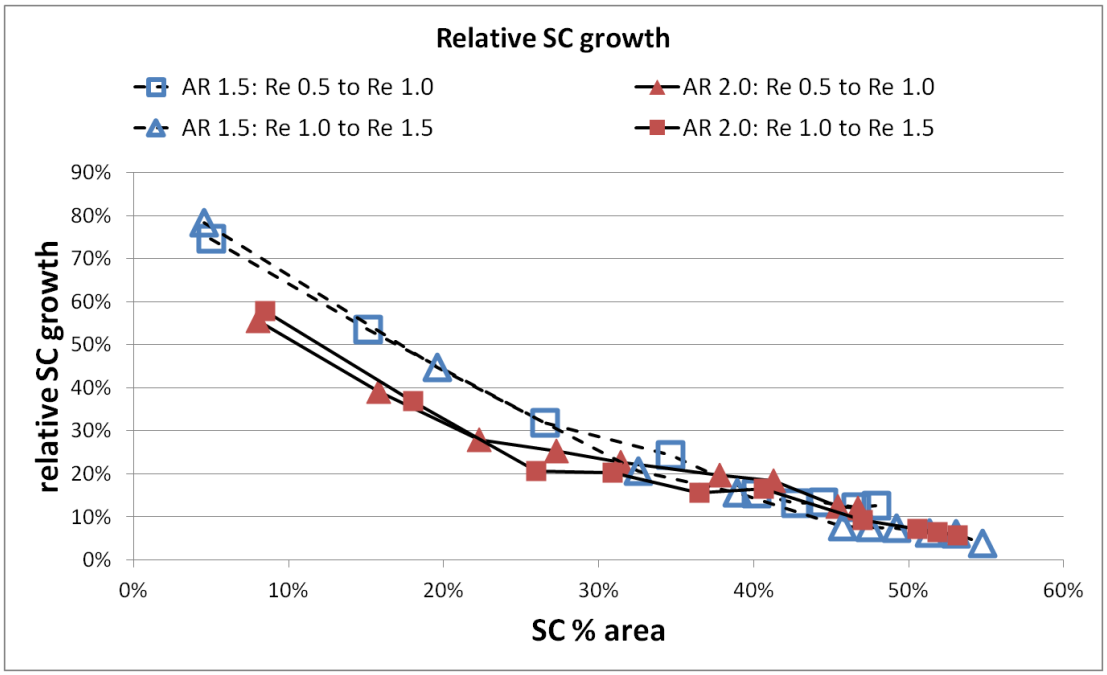

Figure 34: Relative SC growth vs. relative SC area, for the AR = 1.5 and AR = 2.0 cases. For a $0.5x10^6$ increment in Re number, the SC growth does not depend on the initial Re number.

It is observed (Figure 35) that as the Re number increases, the earliest separation point moves upstream contrary to what would be expected in 2D separation. Also unlike 2D separation the angle of attack at which a SC is first formed (α_{SC}) decreases with Re number, i.e. raising the Re number does not lead to delay of stall as expected (Jacobs & Sherman, 1937), see Figure 36 where α_{SC} is plotted against the Re number for AR = 1.5 with and without the ZZ tape. The same behaviour was observed for the AR = 2.0 cases, as well. The fact that this behaviour is not altered by the use of ZZ tape suggests that this is not a local ZZ tape effect.

Both of these "unexpected" phenomena were observed by (Yoshida & Noguchi, 2000) who used a NACA 8313 profile and report onset of separation at a lower angle of attack as Re number increases from $0.5x10^6$ to $1.0x10^6$ and that for a given angle (e.g. 16°) the separation line moves upstream as Re number increases in the same range. Yoshida and Noguchi attribute this "adverse Re number effect" to the three-dimensionality of the separated flow but make no reference to SCs. Still, the three-dimensional separation line on the wing could justify the presence of multiple SCs next to one another, see e.g. Fig. 11 in (Yoshida & Noguchi, 2000).

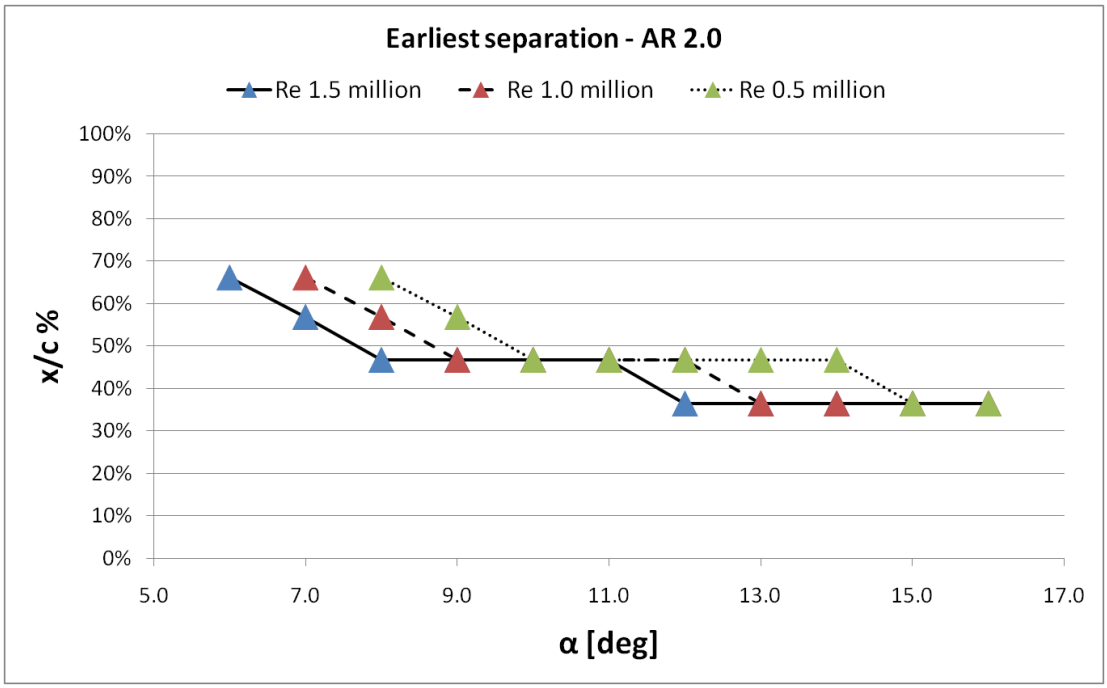

Figure 35: Earliest separation location vs. angle of attack, AR = 2.0 at the three Re numbers considered. Unlike in 2D separation, the SC separation line advances forward as the Re number grows, for the range of AR and Re numbers tested indicating an adverse Re effect.

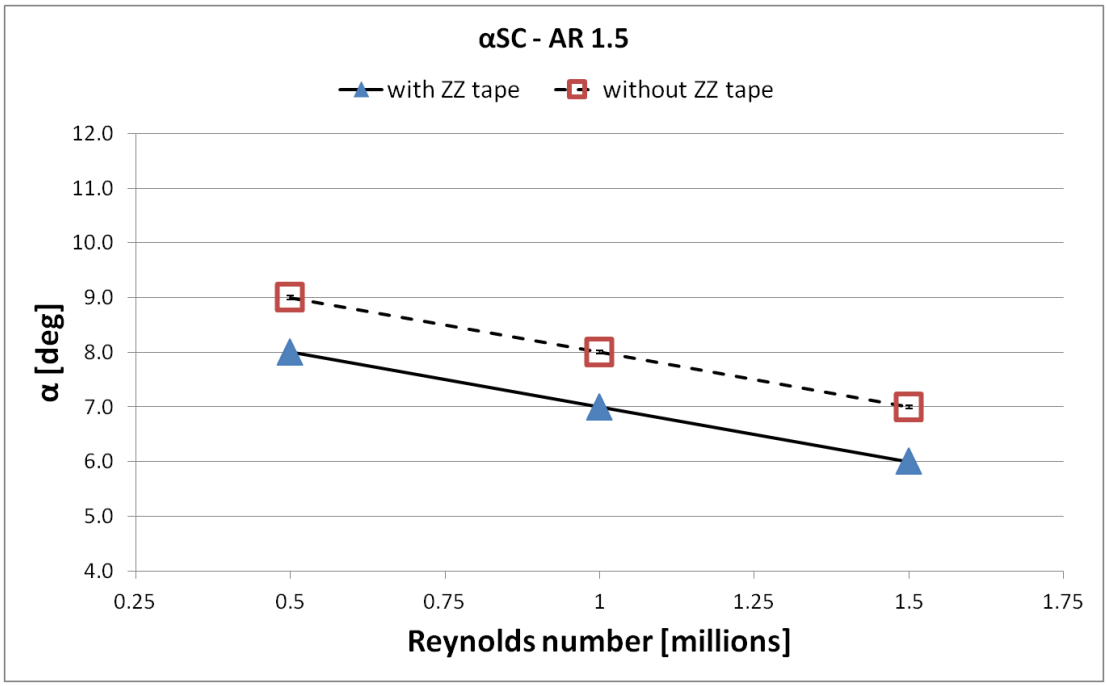

Figure 36: Angle of attack at which a SC is initially formed (α_{sc}) against Re number for AR = 1.5 with and without the ZZ tape. Unlike in 2D separation increasing the Re number leads to earlier onset of stall for the range of AR and Re numbers tested.

4.4 Summary

In the present study the dynamic behaviour of SCs formed on the suction side of a stalled wing (moving and/or spontaneous creation-destruction) reconfirms previous findings. The prerequisite for dynamic SCs to form is that the spanwise flow conditions are uniform (fully tripped or fully un-tripped) which subjects the flow to self-excited perturbations. By applying

a local disturbance to the flow (and therefore violating the spanwise uniformity) the flow was forced to create a single stabilized SC. Comparing cases with and without local disturbance indicated that the disturbance does not affect the overall characteristics of the SC size. The effects of Re number and AR (keeping the chord length constant) on this coherent and stable structure were studied experimentally based on tuft visualizations. The main findings of the flow-visualisation tests can be listed as follows:

1. The angle at which a SC is first created does not depend on AR and is considered a profile characteristic.
2. As Re increases, the angle at which a SC is first created decreases linearly for the specific profile.
3. Over the range of angles of attack the SC is formed, increasing the Re number results in the upstream advancing of the separation line unlike two-dimensional separation. This adverse Re number effect, could be profile specific, but was also noted on a NACA 8318 profile (Yoshida & Noguchi, 2000).
4. SC relative area grows asymptotically with angle of attack for all the cases tested.
5. Until the SC width entirely covers the available span, the actual SC area is independent of the wing span, over the range of values considered.
6. At high angles of attack, the relative SC area is independent of the AR, over the range of values considered.
7. The relative SC area is higher for the AR = 1.5 case at intermediate angles of attack as compared to that of AR = 2.0.
8. For increments of 0.5×10^6 in Reynolds number, the growth of the relative SC area is independent of the Reynolds number.

5 Stall Cell structure analysis

In the current section both experimental and computational data (2D and 3D) regarding the stabilized SC are presented and discussed. The lift (Cl) and drag (Cd) force coefficients are derived from the measured pressure distribution along the wing chord and the wing wake. Both force coefficients and the pressure distribution are compared with the relevant computational results. Then, a comparison of the measured and predicted SC size on the wing surface follows, along with a discussion on the wake downstream development. The agreement between the tests and the simulations is found to be good and on this basis a qualitative analysis of the complex vortex structures within a SC is performed.

5.1 CFD Validation

5.1.1 Grid

A c-type grid was used that extended 50 chords around the airfoil. The boundary layer mesh ensured the y+ value was lower than 1 throughout the wing surface. In order to create the 3D grid, the 2D grid (which was used for the two-dimensional calculations) was extruded in steps ranging from 0.0248 at the centre of the span to 0.0646 non-dimensional length units at the tip. The grid covered half of the span. At one end, symmetry condition was used while at the other (fence position), inviscid wall boundary conditions were implemented. SCs are not a tip effect and fully resolving the complex corner flow between the wing and the fence was not the aim of this study. The result was a computational domain, which will be referred to as the baseline grid. The symmetry condition had no effect on the results.

Table 4 below summarizes the details and some of the results for the grid cases tested. The differences in results between the baseline grid ($0.9x10^6$ cells) and the denser grids were at the order of 1% for Cl and 7% for Cd at $\alpha=9^o$. Still, it was decided to proceed with the baseline grid due to the computational cost. It was not possible to run higher density meshes with the available resources.

Case	Far field boundary distance	Domain Size	Earliest Separation Point	Cl at midspan	Cd at midspan
20c	20c	(250x110x24) $0.66x10^6$ cells	75.9%	1.31762	0.02858
50c (Baseline)	50c	(280x140x24) $0.94x10^6$ cells	76.9%	1.32475	0.02461
Increased spanwise density	50c	(250x110x40) $1.10x10^6$ cells	75.5%	1.33550	0.02379
Increased density in x and y directions.	50c	(470x230x24) $2.59x10^6$ cells	79.4%	1.33915	0.02290

Table 4: Computational details and selection of results for the different computational grids tested. $\alpha = 9.0°$, $Re = 1.0x10^6$.

5.1.2 Zigzag tape modelling

The flow in the experiments was locally disturbed for 10% of the wing span on the suction side using a 0.4mm thick ZZ tape of 60^o. According to (Elsinga & Westerweel, 2011) undulating spanwise vortices are shed from zigzag tape edge, which lead to turbulence. In the present case, however, of interest is the disturbance introduced to the flow rather than

the mechanism of transition. Hence, it was decided to model the macroscopic effect of the tape rather than to fully resolve its geometry in the flow.

Several oil film surface visualization studies (Lyon et al., 1997; Boermans, 2006; Van Raemdonck & Van Tooren, 2008), report the formation of oil stripes downstream of ZZ tape, which are associated with streamwise vortices created by it. This was confirmed through oil flow visualization tests done for various Re numbers. Figure 37 shows the result after one such test for the Re = 0.87×10^6 and $\alpha = 7°$. In other words the ZZ tape's "legs" can act as vortex generating surfaces to the incoming flow. It was hence attempted to model the trip tape in the 3D computations as a vortex generating surface using the jBAY model (Jirasek, 2005). No ZZ tape model was used in the 2D computations.

The BAY model (see Chapter 3) has been found to give similar results to the fully resolved case for vortex generators on a flat plate, even though none of the two computational approaches could fully reproduce the experimental results, mainly due to excessive vorticity diffusion, see (Dudek, 2011).

Fully resolving every leg of the trip tape in the computational model would be too expensive computationally and out of the scope of this research. Instead the ZZ tape was modelled as a limited number of attached vortex generating surfaces using the BAY model. The actual and the three simplified geometries tested are shown in Figure 38. The "2-legged" BAY model (green dashed line) was closer to the experimental results and was the one adopted for the present study.

It is important to note that the flow was always considered fully turbulent on both sides of the airfoil. That is to say that the trip tape effect was modelled macroscopically and not as a local transition point from laminar to turbulent flow. This is of course different to the experiment. However, as shown later, this approximation is good enough to qualitatively study a SC.

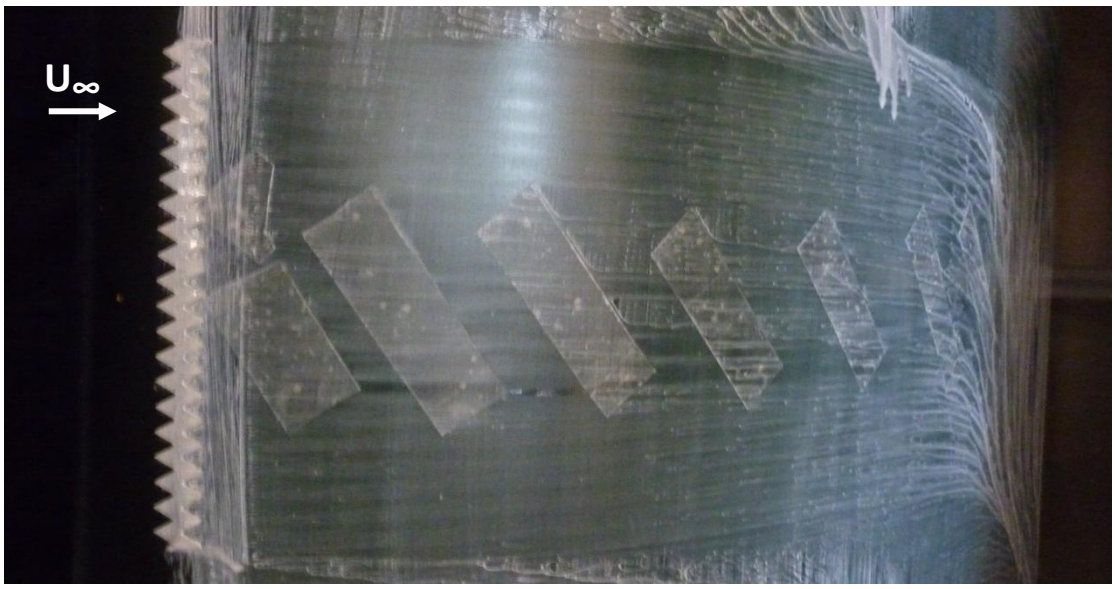

Figure 37: Oil flow visualization downstream of the ZZ tape used as a localized disturbance. Re = 0.87×10^6, $\alpha = 7°$. Tapes on the wing surface were located to cover the pressure taps.

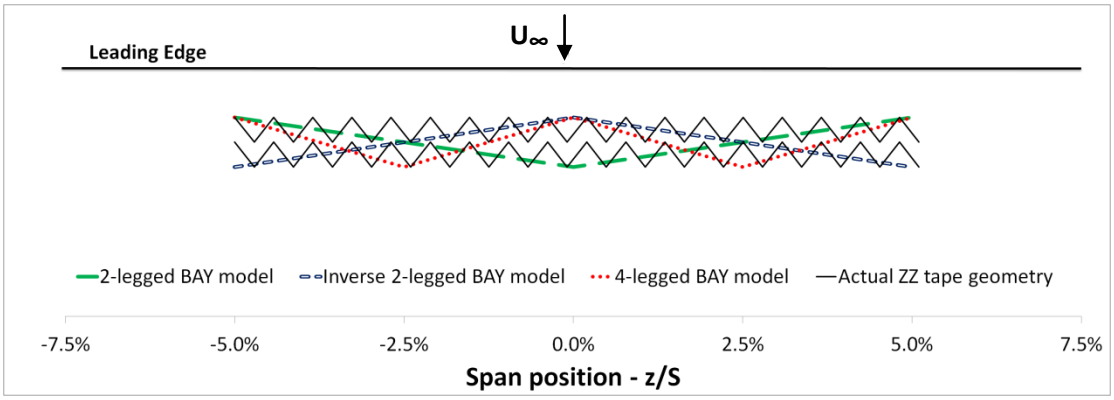

Figure 38: Actual trip tape geometry and BAY model surfaces.

5.1.3 Force coefficients and pressure distribution along the wing chord / span

Lift and drag curves are given in Figure 39 and Figure 40, respectively. Data from the experiments, 3D and 2D simulations are given. For clarity, 2D data are only shown for $\alpha > 6^o$, since up to this angle there is very little difference between the 2D and the 3D computational results.

CFD predicts lift very well especially over the linear part, $\alpha < 7^o$ while the drag is overpredicted by ~0.003. The latter is connected to the fact that the simulations are fully turbulent on both sides of the airfoil and friction drag is a significant part of the Cd in attached flow conditions. At 0^o XFOIL predicts the pressure side free transition at 0.56c whereas the flow is laminar throughout the pressure side for angles of attack higher than 11^o. The additional friction drag is partly responsible for the disagreement between the experimental and the computational value of Cd. Also, as shown in Table 4 (in page 51) a denser grid could have reduced the value of Cd even further. Finally, it is perhaps worth noting that estimating profile drag from the experimental pressure distributions in the wing or the wake could include significant errors, e.g. see (Goett, 1939; Barlow et al., 1999).

At higher angles of attack ($\alpha > 6^o$) the 3D CFD predicted Cl follows closely the trend in the measurements with a small over-shift of 0.06. 2D CFD, however, follows a completely different trend reaching the maximum value of Cl at 12^o (cf. 9^o for tests and 3D simulations). This indicates that 2D simulations are not capable of describing the flow when SCs develop, as (Elimelech et al., 2012) also showed, albeit for a much lower Re number ($O(10^4)$).

Over the same range of angles of attack ($\alpha > 6^o$) drag is significantly underpredicted in both 2D and 3D simulations. It is noted that according to measurements at $\alpha = 7^o$ a SC is first formed on the suction side of the wing. Beyond that angle, the experimental Cd increases at a much higher rate due to the formation of a SC that rapidly increases in size for increasing angle of attack. In the 3D simulations, a proper SC is first formed at $\alpha = 10^o$, which leads to a local step-like decrease in Cd. This is followed by a growing Cd at a rate similar to the tests keeping constant, however, the difference with respect to tests seen at ~10^o.

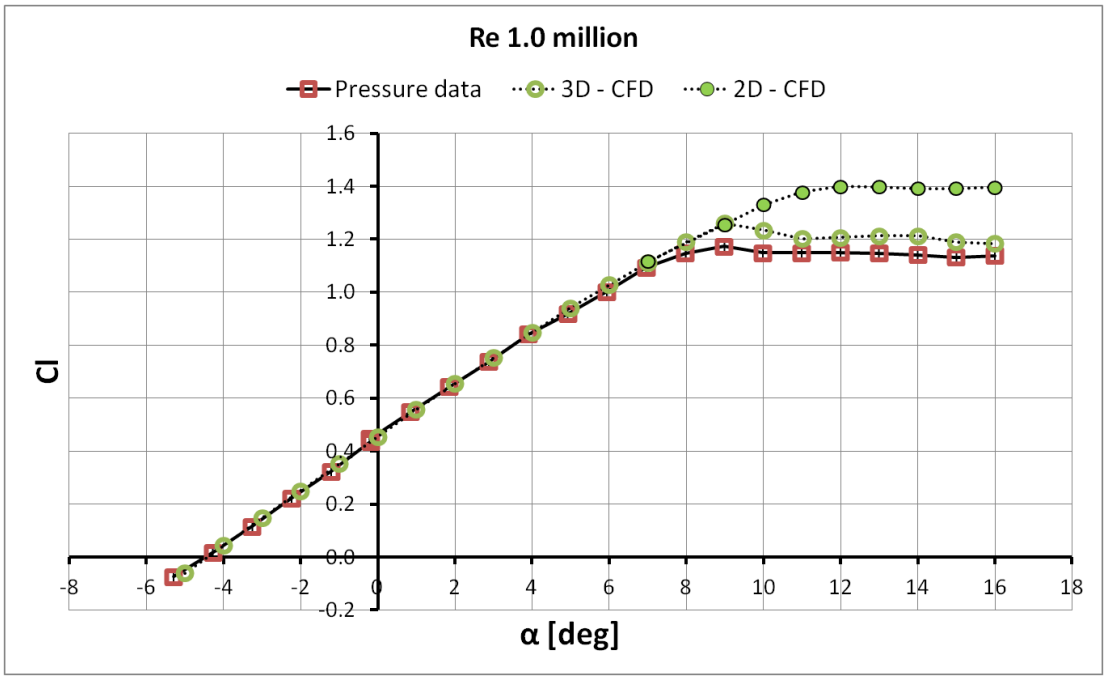

Figure 39: Lift coefficient variation with angle of attack. Midspan value for experiments and 3D CFD. AR = 2.0, Re = 1.0x10^6.

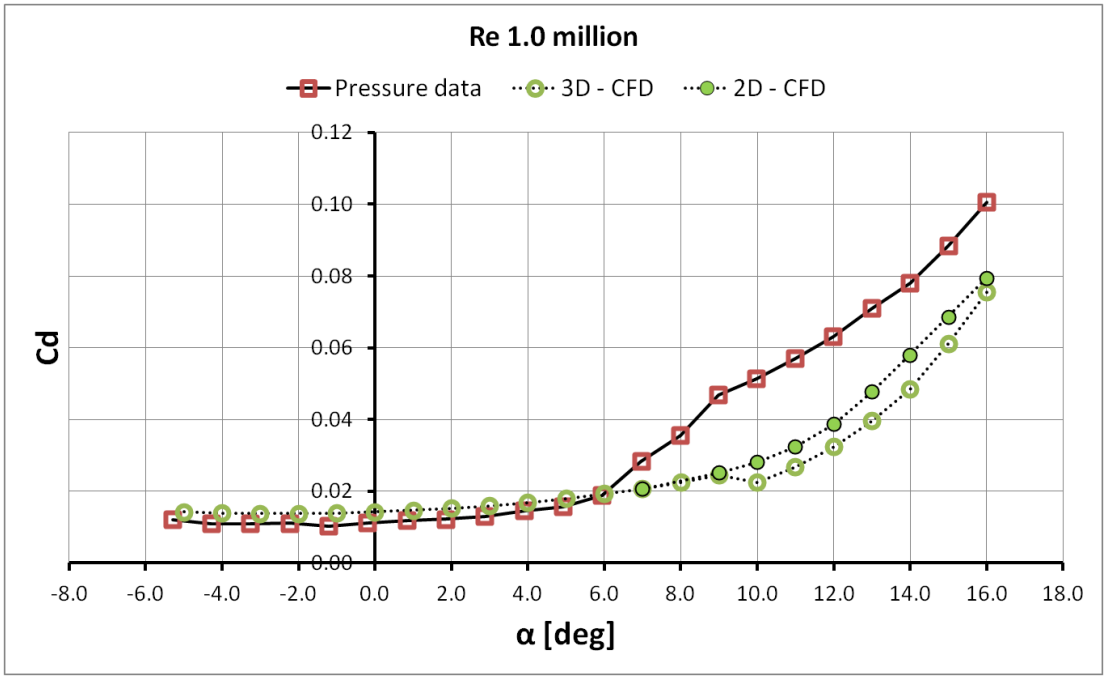

Figure 40: Drag coefficient variation with angle of attack. Midspan value for experiments and 3D CFD. AR = 2.0, Re = 1.0x10^6.

In order to get a more detailed account on the differences between CFD simulations and measurements, the pressure coefficient distributions are compared in Figure 41, Figure 42 and Figure 43 for α = 7°, 10° and 16°, respectively. Pressure perturbations around x = 0.02% in the experimental data are due to the local effect of the ZZ tape on the pressure taps right upstream and downstream of it. The CFD pressure coefficient variation at x/c ≈ 0.4% is the result of the modelling of the ZZ tape.

At $\alpha = 7^o$ the agreement between tests and 3D CFD is still very good until the TE region is reached, see Figure 41. A small SC is formed in the experiments but not in the computations. On the contrary there is little difference between the 2D and the 3D CFD results. At $\alpha = 10^o$ the SC is formed in the computational results, too, but it is still smaller than the one experimentally observed at the specific angle of attack, see Figure 42. The pressure distribution prediction for the 3D case improves as the angle of attack increases, e.g. see Figure 43 for $\alpha = 16^o$. On the other hand the separated flow region is always significantly smaller in the 2D results.

3D CFD can provide an insight to the force variation on the wing along its span. Figure 44 and Figure 45 show the Cl and Cd variation along the wing span for three different angles of attack (7^o, 10^o and 16^o). As the SC grows from its first formation ($\alpha = 7^o$) so does the lift and drag variation with span position. Lift is always minimum at the centre of the wing span (z/S = 0%) and grows towards the wing tip (z/S = 50%). The drag value is also minimum at the centre of the wing span, then grows to its peak prior to the wing tip and is then reduced.

In fact, the Cp distribution at the tip (z/S = 50%) is very similar to the result of the 2D computation which is also drawn in Figure 46 for $\alpha = 10^o$. This would suggest that the flow in that region is not affected by the SC vortex. Similar agreement was found by (Elimelech et al., 2012).

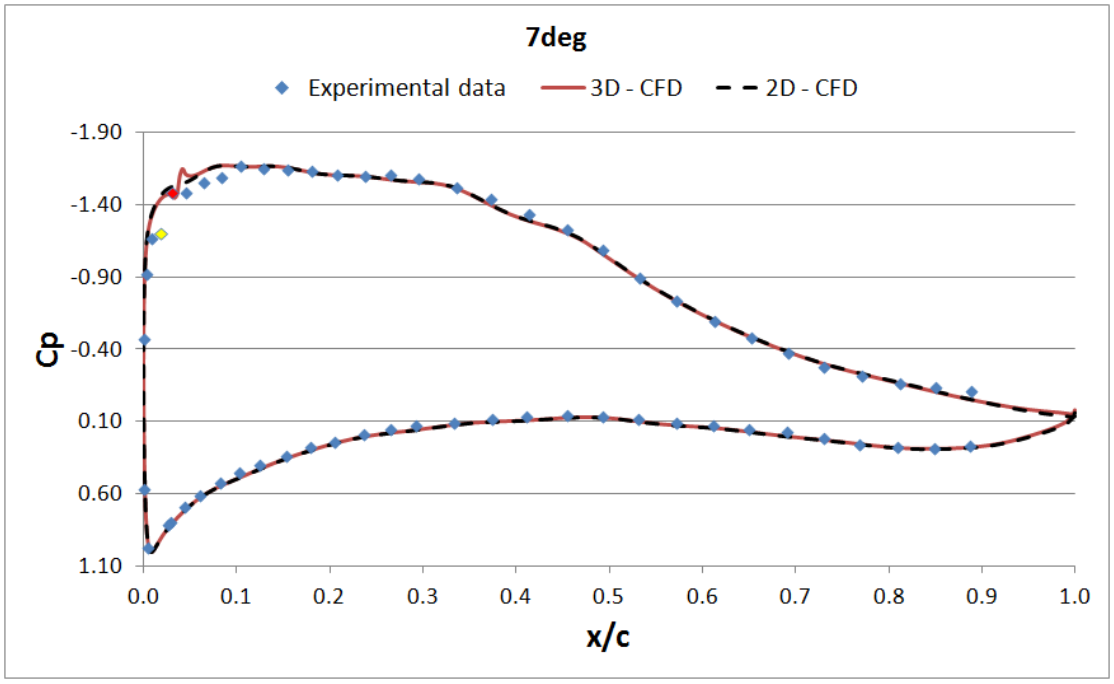

Figure 41: Pressure coefficient distribution along the wing chord at midspan. AR = 2.0, Re = 1.0×10^6, $\alpha = 7^o$. The yellow and red point correspond to the pressure taps just upstream and downstream of the ZZ tape, respectively.

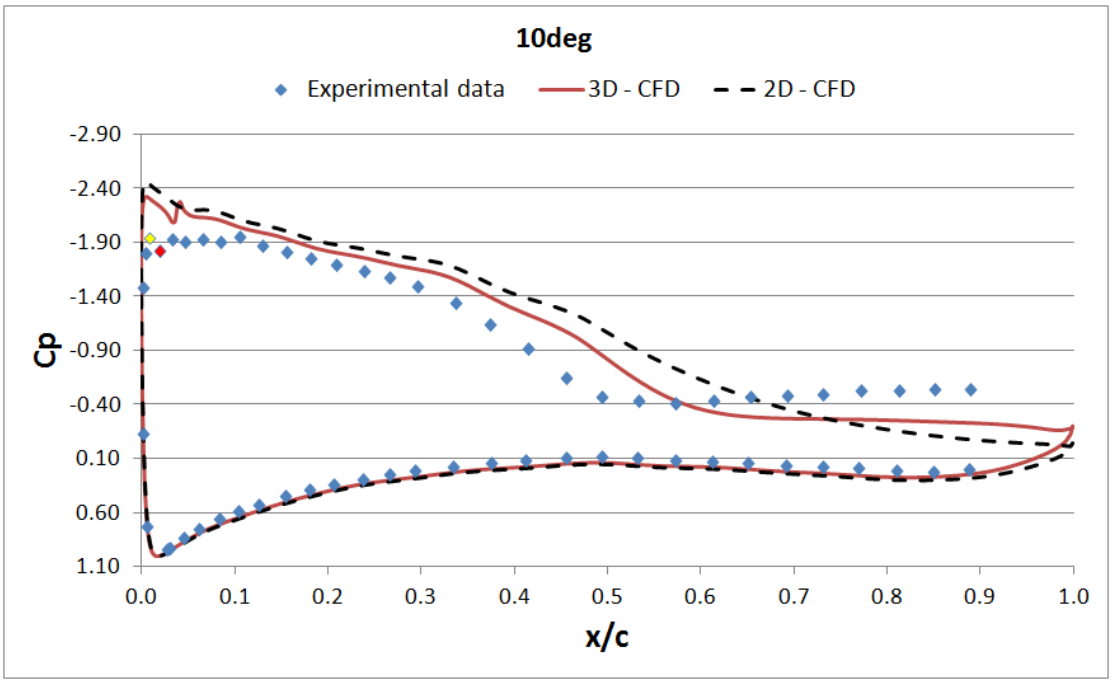

Figure 42: Pressure coefficient distribution along the wing chord at midspan. AR = 2.0, Re = 1.0x10^6, α = 10^o. The yellow and red point correspond to the pressure taps just upstream and downstream of the ZZ tape, respectively.

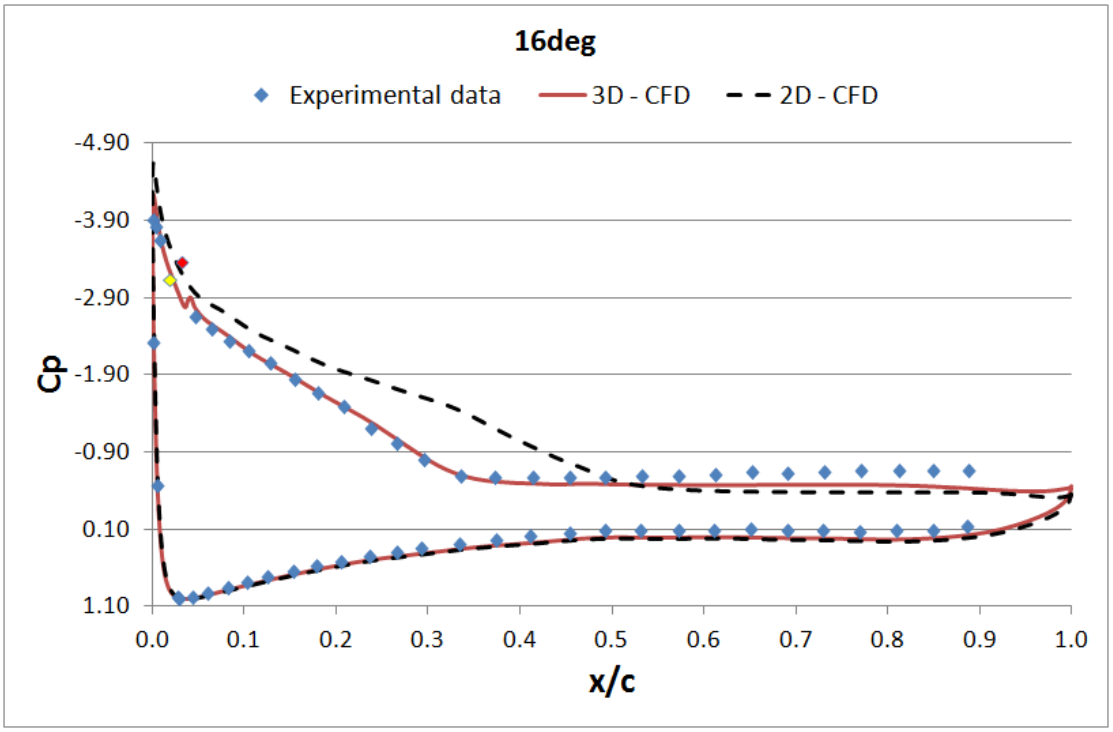

Figure 43: Pressure coefficient distribution along the wing chord at midspan. AR = 2.0, Re = 1.0x10^6, α = 16^o. The yellow and red point correspond to the pressure taps just upstream and downstream of the ZZ tape, respectively.

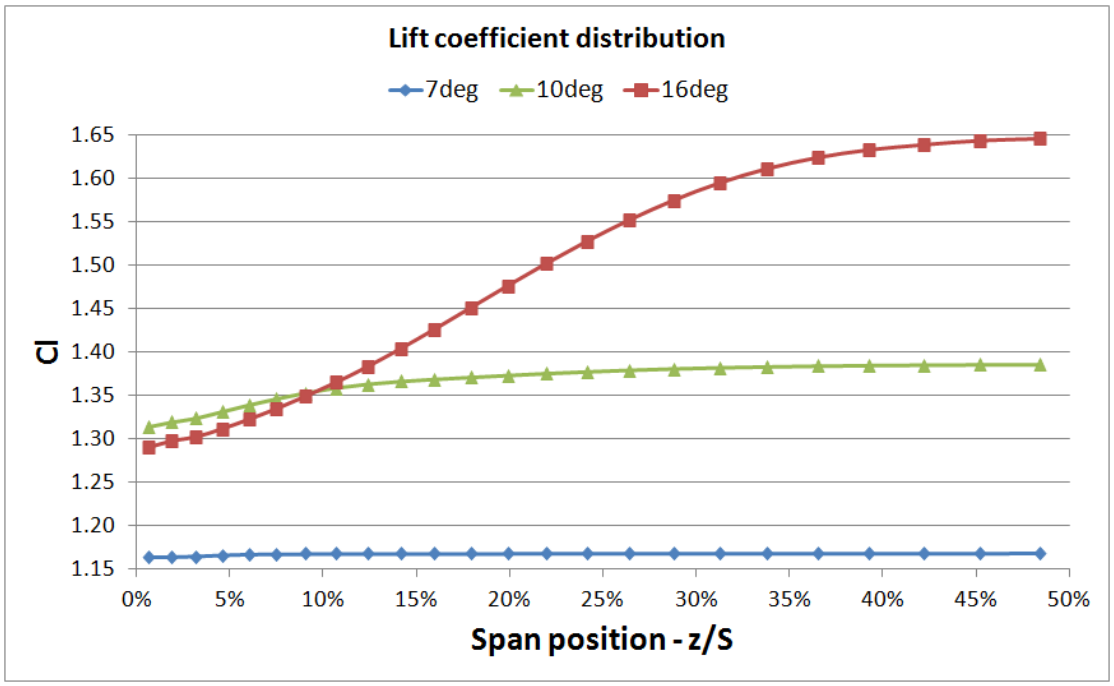

Figure 44: Lift coefficient along the wing half span. CFD data. AR = 2.0, Re = 1.0x10^6. z/S = 0% is the wing symmetry plane and z/S = 50% is the wing tip.

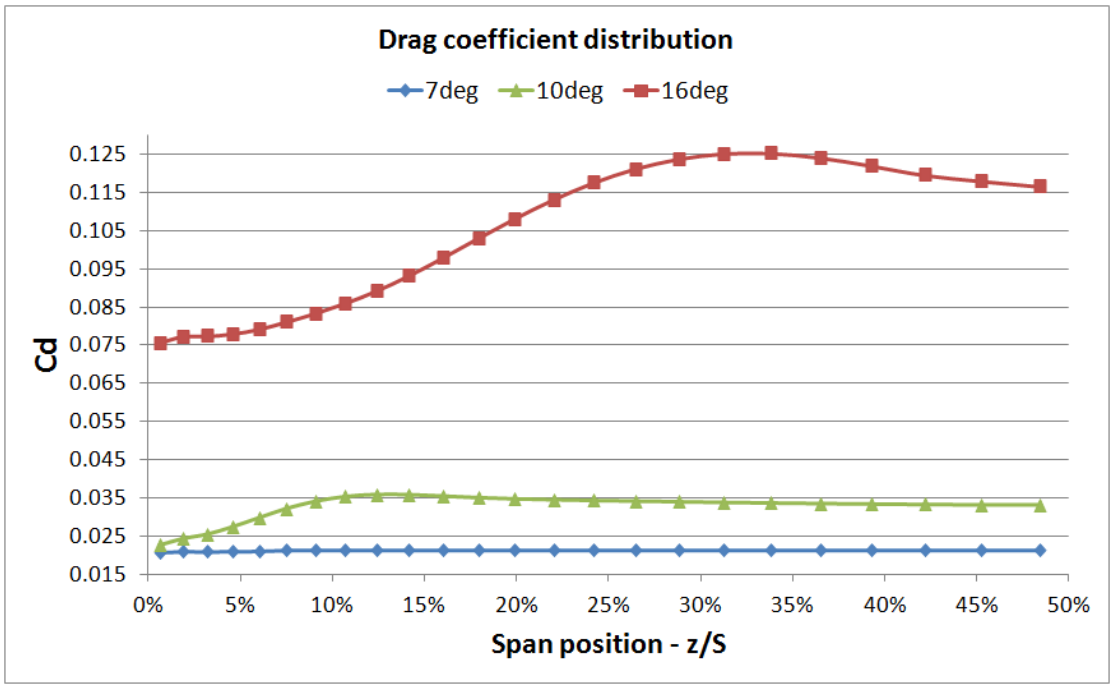

Figure 45: Drag coefficient along the wing half span. CFD data. AR = 2.0, Re = 1.0x10^6. z/S = 0% is the wing symmetry plane and z/S = 50% is the wing tip.

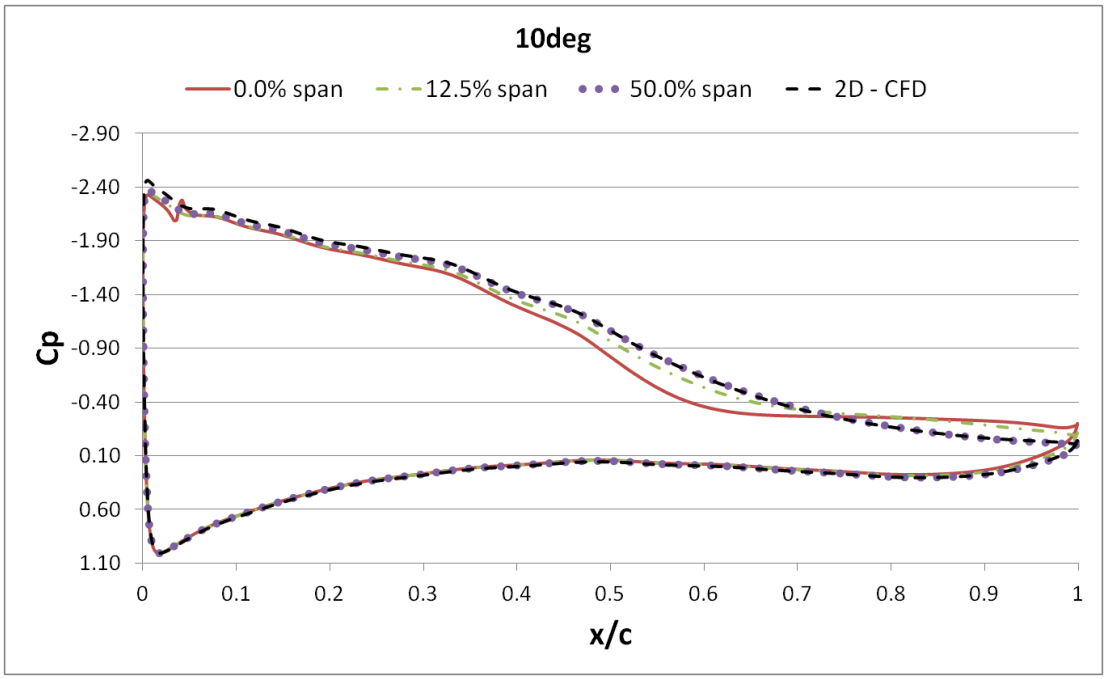

Figure 46: Pressure coefficient distribution along the wing chord at various positions along the wing span and for the 2D solution. z/S = 0% is the wing symmetry plane and z/S = 50% is the wing tip.

5.1.4 Stall Cell size

The SC size on the wing surface is characterized by the SC maximum length (at its centre between the two vortices) and width at the TE. Figure 47 depicts the SC chordwise length variation with respect to the angle of attack. Tuft, pressure and CFD data are compared. The agreement between the tuft and pressure data is very good. CFD correctly predicts the earliest location of separation only when $\alpha > 10^{o}$. Similar behaviour is observed in the SC width prediction, as Figure 48 shows. For the CFD data the SC limit was defined as the most outboard position at which the spanwise velocity component was greater than 1% of the free stream flow.

In order to check whether this delay in predicting the SC formation is due to the modelling of the ZZ tape, CFD simulations were carried out without the ZZ tape model. In that case a SC first appears at 9°, according to the tuft experimental data. In CFD the first fully formed SC appears at 12°, i.e. again with 3° delay as in the case with the ZZ-tape effect switched on, see Figure 49. This suggests that the modelling of the ZZ tape is not responsible for the delay in the SC formation which could be attributed to the turbulence model, since eddy viscosity models have known difficulties in accurately predicting 3D separation.

The exact reason for the inability of CFD to correctly predict the onset of separation remains unclear. Apart from the already mentioned unsuitability of eddy viscosity models for such a complex three-dimensional separated flow a couple of other issues could be mentioned. On one hand, this was a steady state simulation of an inherently unsteady separated flow while on the other, simulations did not include the wind tunnel walls or the boundary layer on the wing fences. It is planned to investigate these aspects of the flow in the future.

It is perhaps worth noting that as in the experiments, the steady CFD simulations without the spanwise perturbation resulted in various SC combinations. In more detail, for

$12^{o} < \alpha < 16^{o}$ two SCs were formed on the wing surface whereas at $\alpha = 16^{o}$ a combination of a single central SC along with two "half" SCs at the wing tips appeared. Unlike the highly unsteady SC combinations in the tests, however, no unsteadiness was found, even when unsteady simulations were performed. It was, hence, decided to proceed with the analysis of steady simulations with the ZZ tape model switched on, as their relevance to the disturbed tests was closer.

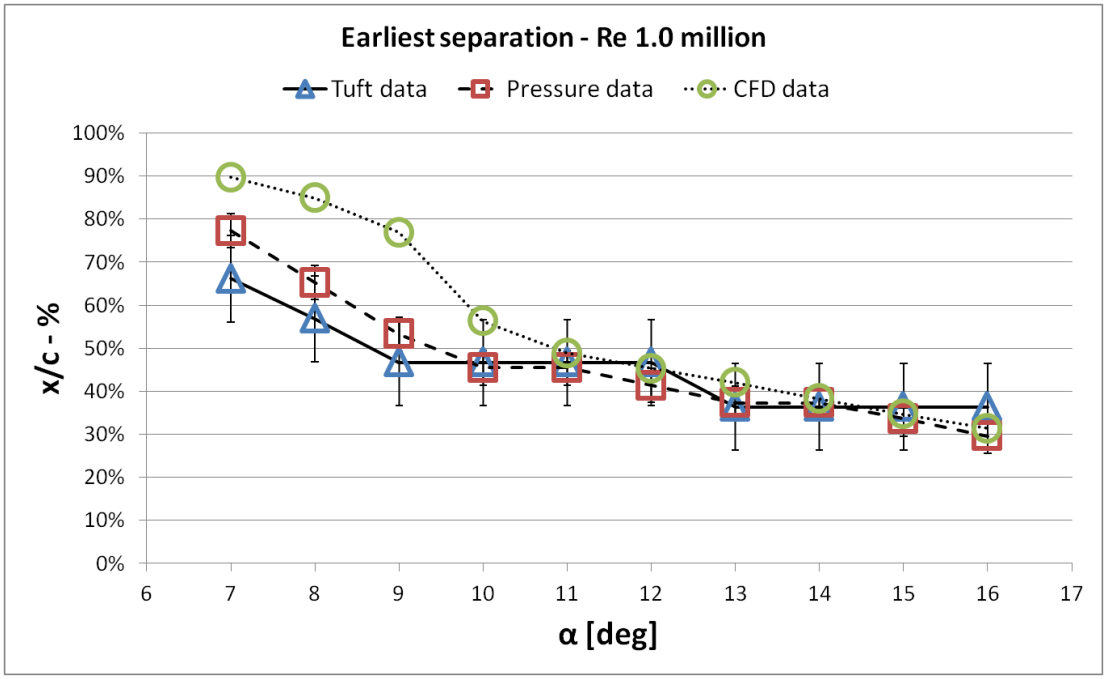

Figure 47: Earliest separation location as found from tuft, pressure and CFD data. AR = 2.0, Re = 1.0x106.

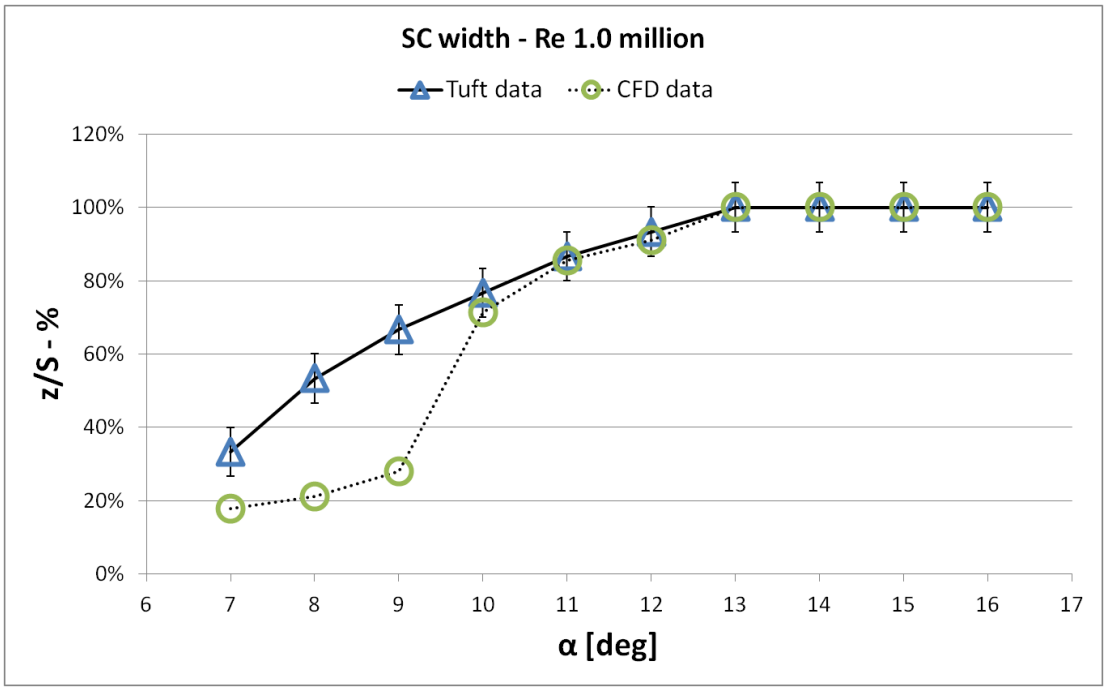

Figure 48: SC width on the wing surface as found from tuft and CFD data, AR = 2.0, Re = $1.0x10^{6}$.

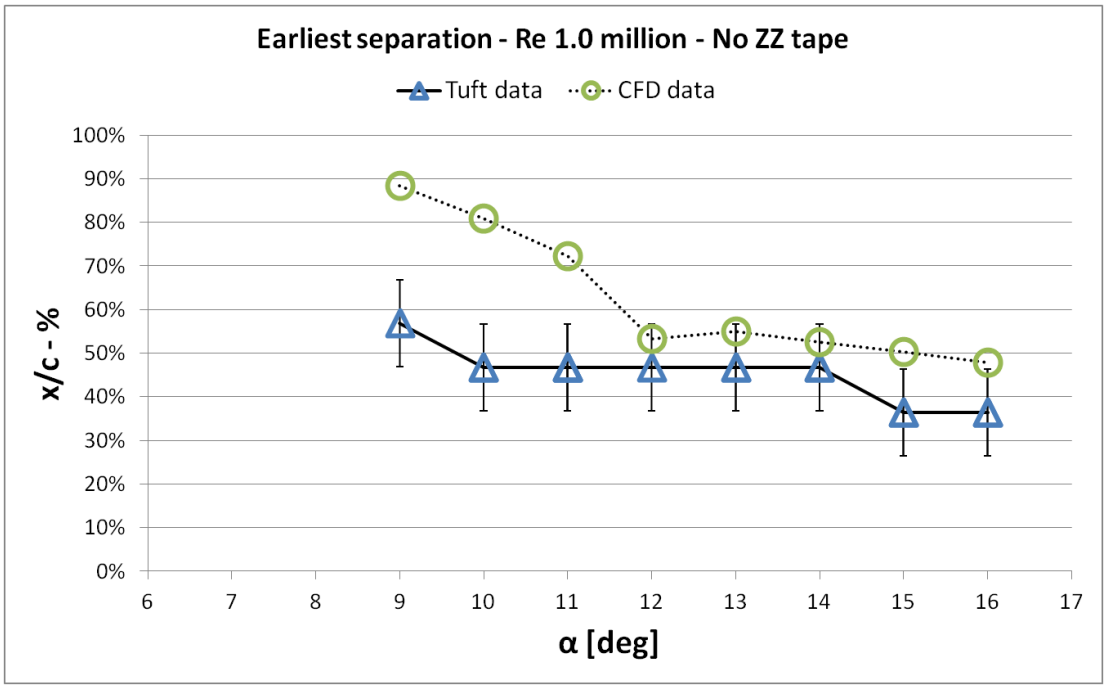

Figure 49: Earliest separation location as found from tuft and CFD data. AR = 2.0, Re = 1.0x10^6 case without ZZ tape.

5.1.5 Wake three-dimensionality

So far it has been made clear that the flow is highly three-dimensional on the wing surface and, unsurprisingly, so is the wake flow. A measure of the three-dimensionality of the flow is given by the wake height variation along the span. Experimentally the wake height was measured with the total pressure tubes of the wake rake (i.e. 0.8c downstream of the TE) in planes normal to the flow and the wing span. Computationally it was defined, as shown in Figure 50, where contours of normalized total pressure on a plane normal to the flow at the rake position are shown. The area in which the SC develops in the wake is also seen in this figure. The vortex structure inside this region is discussed in a later paragraph.

In Figure 51 the experimentally measured wake height is plotted for various angles of attack. At 0^o there is small initial three-dimensionality of the flow (due to the ZZ tape) which grows substantially as the SC quickly grows after 7^o. The wake shape observed by the wake pressure measurements is in qualitative agreement with (Winkelmann, 1981) (Re number 0.48x10^6, Clark Y-14 airfoil), who studied SC wake, however, at higher angles of attack (α=21.4^o and α=28.4^o).

By comparing data from Figure 48 and Figure 51 it is possible to examine the SC evolution in the wake. For example at 10^o the SC width at the wing suction surface is approximately 76% of the wing span (Figure 48) whereas the SC extends approximately from -20% to 20% of the span 0.8c downstream of the TE. This suggests that the SC contracts in the spanwise direction as it moves downstream and a similar behaviour is observed throughout the angle of attack range. As shown next, this is due to the vortex interaction inside the SC above the wing surface.

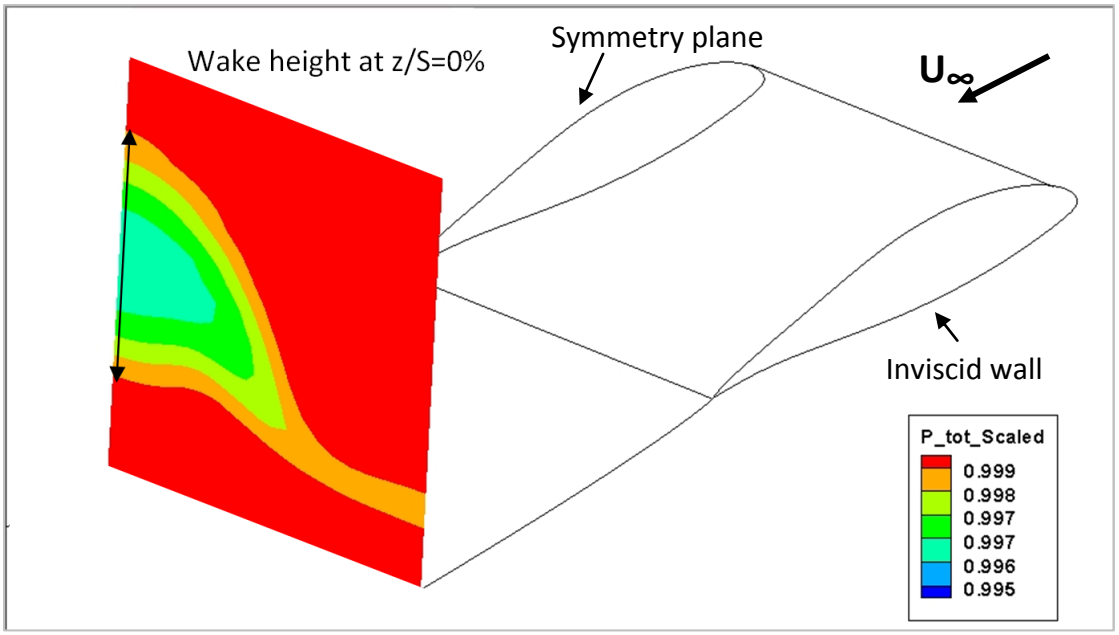

Figure 50: Contours of normalized total pressure on a plane normal to the free stream at the rake position (0.8c downstream of the TE). The definition of the wake height is also shown for z/S = 0% span. Symmetry plane is at the left of the picture.

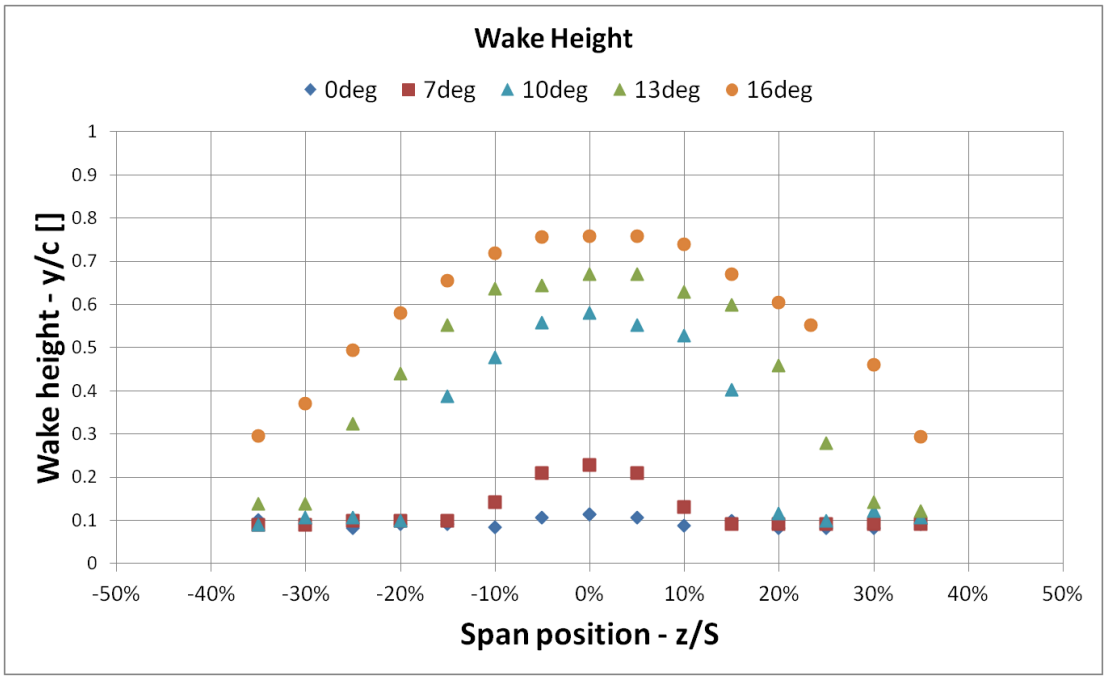

Figure 51: Wake height at the rake position (0.8c downstream of the TE) for AR = 2.0, Re = 1.0x10^6 and α = 0°, 7°, 10°, 13° and 16°. Error bars not included for clarity.

In general CFD predicts well the (parabolic) shape of the SC wake but underpredicts the wake size, e.g. see Figure 52 and Figure 53 where the relevant CFD and experimental data are compared for 10 and 16°, respectively. Even though CFD offers a good prediction for SC size on the wing surface at 16° (see Figure 47 and Figure 48) it fails to do so further downstream (Figure 53). This could possibly be attributed to excessive vorticity diffusion inside the wake. Still the general shape of the wake appears correct and permits a qualitative analysis.

The distance between the wake rake total pressure tubes ranged from 6mm at its centre to 15mm at its sides. The maximum uncertainty for the wake height measurement was then +/- 30mm or 0.05c, which is the value indicated by the error bars in Figure 52 and Figure 53.

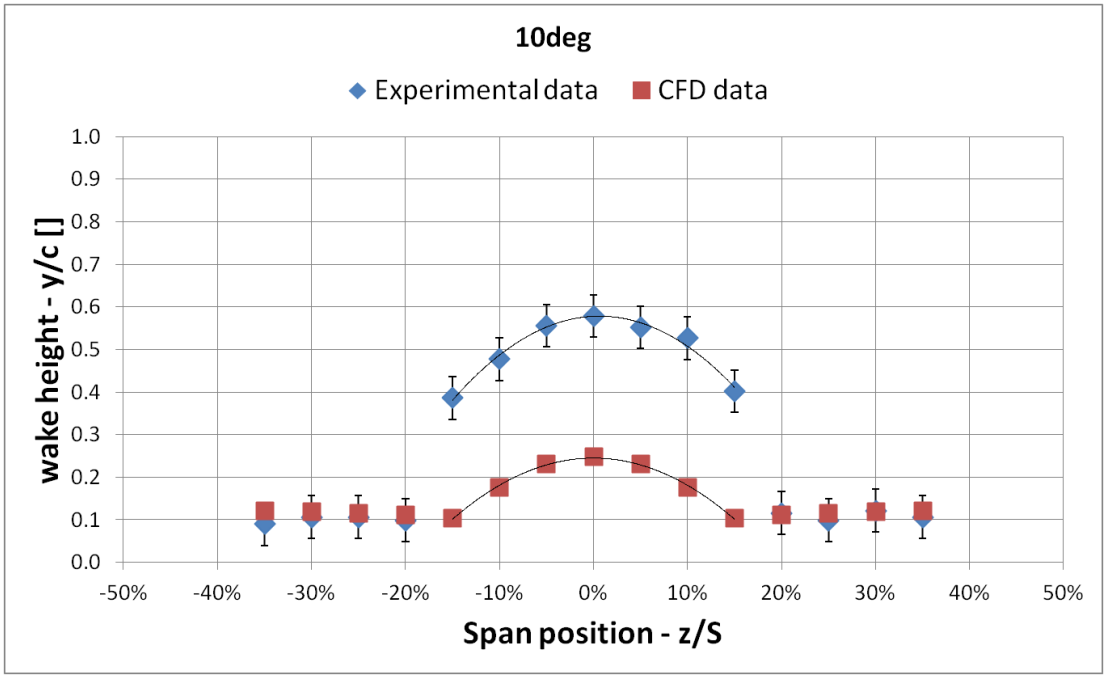

Figure 52: Wake height at the rake position (0.8c downstream of the TE) for α = 10° based on experimental and CFD data. CFD data were only available for half span due to the symmetry condition and where are mirrored for the other half of this graph. 2nd order trendlines are drawn over the data from -15% to 15% span. Error bars value is 0.05c.

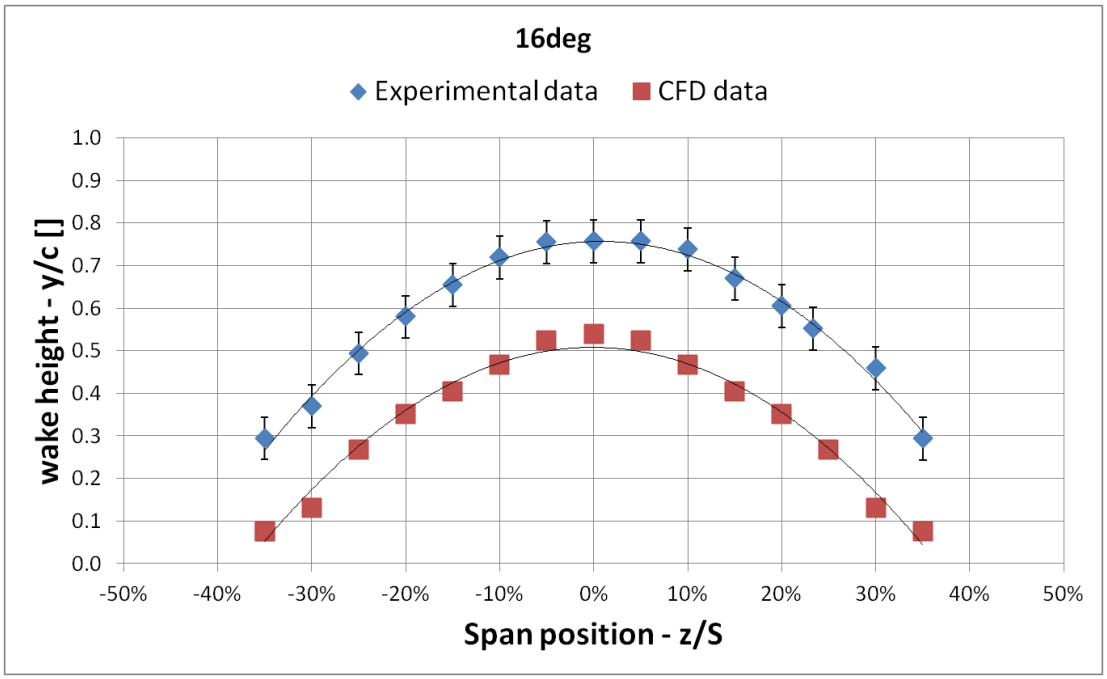

Figure 53: Wake height at the rake position (0.8c downstream of the TE) for α = 16° based on experimental and CFD data. CFD data were only available for half span due to the symmetry condition and where are mirrored for the other half of this graph. 2nd order trendlines are drawn over the data from -35% to 35% span. Error bars value is 0.05c.

5.2 Stall Cell structure

In an early study (Winkelmann & Barlow, 1980) proposed a “tentative flow model" in an attempt to explain the SC structure. It was then suggested that the two nodes observed on the wing surface are "the time averaged effect of a vortex flow that loops from one node to the other". However, in a later article, (Yon & Katz, 1998) showed that this model was inconsistent with their pressure data and argued that if the SC vortices trailed downstream the induced flowfield would be in agreement with their measurements.

In this section an attempt is made to gain insight into the structure of SCs based on the CFD results. As discussed next, the CFD data suggest that SC vortices start from the wing surface and continue downstream in the wake as suggested in (Yon & Katz, 1998). At the same time the SC vortices interact with the *separated line vortex* and the *TE line vortex* (definitions of the basic line vortices are given in the following paragraphs).

The discussion focuses on the case of 16^{o} angle of attack at which the overall CFD flow characteristics match best with the measured data. Surface stream lines, in-plane stream lines on x- and z-planes in combination with contours and isosurfaces of the Q criterion (Hunt et al., 1988) are used for the analysis. In-plane stream lines are, of course, artificial, unless the flow has zero velocity normal to the plane under consideration. However, they can provide indication on vortex location and improve the understanding of the flow.

Figure 54 shows surface stream lines on the wing surface and in-plane stream lines on several z- planes. The SC vortex can be clearly seen on the wing surface (with vortex centre at z/S ≈ 37%) while on the z planes, two spanwise line vortices of opposite vorticity can be detected. The one here named "*separated line vortex*" (SLV) stands above the wing surface while the other named “*TE line vortex*” (TELV) is aligned with the TE and is located in a short downstream distance of it. Both have cores that increase in size when moving from tip to the centre of the SC. The increase of the core size is bigger for the SLV which undergoes substantial upstream deflection when approaching the mid-span. On the contrary the deflection of the TELV is smaller and for most of its length remains almost parallel to the TE.

In order to examine how the SLV and the TELV develop in space, a more detailed look at the in-plane flow lines of Figure 54 is needed. Figure 55 is a side view of Figure 54, but now flow lines are limited to the vortex core regions. In-plane flow lines are coloured by their spanwise position, which is indicated on the figure. It is clear that the SLV core moves upwards and upstream towards the centre of the SC (z/S = 0%). Note that the flow lines corresponding to the TELV core do not form circles towards the side of the SC (z/S = 50%) where the vortex is weaker, but they do so at the centre of the SC. The TELV core appears to move upwards and downstream towards the centre of the SC (z/S = 0%). A possible explanation for the vortex cores movement could be that the SC vortex pushes the separation line as well as the inboard part of the SL vortex, upstream over the midspan plane. Thus, the SL vortex grows and as a result the TE line vortex grows and is pushed downstream.

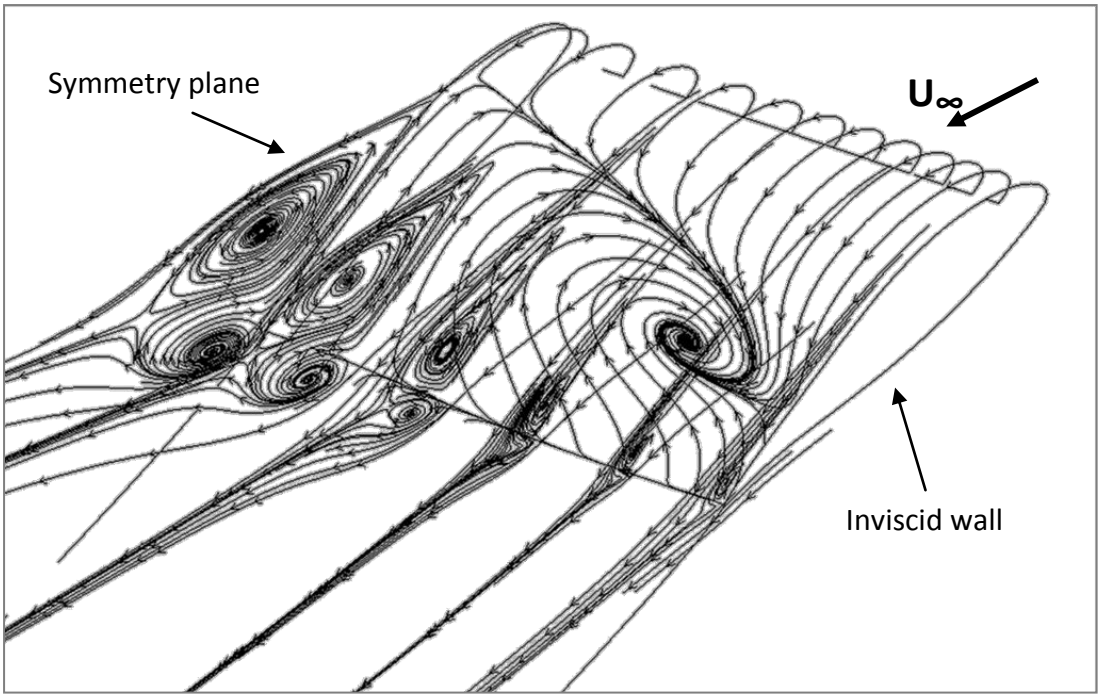

Figure 54: Surface flow lines on the wing suction surface along with in-plane flow lines on planes z/S = 0% (symmetry plane), z/S = 10%, z/S = 20%, z/S = 30%, z/S = 40%, z/S = 50% (wing tip, right hand side). Wing half span only. AR = 2.0, Re = 1.0x10^6, α = 16°.

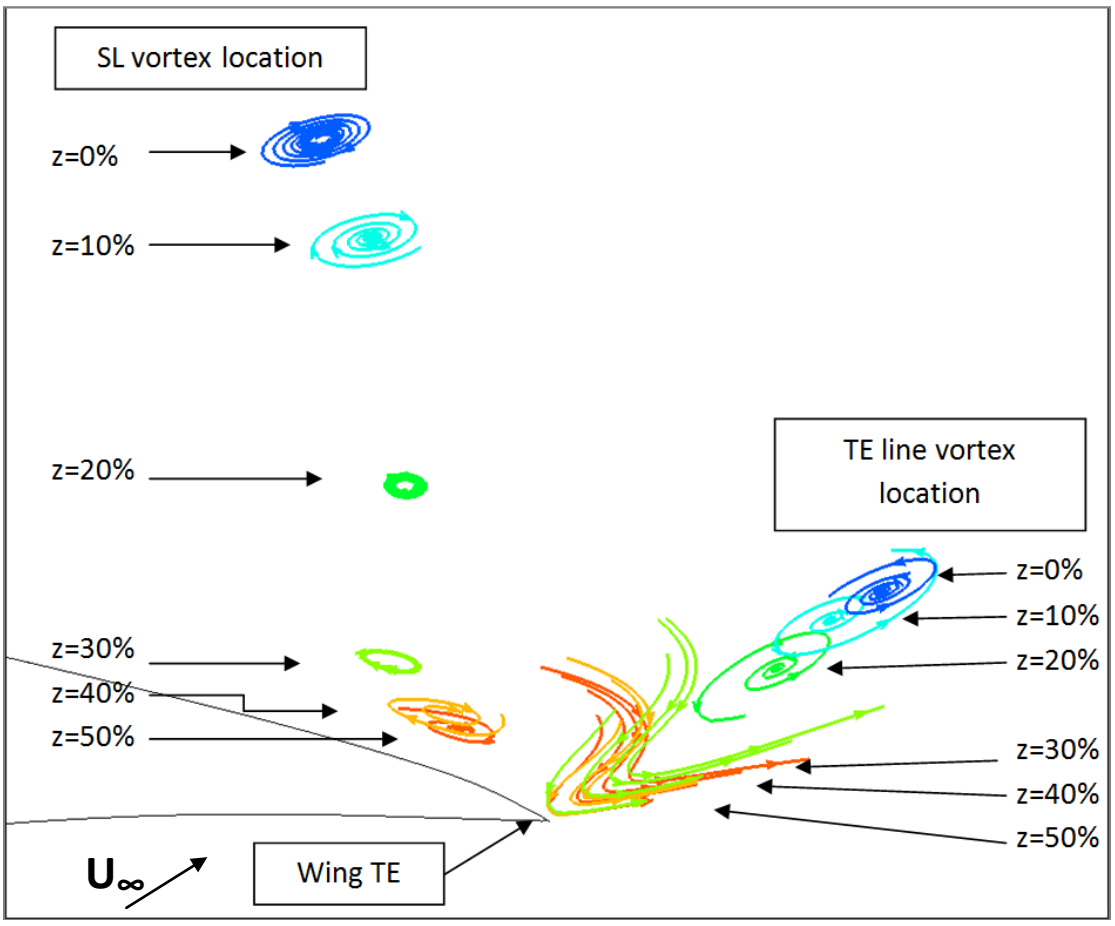

Figure 55: Side view detail of the wing TE. In-plane flow lines coloured by z dimension on planes at z/S = 0% (symmetry plane), z/S = 10%, z/S = 20%, z/S = 30%, z/S = 40%, z/S = 50% (tip). AR = 2.0, Re = 1.0x10^6, α = 16°.

At the same time, the SLV affects the development of the SC vortex. Figure 56 shows flow lines on the wing suction surface and in-plane stream lines on two planes normal to wing span (z/S = 30%, z/S = 10%) and on one plane normal to the free stream flow (at the TE, x/c = 1.0). It is observed that by the time the SC vortex has reached the TE it has already moved inboard compared to its node on the wing suction surface. It is conceivable that this happens because from tip to mid span, the core of the SLV grows, its centre moves in the positive z direction and the negative x direction (see Figure 55), and therefore attracts the SC vortex inboard.

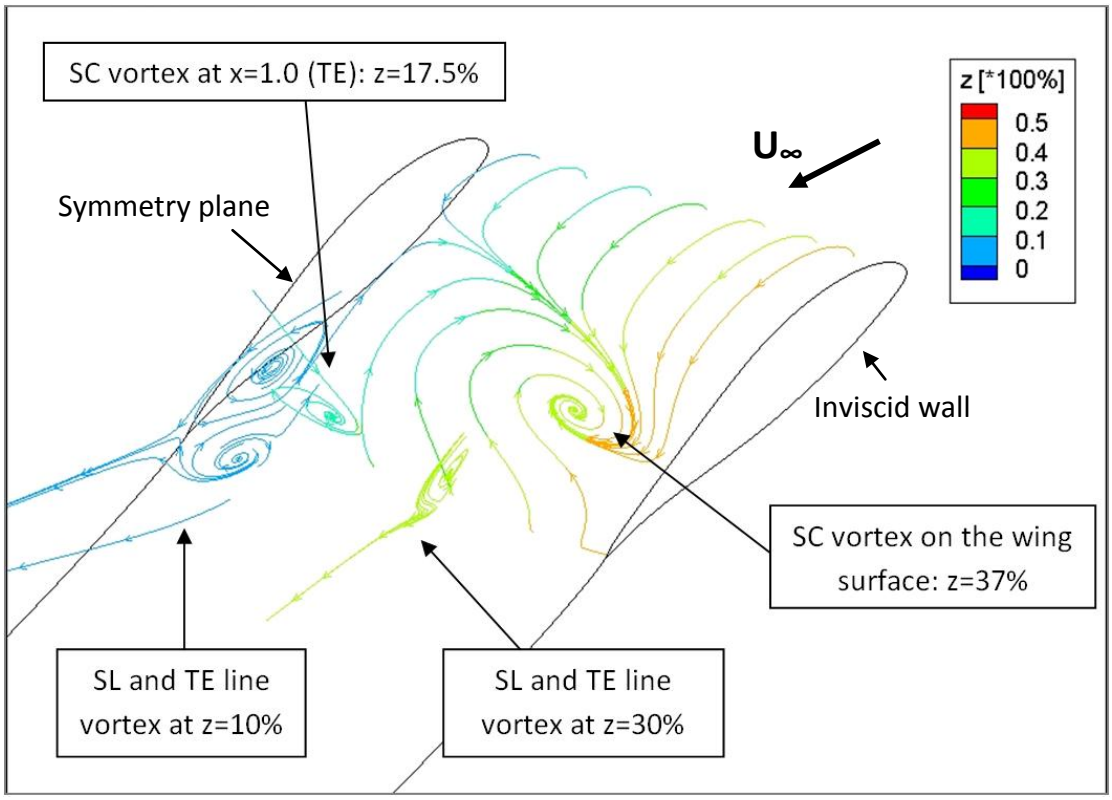

Figure 56: Surface flow lines on the wing suction surface. in-plane flow lines on planes z/S = 10% and z/S = 30% (normal to the wing span) and x/c = 1.0 (normal to the free stream at the TE). All flow lines are coloured by spanwise location. Symmetry plane is at the left hand side (z/S = 0%). AR = 2.0, Re = 1.0x10^6, α = 16°.

Figure 57 shows in-plane stream lines and Q contours on planes vertical to the flow at x/c = 1.0 (TE), x/c = 2.0 and x/c = 3.0. In the planes at x/c = 2.0 and x/c = 3.0 the Q contour gives a clearer indication of the SC vortex location. This is not the case for the plane at x = 1.0 because at that location multiple vortices are present, as already discussed. Looking at the in-plane stream lines, however, the vortex core can be located at about z/S = 17.5% for all the downstream planes. This suggests that after the initial inboard shift of the SC vortex, no significant spanwise movement occurs in the wake.

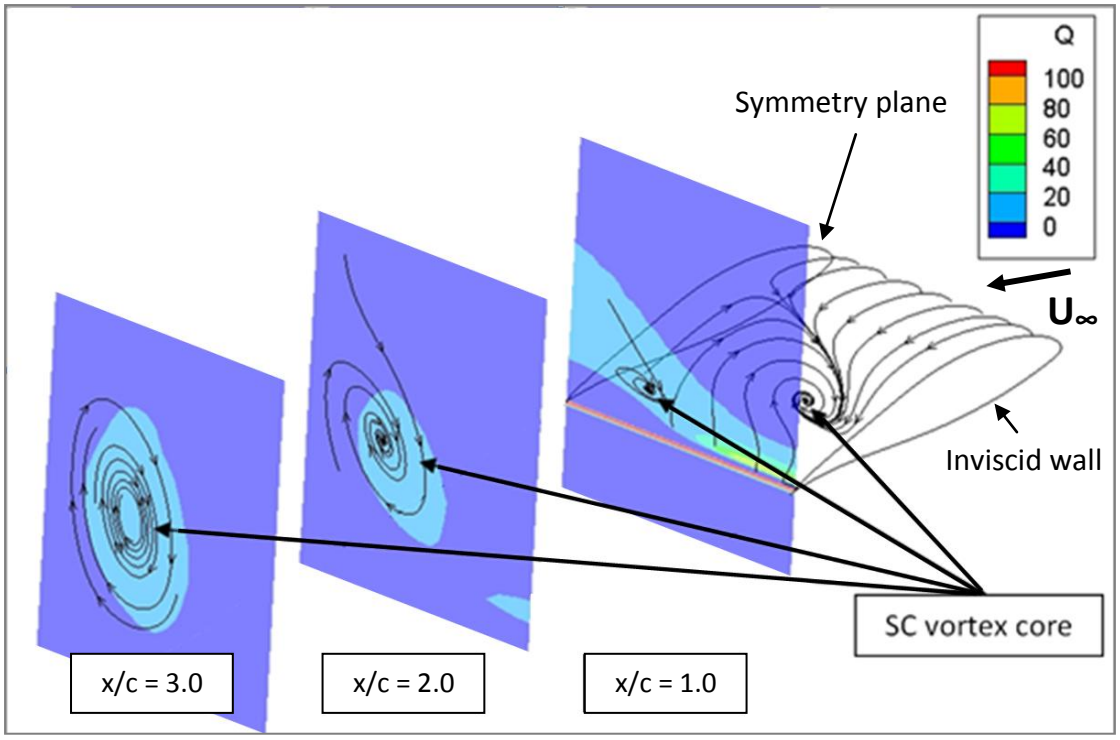

Figure 57: Surface flow lines on the wing suction surface along with in-plane flow lines and Q contours on planes normal to the free stream flow at x/c = 1.0 (TE), x/c = 2.0 and x/c = 3.0. Vortex core spanwise location is z/S = 37% on the wing surface and z ≈ 17.5% in the downstream planes. Symmetry plane is at the left hand side (z/S = 0%). AR = 2.0, Re = 1.0x10^6, α = 16°.

A qualitative visualization of the vortex core lines based on Q isosurface locations is given in Figure 58 along with the vorticity direction. One can distinguish three continuous surfaces:

a. One corresponding to the TELV
b. One that includes the SLV and the initial part of the SC vortex.
c. One that stands for the continuation of the SC vortex in the wake.

The gap along the SC core line could possibly be attributed to the inadequacy of the Q criterion when a vortex expands in a non-uniform strain field (Jeong & Hussain, 1995).

It is conceivable that the SC vortex starts normal to the wing suction surface, but is quickly deflected by the SL vortex and the oncoming flow. By the time the SC vortex reaches the wing TE, it has moved inboard and its vorticity is parallel to the free stream flow.

Finally, Figure 59 (page 67) shows surface flow lines on the wing suction surface along with in plane flow lines and velocity magnitude contours on planes normal to the free stream flow at x/c = 1.0 (TE), x/c = 2.0 and x/c = 3.0. As the SC vortex moves downstream it interacts with its symmetric vortex pushing each other higher and at the same time deforming the wing wake, pushing it lower at the tips and higher at the centre of the SC.

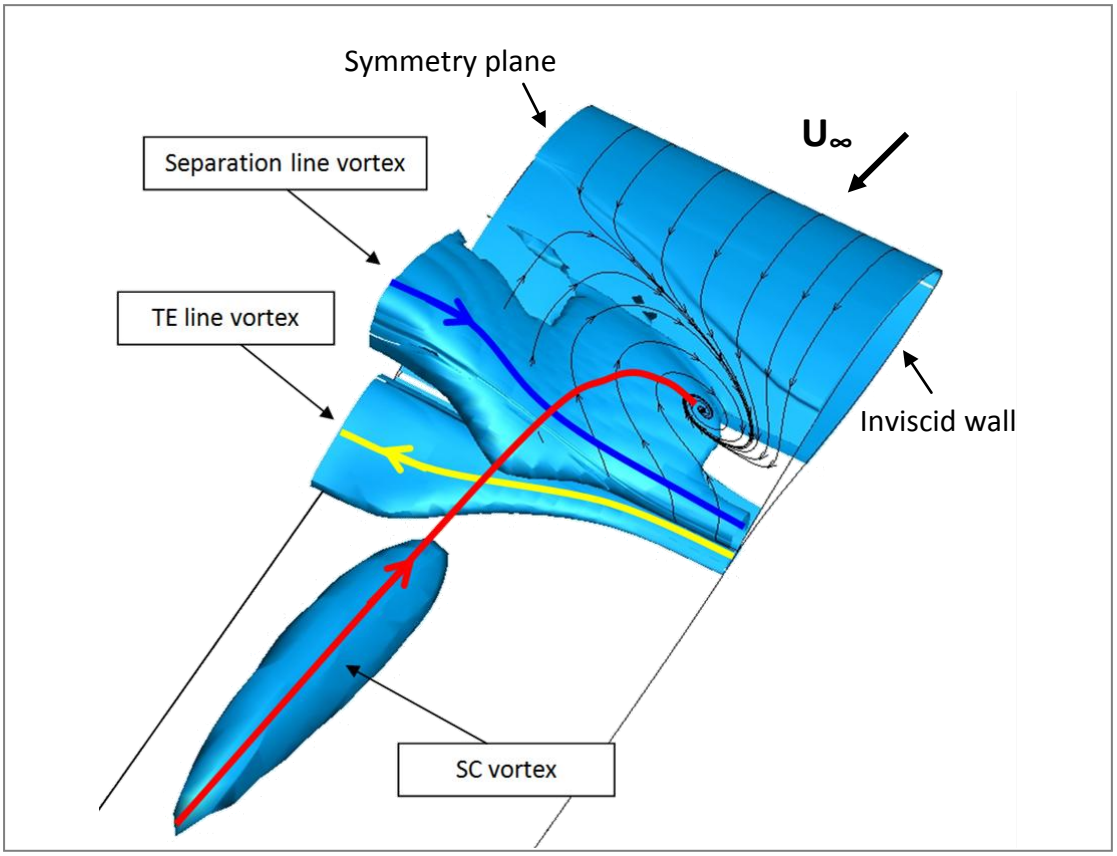

Figure 58: Surface flow lines on the wing suction surface and Q isosurface for Q=1. Interpreted vortex core lines with vorticity direction also shown. Symmetry plane is at the left hand side (z/S = 0%). AR = 2.0, Re = 1.0x10^6, α = 16°.

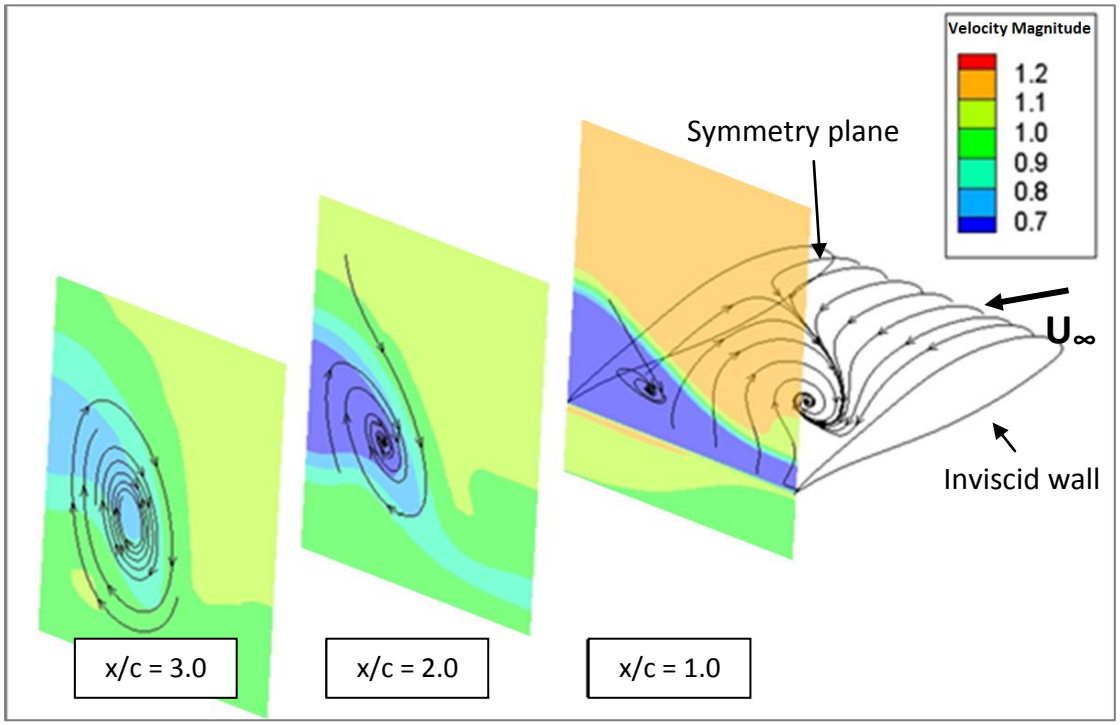

Figure 59: Surface flow lines on the wing suction surface along with in-plane flow lines and velocity magnitude contours on planes normal to the free stream flow at x/c = 1.0 (TE), x/c = 2.0 and x/c = 3.0. Symmetry plane is at the left hand side (z/S = 0%). AR = 2.0, Re = 1.0x10^6, α = 16°.

5.3 Summary

The flow over a rectangular wing was studied both experimentally and computationally. At higher angles of attack inherently unstable SCs were formed on the suction side of the wing. The flow was stabilized by using a ZZ tape strip locally as a spanwise disturbance. In the 3D simulations the macroscopic effect of ZZ tape was modelled as a pair of vortex generating surfaces using the BAY model.

Using the experimental and CFD data in comparison, the following conclusions can be drawn:

1. There is good qualitative and quantitative agreement between experimental and CFD data until a SC is first formed ($\alpha < 7^o$).
2. At higher angles, $\alpha > 7^o$, the 3D CFD data reproduce the experimental data with a 3^o delay which allows a trustworthy qualitative analysis of the vortex structures inside a SC.
3. The SC vortices start normal to the wing surface and extend downstream in the wake in agreement with the model suggested by (Yon & Katz, 1998).
4. The SC vortices interact strongly with the SL and the TEL vortices:
    a) By the time the SC vortex line reaches the wing TE it has already been deflected inboard and aligned with the free stream flow.
    b) The SL and TEL vortex cores grow and move higher towards the SC centre.
5. Due to the inboard deflection of the SC vortices, the SC trace in the wake contracted in the spanwise direction, compared to the SC width on the wing surface.
6. The three-dimensionality of the flow results in a significant spanwise variation of the force coefficients. In all cases sectional lift and drag attain their minimum value at the centre of the SC.
7. Well away from the SC vortex, the pressure distribution becomes similar to that of a 2D flow.
8. Under the influence of the SC vortices the wing wake is pushed upwards at the centre of the SC and downwards at the sides.

6 Stereo PIV study of a Stall Cell

In this chapter the findings of a Stereo PIV investigation of the stabilized SC are presented and discussed. The main description of the experimental set-up and data processing is given in Chapter 2. Here, the measurement planes are described in detail for a better understanding of the results that follow. The mean flow data are in complete agreement with the SC vortical structure given in the previous chapter. The turbulence characteristics of the flow are found to be highly anisotropic. In the final section a topological description of the SC flow is given, followed by a hypothesis regarding the SC formation mechanism.

Measurement planes

In order to capture the complex three-dimensional structure inside the SC, measurements were taken in planes normal to the flow and in planes normal to the wing span for two angles of attack, 10° and 7°. In particular for the 10° case the velocity was measured in planes normal to the flow at three chordwise positions x/c = 0.6 (plane A), x/c = 0.8 (plane B) and x/c = 1.06 (plane C). The TE position is at x = 1c. For the 7° case the only normal plane measured was at x/c = 1.05. For both angles of attack the flow was also measured at five planes normal to the wing span, one located at the centre of the wing and four at 8cm and 16cm, above and below it. The planes normal to the wing span are labelled α to ε. A side view of the measurement planes for the 10° case is shown in Figure 60. More details about the planes location is given in the results section.

SCs being large scale structures, the area covered by the velocity measurements had to be of large extent, especially as regards the planes normal to the flow. For this reason measurements were performed at a series of adjacent frames normal to the flow with at least 20% overlapping for each of the normal planes. A schematic view of the test set up with the measurement frames (normal and parallel to the flow) downstream of the TE is given in Figure 61. Measurement details for all the planes are given in Table 5, in page 71.

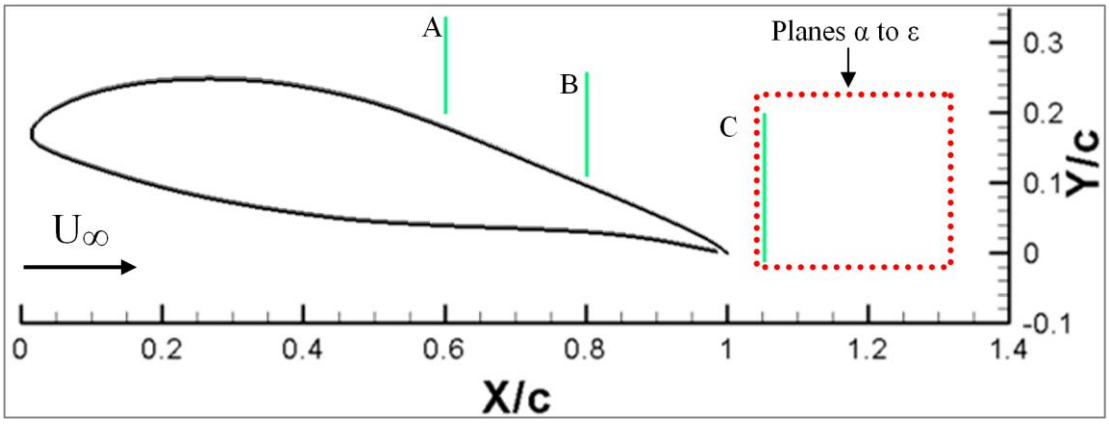

Figure 60: Stereo PIV measurement planes for the 10° case. Planes normal to the flow are shown with solid green line. The red dotted line shows the planes normal to the wing span.

Finally, as guidance, a schematic of the expected vortex core positions with respect to the measurement planes is given in Figure 62. For clarity the figure is split in two parts. The left part (a) shows only the two counter rotating SC vortices that start normal to the wing surface and extend downstream. The SLV and the TELV which run parallel to the wing TE and also have vorticity of opposite sign are shown in the right part of the figure (b).

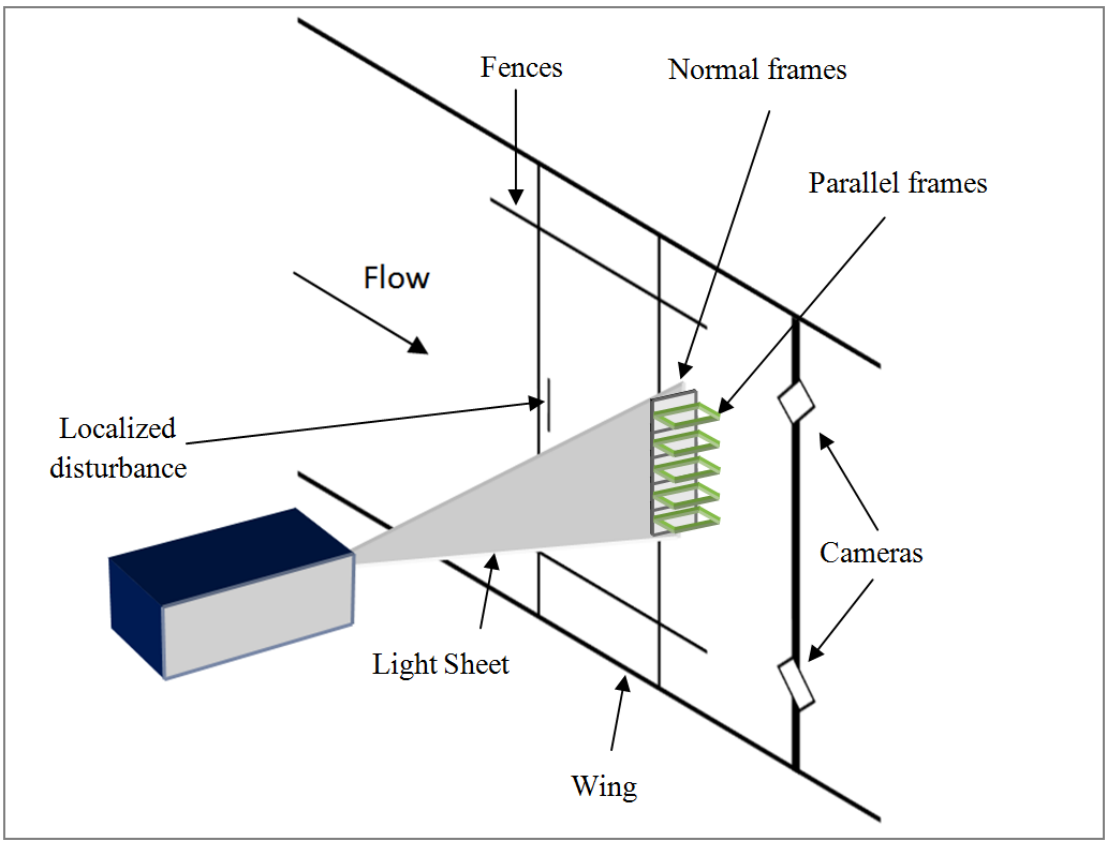

Figure 61: Schematic view of the Stereo-PIV set up. The light sheet is shown in position for normal plane measurement along with measurement frames normal to the flow at x/c = 1.06 and normal to the wing span at all spanwise positions. Camera positioning downstream of the wing is also shown.

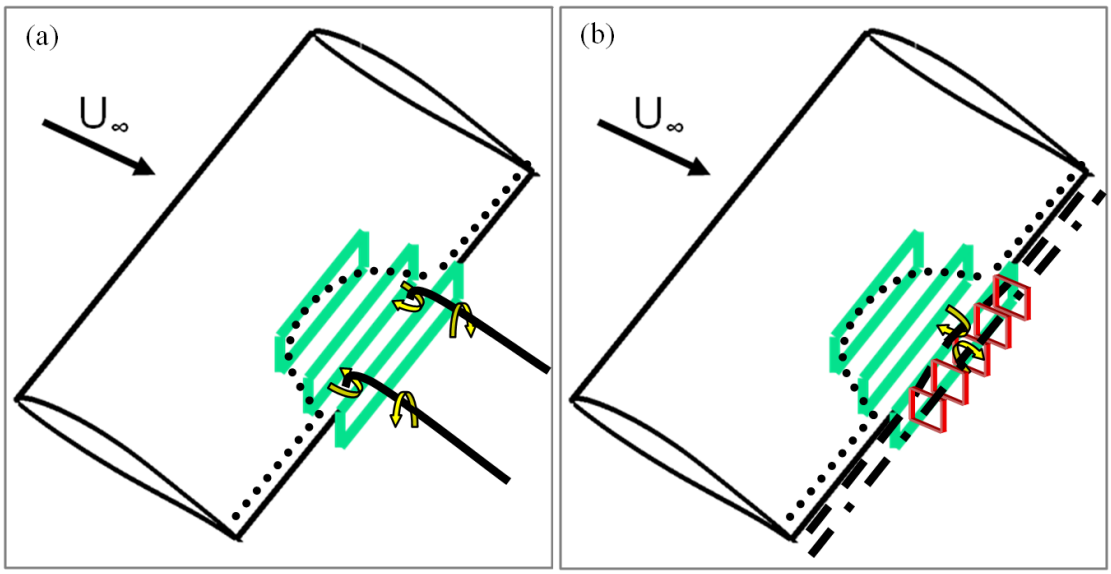

Figure 62: (a) Schematic of the SC vortices in relation to the measurement planes normal to the flow. (b) Schematic of the TELV (dashed line) and the SLV (dashed-dotted line) in relation to the measurement planes. The dotted line on the wing suction surface represents separation line. Planes normal to the flow are shown with thick green line. The thin red line shows the planes normal to the wing span.

Angle of attack	7°		10°			
Plane orientation with respect to free stream	normal	parallel	normal	normal	normal	parallel
Plane Names			A	B	C	α - ε
Chordwise location	1.05c	-	0.6c	0.8c	1.06c	-
# of adjacent frames	5	-	2	3	3	-
Lenses	90mm	90mm	90mm	90mm	50mm	50mm
Focal ratio	1/2.8	1/2.8	1/2.8	1/2.8	1/1.4	1/1.4
Camera contained angle	62°	62°	62°	69°	62°	73°
Final interrogation area size [px]	32x32	32x32	32x32	32x32	32x32	32x32
Final interrogation area size [mm]	2.0x2.0	2.2x2.2	3.1x3.1	2.6x2.6	4.0x4.0	3.9x3.9
Minimum resolved velocity [m/s]	0.3	0.3	0.5	0.4	0.6	0.6
Minimum resolved velocity [normalized with respect to the free stream]	0.01	0.01	0.02	0.02	0.02	0.02

Table 5: Stereo PIV test details for all the planes measured.

6.1 Results and discussion

In the following graphs the wing TE is always located at x/c = 1.0 and the middle plane of the wing span is at z/S = 0%, where S is the wing span. At this spanwise station a profile of the airfoil at the relevant angle of attack is drawn for reference. The free stream velocity and the wing chord have been used for the non-dimensionalization of the presented quantities. The 10° case will be analysed first since the SC is bigger and more measurement planes were taken, which makes the analysis of the SC structure easier. Then data from the 7° case will be presented and discussed in comparison to the 10° case.

Figure 63 shows the oil flow pattern on the wing suction side for α = 10°, Re = $0.87x10^6$. The flow is from left to right, but the wing front part is not shown in the picture for greater detail. As the wing is located vertically in the tunnel, gravity affects the final image since it pulls the oil mix downwards at areas of low velocity. Still, the SC structure is clearly visible. The surface foci of the SC vortices are located approximately at z/S = 13% above and below the wing mid span (z/S = 0%). Their chordwise location is x/c ≈ 0.91 and the most upstream point of the SC was found to be at x/c ≈ 0.48.

The thick red vertical lines in the figure indicate the location of the three measurement planes normal to the flow at chordwise locations 0.6c (plane A), 0.8c (plane B) and 1.06c (plane C). For planes A and B, which are above the wing surface the nearest velocity vector is at 1.3mm and 0.9mm from the wing surface, respectively. Due to strong reflections it was not possible to measure the flow closer to the surface. The location spanwise of planes α to ε which are located normal to the wing span and downstream of the wing TE (see Figure 60) is given by the thick white lines. The exact spanwise positions of these planes are: z/S = -13.3% (plane α), z/S = -6.7% (plane β), z/S = 0.0% (plane γ – mid-span), z/S = 6.7% (plane δ), z/S = 13.3% (plane ε). For the 7°, Re = $0.87x10^6$ case the same normal to the wing span planes were measured. However, since at 7° the SC is much smaller the only plane that was measured normal to the flow was at x/c = 1.05.

In some of the contours that are shown below discontinuities exist, especially in those depicting vorticity. They appear where the adjacent frames are patched together. No smoothing was applied to the contours and, since the vorticity is computed from different sets of velocity vectors, exact match was not expected at the borders. Besides, the various

frames were taken under the same conditions, but on different days, and some small discrepancies, due to e.g. not perfect model positioning, may be expected.

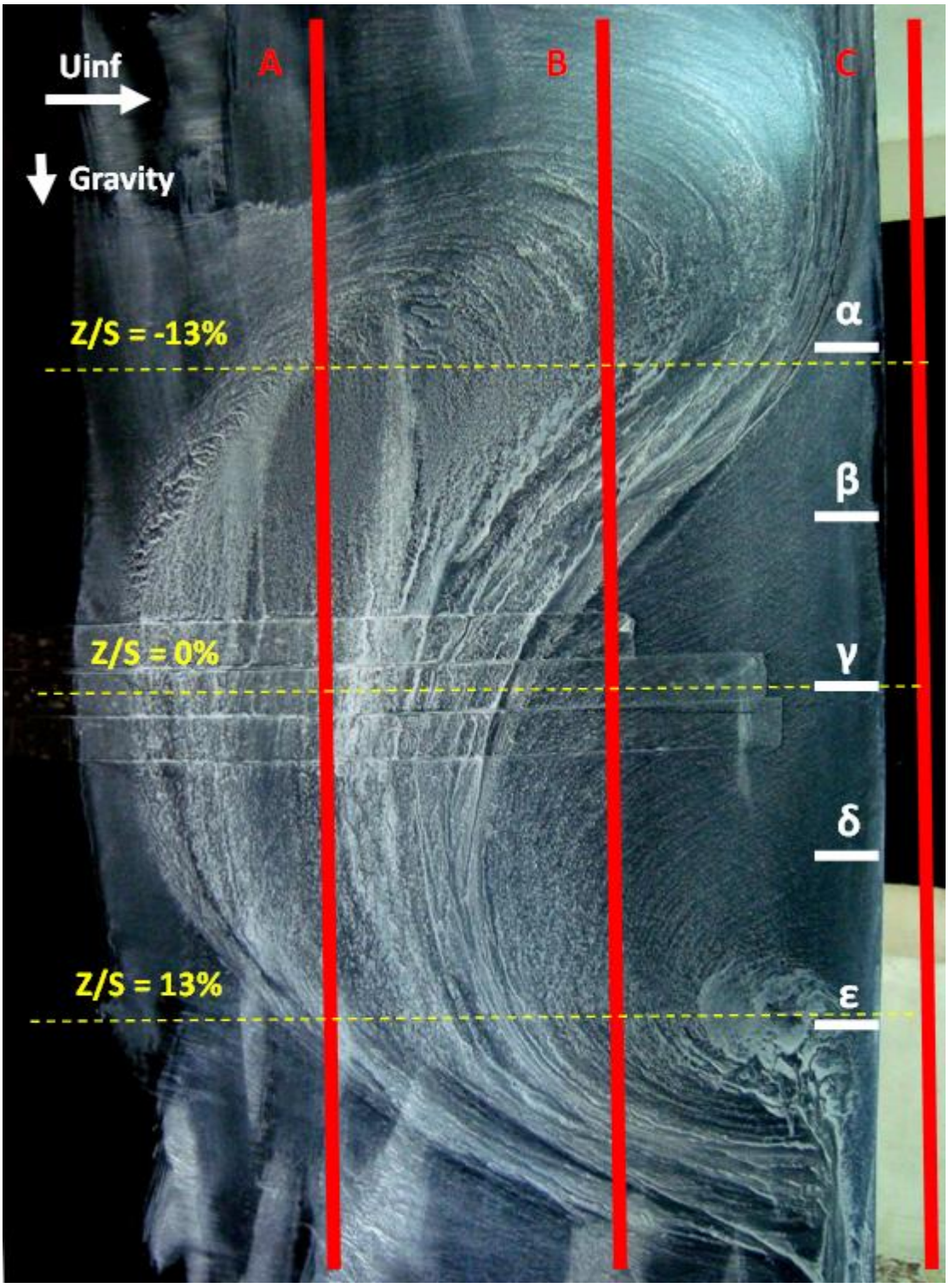

Figure 63: Oil flow pattern on the wing suction side for α = 10°, Re = 0.87x10^6. The flow is from left to right. The wing is located vertically in the tunnel and, hence, gravity is pulling the oil mix downwards, affecting the final image. The red solid lines indicate the measurement planes normal to the flow, A, B and C. Thick white thick marks indicate the spanwise position of planes normal to the wing span, α to ε. Thin yellow lines indicate the wing centre span (z/S = 0.0%) and the interpreted locations of the two SC vortex cores.

6.1.1 The α = 10° case

Mean quantities

In Figure 64 contours of normalized streamwise velocity (U) are plotted on planes A, B and C. The dashed isoline corresponds to streamwise velocity value of zero. Dark blue regions correspond to reversed flow. The amount of reversed flow is initially very limited (plane A, x/c = 0.6) and grows moving downstream. The highest values of reversed flow appear on plane B, i.e. close to the wing surface between the two SC vortices. Interestingly the reversed flow region on plane C is narrower than that on plane B, suggesting that the SC wake is contracted in the spanwise direction downstream of the wing TE compared to its cross section shape on the wing surface.

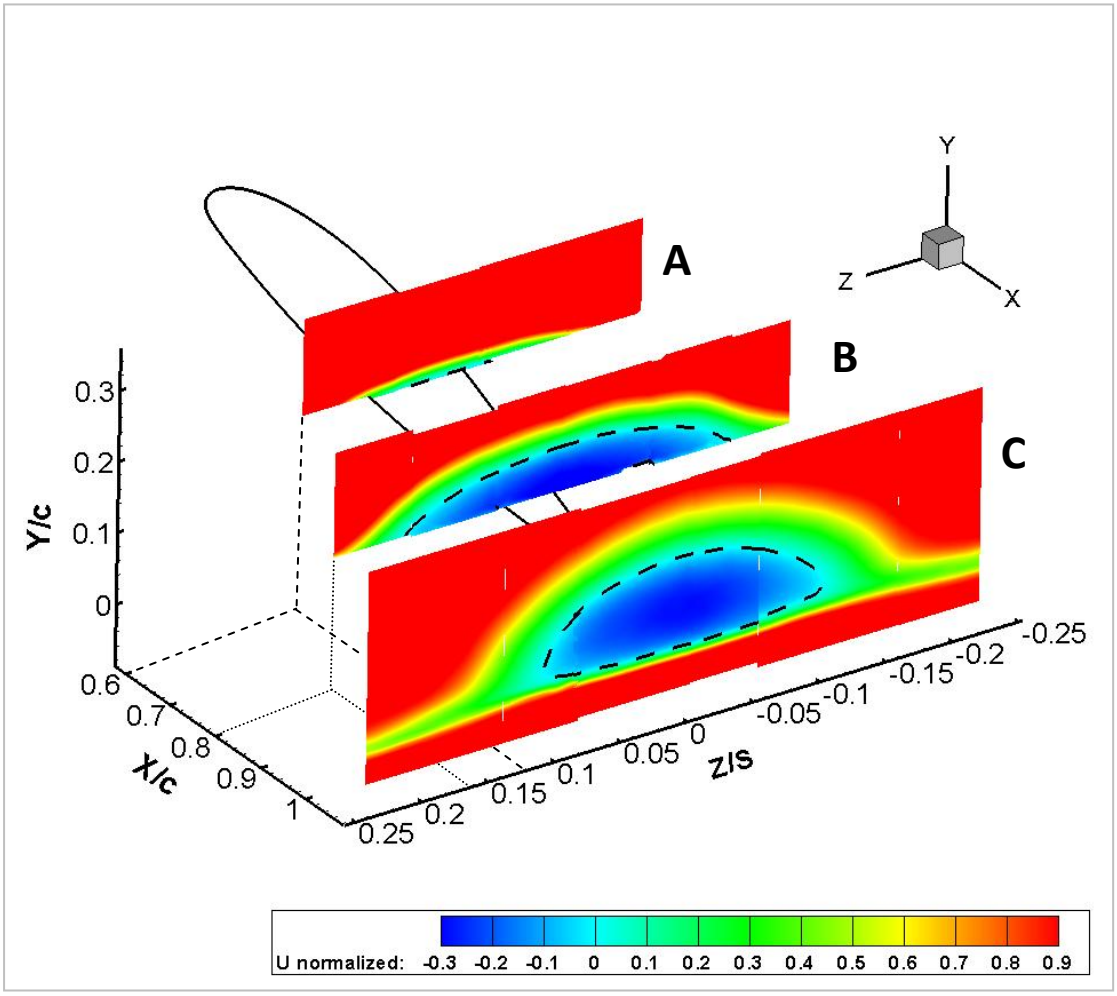

Figure 64: Contours of normalized streamwise velocity at planes normal to the free stream, at chordwise locations 0.6c, 0.8c and 1.06c. The dashed isoline corresponds to streamwise velocity value of zero. (α = 10°, Re = 0.87x10^6).

Figure 65 shows contours of normalized streamwise vorticity at planes A, B and C. The dashed line on each plane is an isoline of zero streamwise velocity corresponding to the boundary of the reversed flow region. On plane C, two large regions of opposite vorticity are observed at the upper part of the plane and two elongated narrow regions of vorticity below them. All high vorticity areas are located outside the reversed flow region. Each of the elongated regions has vorticity of opposite sign compared to the large region above it. The top regions correspond to the SC vortices which by the time they have reached plane C have

strong x-vorticity component resulting from the streamwise alignment process they undergo. The elongated regions of vorticity in the lower part, as explained below, correspond mostly to shear in the wake.

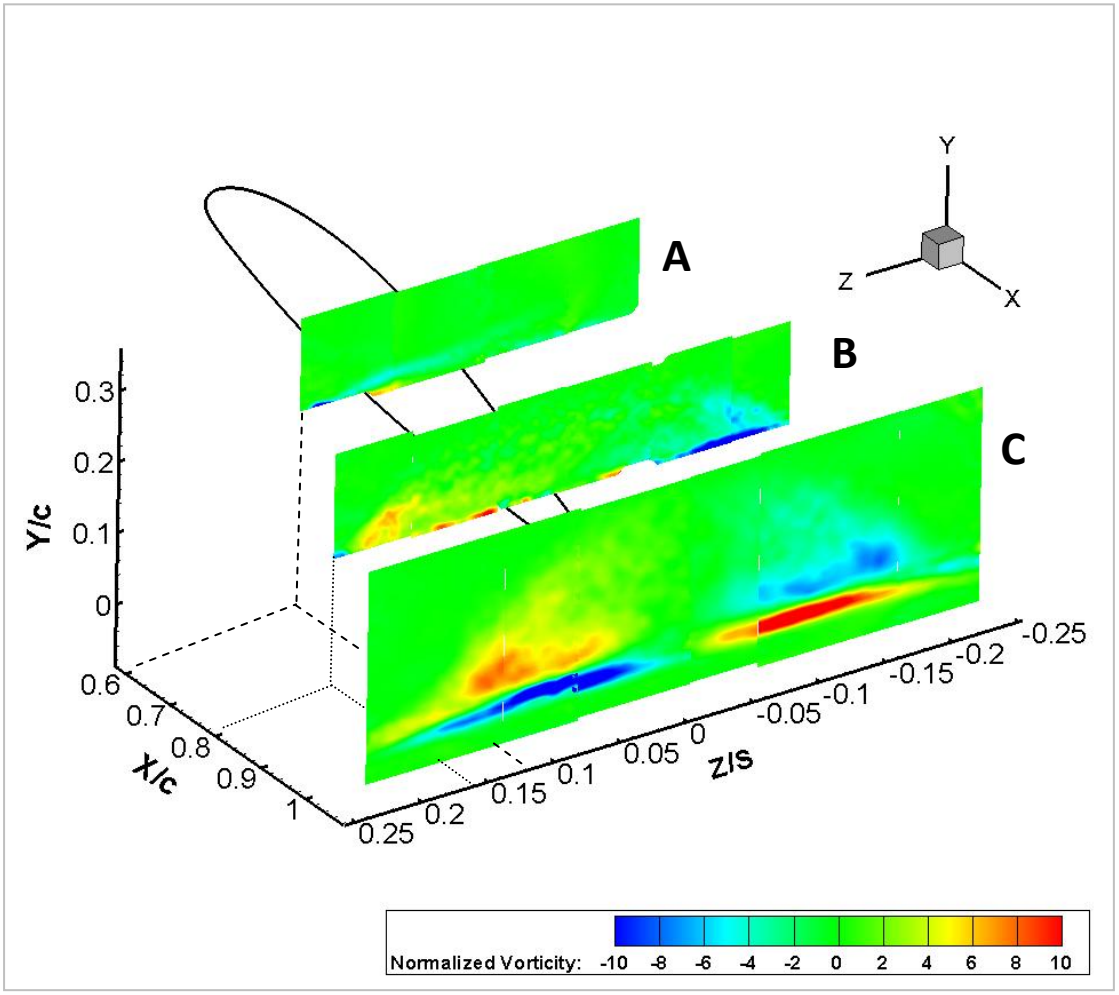

Figure 65: Contours of normalized streamwise vorticity at planes normal to the free stream, at chordwise locations 0.6c, 0.8c and 1.06c. The dashed isoline corresponds to streamwise velocity value of zero. (α = 10°, Re = 0.87x10^6).

Figure 66 shows contours of the Q criterion (Hunt et al., 1988) and of the streamwise vorticity together with in-plane velocity vectors on plane C. One out of every 16 vectors is shown for clarity. Again, the dashed line encloses the area of reversed flow. The upper regions of high vorticity on plane C coincide with the regions of maximum Q. These regions are centred very close to the spanwise position that corresponds to the centres of the SC vortices on the wing suction surface (z/S ≈ ±13%). Two more peaks of Q appear at z/S ≈ ±7%, within the elongated regions of vorticity underneath the SC vortices. It is possible that these correspond to the TE vortex, at the point where it is bent away from the wing TE, inboard of the two SC vortices. This kind of curving of the TELV is clear in Figure 58 in Chapter 5 and in the Stereo - PIV data on planes normal to the wing span, which are discussed later.

With regard to vortex identification criteria it is recognized that no single criterion works in all cases (Kolář, 2007). In the present case the Q criterion was used for continuity reasons.

Nevertheless application of the λ_2 criterion (Jeong & Hussain, 1995) to the 2D in-plane flow gave very similar results and could have been equally used.

The two areas of opposite vorticity in plane B (Figure 65) do not correspond to the SC vortices, since, as shown in Figure 63, plane B is located upstream of the SC vortex foci on the wing surface. These regions of vorticity correspond to the flow curving as it goes above and around the SC bubble, see e.g. the projected vectors on plane B in Figure 67, where the vorticity contours are also shown.

For completeness, contours of normalized velocity magnitude on planes A, B and C are shown in Figure 68, along with the isoline for streamwise velocity value of zero. The velocity magnitude at the centre of the reversed flow region on plane C appears to grow. This area is between the SLV and the TELV which, as it will be shown, grow stronger at the centre of the SC. This is why the reversed flow has higher velocity magnitude at the centre of this region.

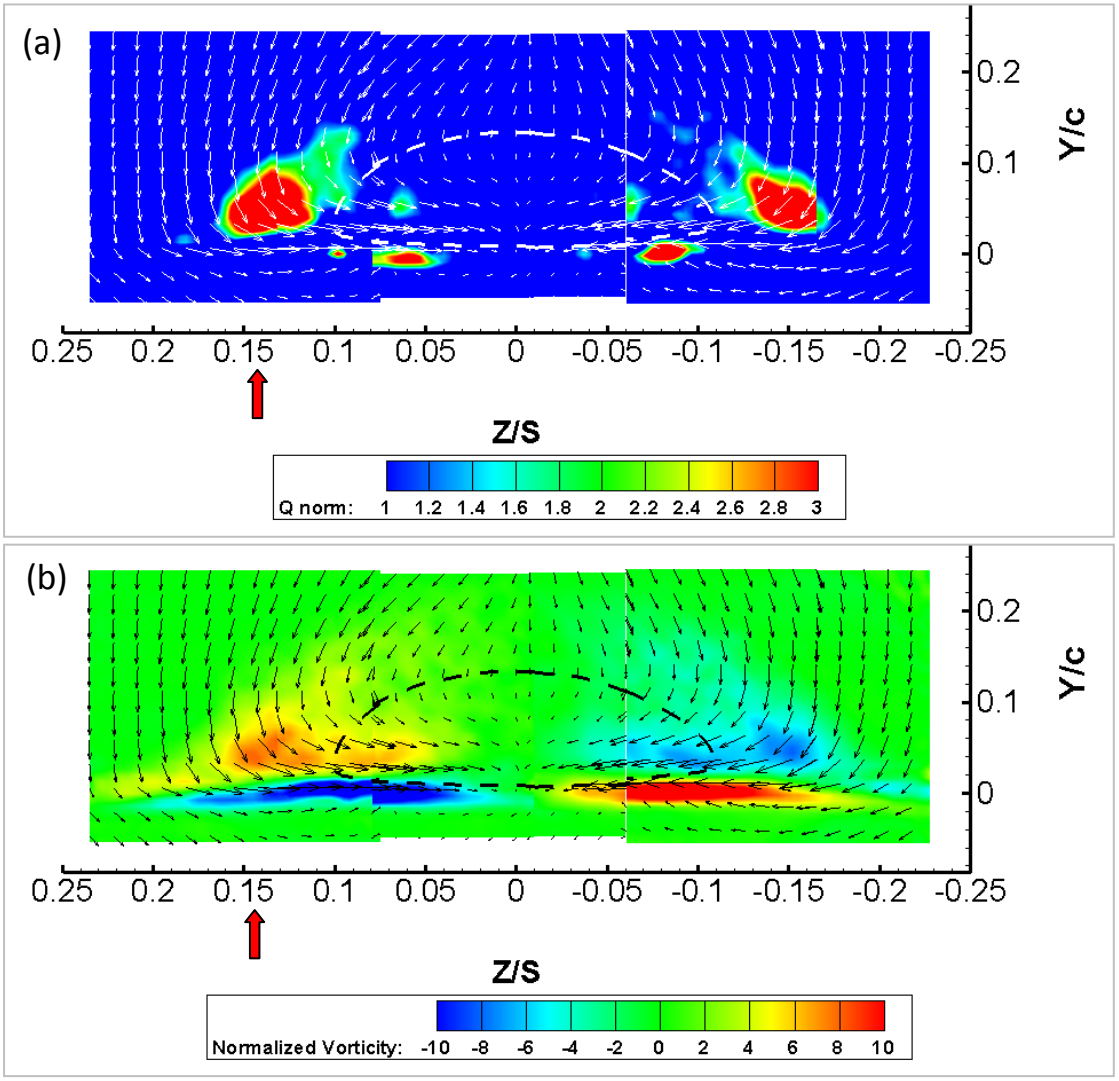

Figure 66: Contours of (a) the Q criterion and (b) normalized streamwise vorticity at the plane normal to the free stream, at chordwise location x/c = 1.06 (plane C). In-plane velocity vectors are also drawn. One out of every 16 vectors is plotted for clarity. The dashed isoline corresponds to streamwise velocity value of zero. The red vector at z/S = 0.145 indicates the spanwise position along which vorticity and shear stress angle are plotted in Figure 86 and Figure 84, respectively. (α = 10°, Re = 0.87x10^6).

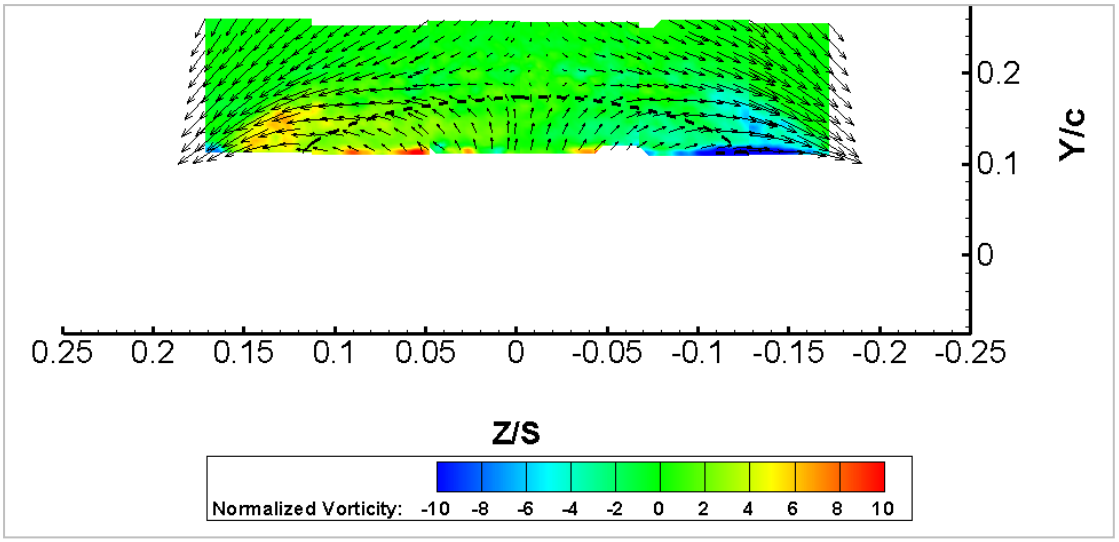

Figure 67: Contours of normalized streamwise vorticity and velocity vectors at the plane normal to the free stream, at chordwise location x/c = 0.8 (plane B). In-plane velocity vectors are also drawn. One out of every 16 vectors is plotted for clarity. The dashed isoline corresponds to streamwise velocity value of zero (α = 10°, Re = 0.87x10^6).

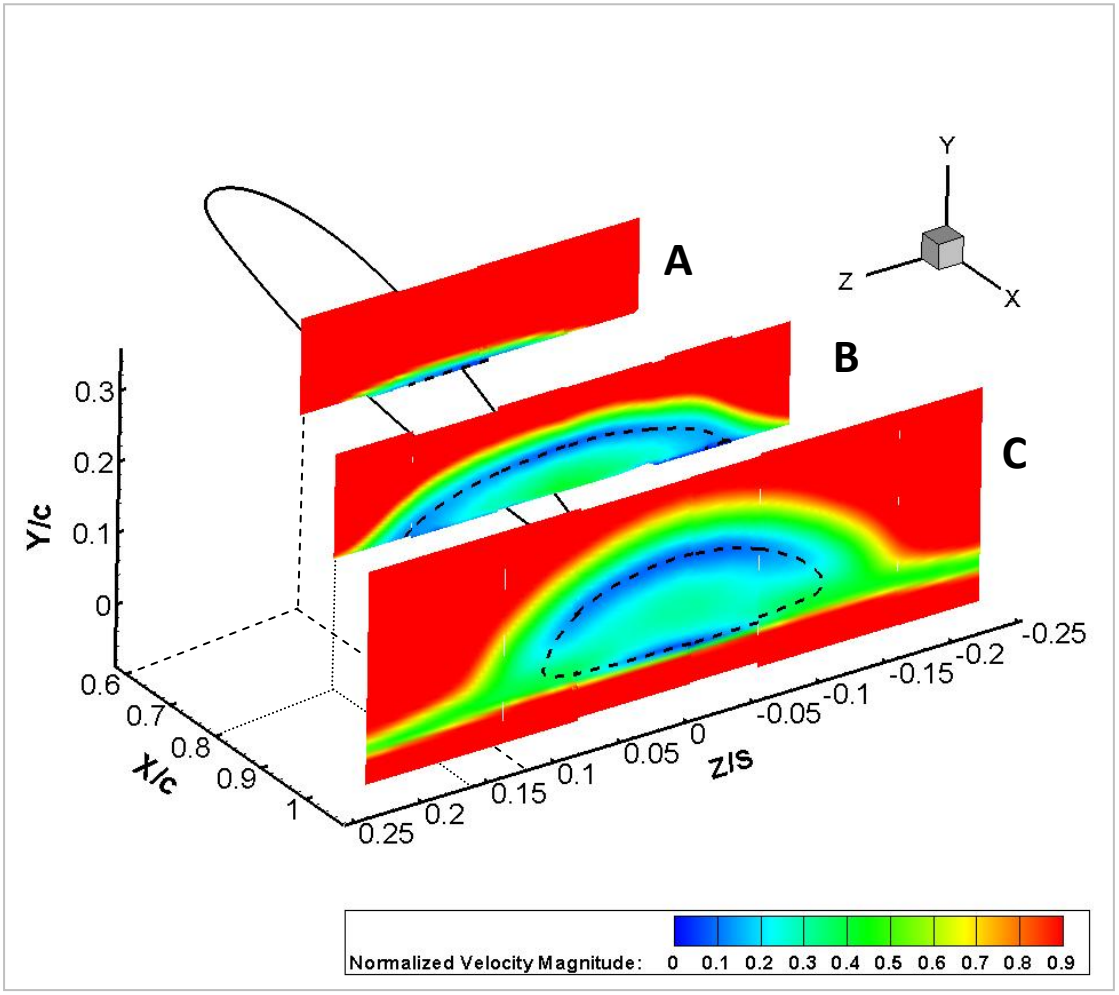

Figure 68: Contours of normalized velocity magnitude at planes normal to the free stream, at chordwise locations 0.6c, 0.8c and 1.06c. The dashed isoline corresponds to streamwise velocity value of zero (α = 10°, Re = 0.87x10^6).

In Figure 69 contours of normalized spanwise velocity (W) at planes normal to the wing span are shown together with in-plane stream lines. The spanwise velocity contours reveal regions of spanwise flow which are symmetric with respect to the mid plane. The spanwise velocity magnitude is greater for the two outboard planes (α and ε), which is not unexpected since these planes are approximately downstream of the SC vortex cores, see e.g. Figure 63.

The position of the SLV and the TELV is easier to see in Figure 70 where contours of the normalized spanwise vorticity at planes normal to the wing span are shown. Both the SLV and the TELV appear to grow significantly in size and strength at the centre of the SC (planes β, γ and δ), as the flow lines in Figure 69 reveal. As Figure 63 shows, β, γ and δ are in between the two SC vortices implying that the SLV and the TELV grow due to their interaction with the SC vortices.

The spanwise development of the SLV and the TELV is also clear in Figure 71 where contours of the Q criterion at planes normal to the wing span are drawn. Once inboard of the two SC vortices, i.e. for planes β, γ and δ, both vortices grow in size and strength. The TELV moves downstream, away from the TE in this region. The elongated shape of the TELV at the centre of the SC was also predicted by CFD (see Figure 58 in Chapter 5).

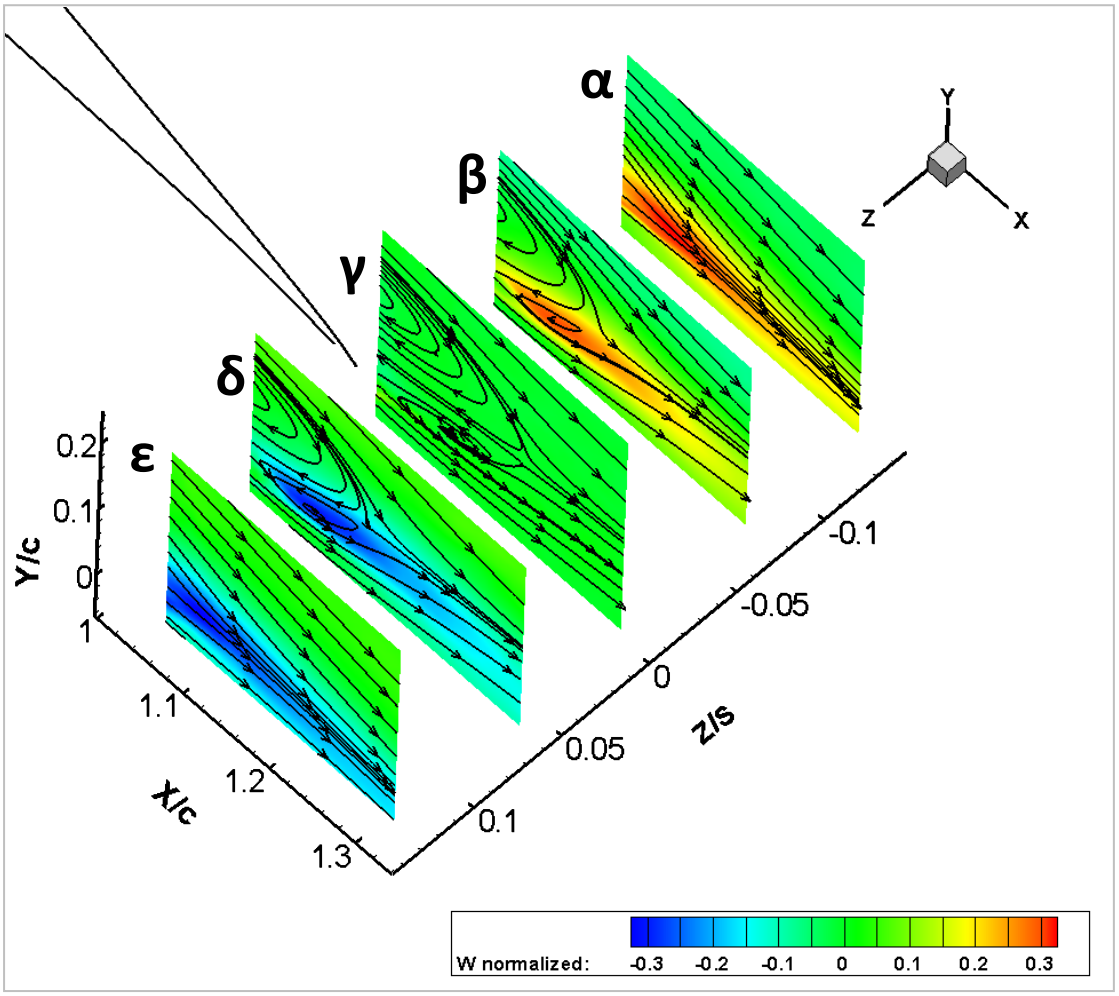

Figure 69: Contours of normalized spanwise velocity at planes normal to the wing span, at the wing mid-span (z/S = 0.0%) and at spanwise locations z/S = ±6.7% and z/S = ±13.3%. In plane flow lines are also shown (α = 10°, Re = 0.87x10^6).

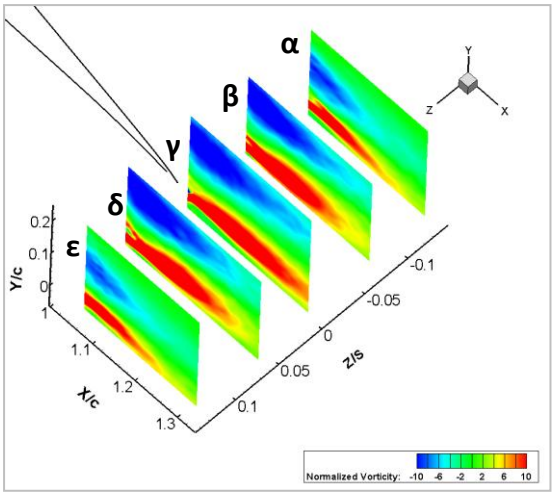

Figure 70: Contours of normalized spanwise vorticity at planes normal to the wing span, at the wing mid-span (z/S = 0.0%) and at spanwise locations z/S = ±6.7% and z/S = ±13.3%S. (α = 10°, Re = 0.87x10^6).

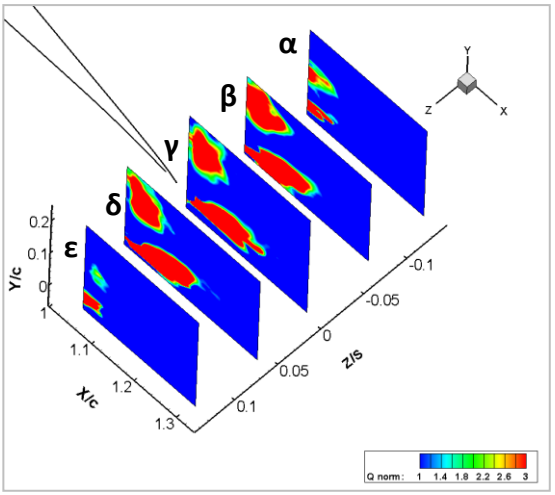

Figure 71: Contours of the Q criterion at planes normal to the wing span, at the wing mid-span (z/S = 0.0%) and at spanwise locations z/S = ±6.7% and z/S = ±13.3%. (α = 10°, Re = 0.87x10^6).

In relation to CFD results

In Figure 72 and Figure 73 contours of normalized streamwise velocity and vorticity, are drawn respectively. The measurement plane is at chordwise location x/c = 1.06 (plane C) and both Stereo PIV (left side, positive z/S values) and CFD data (right side, negative z/S values) are presented. On the CFD side, spanwise vorticity isolines for ω_z=-4 (dashed line) and ω_z=4 (solid line) are drawn enclosing the separation shear layer and the TE shear layer respectively. On the Stereo-PIV side lines for $\partial U/dy = \pm 4$ are drawn as indicators of the shear layers. Spanwise vorticity cannot be computed for the experimental data because the velocity variation along the X axis is not available for plane C, however it is assumed that $\omega_z = \frac{\partial V}{\partial x} - \frac{\partial U}{\partial y} \approx -\frac{\partial U}{\partial y}$.

In both measurements and CFD, vorticity is a derived quantity and therefore its values will depend on grid resolution. Since the grids are substantially different, the two sets of values are not directly comparable, however, the general shape and trends are.

The agreement appears good. CFD, as expected, captures the main shape of the wake although the SC is smaller in size. In particular, the reversed flow region is smaller and the SC vortex appears slightly more inboard than in the Stereo-PIV data.

Interestingly, according to the CFD data, both areas of high streamwise vorticity, i.e. the SC vortex and the vorticity below it, are located inside the separation and TE shear strips indicated by the spanwise vorticity isolines, see Figure 73. The same holds for the experimental data, suggesting that the SC vortices are embedded in the separation shear layer. This also supports the view that the small Q peaks in the lower part of Figure 66 correspond to the curved TELV.

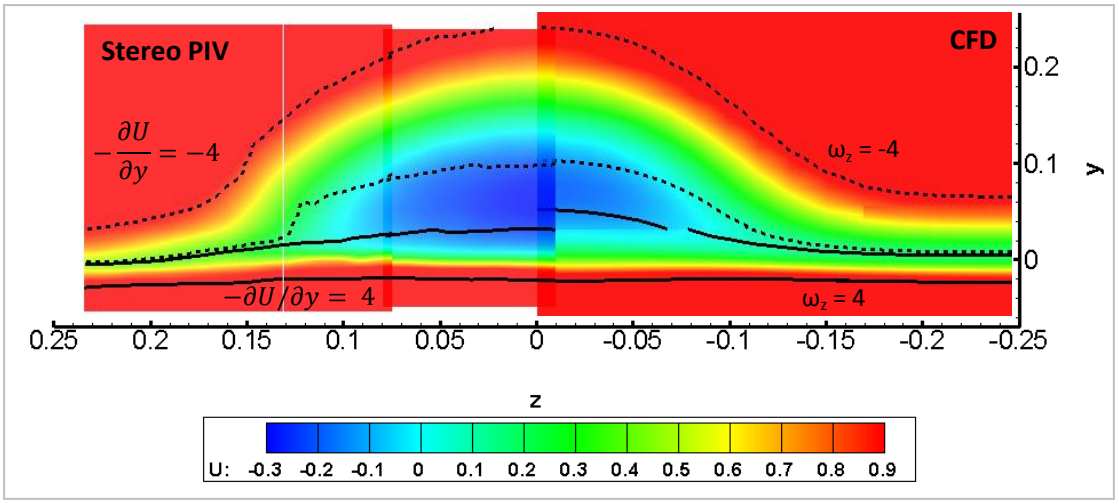

Figure 72: Contours of normalized streamwise velocity at chordwise location x/c = 1.06 (plane C). Stereo PIV (left) and CFD data (right). On the CFD data isolines of normalized spanwise vorticity are drawn for ω_z=-4 (dashed lines) and ω_z=6 (solid lines) indicating the strips corresponding to the separation and the TE shear layer respectively. On the Stereo - PIV data isolines of $\partial U/dy = \pm 4$ are drawn for the same reason.

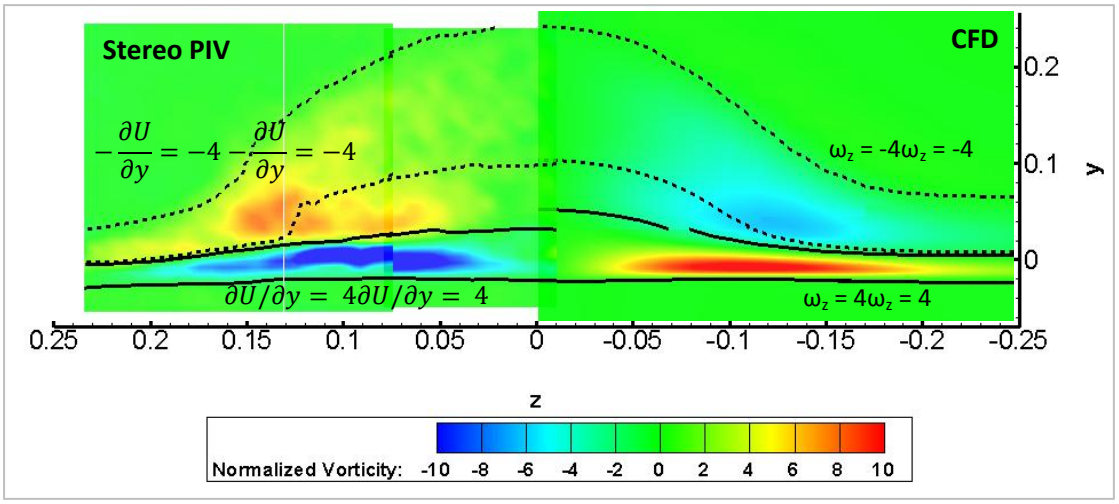

Figure 73: Contours of normalized streamwise vorticity at chordwise location x/c = 1.06 (plane C). Stereo PIV (left) and CFD (right) data. On the CFD data isolines of normalized spanwise vorticity are drawn for ω_z=-4 (dashed line) and ω_z=4 (solid line) indicating the strips corresponding to the separation and the TE shear layer respectively. On the Stereo - PIV data isolines of $\partial U/dy = \pm 4$ are drawn for the same reason.

Velocity plots

Figure 74 gives the spanwise velocity profiles at the spanwise locations of planes α to ε. Solid black lines refer to the streamwise position x/c = 1.06 (right after the TE), red squares to x/c = 1.18 and cyan circles to x/c = 1.30. The scale is the same for all curves. The velocity profile at the centre of the wing span (z/S = 0) is always practically zero. The profiles on both sides of the wing mid-span are symmetric. Examining the profiles at the z/S = ±6.7% stations it is clear that the spanwise velocity peak is higher at x/c = 1.18 (red squares) than at x/c = 1.06 (black line). This suggests that under mutual induction the SC vortices are pushed upwards.

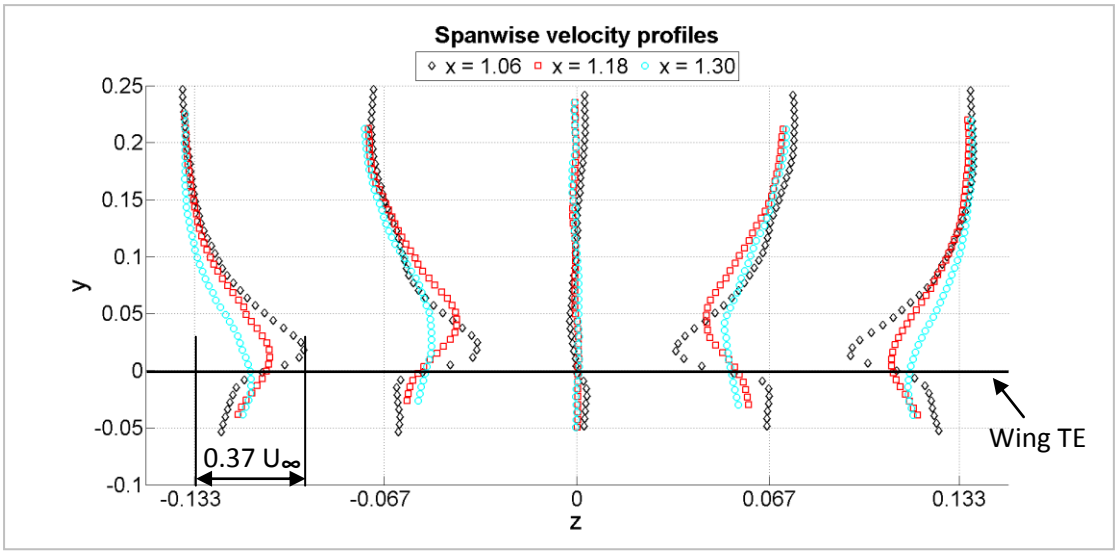

Figure 74: Spanwise velocity profiles at the spanwise locations z/S = 0, z/S = ±6.7%, z/S = ±13.3%. Solid black lines refer to the streamwise position x/c = 1.06 (right after the TE), red squares to x/c = 1.18 and cyan circles to x/c = 1.30. The scale is the same for all curves. (α = 10°, Re = 0.87x10^6).

Figure 75 to Figure 77 show the streamwise velocity development along the x-axis on the three spanwise locations of planes γ (mid-span), δ and ε. The streamwise velocity behaviour on planes α (z/S = -13.3%) and β (z/S = -6.7%) is very similar to that of planes ε and δ, respectively, and is hence not shown here. For planes γ and δ (Figure 75 to Figure 76) five profiles are drawn. Two are from the respective spanwise measurement plane at two chordwise locations (x = 1.18c and 1.3c), and the other three from planes A (x/c = 0.6), B (x/c = 0.8) and C (x/c = 1.06). For plane ε (Figure 77), only four profiles are drawn since Plane A (x/c = 0.6) did not extend up to z/S = 13.3% and is hence not included. In these graphs, negative velocity values, when they exist, are indicated with filled blue circles. The fact that for the spanwise position z/S=6.7% there are negative x velocity components at x/c = 1.06 but not at x = 1.18c is in agreement with the statement that the wake is contracted in the spanwise direction downstream of the TE (compare Figure 76 to Figure 77).

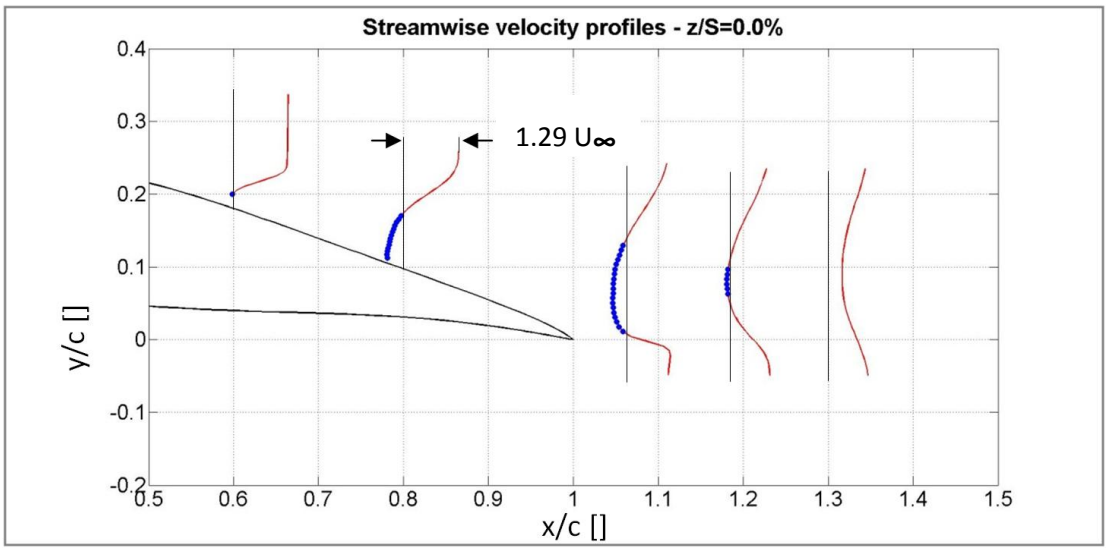

Figure 75: Normalized streamwise velocity profiles at chordwise locations x/c = 0.6, 0.8c, 1.06c, 1.18c, 1.30c at the spanwise position z/S = 0.0% (mid span, plane γ). Blue dots correspond to negative streamwise velocity values. The thin black vertical lines correspond to U = 0m/s. The scale is the same for all curves. (α = 10°, Re = 0.87x10^6).

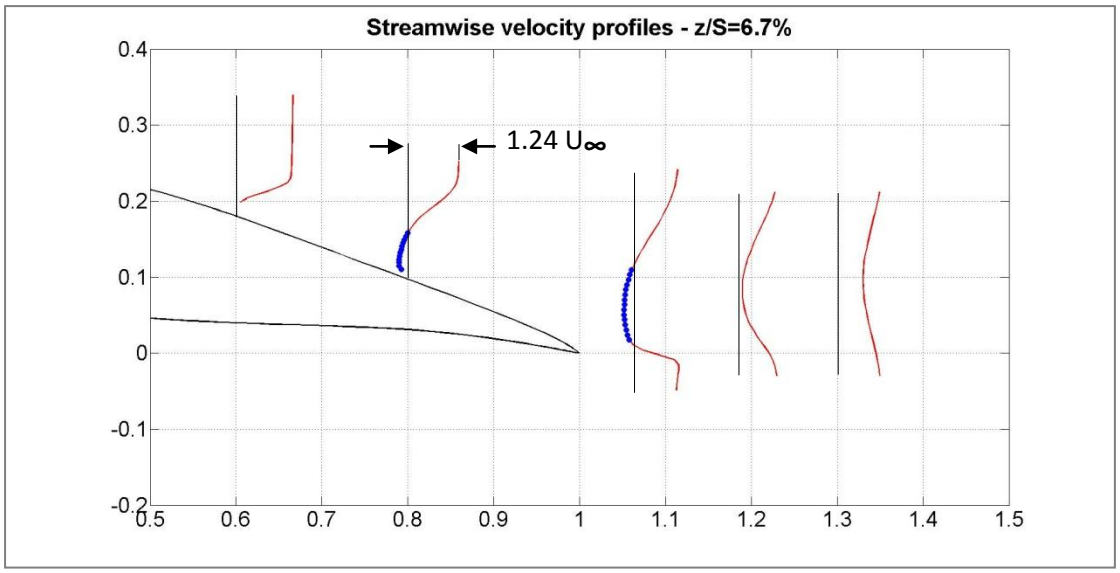

Figure 76: Normalized streamwise velocity profiles at chordwise locations x/c = 0.6, 0.8c, 1.06c, 1.18c, 1.30c at the spanwise position z/S=6.7% (plane δ). Blue dots correspond to negative streamwise velocity values. The thin black vertical lines correspond to U = 0m/s. The scale is the same for all curves. (α = 10°, Re = 0.87x10^6).

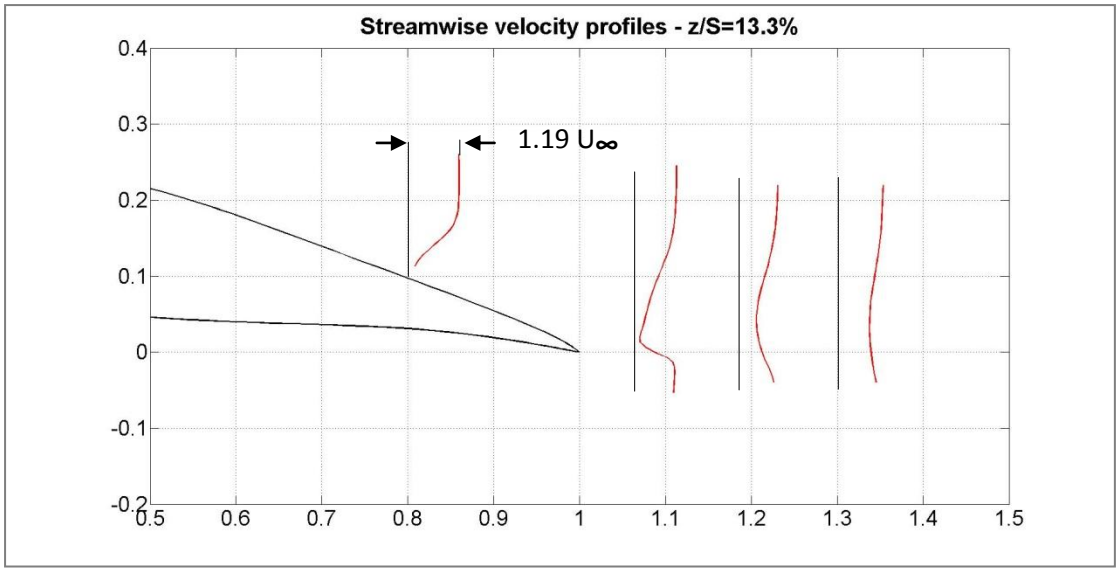

Figure 77: Normalized streamwise velocity profiles at chordwise locations x/c = 0.8, 1.06c, 1.18c, 1.30c at the spanwise position z/S = 13.3% (plane ε). The thin black vertical lines correspond to U = 0m/s. The scale is the same for all curves. (α = 10°, Re = 0.87x10^6).

Reynolds stress data

Figure 78, Figure 79 and Figure 80 show the $\overline{u'^2}/U_\infty^2$, $\overline{v'^2}/U_\infty^2$ and $\overline{w'^2}/U_\infty^2$ normal Re stress distribution on all planes. Accordingly, Figure 81, Figure 82 and Figure 83 show contours of $\overline{u'v'}/U_\infty^2$, $\overline{v'w'}/U_\infty^2$ and $\overline{u'w'}/U_\infty^2$, respectively. Normal stresses appear to have significant anisotropy and their values are in general an order of magnitude higher than the shear stresses.

High $\overline{u'^2}/U_\infty^2$ values are observed at the regions of the separation shear layer and the TE shear layer on both the planes normal to the free stream (Figure 78a) and normal to the wing span (Figure 78b). Peak $\overline{u'^2}/U_\infty^2$ values appear on plane B (x/c = 0.8 - Figure 78-a), at the centre of the SC region, upstream of the SC vortices.

Peak values for the $\overline{v'^2}/U_\infty^2$ and $\overline{w'^2}/U_\infty^2$ normal stresses appear on planes β and δ (Figure 79-b and Figure 80-b), respectively, downstream of the wing TE. These regions are between the two shear layers and should not be correlated with them. It is conceivable that regions of high $\overline{v'^2}/U_\infty^2$ appearing in proximity to vortices (here the SC vortices) indicate fluctuation of the vortical structure in the spanwise direction. Similarly regions of high $\overline{w'^2}/U_\infty^2$ indicate fluctuation in the vertical direction. The fact that these regions appear further downstream of the wing TE (at x/c ≈ 1.16) and not directly after it, is attributed to the inboard movement of the SC vortices downstream of the wing TE. The fact that $\overline{w'^2}/U_\infty^2$ values are smaller but at the same regions suggests that the vertical movement of the SC vortices is smaller.

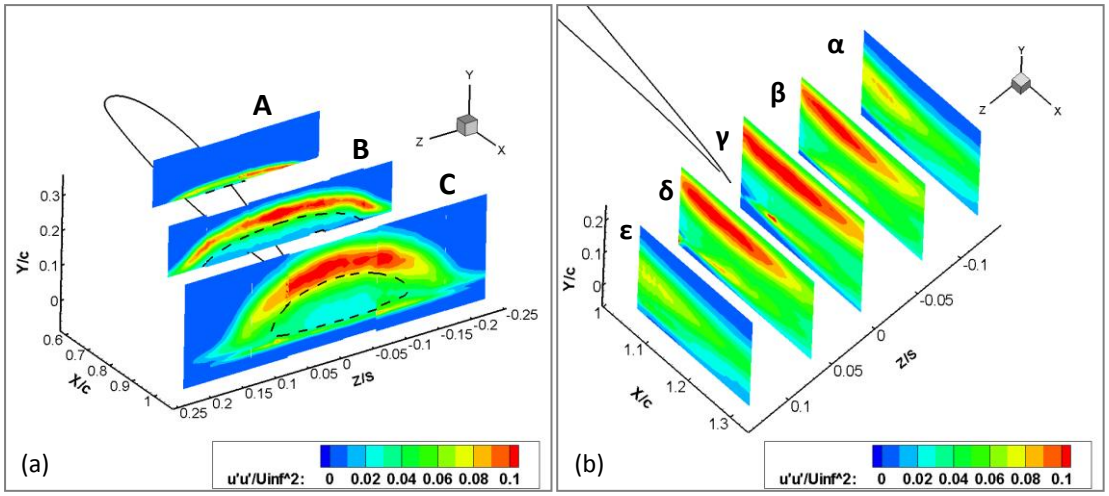

Figure 78: Contours of the $\overline{u'^2}/U_\infty^2$ Re Stress (a) at planes normal to the flow, at chordwise locations 0.6c, 0.8c and 1.06c. The dashed isoline corresponds to streamwise velocity value of zero. (b) at planes normal to the wing span, at the wing mid-span (z/S = 0.0%) and at spanwise locations z/S = ±6.7% and z/S = ±13.3%. (α = 10°, Re = 0.87x10^6).

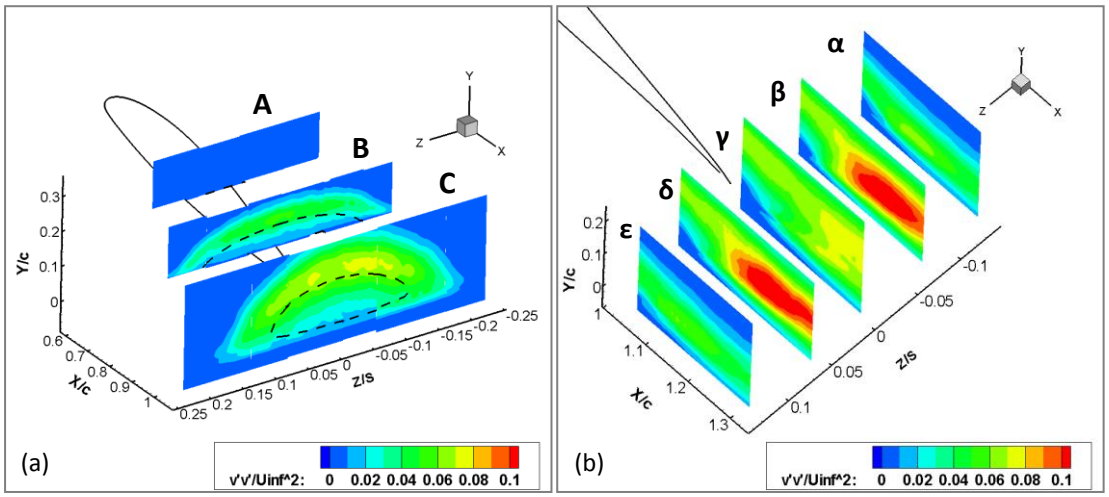

Figure 79: Contours of the $\overline{v'^2}/U_\infty^2$ Re Stress (a) at planes normal to the flow, at chordwise locations 0.6c, 0.8c and 1.06c. The dashed isoline corresponds to streamwise velocity value of zero. (b) at planes normal to the wing span, at the wing mid-span (z/S = 0.0%) and at spanwise locations z/S = ±6.7% and z/S = ±13.3%. (α = 10°, Re = 0.87x10^6).

Concentration of high negative $\overline{u'v'}/U_\infty^2$ Re shear stress along the separation shear layer and high positive $\overline{u'v'}/U_\infty^2$values along the TE shear layer is observed (Figure 81), as expected in shear layers. The $\overline{u'v'}/U_\infty^2$ shear stress values are significantly higher in planes β, γ and δ where the SLV and the TELV grow. The absolute maximum $\overline{u'v'}/U_\infty^2$ values are almost two times higher than the other shear stresses values.

Regarding $\overline{v'w'}/U_\infty^2$ antisymmetric peaks are observed on plane C (Figure 82-a) and then further inboard and downstream on planes β and δ (Figure 82-b). These peaks are also linked to the presence of the SC vortices, which converge towards the centre downstream of the wing TE.

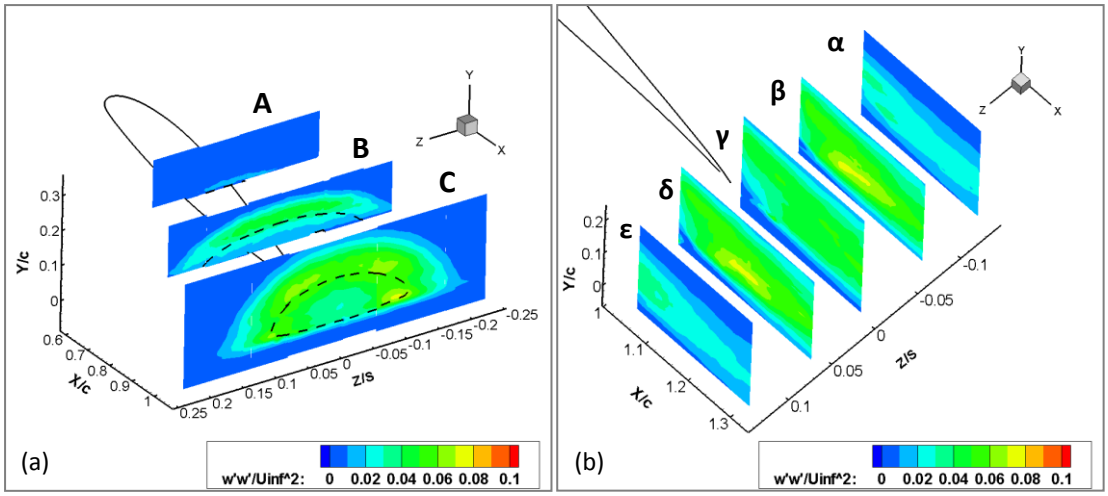

Figure 80: Contours of the $\overline{w'^2}/U_\infty^2$ Re Stress (a) at planes normal to the flow, at chordwise locations 0.6c, 0.8c and 1.06c. The dashed isoline corresponds to streamwise velocity value of zero. (b) at planes normal to the wing span, at the wing mid-span (z/S = 0.0%) and at spanwise locations z/S = ±6.7% and z/S = ±13.3%. (α = 10°, Re = 0.87x10^6).

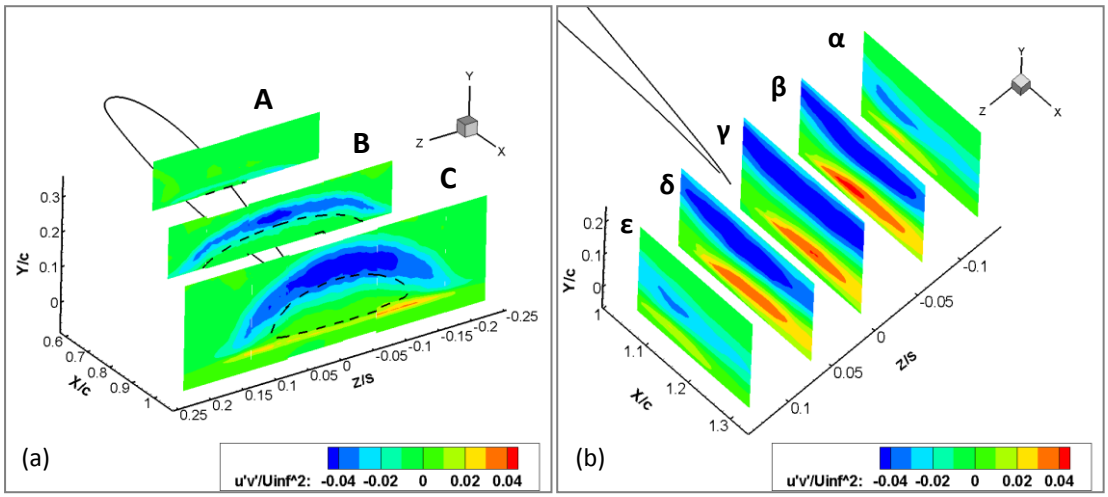

Figure 81: Contours of the $\overline{u'v'}/U_\infty^2$ Re Stress (a) at planes normal to the flow, at chordwise locations 0.6c, 0.8c and 1.06c. The dashed isoline corresponds to streamwise velocity value of zero. (b) at planes normal to the wing span, at the wing mid-span (z/S = 0.0%) and at spanwise locations z/S = ±6.7% and z/S = ±13.3%. (α = 10°, Re = 0.87x10^6).

The $\overline{u'w'}/U_\infty^2$ shear stress distribution in Figure 83 shows lower peaks than the other shear stresses. Considering that $\overline{u'w'}/U_\infty^2$ is the shear stress that transports momentum and indicates rotational motion along the Y axis, the peaks on plane C (Figure 83-a) and on the planes normal to the wing span (Figure 83-b) are related to the three-dimensionality of the SLV and the TELV. The peaks on plane B and C (Figure 83-a) appearing outside of the reversed flow region, are in turn linked to the flow curvature as it goes around the SC separation bubble.

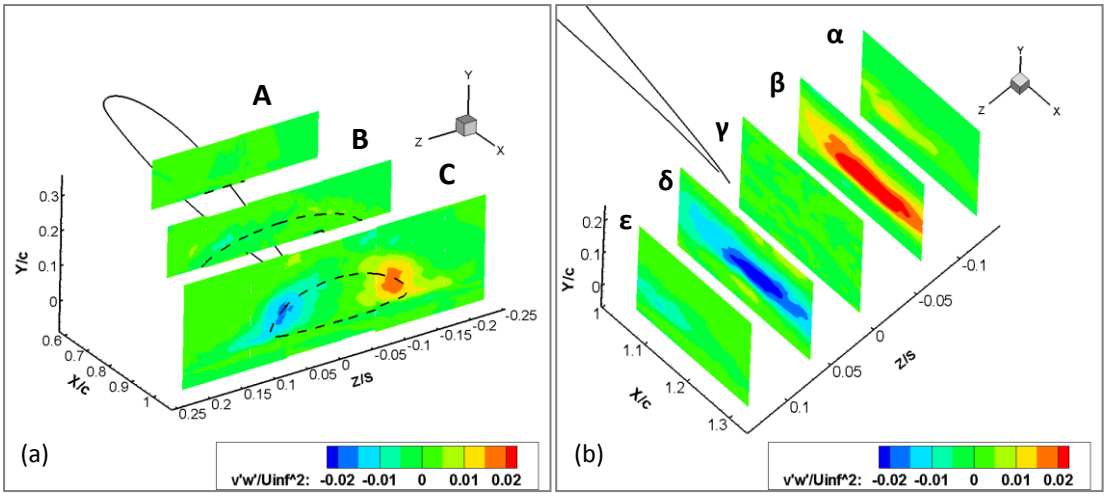

Figure 82: Contours of the $\overline{v'w'}/U_\infty^2$ Re Stress (a) at planes normal to the flow, at chordwise locations 0.6c, 0.8c and 1.06c. The dashed isoline corresponds to streamwise velocity value of zero. (b) at planes normal to the wing span, at the wing mid-span (z/S = 0.0%) and at spanwise locations z/S = ±6.7% and z/S = ±13.3%. (α = 10°, Re = 0.87x10^6).

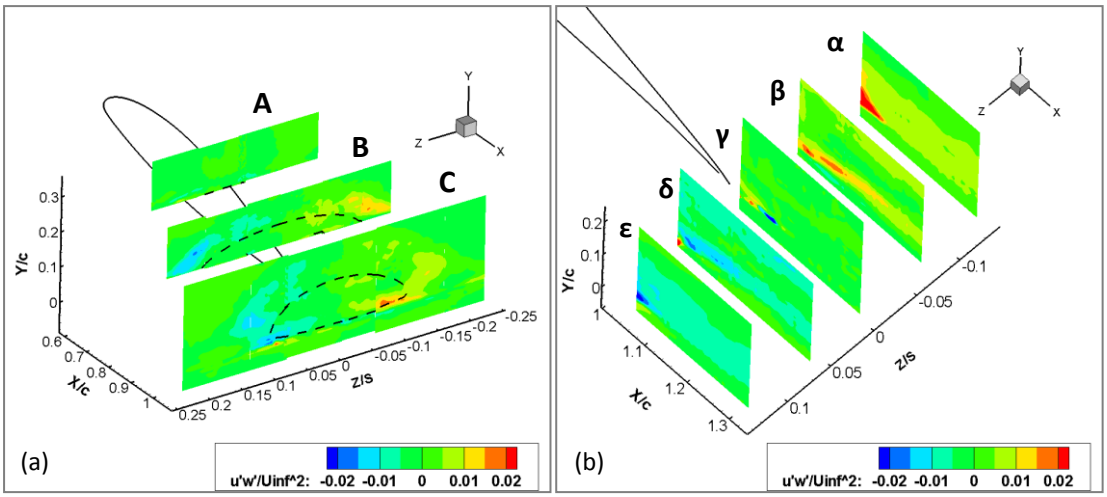

Figure 83: Contours of the $\overline{u'w'}/U_\infty^2$ Re Stress (a) at planes normal to the flow, at chordwise locations 0.6c, 0.8c and 1.06c. The dashed isoline corresponds to streamwise velocity value of zero. (b) at planes normal to the wing span, at the wing mid-span (z/S = 0.0%) and at spanwise locations z/S = ±6.7% and z/S = ±13.3%. (α = 10°, Re = 0.87x10^6).

Relevant to numerical simulations is the level of anisotropy exhibited in the flow. An estimate can be obtained by considering the shear stress angle (SSA). For a plane normal to the flow the SSA is defined as

$$SSA = \arctan\left(\frac{-\overline{u'w'}}{-\overline{v'w'}}\right) \tag{11}$$

Making use of the Boussinesq assumption, an evaluated shear stress angle (EV_SSA) can be defined as follows

$$EV\_SSA = \arctan\left(\frac{\frac{\partial W}{\partial x} + \frac{\partial U}{\partial z}}{\frac{\partial W}{\partial y} + \frac{\partial V}{\partial z}}\right) \tag{12}$$

All velocity gradients in Eqn. (12) are available from the measurements on planes normal to the flow, except $\partial W/\partial x$.

Although the SC separation region cannot be considered as a thin shear flow one could accept that $\frac{\partial W}{\partial x} + \frac{\partial U}{\partial z} \approx \frac{\partial U}{\partial z}$, at least when $\frac{\partial U}{\partial z} \neq 0$, since the variation of U along z is greater than that of the spanwise velocity W, along the streamwise axis. Indeed $\frac{\partial W}{\partial x}$ values from planes normal to the wing span are generally an order of magnitude lower than $\frac{\partial U}{\partial z}$. Then EV_SSA becomes

$$EV\_SSA = arctan\left(\frac{\frac{\partial U}{\partial z}}{\frac{\partial W}{\partial y} + \frac{\partial V}{\partial z}}\right) \quad (13)$$

The variation of SSA and EV_SSA for plane C and z/S = 0.145, i.e. at a spanwise position through the centre of the SC vortex is given in Figure 84. The comparison reveals that the flow is highly anisotropic and that the Boussinesq assumption is not valid and by that eddy viscosity models are not capable of providing detailed information regarding the turbulence characteristics of the flow inside the SC.

However, this does not necessarily mean that eddy viscosity based CFD cannot provide a correct qualitative description of the Re averaged flow. Such a conclusion was deduced in Chapter 5 and further supported in the present paper. This implies that turbulence detailed characteristics do not define the development of the averaged flow, once a SC is formed, and that SC formation is mainly affected by vorticity transport and deformation in scales larger than those characterizing turbulence. In support to this view point is the fact that SCs have been observed for a very wide range of Re numbers, from Re = 200, (Rodríguez & Theofilis, 2010) to Re = 7.4x10^6, (Schewe, 2001).

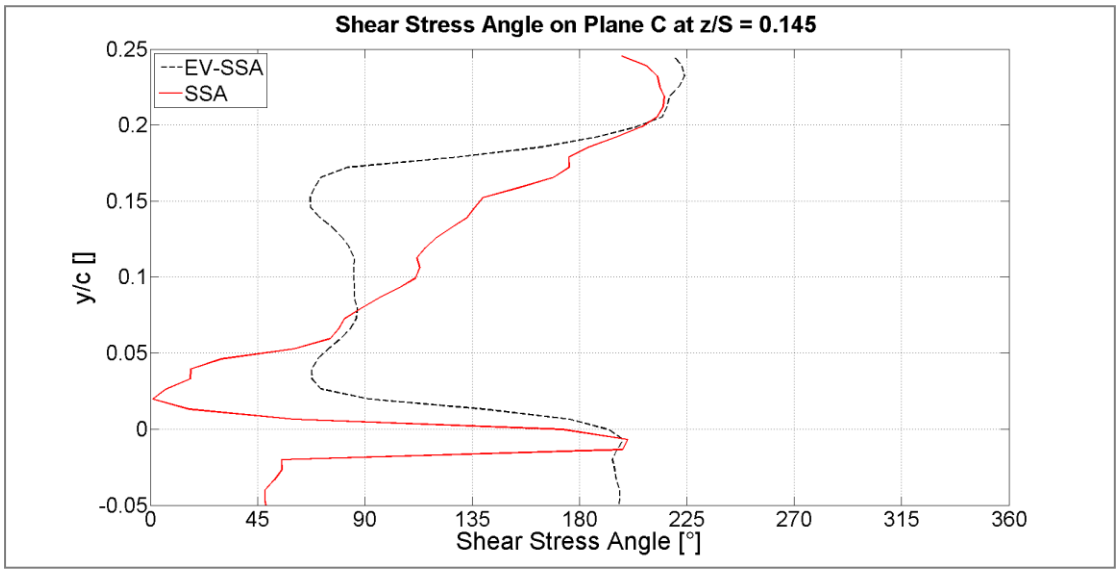

Figure 84: Shear stress angle variation along a vertical line through the SC vortex core, at z/S = 0.145. The spanwise position of the line is shown with red vectors in Figure 66.

6.1.2 The α = 7° case

As regards the SC formation at 7° the conclusions on its structure are the same. As expected, at this lower angle of attack the SC is significantly smaller in size, see e.g. Figure 78 where contours of Q criterion and of normalized vorticity are plotted for the 7° case. Again the dashed line indicates the boundary of the reversed flow region (negative U). The peaks of Q corresponding to the SC vortices are now centred further inboard (z/S ≈ ±0.10) compared to the 10° case (z/S ≈ ±0.13). This confirms that as the angle of attack grows so does the SC and the two SC vortices move outboard and away from each other.

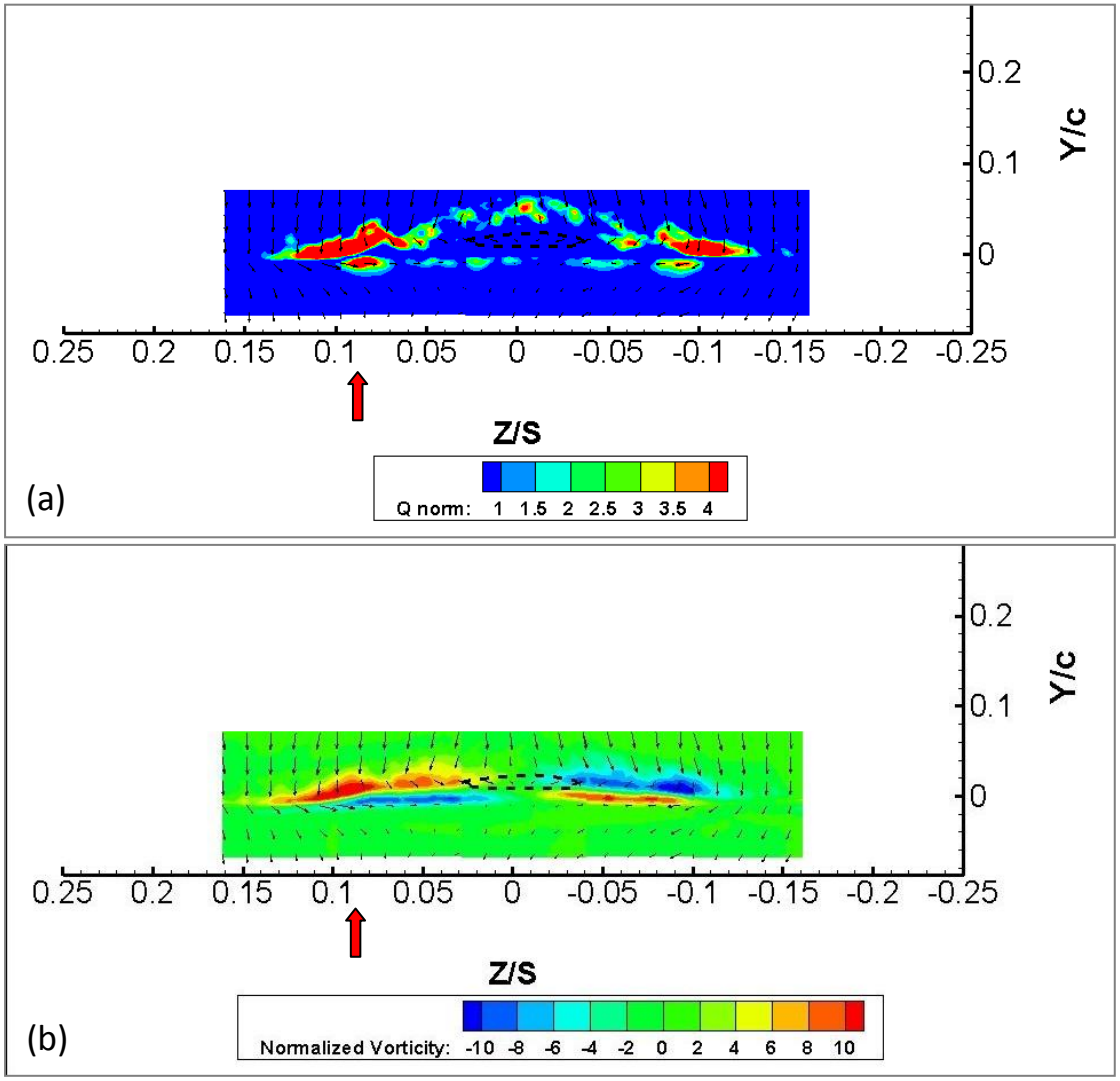

Figure 85: Contours of (a) the Q criterion and (b) normalized streamwise vorticity on a plane normal to the free stream, at chordwise location x/c = 1.05. In-plane velocity vectors are also drawn. One out of every 64 vectors is plotted for clarity. The dashed isoline corresponds to streamwise velocity value of zero. The red vector at z/S = 0.088 indicates the spanwise position along which vorticity and spanwise velocity are plotted in Figure 86 for the 7° case. (α = 7°, Re = 0.87x10^6).

Another difference is that the shape of the regions of high vorticity corresponding to the SC vortices, are now more elongated, indicating that at the particular station their evolution is still going on. There is also a difference in peak vorticity which can be attributed to less diffusion taking place between the point of formation and the measuring station. The above arguments are supported by the plots in Figure 86 where the variation of normalized spanwise velocity, w, and normalized streamwise vorticity along the vertical lines

approximately at the centre of the SC vortex for each angle of attack are plotted. The vertical lines are shown with red vectors in Figure 66 and Figure 78 for the 10° and 7°, respectively. Although the overall change in spanwise velocity is smaller for the 7° case it happens in a much smaller space and this explains the higher vorticity peak.

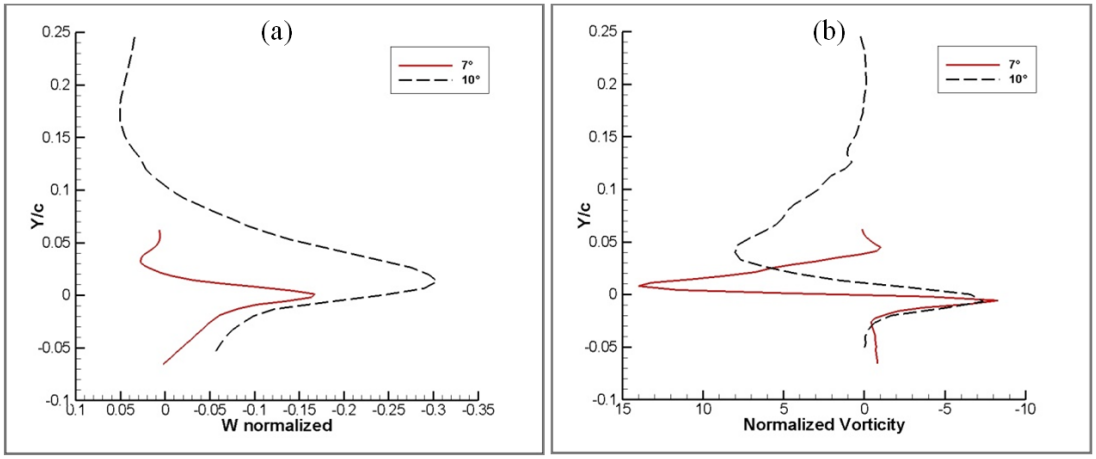

Figure 86: Normalized spanwise velocity (a) and streamwise vorticity variation (b) along a vertical line through the SC vortex core for 10° and 7°.The spanwise position of the lines through the SC vortex cores are shown with red vectors in Figure 66 and Figure 78 for the 10° and 7° case, respectively. x/c = 1.06 for the 10° case and x/c = 1.05 for the 7° case.

6.2 Stall Cell Topology and formation mechanism hypothesis

In this section first a topological description of a SC is given and, then, a synthesis of previous works and the findings of the combined investigation at NTUA, is carried out in an attempt to further detail the formation mechanism of SCs.

6.2.1 Stall Cell topological description

For a steady flow skin friction lines on a body surface can be considered as trajectories having properties consistent with those of a continuous vector field, the principal one being that through any regular (non-singular) point there must pass one and only one trajectory (Lighthill, 1963). Singular points occur at isolated points on the surface and are classified as nodes and saddle points. Nodes are further subdivided into nodal points and foci.

Figure 87 shows examples of singular points. Solid lines indicate skin friction lines and dashed lines are tangent to the surface vorticity vector. At nodal points all skin friction lines except one (labelled AA Figure 87(a)) are tangent to a single line (labelled BB Figure 87(a)) and are directed either away from the node (attachment node) or towards the node (separation node). Foci, shown in Figure 87(b), have no common tangent line and an infinite number of skin friction lines spiral either away from it (focus of attachment) or into it (focus of separation).

Saddle points are characterised by two skin friction lines (labelled CC and DD in Figure 87(c)), one of which is directing inward, towards the point and the other outward. The characteristic lines act as barriers (asymptotic lines) splitting the skin friction lines into sets making one set of lines inaccessible to the others. A skin friction line emerging from a saddle point is a global line of separation and leads to global separation. As (Tobak & Peake, 1982) explain, the global line of separation traces a smooth curve on the wall which forms the base

of the stream surface, the streamlines of which have all entered the fluid through the saddle point. This stream surface is called a dividing surface and is relevant to the description of SC 3D topology.

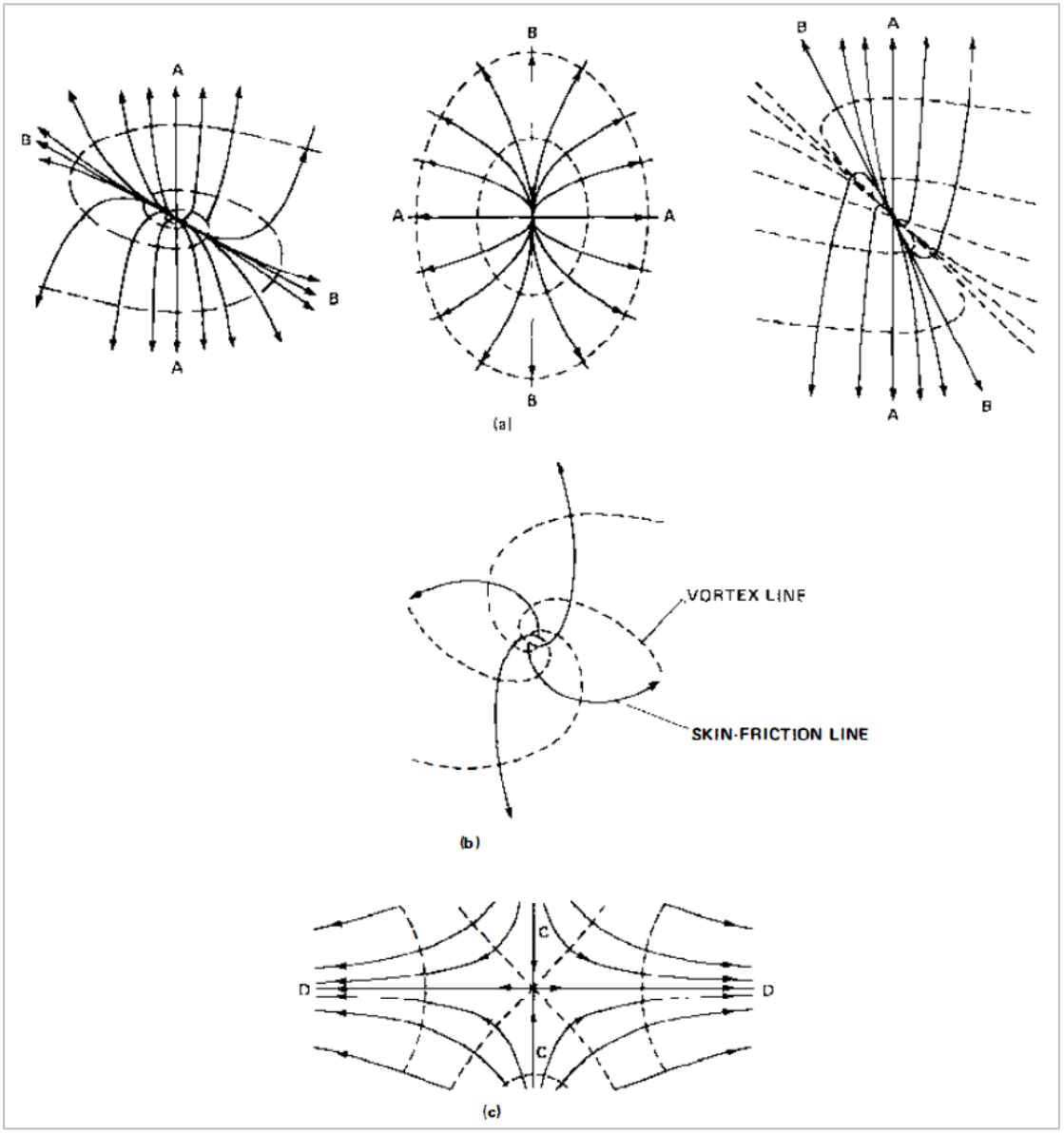

Figure 87: Singular points (a) node; (b) focus; (c) saddle point. Figure from (Tobak & Peake, 1982).

The notion of singular points can be extended from surface skin friction lines to streamlines on plane cuts through a 3D body, e.g. a spanwise plane $z = z_0$ cutting the wing surface (Hunt et al., 1978). In this case singular points at the solid boundary are defined as half nodes and half saddle points, see Figure 88.

Singular points on either body surfaces or planes in the flow should obey topological rules and a generic rule for multiple bodies can be derived (Hunt et al., 1978). For convenience, only the special rules applying to the examined problem are listed here (Tobak & Peake, 1982).

- For skin friction lines on a 3D body surface the sum of nodes (N) and foci (F) should exceed the sum of saddle points by two:

$$\sum(N+F)-\sum S=\ 2 \tag{14}$$

- For in-plane flow lines on a 2D plane cutting a 3D body the sum of nodes and foci plus half the sum of half-nodes (N') should be less than the sum of saddle points and half the sum of half-saddles (S') by one:

$$\left(\sum(N+F)+0.5*\sum N'\right)-\left(\sum S+0.5*\sum S'\right)=\ -1 \tag{15}$$

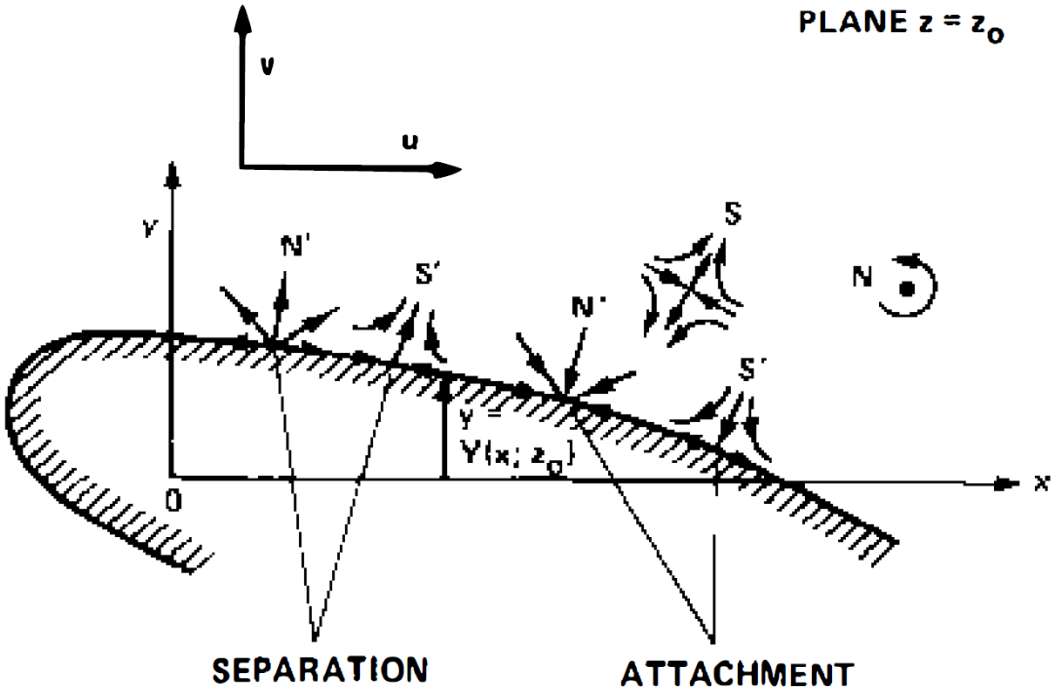

Figure 88: Singular points on a plane normal to the wing span. Figure from (Hunt et al., 1978).

Based on the experimental results presented in this chapter and the computational data from the previous one, conjectured patterns of skin friction lines on the wing surface are shown in Figure 89, a). A saddle point exists at the centre of the SC at the most upstream point of separation. A global line of separation connects the saddle point with the foci of the SC vortices. The global separation line then extends all the way to the wing tips at the sides of the SC. A global reattachment line exists between the SLV and the TELV, whose distance from the TE becomes greater at the wing centre. The distance of the reattachment line from the TE is exaggerated for clarity.

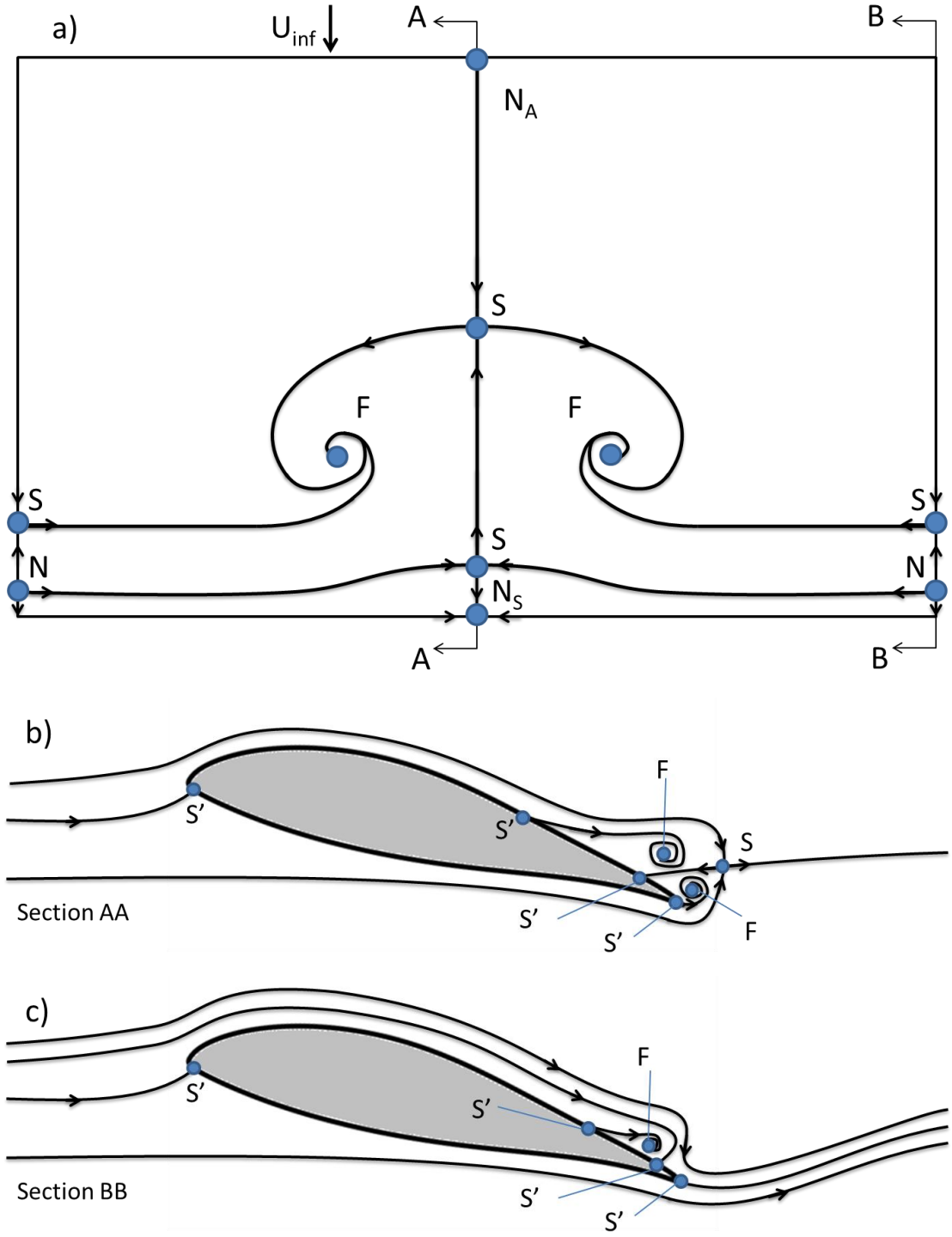

Figure 89: Conjectured patterns of skin friction lines on the wing suction surface (Top) and in-plane streamlines on Section AA at the centre of the wing (middle) and at the side. Singular points on each plane are indicated.

According to this description the dividing surface starting from the separation line on the wing surface is curled by the SC vortices, which in turn is in agreement with the presented experimental and computational data, where the SC vortex appears embedded in the separation shear layer, see Figure 73.

Figure 89 b) and c) show in-plane stream lines for a plane at the centre of the wing span and at the wing tip, respectively. Starting with section AA, at the centre of the wing span, half-

saddle points are found at the stagnation point (at the LE), at the separation point, at the reattachment point and at the TE. The two foci of the SLV and the TE line vortex are also seen, along with a saddle point in the wake. In section BB, at the side of the wing, the TELV is not as strong and no focus point is formed. As a result the saddle point in the wake has vanished as well.

6.2.2 Stall Cell formation hypothesis

Recently (Elimelech et al., 2012) showed that the amplification of a two-dimensional perturbation could not justify the formation of structures of such a large scale as the SCs and that SCs could be only explained as result of a spanwise 3D perturbation. In agreement with this statement, (Rodríguez & Theofilis, 2010) attributed the generation of SCs to the amplification of a large enough spanwise instability.

In deep stall, the separation bubble is initially formed by two intense shear layers, one originating from the TE and the other from the separation line. They release vorticity of opposite sign into the flow, see Figure 90. Under these conditions, a spanwise perturbation can trigger the development of a Crow like instability (Crow, 1970) which, as (Weihs & Katz, 1983) suggested, could lead to the formation of SCs, Figure 91 for a wing with high enough AR so that a single SC can develop.

Following the initial perturbation of the SLV and TELV, the flow field they induce will perturb the separation line (SL) on the wing suction surface pushing the left and right parts of the separation line closer to the TE, while the central part will start moving upstream, see Figure 91. Also in Figure 91, trajectories are drawn for the particles approaching the SC from upstream as well as for those moving within the reversed flow region. The latter will exhibit high curvature at their turning point which will generate pressure gradients that will force the separated shear layer, or the dividing stream surface in topological terms, to roll-up, see Figure 92. As a result the formation of the SC focal points on the wing surface will begin. This can explain why the SC vortices appear inside the separation shear layer, as shown in Fig. 19. The particles “trapped” in the SC focus will follow a spiral path and by that will gradually form the SC vortices. A schematic of the final time averaged form of the vortices inside a SC is given in Figure 93.

The above description, while agreeing with (Weihs & Katz, 1983) in that a Crow like instability triggers the formation of SCs, proposes a different evolution and a different final state. According to (Weihs & Katz, 1983) the two perturbed vortices of Figure 91 break and merge with each other to form rings, each of which correspond to a single SC. However, such a break-merge mechanism was not detected in either the measurements or the simulations. Instead the SLV and the TELV exist along with the SC vortices and run parallel to the wing TE at the sides of the SC. This suggests that the break-merge mechanism cannot explain the creation mechanism of Stall Cells at least for the range of angles of attack considered.

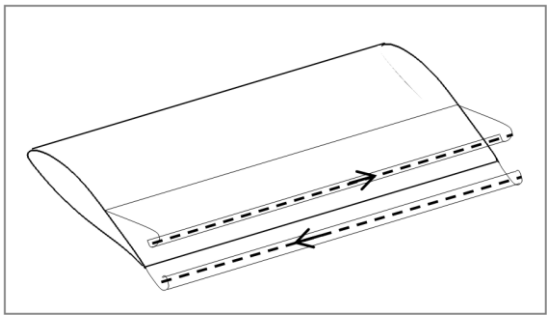

Figure 90: Initial 2D parallel formation of the SLV and the TELV. Vorticity direction is also shown.

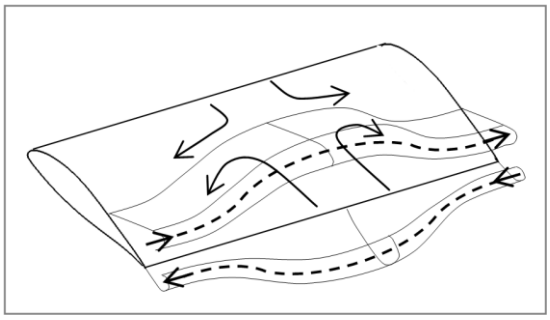

Figure 91: SLV and the TELV cores after a Crow like 3D instability develops. Curved vectors show possible surface flow direction. Vorticity direction is also shown.

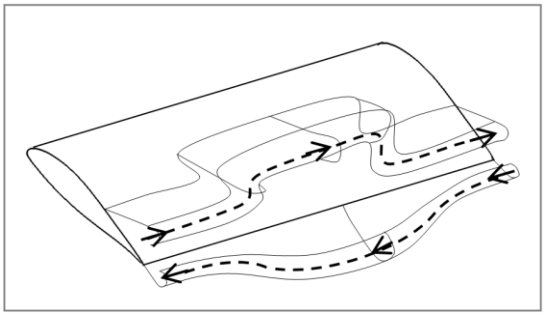

Figure 92: The separation shear layer starts to roll up creating the SC vortices.

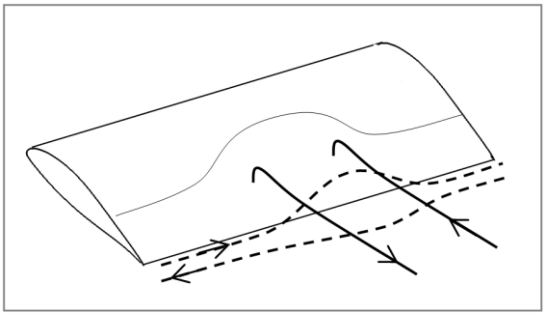

Figure 93: Schematic of the separation line and the time averaged form of the vortical flow structures. Vorticity direction is also shown.

6.3 Summary

A SC was studied using Stereo PIV for the first time. The SC was stabilized using a large enough spanwise disturbance. The cameras were located inside the test section and a quantitative analysis of their vibration showed that the resulting error was negligible.

Results confirm the CFD findings in terms of the structure of the time averaged flow. It is found that flow inside a SC consists of three types of vortices: (a) the Stall Cell (SC) vortices that have opposite vorticity, start normal to the wing suction surface and continue downstream aligned with the free stream, (b) the Separation Line Vortex (SLV) and (c) the Trailing Edge Line Vortex (TELV). The two latter are spanwise vortices which grow significantly at the centre of the SC under the influence of the SC vortices. It is also found that the wake is pushed upwards at the centre of the SC and that downstream of the wing TE it contracts in the spanwise direction, with respect to the SC size on the wing suction surface. For the airfoil in question the SC grows significantly from 7° to 10° as the two SC vortices move outboard away from each other.

The Re stresses derived from measurements are in agreement with the above description and the turbulence characteristics are found to be highly anisotropic. RANS computations using an eddy viscosity model gave good qualitative representation of the averaged flow which suggests that SC formation is dominated by large scale vorticity transport mechanisms rather than small scale (turbulence) effects.

Finally, a topological description of the SC flow is given and a hypothesis is made regarding the SC generating mechanism. According to it SCs are a result of a Crow like instability between the SLV and the TELV. The perturbed shear layers lead to three-dimensional separation and hence to spanwise flow on the wing suction surface. As a result the separation shear layer is folded and the SC vortices are formed.

7 Reynolds number effect

7.1 Introduction

In this chapter a closer look at the Re number effect on the basis of pressure measurements and RANS simulations, is taken. Tuft flow visualization data in Chapter 4 showed that the separation line on the wing moved upstream as the Re number increased. This suggests there is an Adverse Reynolds Number Effect (ARNE) i.e. there is a decrease in wing effectiveness with increasing Re number, unlike what is expected in 2D flow.

Very few references to ARNE exist in the published literature. (Yoshida & Noguchi, 2000) found that as Re number increased from $0.5x10^6$ to $1.0x10^6$ at a given angle (e.g. 16°) the separation line moved upstream combined with a decrease in lift and suction peak, for a wing exhibiting 3D separation. Although the authors do not refer to Stall Cells, they do attribute ARNE to the three-dimensionality of the separated flow on their NACA 8318 wing without further explanation. Furthermore (Rubinstein et al., 2001) state that this is a strictly 3D phenomenon and underline the uncertainty surrounding the modelling of 3D separated flows using RANS.

Pressure measurements presented in this chapter confirm ARNE in the post stall region for the tested model with the localized disturbance. An effort is then made to complement the experimental data and examine the 3D effects and their relation to lift coefficient, suction peak and separation location using RANS simulations.

With regard to the computational approach, no significant difference was observed between the steady and the unsteady computations and therefore all cases were run in steady state to reduce the computational cost. The flow over an airfoil (2D case) and over a wing with AR = 2.0 (3D case) was studied for four different Re numbers for 0.5 to $2.0x10^6$. Only the 12° case is presented here since the same conclusions can be drawn from other angles of attack. The Spalart - Allmaras (Spalart & Allmaras, 1992) turbulence model was used for all computations and the grid used for all cases was the same as that described in Chapter 5.

7.2 Results

7.2.1 Pressure data

Figure 94 shows the lift coefficient variation for three different Reynolds numbers (Re = 0.5, 1.0 and $1.5x10^6$). The figure focuses on the higher end of the angle range where the ARNE is observed. Indeed, for $\alpha > 10°$ Cl is higher for Re = $0.5x10^6$ than for Re = $1.0x10^6$ or Re = $1.5x10^6$. Little difference is observed between the two higher Re numbers.

Figure 95 shows the pressure distribution along the wing chord for the same Re number range and $\alpha = 10°$. The separated region appears smaller for the lower Re number case. Also, contrary to what one would expect from an increase in Re number, the suction peak is smaller for the higher Re number cases.

Both graphs confirm ARNE on both the lift coefficient and the pressure distribution around the airfoil. It is noted, however, that in this case the flow was tripped with the oversized ZZ tape (0.4mm height) at the centre of the wing. This could possibly cause excessive

separation for the higher Re numbers. Unfortunately, it was not possible to examine the lift variation without the ZZ tape as due to the inherent SC instability pressure measurements at the centre were not trustworthy. Still, the experimental results indicate a possible link between ARNE and the SCs.

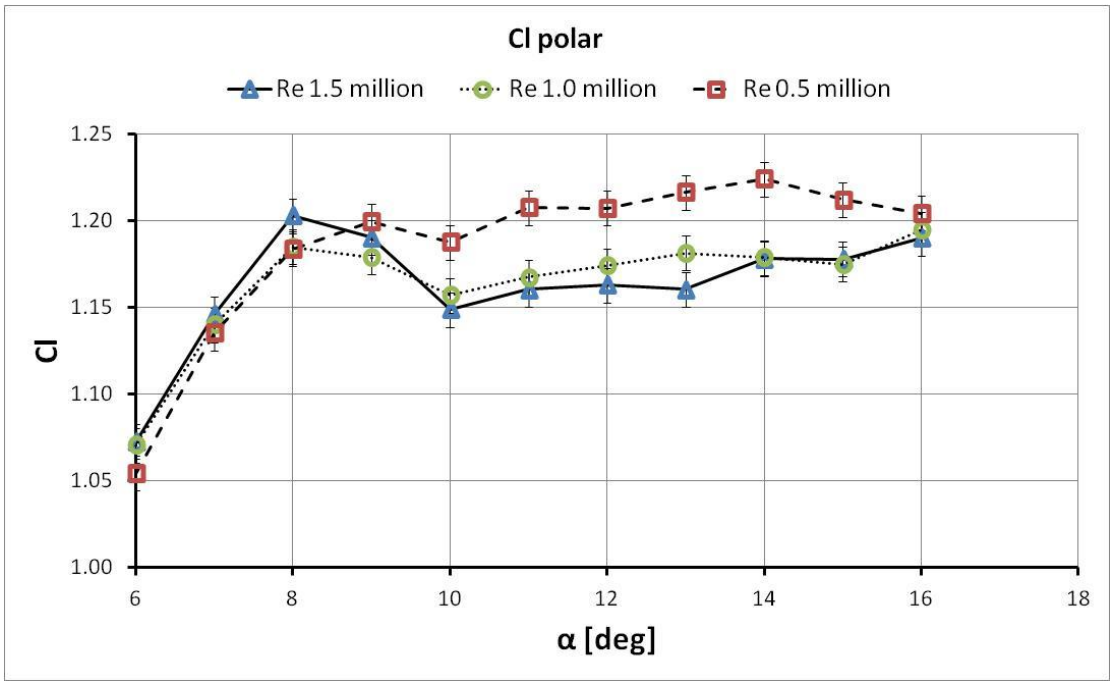

Figure 94: Experimental lift coefficient variation for three different Reynolds numbers (Re = 0.5, 1.0 and 1.5x10^6) and a wing of AR = 2.0 with localized disturbance (ZZ tape). Error bars are also displayed.

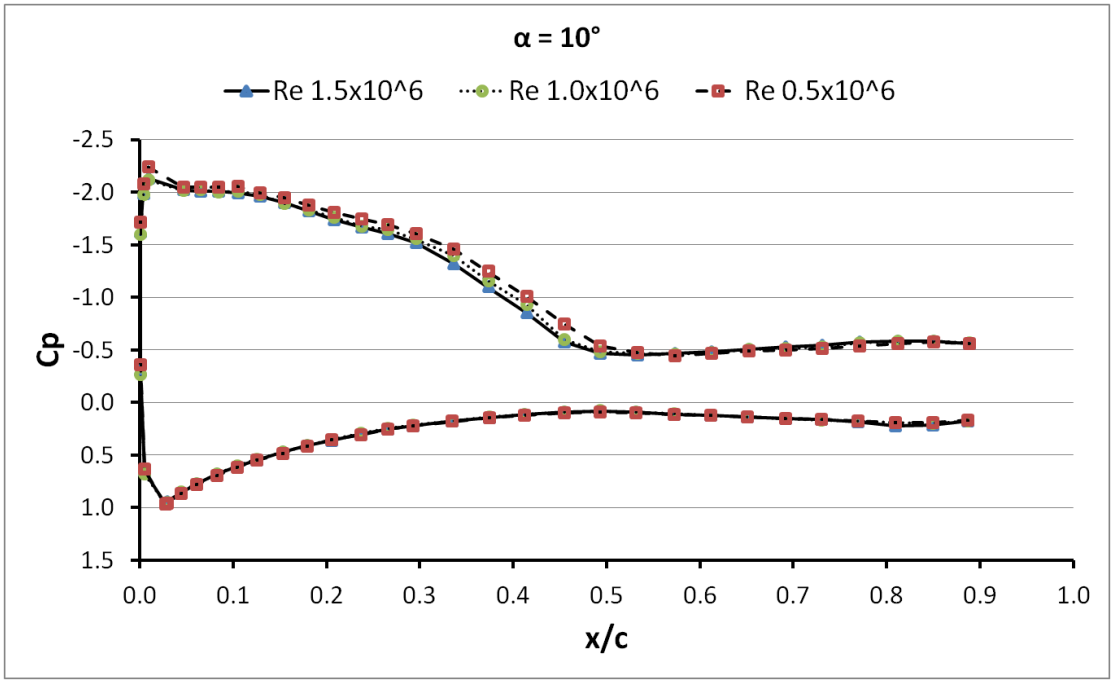

Figure 95: Experimental pressure coefficient distribution for three different Reynolds numbers (Re = 0.5, 1.0 and 1.5x10^6) and a wing of AR = 2.0 with localized disturbance (ZZ tape), α = 10°. Pressure measurements from the taps right before and after the ZZ tap are omitted for clarity.

7.2.2 Simulations

SC structure

The aim in this section was to focus solely on the Re number effect on the flow and to exclude any effect from the ZZ tape or the ZZ tape model. To achieve this, the ZZ tape was not included in the computations.

The fact that no forcing was applied to the flow meant that various combinations of SC structures could form on the wing. Figure 96 shows skin friction lines on the wing suction surface and the various SC formations that were seen. Note that only half of the wing span is shown: there is a symmetry plane on the left and an inviscid wall on the right. The first column in Figure 96 gives the angle of attack, whereas the second, third and fourth column present the skin friction lines for Re numbers $0.5x10^6$, $1.0x10^6$ and $1.5x10^6$, respectively. Only the higher angles of attack are presented ($\alpha > 12°$) since this is when the SCs appear.

Cases with one, two and one and two "half" SCs are observed. No clear correlation between SC number and Re number or angle of attack can be found. A general conclusion, which is in agreement with the tuft flow visualization experiments, is that at the onset of 3D separation always a single SC is formed and that at the highest angle the three-dimensionality of the separation line is reduced. It is worth noting that the SC vortices were visible downstream of the wing TE (e.g. in the form of Q isosurfaces similar to the ones in Figure 58 in Chapter 5) even for the cases with reduced separation line three-dimensionality.

Although the SC combinations resemble those observed experimentally, they were not dynamic like the ones observed using tufts. Even when unsteady computations were run, the results were identical and only very limited variation was observed in Cl ($O(10^{-3})$), resulting from the two SCs slightly moving in the spanwise direction, one growing in size against the other. In no case SC formation/destruction or large scale spanwise movement was found. This is in agreement with (Bertagnolio et al., 2006) who also found that RANS simulations were unable to predict the chaotic 3D nature of the turbulent wake downstream of a wing with SCs.

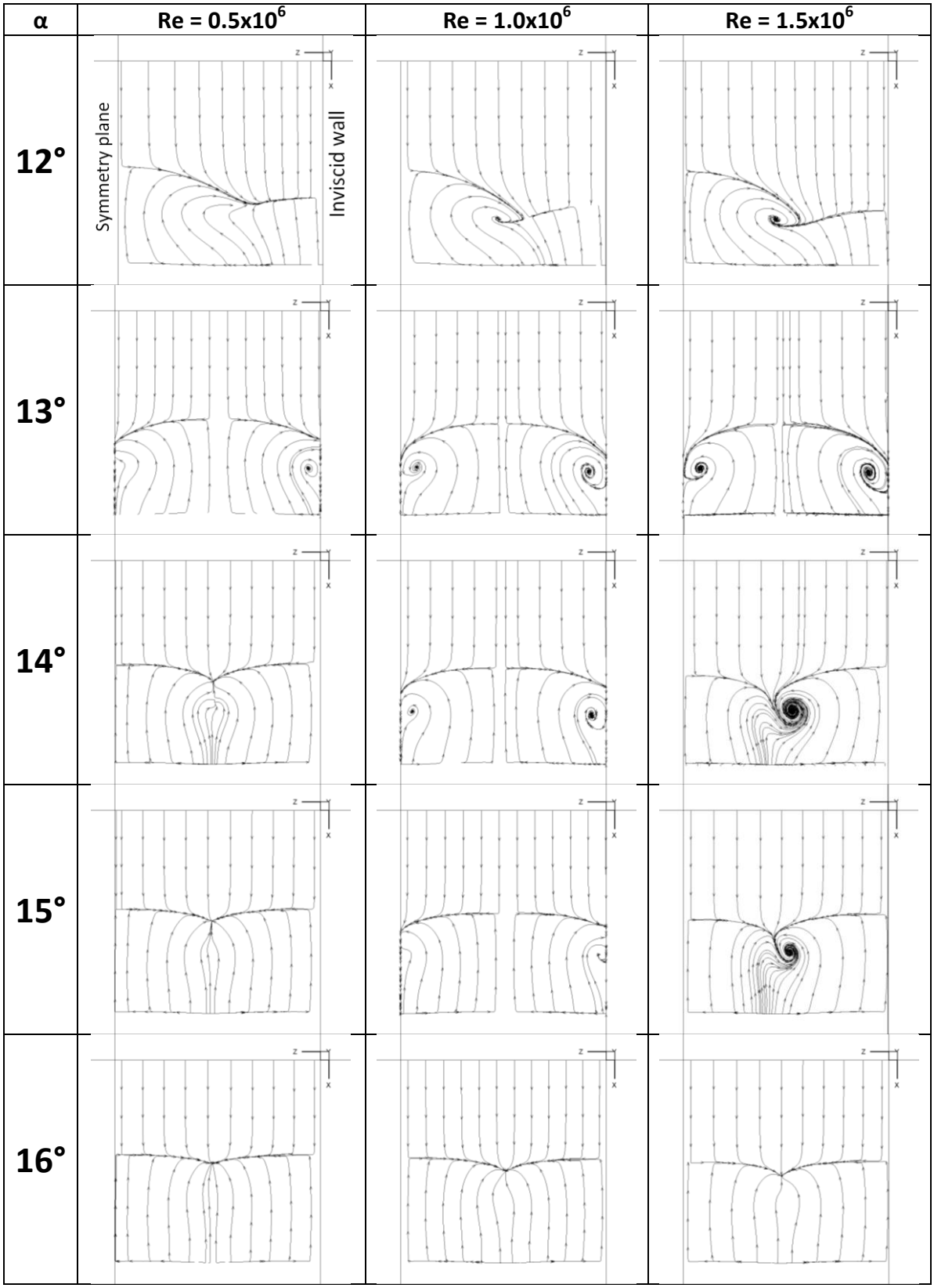

Figure 96: Skin friction lines on the wing suction surface for various Re numbers and angles of attack. The first column gives the angle of attack and the second, third and fourth column present the skin friction lines for Re numbers $0.5x10^6$, $1.0x10^6$ and $1.5x10^6$, respectively. Only half of the wing span is shown, the left hand side being a symmetry plane and the right hand side an inviscid wall. This is only indicated in the top left image for clarity.

Relation between Cl max and SC vortex strength

For the 12° case always a single central SC was formed, even at Re 2.0x10^6 (skin friction lines not shown here). Given the significant spanwise variation of the lift coefficient when a SC is formed (see Chapter 5) in this section three different Cl values are examined:

a. Cl at the centre of the wing span. For a single central SC this coincides with the centre of the SC, between the SC vortices, where Cl is smaller.
b. Cl at the wing tip. For a single central SC this coincides with the SC side, where Cl is higher.
c. Average Cl, which is the spanwise average of the wing Cl.

For the 2D case only a single Cl value is available.

Figure 97 shows the lift variation with Re number at 12^o incidence for the 2D and the 3D case. The lift coefficient increases with Re number for both the 2D and the 3D case. The rate of increase is higher for the 2D case, whereas little, if at all, difference is observed between the rate of increase for the Cl at the wing centreline, at the wing tip or the average Cl.

Apparently the simulations do not predict a decrease in wing performance with Re number increase, contrary to the experimental data. They do, however, suggest that the increase in wing performance is limited compared to the 2D case. In the remaining of this chapter an effort is made to examine whether and how this deficit in Cl increase is related to the SC structure or not.

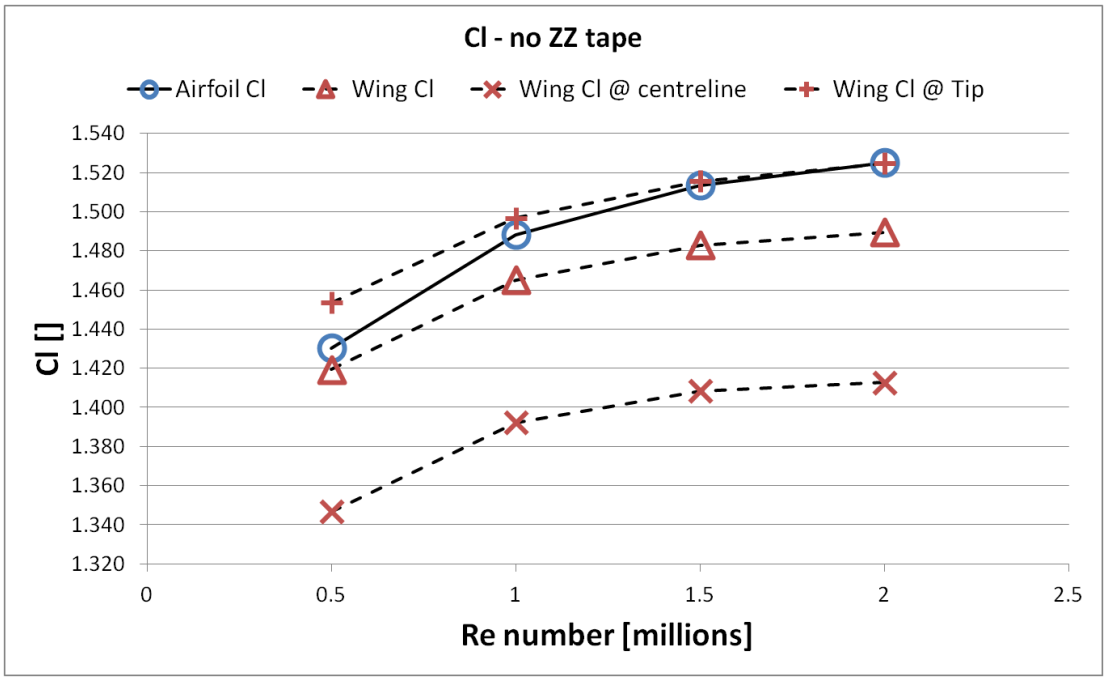

Figure 97: Lift coefficient variation with Re number for the 2D and 3D cases. AR = 2.0, no ZZ tape, α = 12°.

Consider a plane parallel to the suction surface of the wing and close to its TE, as shown in Figure 98. For reference purposes this plane is denoted as Plane A. It is assumed that as long as this plane is close enough to the suction surface then the SC vortex will still be normal to it, i.e. it will not have become parallel to the free stream. The peak vorticity normal to Plane

A is considered a measure of the SC vortex strength since according to the simulation results, the vortex size, shape and location do not change with Re number.

Figure 99 shows contours of vorticity normal to Plane A and in-plane flow lines on Plane A. The round region of negative vorticity corresponds to the SC vortex, which as explained, is normal to plane A, and is also clearly visualized by the in-plane flow lines. The elongated region of positive vorticity corresponds to the SLV. As shown in Chapter 5 the latter is 3D and moves upwards at the centre of the SC (see Figure 58), so a component of vorticity normal to plane A is expected in this region. The peak negative vorticity (ω_{max}) on Plane A for various Re numbers is plotted in Figure 100. Clearly, the SC vortex becomes stronger as the Re number increases.

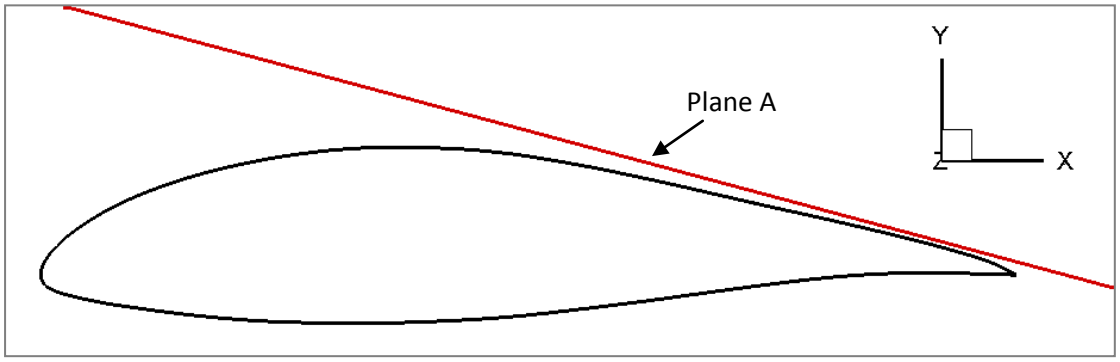

Figure 98: Plane A. Plane parallel to the wing suction surface close to its TE. X axis aligned with the wing chord, and not the free stream.

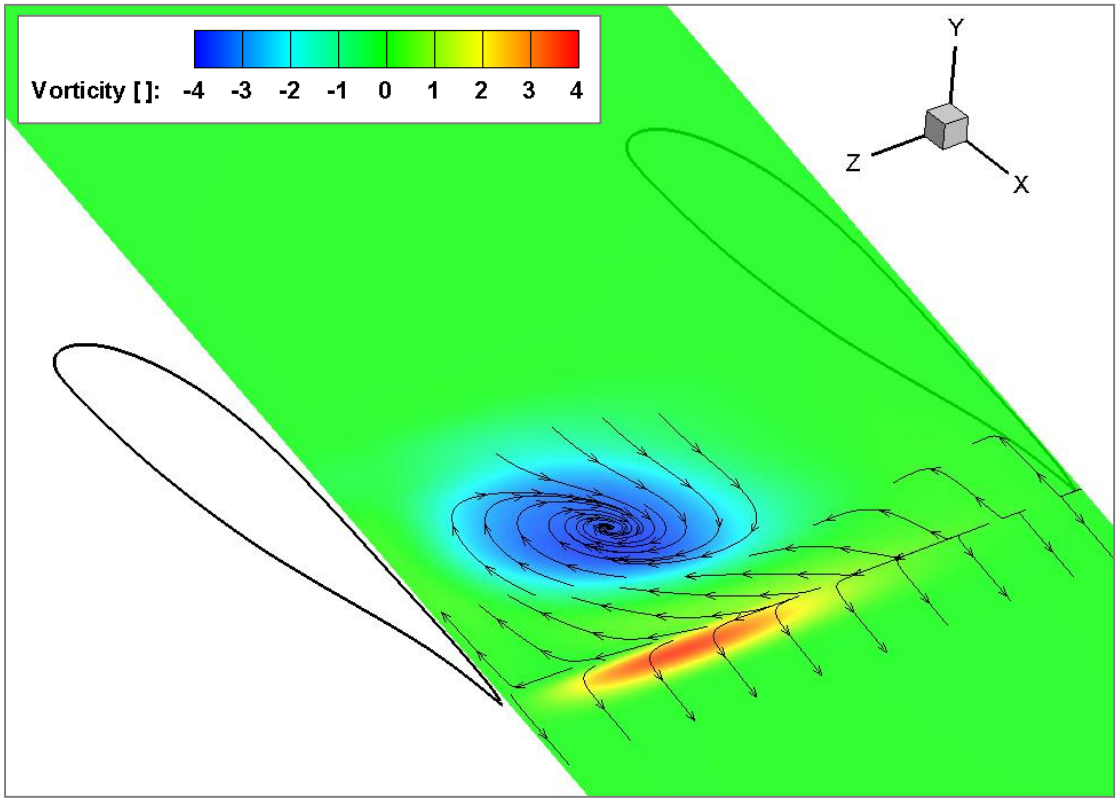

Figure 99: Normalized vorticity contours on Plane A. AR = 2.0, no ZZ tape, Re = 1.0x10^6, α = 12°. X axis aligned with the wing chord, and not the free stream.

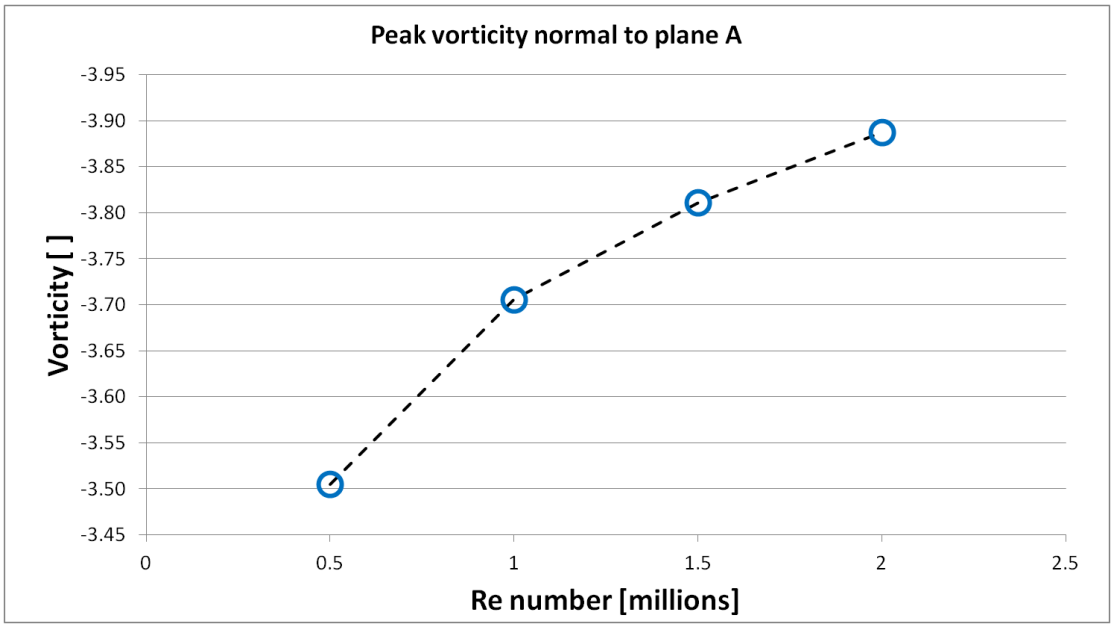

Figure 100: Peak negative vorticity normal to Plane A variation with Re number. AR = 2.0, no ZZ tape, α = 12°.

As a measure of the difference in performance between the airfoil (2D) and the wing (3D) we consider the lift coefficient deficit (dCl), defined as the difference in Cl between the airfoil and the wing, applying to all three relevant lift coefficients: the wing average Cl, the Cl at the wing centre and the Cl at the wing tip.

$$dCl = \mathrm{Cl}_{2D} - \mathrm{Cl}_{3D} \tag{16}$$

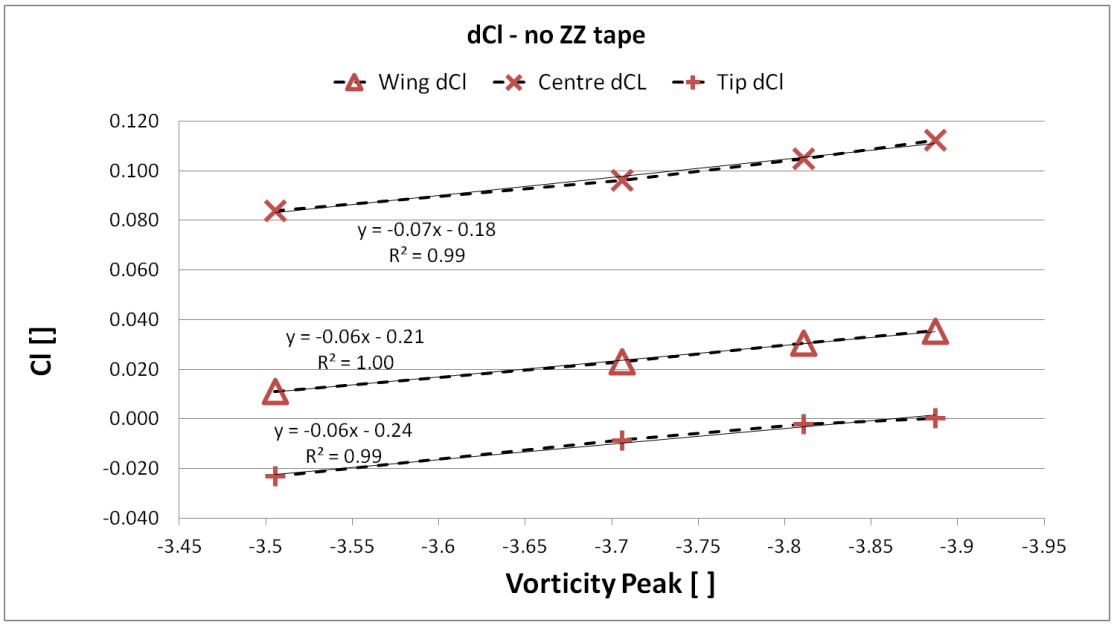

Figure 101: Lift coefficient deficit (dCl) variation with ω_{max} on Plane A for the average Cl, Cl at the centre and Cl at the tip of the wing. The equations of the linear approximations and the coefficients of determination values are also shown. AR = 2.0, no ZZ tape, α = 12°.

Combining dCl and SC vortex peak vorticity on plane A the variation of dCl with respect to ω_{max} is given in Figure 101, in page 101. The lift coefficient deficit scales linearly with ω_{max},

regardless of which lift coefficient (the tip, the centre or the wing average) is considered, suggesting a strong correlation between the SC vortex and the limited increase in Cl for the 3D case.

Relation between suction peak and SC vortex strength

(Yoshida & Noguchi, 2000) in their paper about ARNE observed that parallel to the drop in performance, there was also a drop in suction peak. This was confirmed by the pressure measurements presented in the previous section. In the computational results the suction peak around the airfoil exhibits the same behaviour as the lift coefficient, i.e. it increases (in absolute value) with Re number, but less than it would in a 2D flow. This is shown graphically in Figure 102. It is also observed that the suction peak is greater in absolute value at the tip than at the centre.

The difference in suction peak can be expressed as a difference in maximum velocity around the airfoil, using the equation:

$$U_{max} = \sqrt{1 - \mathrm{Cp}_{\min}} \tag{17}$$

We can then define a velocity deficit, dU, as the difference between the 2D maximum velocity around the airfoil for a specific Re number and the corresponding velocity for the flow around a section of the 3D wing, see equation below. This is applicable to every section along the wing, but we will only consider the sections at the centre and the tip.

$$dU = \mathrm{U}_{\mathrm{max\_2D}} - \mathrm{U}_{\mathrm{max\ \_3D}} \tag{18}$$

The variation of dU with peak vorticity on Plane A is given in Figure 103. It is found that dU also scales linearly with the ω_{max}, again suggesting that the decreased performance of the 3D wing compared to the 2D airfoil is related to the SC vortex strength.

It is also clear from Figure 103 that the velocity deficit difference between the tip and the centre (dU_{centre} - dU_{tip}) remains constant despite the increase in vortex strength, indicating that this difference is not linked to the SC vortex strength.

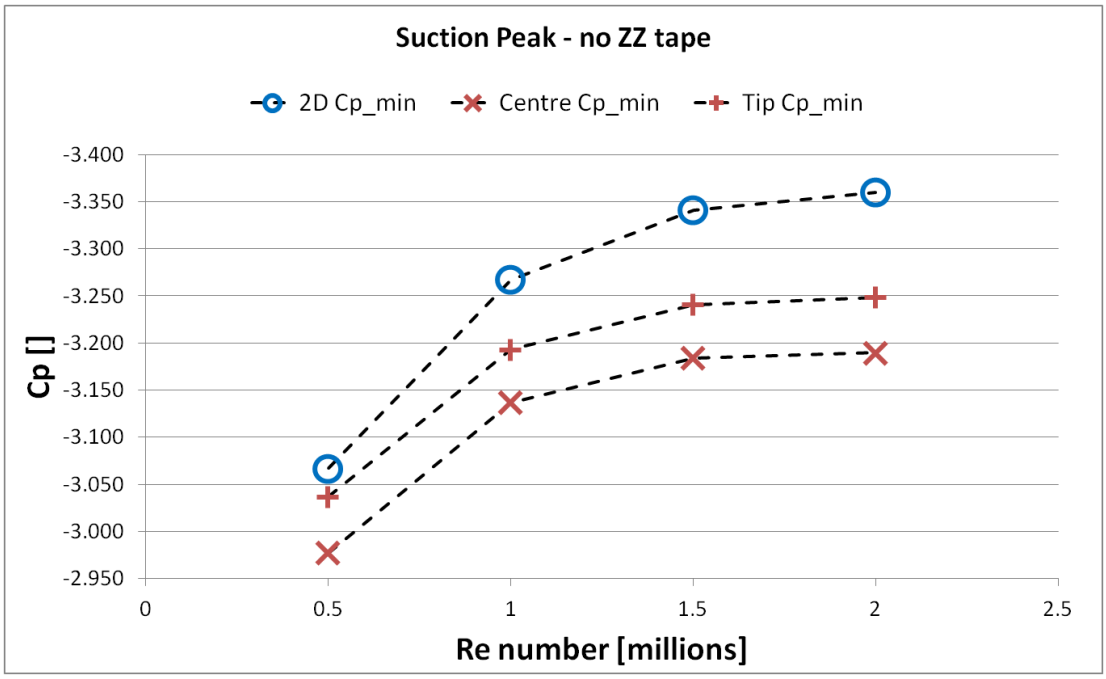

Figure 102: Suction peak variation with Re number for the 2D and the 3D cases (wing centre and tip). AR = 2.0, no ZZ tape, α = 12°.

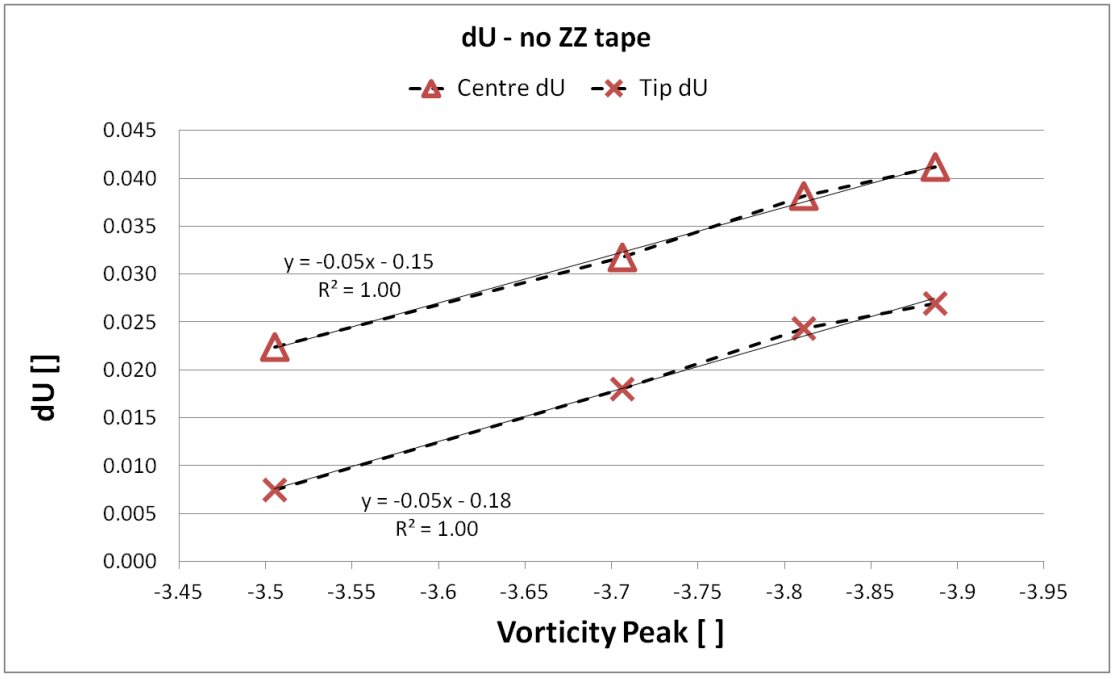

Figure 103: Velocity deficit (dU) variation with peak negative vorticity on Plane A at the centre and the tip of the wing. The equations of the linear approximations and the coefficients of determination values are also shown. AR = 2.0, no ZZ tape, α = 12°.

Relation between separation location and SC vortex strength

What seems to be related to the SC vortex strength is the earliest separation location. Figure 104 shows the separation location variation with Re number for the 2D case and for the wing centre and tip. For the 2D case separation moves downstream as the Re number increases. The same happens for the wing tip and mid-span in a more pronounced and a more moderate way, respectively.

The separation delta, dx_{sep}, is defined as the difference in separation location between the wing centre and tip.

$$dx_{sep} = \mathrm{x_{centre}/c} - \mathrm{x_{tip}/c} \tag{19}$$

Figure 105 shows the variation of dx_{sep} with SC vortex vorticity. As the SC vortex becomes stronger dx_{sep} grows linearly. This means that the SC vortex is linked to the separation location on the wing.

So far the upstream advancement of separation on the SC symmetry plane had been attributed to the upwash induced by the SC vortices once they were in the wake and parallel to the free stream flow (Yon & Katz, 1998). It was argued that the effective angle of attack at the centre of the SC would be greater than that at the sides of it leading to the difference in separation location. It is unclear how helpful the notion of a 2D effective angle of attack would be in such a complex 3D flow. What is more, if indeed the effective angle changes, then the suction peak should change accordingly (i.e. an increase in effective α should lead to an increase in suction peak). As already explained the suction peak difference (or velocity deficit) between the centre of the SC and the sides of it remains constant despite the increase in the SC vortex strength (see Figure 103).

It would be perhaps more suitable if the upstream advancement of separation at the centre of the SC and its opposite trend at its sides was attributed to a local effect by the SC vortices. In more detail the SC vortices start normal to the wing suction surface and induce velocities opposite to the flow at the centre of the SC and along the flow at the sides of the SC, thus increasing / reducing separation at the respective locations.

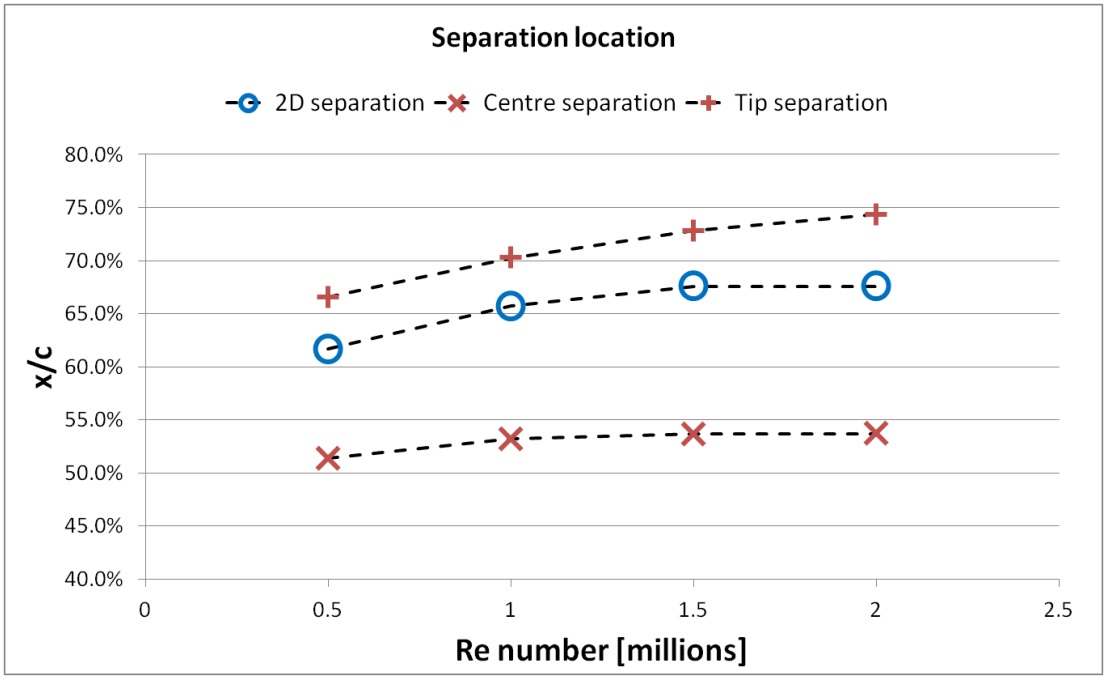

Figure 104: Earliest separation location variation with Re number for the 2D and the 3D (centre and tip) cases. AR = 2.0, no ZZ tape, α = 12°.

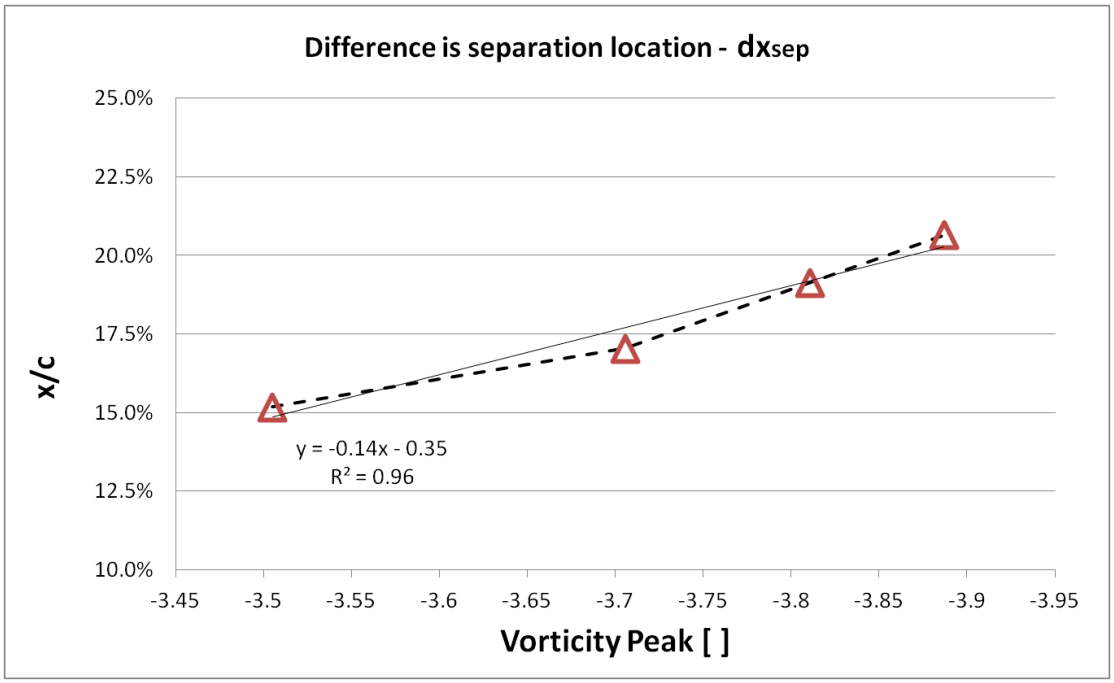

Figure 105: Separation location delta between the wing centre and tip plotted against vorticity peak on Plane A. The equations of the linear approximations and the coefficients of determination values are also shown. AR = 2.0, no ZZ tape, α = 12°.

7.3 Summary

The effect of Re number on the wing Cl and pressure distribution was studied through pressure measurements and RANS simulations. In the experiments a wing of AR = 2.0 with a localized disturbance was used, for a Re number range from 0.5 to 1.5x10^6. Experimental results show a drop in lift coefficient and suction peak combined with upstream advancement of the separation line. This adverse Re number effect has seldom been referenced in the literature.

For the computational study of this phenomenon, a wing without the localized disturbance was investigated in order to exclude any effect from the ZZ tape height and modelling. RANS simulations reveal no decrease in wing performance with Re number increase. They do show, however, that the improvement in wing performance is limited in the 3D case compared to the 2D case. The reduced increase in Cl max and suction peak is found to scale linearly with SC vortex strength. The difference in suction peak between the wing centre and tip does not depend on the SC vortex strength, while the three-dimensionality of the separation line is linked to a local effect of the SC vortex and not the induced upwash / downwash from the wake as had been the case so far.

Part III.

Separation Control

8 Vortex generator configuration optimization

Naturally, there is no single VG configuration that will be optimal for all aerodynamic applications. To examine which VG set-up is most suitable for the present airfoil a computational parametric study was performed. The in-house MaPflow code was used and the VG effect on the flow was modelled using the BAY (Bender et al., 1999) model, see Chapter 3 for more details. Based on the existing literature (see Chapter 1), counter rotating triangular vanes with common flow up were used as a starting point and their parameters were varied aiming to maximize the lift to drag ratio (L/D). The two best performing VG set ups were tested experimentally. A shortcoming of the computational approach was highlighted and flow instabilities were detected. The optimum configuration was selected for the Stereo PIV tests discussed in the next chapter.

8.1 Grid dependence study

A c-type grid that extended 50 chords around the airfoil was used as a starting point. The boundary layer mesh ensured the y+ value was lower than 1 throughout the wing surface. The 2D grid was extruded in the spanwise direction to create the 3D grid. The total span of the computational domain for the grid dependence study was 0.029c and half a counter rotating VG pair, i.e. a single triangular vane type VG, was modelled in that space. Symmetry boundary conditions were used at both sides of the grid. The wing angle of attack was $\alpha = 12.0°$ (where Cl_{max} occurs for the 2D solution, see Figure 39 in Chapter 5) and the VG height was $h = 1\delta$, where δ is the local boundary layer height. The VG angle to the free stream was $\beta = 20°$ and its chord was $l = 3h$. The distance between the VG pairs was $D = 5.7h$ and the distance between the VGs of a single VG pair was $d = 3.7h$. For the definition of the VG positioning parameters see Figure 106.

The dependence on grid density in all three directions was studied separately, starting from a medium grid and then creating a denser and a coarser grid. The grid density was changed mainly in the region of the VG, i.e. on the VG surface for the X-axis and in the BL region for the Y-axis. For the z-axis the grid density was changed uniformly because of the small span of the computational domain. Table 6 (page 114) summarizes the grid details and some of the results for the cases tested. The grid that was chosen for the VG parametric study is labelled mk7 and highlighted in Table 6.

Results show that increasing grid density in the x or y direction had little effect on the results. Using a higher density grid in the spanwise direction (mk8 grid) had little effect on force coefficients and separation location (less than 3%), but a significant effect (+36%) on the peak vorticity value at a distance 2h downstream of the VG TE. The increase in vorticity is not surprising as a higher resolution is expected to reduce diffusion.

In (Dudek, 2011), where a VG on a flat plate was modelled using the BAY model, it was found that even though the peak vorticity downstream of a VG can be computed more accurately with a sufficiently dense grid, vorticity still decays rapidly to the levels of a coarser grid and the overall results do not differ significantly. As the objective of the present parametric study was to examine performance trends and find the optimum VG configuration, but not to quantitatively predict airfoil performance it was decided to use the $1.0x10^6$ cells mk7 grid.

This way the computational cost of the parametric study remained reasonable and a trustworthy prediction of VG performance was obtained.

8.2 Results

8.2.1 Computational parametric study

Based on the published literature counter rotating triangular vanes with common flow up were used as the main concept of the parametric study. The VG shape and positioning parameters are shown in Figure 106. In detail the six parameters that were varied are:

x : chordwise position of the VG array
h : VG height
l : VG length
D : distance between two VG pairs
β : VG angle to the free stream flow
d : spanwise distance between the LE of two VGs of the same pair

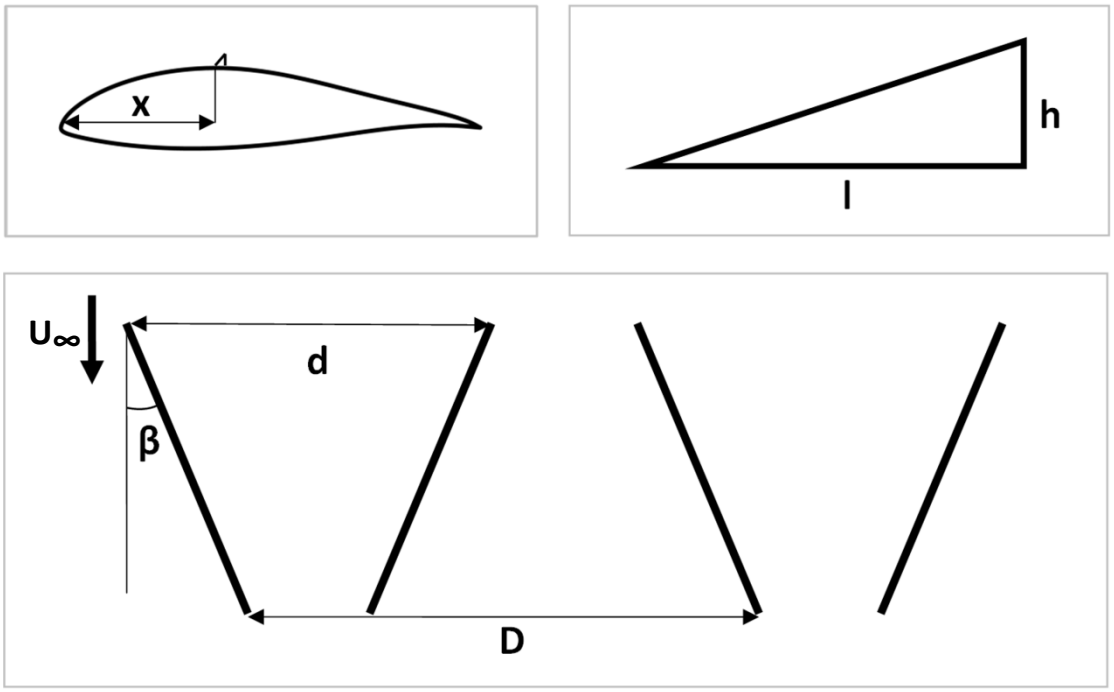

Figure 106: Triangular vane vortex generator parameters. (Top left) Wing side view: global positioning parameter, (top right) VG side view: VG shape parameters, (bottom) Top view: relative positioning parameters.

The parametric study was performed as follows. The configuration described in section 8.1 was set as the Baseline set up. Starting from the Baseline the first five aforementioned parameters were changed one at a time, twice, i.e. once in one direction and once in the opposite direction. The last parameter, distance between the two VG pairs (D), grew in two steps, since the Baseline VG pairs were already relatively close. Based on these results a couple of extra cases were run, which are described in the next paragraphs.

Sketches of all the configurations tested are given in Figure 107 to Figure 111. All runs were done at $\alpha = 12°$ and the Re number was 1.0×10^6, unless otherwise stated. The boundary layer height at x/c = 0.3 for the uncontrolled case (no VGs) was $\delta = 0.01c$ according to 2D

RANS simulations. The configuration details and force coefficient data for all cases are given in Table 7 (page 115).

All VG geometries gave a significant increase in performance compared to the highly separated uncontrolled case. The "educated guess" for the Baseline configuration was very close to the optimal configuration. It was found that locating the VGs further downstream (at x/c = 0.4, Case J) increases Cl without drag penalty and that increasing the spacing between the VG pairs (Case K) reduces Cd without significantly affecting Cl. Combining the two changes (Case K-0.4) gave the highest L/D value. A case similar to Case K-0.4 but with VGs located with common flow down (Case M) was tested, but worse than VG pairs with common flow up.

With regard to the other examined parameters, decreasing the VG height to $h = 0.5\delta$ reduced the VG effectiveness in agreement with (Janiszewska, 2004) as did reducing the VG length. Increasing the distance between the VGs (d) led to greater separation between the VG pair and higher Cd values. Relatively small sensitivity was found to the VG angle for $\beta < 20°$. Further increase of β leads to smaller suction peak around the airfoil, conceivably due to VG blockage effects. Doubling the VG pair distance improves VG performance as the separation is suppressed with minimal drag penalty (only half of the original vortices are now formed). Further increase of the distance between the VG pairs is detrimental as the further reduced number of generated vortices fails to sufficiently suppress separation. Positioning the VG array further downstream improves their performance as the generated vortex remains strong enough to suppress separation and the additional drag, due to skin friction, is reduced.

At this point a weakness of the computational approach should be highlighted. For all cases only half a VG pair is simulated ($AR < 0.18$) since performing the parametric study for half the wing ($AR = 1.0$) would be prohibitively expensive. Computational results not shown here suggest that SCs do not form when $AR < 1$, in agreement with (Taira & Colonius, 2009). This means that the results of the parametric study should be treated with caution especially as far as the VG array chordwise position is concerned. Previous experience (Velte & Manolesos, 2011) has shown that when VGs are placed too far downstream they can be covered by a SC, i.e. the separated region extends upstream of the VGs and the SC vortices dominate the flow cancelling the VG effect.

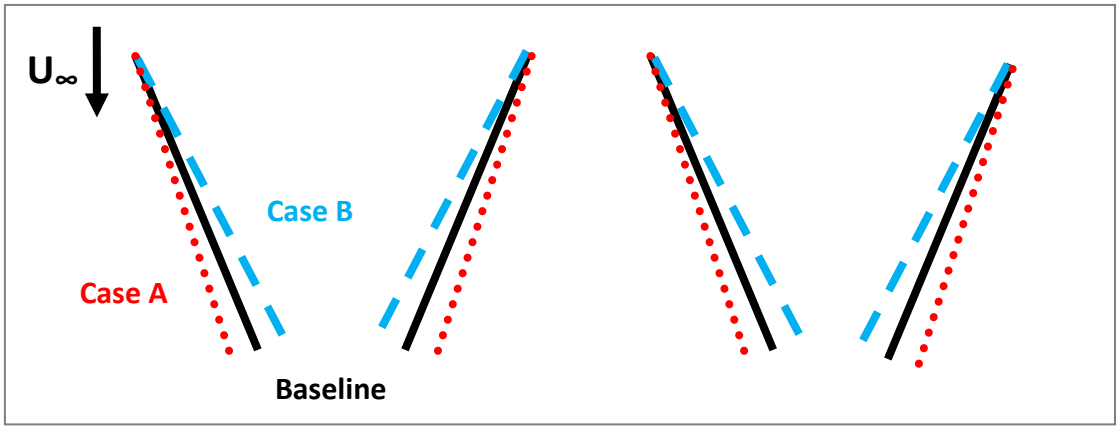

Figure 107: VGs top view. Baseline in solid black line, case A in red dotted line, case B in dashed blue line.

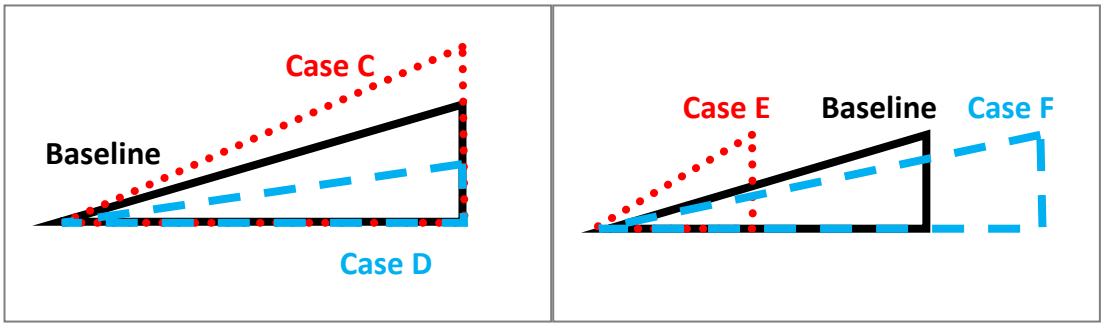

Figure 108: VGs side view (left): Baseline in solid black line, case C in red dotted line, case D in dashed blue line. VGs side view (right): Baseline in solid black line, case E in red dotted line, case F in dashed blue line.

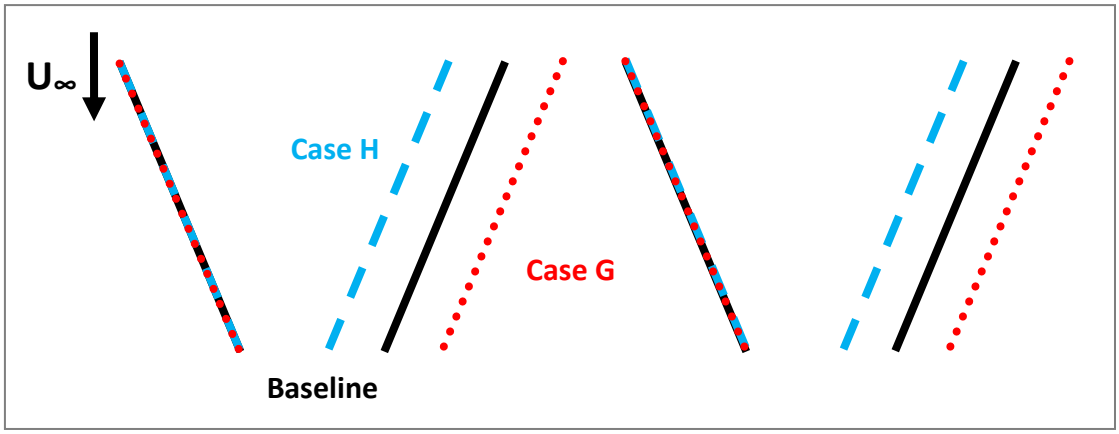

Figure 109: VGs top view. Baseline in solid black line, case G in red dotted line, case H in dashed blue line.

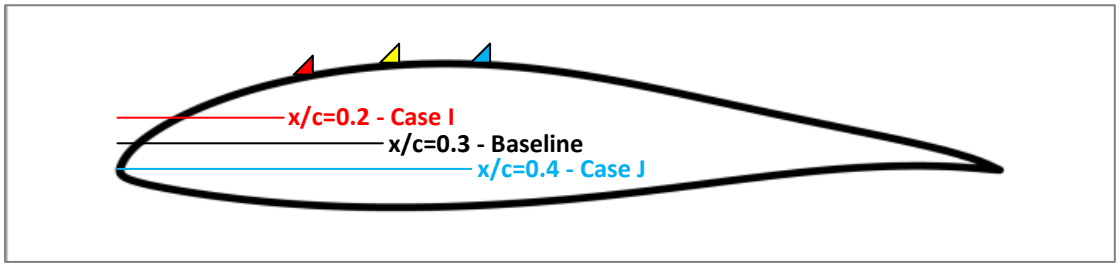

Figure 110: Wing side view. Baseline in yellow filled black line, case I in red filled black line, case J in blue filled black line (VG size not in scale).

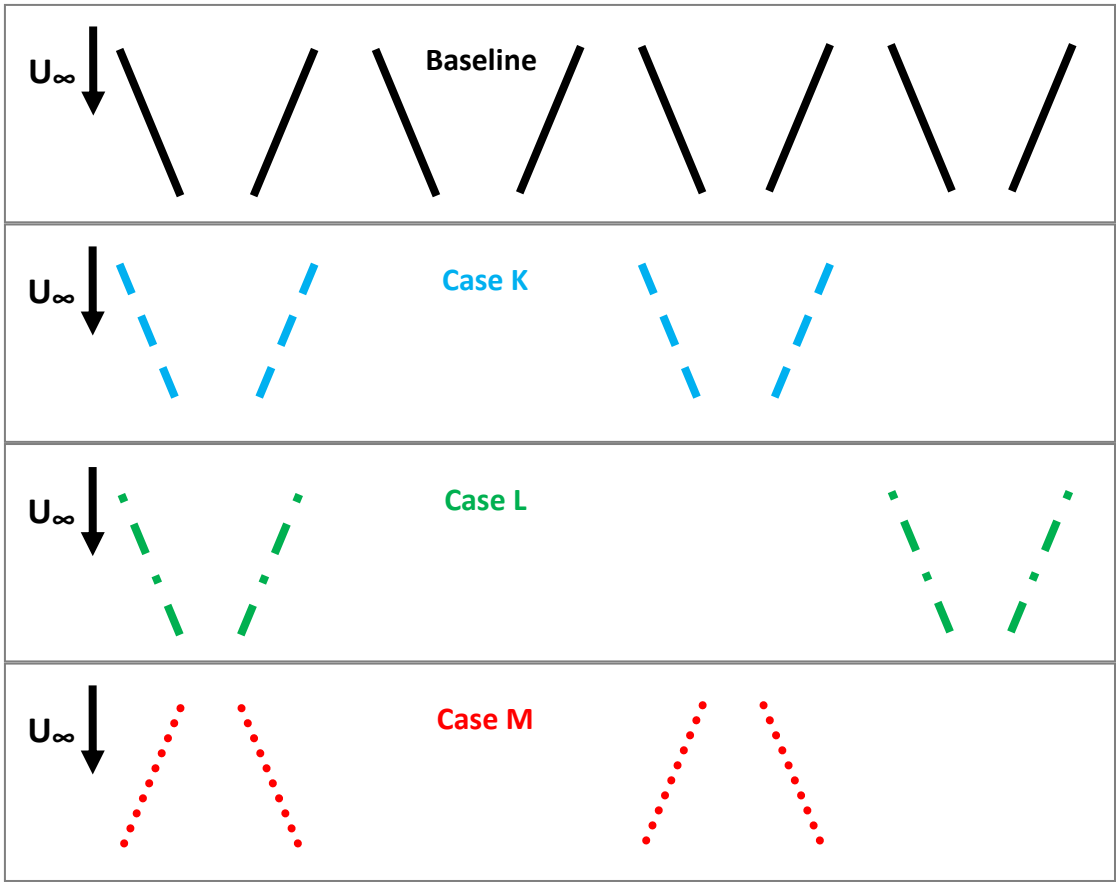

Figure 111: From top to bottom: Baseline in solid black line, case K in dashed blue line, case L in green dash-dot line, case M in red dotted line.

Grid name	Type	Total number of Cells (x10^6)	Number of nodes on airfoil in x direction	Number of nodes up to 2δ above wing surface	Number of nodes in z direction	Cl	Cd	L/D	Separation Location [x/c]	Maximum Vorticity [Non Dimensional]
mk14	Coarse	0.8	359	101	11	1.748	0.0342	51.2	90.6%	119.2
mk7	Medium	1.0	468	101	11	1.736	0.0344	50.5	88.6%	114.6
mk13	Dense	1.2	647	101	11	1.737	0.0342	50.8	88.6%	114.1
mk9	Coarse	0.6	468	51	11	1.741	0.0341	51.1	88.6%	114.5
mk7	Medium	1.0	468	101	11	1.736	0.0344	50.5	88.6%	114.6
mk12	Dense	1.6	468	201	11	1.740	0.0340	51.2	87.6%	114.4
mk11	Coarse	0.5	468	101	6	1.585	0.0394	40.2	54.2%	92.9
mk7	Medium	1.0	468	101	11	1.736	0.0344	50.5	88.6%	114.6
mk8	Dense	1.9	468	101	21	1.753	0.0339	51.7	91.4%	180.0

Table 6: Computational details and selection of results for the different computational grids tested. α = 12.0°, Re = 1.0x10^6. The maximum vorticity value refers to a plane at x = 2h downstream of the VG TE.

Examined Parameter	Case		VG configuration details						Results		
			β [deg]	height (h/δ)	length (l/h)	Distance between VGs (d/h)	Chordwise position (x/c)	VG pair distance (D/h)	Cl	Cd	L/D
	2D - No VGs		-	-	-	-	-	-	1.576	0.036	43.7
β [deg]	-5°	A	15	1.0	3.0	3.7	0.3	5.8	1.727	0.035	50.0
	Baseline		20	1.0	3.0	3.7	0.3	5.8	1.737	0.034	50.7
	+5°	B	25	1.0	3.0	3.7	0.3	5.8	1.711	0.035	48.5
VG height (h/c)	Lower VG	C	20	0.5	6.0	3.7	0.3	5.8	1.647	0.036	45.3
	Baseline		20	1.0	3.0	3.7	0.3	5.8	1.737	0.034	50.7
	Higher VG	D	20	1.5	1.5	3.7	0.3	5.8	1.765	0.035	50.3
VG length (l/c)	Shorter VG	E	20	1.0	1.5	3.7	0.3	5.8	1.710	0.035	48.4
	Baseline		20	1.0	3.0	3.7	0.3	5.8	1.737	0.034	50.7
	Longer VG	F	20	1.0	4.5	3.7	0.3	5.8	1.736	0.034	50.7
Distance between VGs (d/h)	VGs further away	G	20	1.0	3.0	4.6	0.3	5.8	1.721	0.035	48.5
	Baseline		20	1.0	3.0	3.7	0.3	5.8	1.737	0.034	50.7
	VGs closer	H	20	1.0	3.0	2.9	0.3	5.8	1.718	0.034	50.7
Chordwise position (x/c)	VGs further upstream	I	20	1.1	3.0	3.7	0.2	5.8	1.706	0.035	49.3
	Baseline		20	1.0	3.0	3.7	0.3	5.8	1.737	0.034	50.7
	VGs further downstream	J	20	0.9	3.0	3.7	0.4	5.8	**1.767**	**0.034**	**52.1**
VG pair distance (z/h)	Baseline		20	1.0	3.0	3.7	0.3	5.8	1.737	0.034	50.7
	VG pairs wider 1	K	20	1.0	3.0	3.7	0.3	11.7	**1.711**	**0.032**	**53.0**
	VG pairs wider 2	L	20	1.0	3.0	3.7	0.3	17.5	1.669	0.033	51.3
Additional Cases	VG pairs wider 1 at x/c = 0.4	K-0.4	20	1.0	3.0	3.7	0.4	11.7	**1.734**	**0.032**	**54.3**
	As case K but VG pair with common flow down	M	20	1.0	3.0	3.7	0.3	11.7	1.719	0.040	43.3

Table 7: VG configuration parametric study data. In the configuration part of the table the changing parameter is highlighted. In the results part of the table the three best performing cases (Case J, Case K and Case K-0.4) are highlighted. All cases are at α = 12°, Re = 1.0x10^6.

8.2.2 Experiments

The two best performing VG configurations, Case K (VGs placed at x/c = 0.3) and Case K-0.4 (VGs placed at x/c = 0.4), were examined experimentally. Details about the construction of the VG model for wind tunnel testing can be found in Chapter 2. All results refer to a wing of AR = 2.0 with the localized disturbance tested at Re = 0.87×10^6. Details of the VG geometry are given below.

β	=	20°	VG angle to the free stream flow
h	=	δ = 6mm	VG height
l	=	3h	VG length
D	=	11.7h	distance between two VG pairs
d	=	3.7h	spanwise distance between the LE of two VGs of the same pair

Figure 112 shows the lift coefficient polar for Case K and for the uncontrolled case. As discussed later on, at 16° the pressure recordings indicate bifurcation of the flow here denoted by a vertical dashed line. The improvement in lift for the controlled case is clear, as is the continuous increase of Cl until α = 16°. The linear part extends to α = 11° compared to α=6° for the uncontrolled case and the maximum lift coefficient value is now observed at 16°, increased by 0.5 or 44%.

Figure 113 shows the lift variation with the angle of attack for the case with the VGs located at x/c = 0.4 and for the uncontrolled case. Now the improvement in Cl is limited up to α = 13°. Beyond that point the flow is highly separated and the separated flow region extends upstream of the VGs. A flow hysteresis also discussed later on is observed around α = 13°.

The pressure distribution along the wing chord for α = 14° for the two controlled cases and for the uncontrolled case is given in Figure 114. When VGs are place at x/c = 0.3, separation is successfully suppressed. The flow remains attached at least up to x/c ≈ 0.58 and the suction peak is increased. The pressure data close to the trailing edge suggest recovery at higher values which explains the small pressure difference over the pressure side of the airfoil. With the VGs at x/c = 0.4 the separation extends upstream of the VGs and the pressure distribution is very similar to that of the uncontrolled case.

Figure 116 shows oil flow visualization experiments for the case with the VGs at x/c = 0.3 (left) and with the VGs at x/c = 0.4 (right). Indeed a fully developed SC is formed when the VGs are located x/c = 0.4. The SC reaches up to the VGs at its centre and no VG vortices can be seen there. At the sides of the SC, though, traces of VG vortices appear. These are curved and seem to go around the SC all the way to the wing TE. Separation line is three dimensional for the case with VGs located at x/c = 0.3, however no clear SC formation appears here.

The presented experimental data suggest that locating the VGs at x/c = 0.3 is the optimum configuration for the studied airfoil and this set up is further studied in Chapter 9. The drag coefficient variation with respect to the angle of attack for this case is given in Figure 115. A relatively small drag penalty of 0.002 is clearly seen for α < 6°. Beyond that point, drag is significantly reduced for the controlled case up to α < 16°.

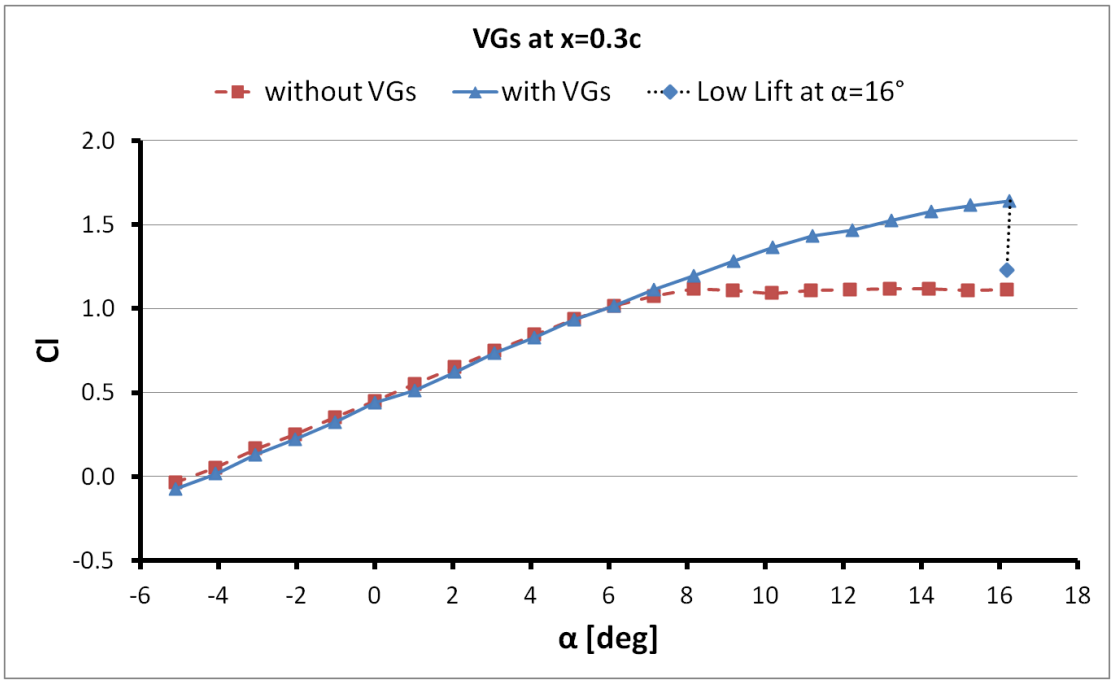

Figure 112: Experimental lift coefficient polar for a wing with VGs at x/c = 0.3 and without VGs. Re = 0.87x10^6.

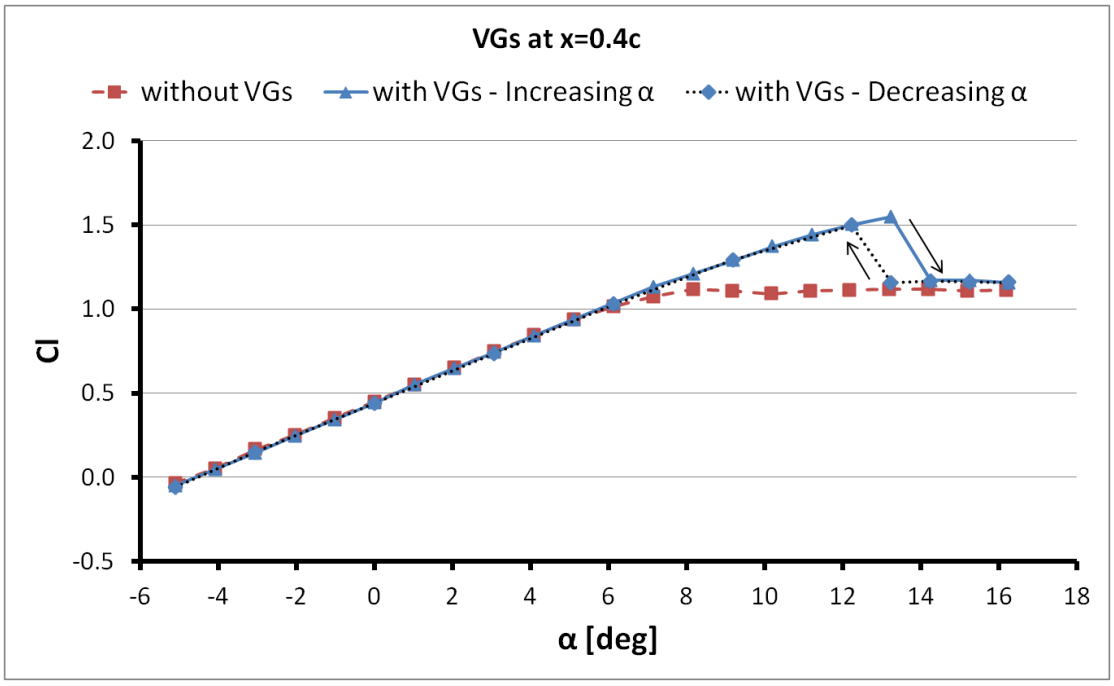

Figure 113: Experimental lift coefficient polar for a wing with VGs at x/c = 0.4 and without VGs. For the controlled case two curves are shown, one for increasing and one for decreasing angle of attack. Re = 0.87x10^6.

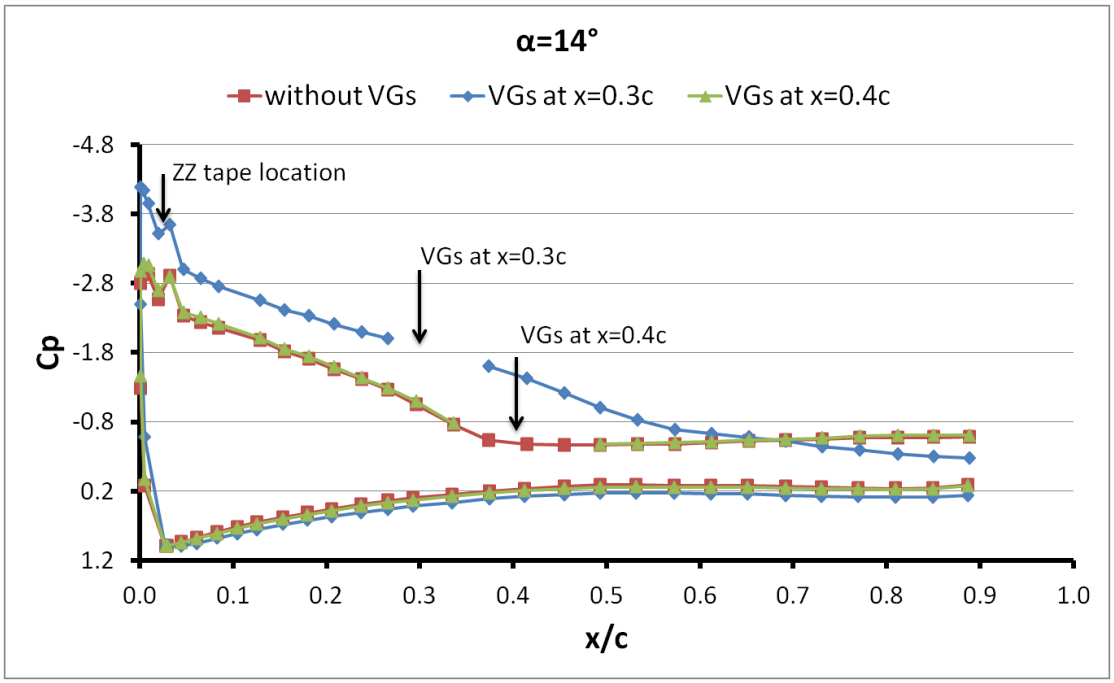

Figure 114: Pressure distribution along the wing chord for a wing with VGs at x/c = 0.3, with VGs at x/c = 0.4c and without VGs. α = 14°, Re = 0.87x10^6. Pressure perturbations around x/c = 0.02 in the experimental data are due to the local effect of the ZZ tape on the neighbouring pressure taps. Pressure measurements from the region around the VG strip are omitted.

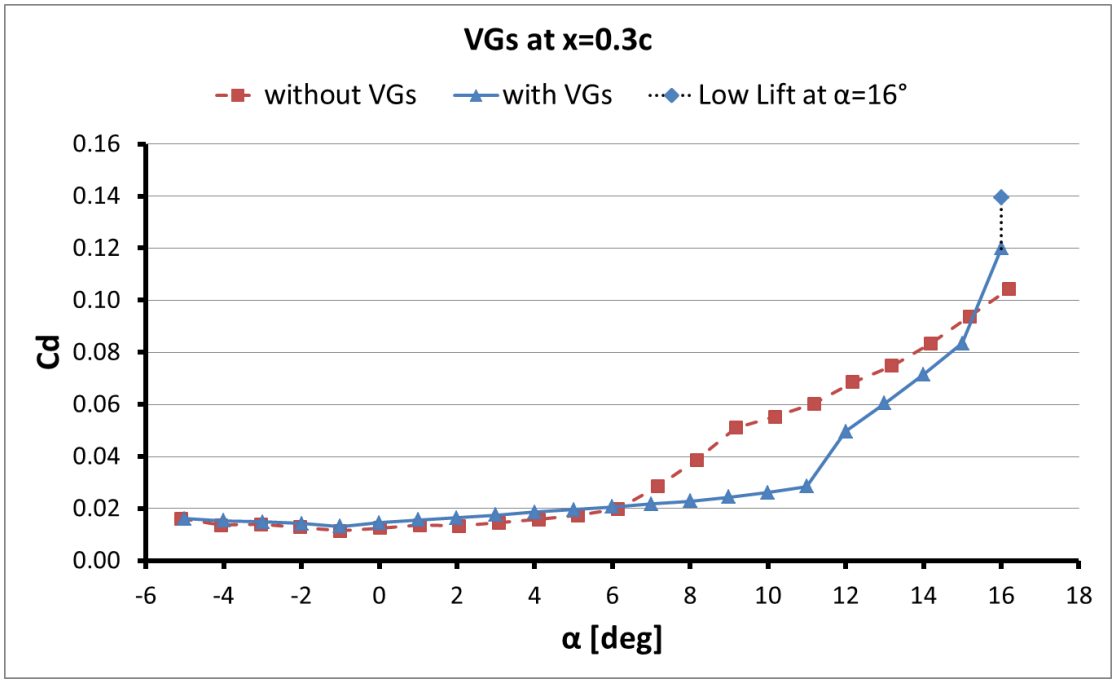

Figure 115: Experimental drag coefficient polar for a wing with VGs at x/c = 0.3 and without VGs. Re = 0.87x10^6.

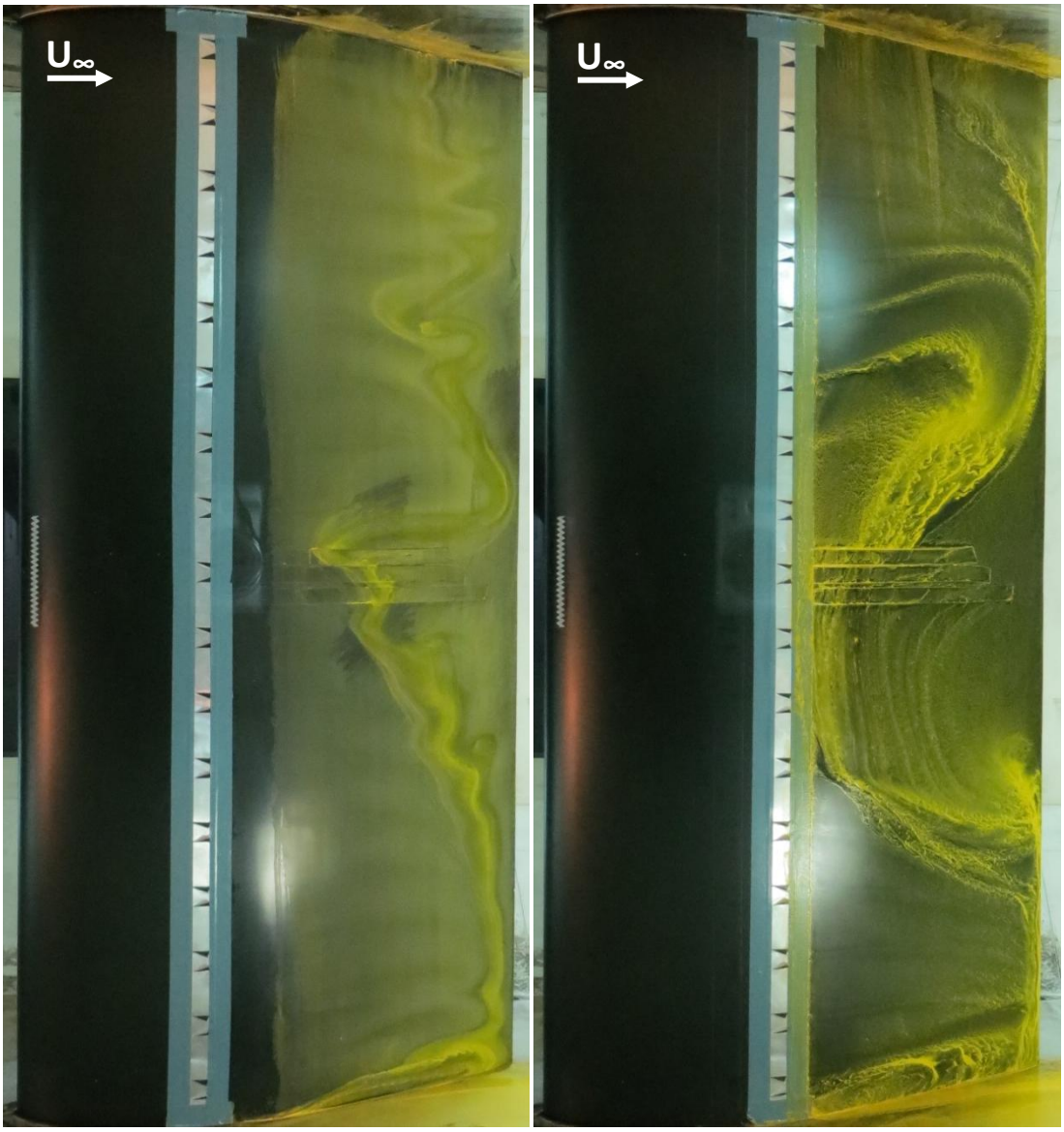

Figure 116: Oil flow visualization for the case with the VGs at x/c = 0.3 (left) and with the VGs at x/c = 0.4 (right). α = 14°, Re = 1.0x10^6. A SC is formed in the first case.

Bifurcation at α = 16° for the case with VGs at x/c = 0.3

Initially all pressure measurements were taken at 200Hz sampling rate and for 5". During the measurements for the case with VGs at x/c = 0.3 at 16°, however, significant unsteadiness was observed that led to longer samples (50"). No unsteadiness was observed for angles of attack lower than 16°, even when longer samples were taken.

It was found that the flow alternated between two distinct states. One of the states, the High Lift state, dominated the time series, whereas the less frequent state, the Low Lift state, would appear for time intervals that would not exceed 3". The difference in pressure level between the two states was more pronounced on the suction side, both upstream and downstream of the VGs. As an example, the time series from the suction side pressure transducer at x/c = 0.265 is given in Figure 117 clearly showing the two states.

A separate time average value for each state was computed and thus two different pressure distributions were produced, as shown in Figure 118 (page 121), where the pressure

distribution for the uncontrolled case is also plotted (blue-diamonds curve). The red-squares curve and the green-triangles curve correspond to the High and Low Lift states, respectively. The High Lift state follows the trend of the smaller angles, i.e. higher suction peak and limited separation compared to the uncontrolled case. On the other hand the similarity between the uncontrolled case and the Low Lift state is clear, suggesting that it is the same, highly separated, state.

According to the pressure distributions obtained at mid span, the point of separation in the Low Lift state appears at x/c ≈ 0.35 while in the High lift state appears at x/c ≈ 0.6. The triggering mechanism that could bring the separation point at such an upstream location is unclear although it is tempting to charge it on vortex instabilities leading to breakdown of the VG vortices. Once the VG vortices break down the SC is free to form to its uncontrolled size. In any case the onset of such a bifurcation could lead to fatigue loads and therefore the operational envelope will be reduced.

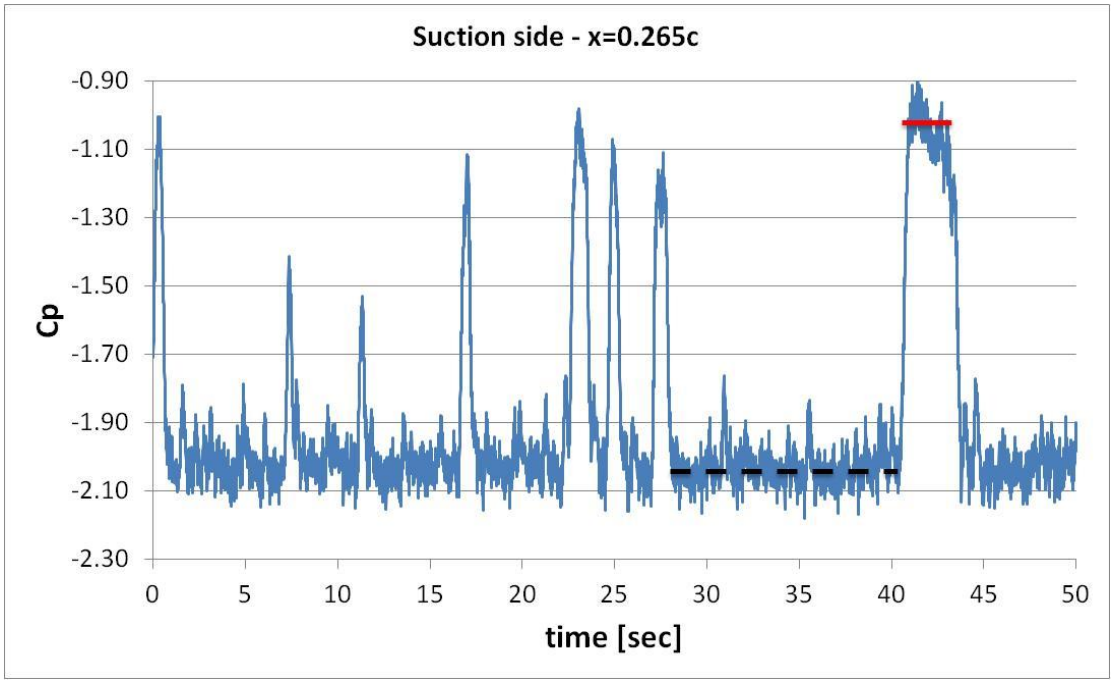

Figure 117: Time series of pressure measurement taken from the pressure tap on the suction side of the wing located at x/c = 0.265. , α = 16°, Re = 0.87x10^6. The states of High (black dashed line at Cp ≈ -2) and Low Lift (red solid line at Cp ≈ -1) are indicated. VGs located at x/c = 0.3.

Hysteresis at α = 13° for the case with VGs at x/c = 0.4

As already mentioned when the VGs were located at x/c = 0.4, a flow hysteresis was detected around α = 13°. More specifically with the tunnel running, when the angle of attack was increased to 13° from lower angles of attack the flow remained mostly attached. Further increase to 14° or higher resulted in a highly separated flow. When decreasing the incidence to 13° from higher angles of attack the flow remained highly separated. Further decrease to 12° resulted in the flow being again mostly attached. No such behaviour was observed when the VGs where located at x/c = 0.3.

When the wing was set to 13° and the wind tunnel started, the flow would randomly select one of aforementioned states, for no apparent reason. Longer tests (up to 30 minutes) at α =

13° did not reveal any instability similar to the one described in the previous paragraph. The flow would select one of the two possible states and then stably maintain it.

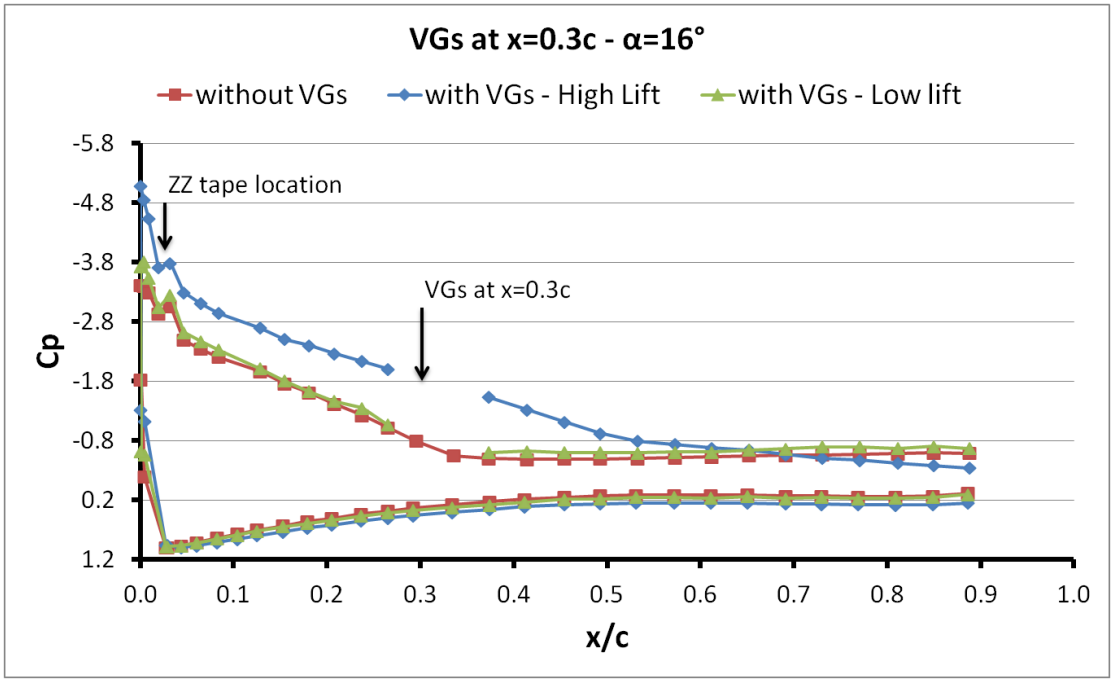

Figure 118: Pressure distribution along the wing chord for a wing with VGs at x/c = 0.3 and without VGs. In the case with VGs, the two curves correspond to the high lift state (red squares) and the low lift state (green triangles). α = 16°, Re = 0.87x10^6. Pressure perturbations around x/c = 0.02 in the experimental data are due to the local effect of the ZZ tape on the neighbouring pressure taps. Pressure measurements from the region around the VG strip are omitted.

Figure 119 shows the pressure distribution along the wing chord for increasing and decreasing α and for the uncontrolled case. It is clear that when α is increased the VG effect is strong and suppresses separation while when α is decreased, separation extends upstream of the VGs cancelling their effect.

Aerodynamic hysteresis is a subcritical bifurcation (Tobak & Peake, 1982) and is not uncommon in flows with streamwise vortices (Lowson, 1964; Gresham et al., 2010). It has also been mentioned for the flow over a wing experiencing SC separation (Winkelmann, 1981). In the present case, the exact mechanism through which the vortices shed by the VGs and the SC vortices interact remains unclear. It is noted, however, that the bifurcation occurs around α = 13°, an angle of attack where separation for the uncontrolled case extends to x/c = 0.37, i.e. upstream of the VGs locations. The earliest point of separation as found from pressure data for a wing with VGs at x/c = 0.4 and without VGs is given in Figure 120.

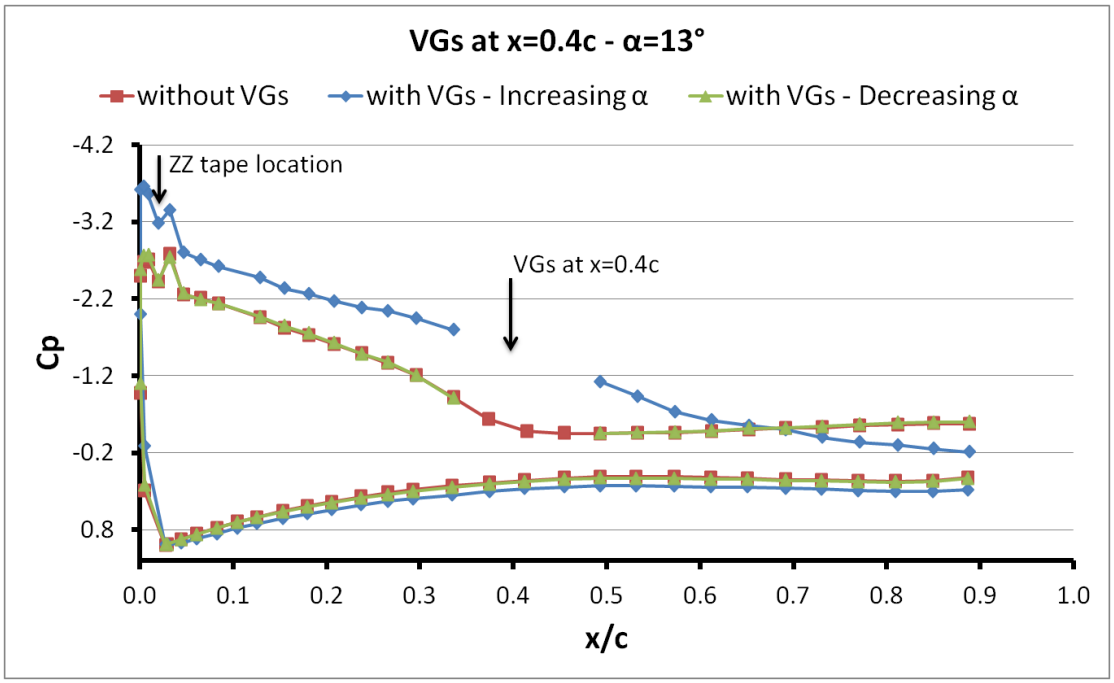

Figure 119: Pressure distribution along the wing chord for a wing with VGs at x/c = 0.4 and without VGs. For the controlled case two curves are shown, one for increasing and one for decreasing angle of attack. α = 13°, Re = 0.87x10^6. Pressure perturbations around x/c = 0.02 in the experimental data are due to the local effect of the ZZ tape on the neighbouring pressure taps. Pressure measurements from the region around the VG strip are omitted.

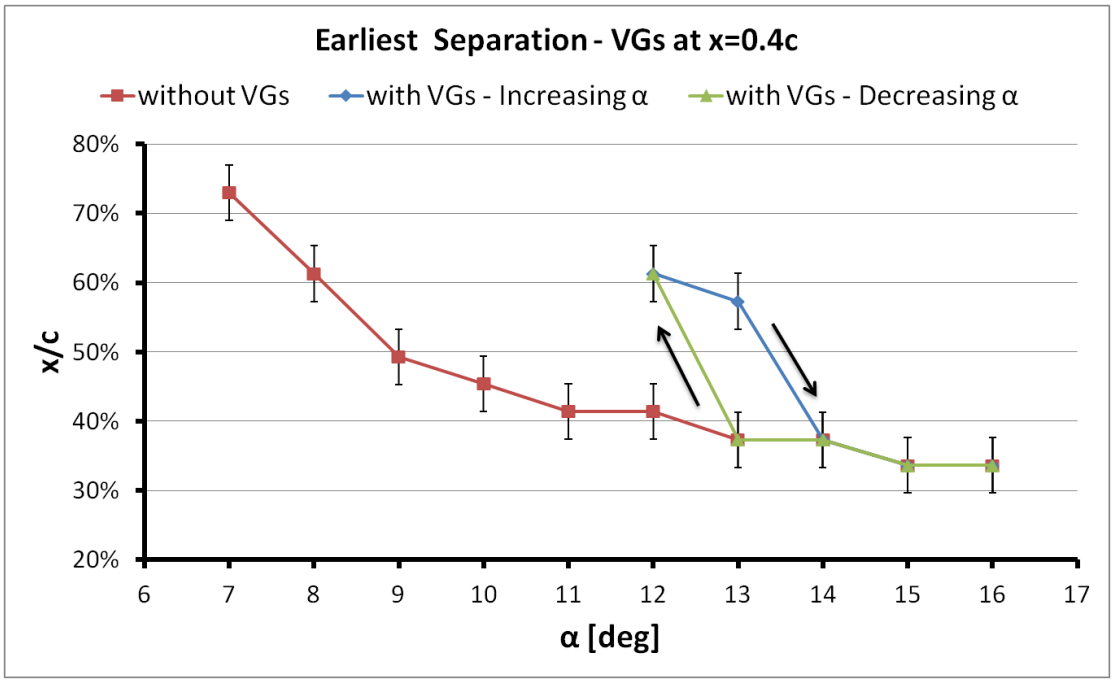

Figure 120: Earliest point of separation as found from pressure data for a wing with VGs at x = 0.4c and without VGs. For the controlled case two curves are shown, one for increasing and one for decreasing angle of attack. Error bars are equal to 0.04, i.e. equal to the chordwise distance of two consecutive pressure taps. Re = 0.87x10^6.

8.3 Summary

A computational parametric study was performed to examine which VG configuration was better suited for the present airfoil. Based on the existing literature, counter rotating

triangular vanes were chosen as the Baseline configuration. The effect of changing the shape and positioning parameters was examined on a small AR wing, with span equal to that of half a VG pair. The best performing set ups were tested experimentally.

It was found that small AR simulations, i.e. simulations that cannot predict SC formation, fail to predict the flow behaviour at higher angles of attack. Experimental results suggest that VGs should always be placed upstream of the most upstream separation location of the uncontrolled flow, so that VGs are not engulfed inside the SC. Flow instability and flow hysteresis have been observed for the cases with the VGs located at x/c = 0.3 and x/c = 0.4, respectively, which require further investigation.

9 Experimental study of the vortex generator induced flow

In this section the flow downstream of the VGs is studied on the basis of Stereo PIV experiments. This method provides an insight to the vortical structure and the turbulence characteristics, both useful in turbulence modelling validations. The flow is examined at a Re number of 0.87×10^6 and at an angle of attack $\alpha = 10°$, so that results are directly comparable to the SC study in Chapter 6. Out of the Stereo PIV measurements, vortex size, path and strength are estimated and an investigation on the turbulence characteristics of the flow is carried out by correlating Re stresses production to mean flow gradients

9.1 Stereo PIV set up

Measurement planes

The flow was measured in three planes downstream of the central VG pair, at x/c = 0.6 (plane A), x/c = 0.7 (plane B) and x/c = 0.8 (plane C), see Figure 121. In terms of VG height (h) plane A, B and C were at Δx = 27.2h, Δx = 37.2h and Δx = 47.2h downstream of the VG TE, respectively. Δx is the distance from the VG TE defined as:

$$\Delta x = x - x_{VG} = x - 0.328c \qquad (20)$$

where x_{VG} is the VG TE location and c is the wing chord.

All Stereo-PIV measurements were taken at $\alpha = 10°$ and $Re = 0.87 \times 10^6$. More details about the measurement planes are given in Table 8, in page 126. For each plane 2000 snapshots were taken and the results presented here are the averaged data. For that number of realization the 95% confidence interval for the rms quantities is 6.0%.

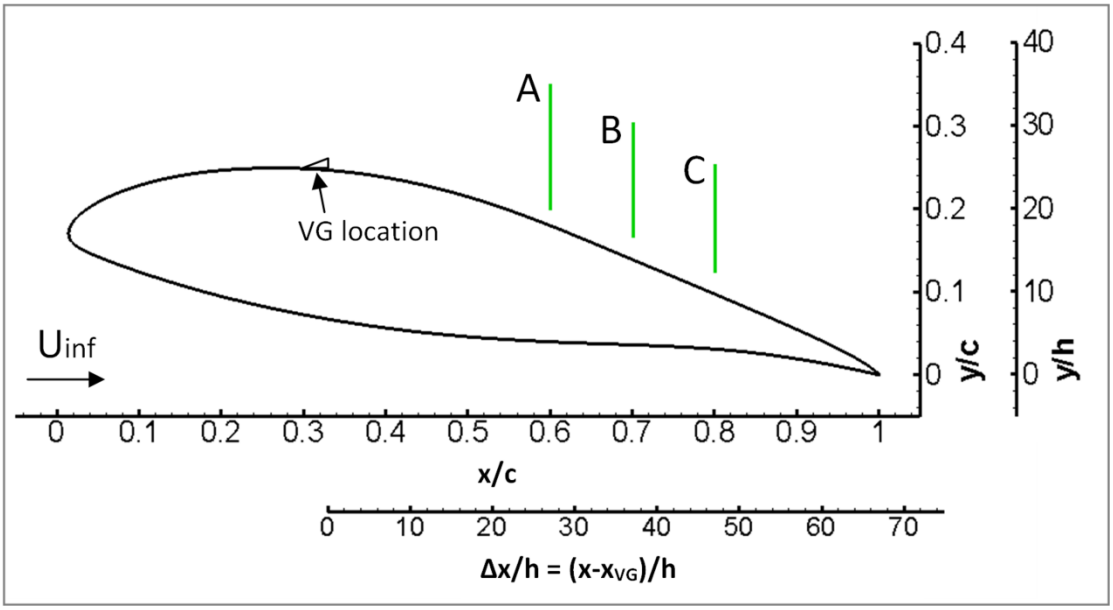

Figure 121: Stereo PIV measurement planes for the 10° case. Planes A, B and C are shown with solid green line. The axes are shown twice, once non-dimensionalized with the wing chord (c) and once with the VG height (h). In the latter case the x axis starts at the VG TE, see Eqn. (20).

Parameter	Plane A	Plane B	Plane C
Chordwise location	0.6c	0.7c	0.8c
Distance from VG trailing edge [h]	27.2	37.2	47.2
Lenses	150mm	150mm	150mm
Camera contained angle	62°	65°	69°
Final interrogation area size [px]	16x16		
Final interrogation area size [mm]	0.8x0.8		
Minimum resolved velocity [m/s]	0.4		
Minimum resolved velocity [normalized with respect to the free stream]	0.02		
Number of Snapshots	2000		

Table 8: Stereo PIV test details for all the planes measured.

Stereo PIV Calibration

A dual plane double sided target was used allowing the calibration coefficients computation without traversing the target in the out-of-plane direction. As a result the velocity component normal to the plane is first order accurate (M. Ramasamy & Leishman, 2006). The side of the target was fitted with a mirror, aligned with the centreline between the two planes of one side of the target. The optical path of the reflected sheet was made co-planar with the incident sheet to ensure the best possible alignment of the laser sheet with the calibration target.

Pulse separation time

In order to reduce errors associated with flow acceleration and curvature effects a small pulse separation time should be used (M. Ramasamy & Leishman, 2006). Furthermore when the measurement plane is normal to the main velocity component, as in the present case, a small pulse delay is required in order to reduce the number of particles that go out of the measurement window. On the other hand, reducing the pulse delay reduces the measurement dynamic range and increases the relevant measurement error, so a compromise is necessary.

In the present case a pulse separation time of 12 μsec was used, as higher values would increase the measurement noise and make peak detection harder. For all planes the number of spurious vectors was always below 2% and the particle displacement was in all cases less than 1/4 of the 16x16px final interrogation area. The minimum estimated velocity for a pulse separation time of 12 μsec is given in Table 8 above. Any estimated velocity below the relevant value for each plane is not reliable.

Spatial Resolution

Stereo-PIV is a very popular technique for measuring vortex flows (M. Ramasamy & Leishman, 2006; Godard & Stanislas, 2006; Manikandan Ramasamy et al., 2011; Velte & Hansen, 2012) since, apart from being non-intrusive, it has the advantage of providing instantaneous realizations of all three velocity components in a plane. However, spatial resolution can be an issue, especially for flows with steep spatial gradients. To sufficiently resolve a vortex flow (Martin et al., 2000) the ratio of probe size to vortex core radius, α_{RES}, should be:

$$a_{RES} = \frac{L_m}{r_c} < 0.1 \quad (21)$$

where L_m is the length of the interrogation area and r_c is the vortex radius.

In the present set of experiments this was particularly challenging given the distance of the cameras from the measurement planes and the small size of both the VGs and the resulting vortices. For plane A, where distance from cameras is the greatest and vortex size is the smallest, the vortex radius, defined as the half distance between the two vorticity peaks, was found to be 8mm. To achieve the desired resolution Macro lenses (150mm) and high resolution cameras (4Mpixel) were used. The image deformation technique, as described in (M. Ramasamy & Leishman, 2006), was applied to the data. The final interrogation area size was 0.8x0.8 mm, see Table 8 (page 126).

Image Processing

The image processing was done using TSI Insight 4G software. In pre-processing a background reflection image was subtracted from the measurement images to remove unwanted reflections. In processing, the overlap between interrogation areas was set to 50% and a Gaussian peak estimator was used. The signal-to-noise ratio was set to 1.5 and spurious vectors were replaced using a 3x3 local mean. Velocity derivatives were computed using the least squares method which is second order accurate and cancels out the effect of oversampling and produces smoother results (Raffel et al., 1998). No peak locking was observed in the results.

Camera vibration analysis

The cameras were located inside the test section, 1.2c downstream of the wing TE. The camera base was secured on elastic anti-vibrating pads and both cameras were mounted on reinforced Scheimpflug angle adjustable mountings. As described in detail in Chapter 2 the camera vibration effect was quantified and it was found that expressed in m/s the 95% confidence interval for the measured velocities due to camera vibration was 0.04 m/s, i.e. an order of magnitude smaller than the minimum resolved velocity for each plane, see Table 8 (page 126).

9.2 Results

9.2.1 Oil flow visualization

Figure 122 shows the oil flow pattern on the wing suction side for α = 10°, Re = 0.87x10^6, for the uncontrolled (left) and the controlled case (right). The flow is from left to right and, as the wing is located vertically in the tunnel, gravity affects the final image as it drags the oil mix downwards in areas of low velocity. Only the region for x/c > 0.3 is shown for greater detail.

The SC structure is clearly visible for the uncontrolled case, as is the three-dimensionality of the flow due to the localized disturbance at the centre of the wing span. The surface foci of the SC vortices are located approximately at z/S = 13% above and below the wing mid span (z/S = 0%). Their chordwise location is x/c ≈ 0.91 and the most upstream point of the SC was found to be at x/c ≈ 0.48. This case is described in detail in Chapter 6.

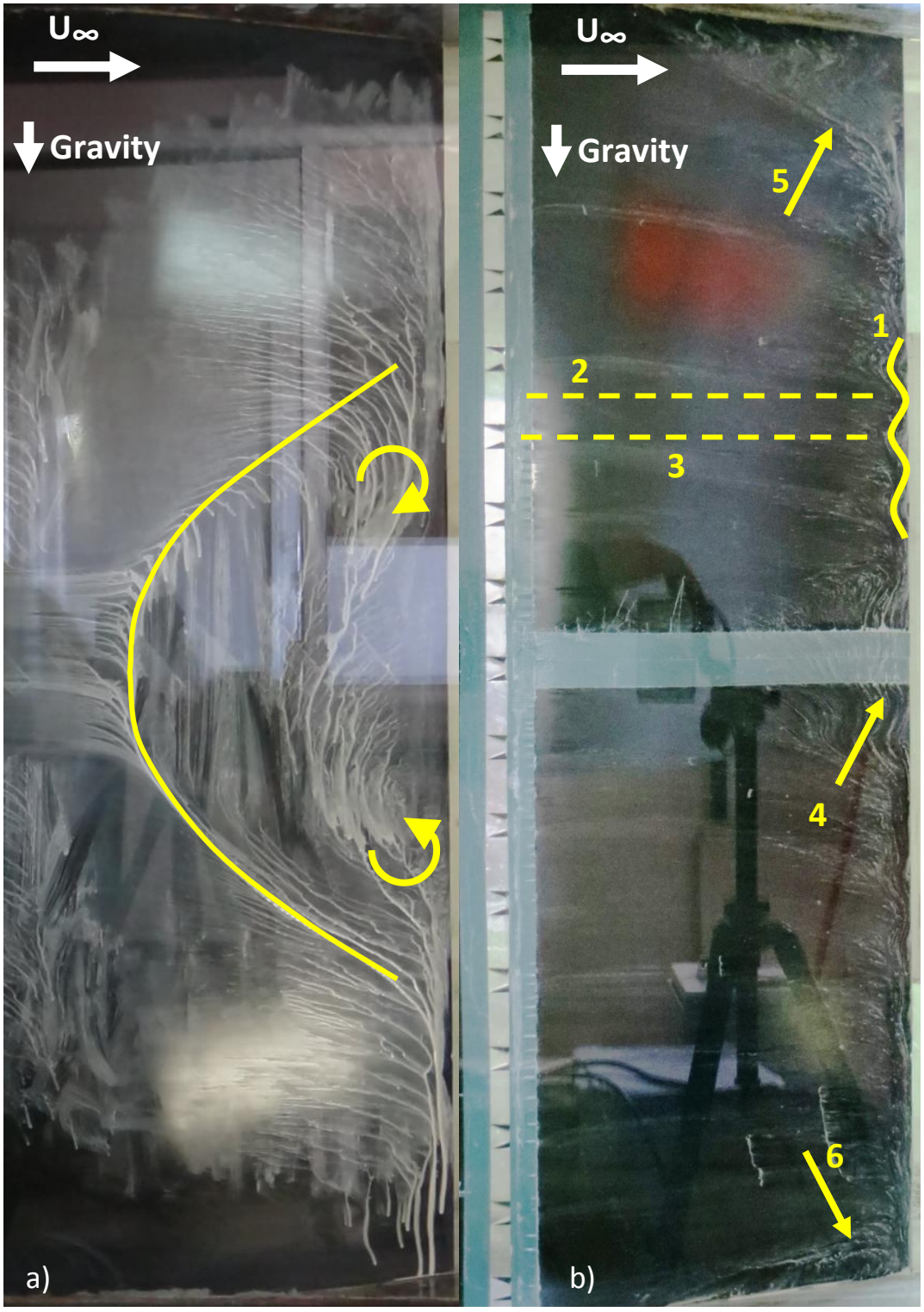

Figure 122: Oil flow visualization for the case without VGs (left) and with VGs (right), α = 10°, Re = 0.87x10^6.

Separation is significantly reduced to x/c ≈ 95% for the controlled case and the formation of the SC is suppressed. The separation line has a wavy form as a result of the VG vortices, and part of it is highlighted by the wavy curve #1. Separation is smaller downstream of the downwash regions (see dashed line #2) and grows downstream of the upwash regions (see dashed line #3). Separation is also increased downstream of the localised disturbance (see arrow #4), which is expected, as the flow is less energetic at this region due to the ZZ tape.

Vortex paths continue all the way to the separated region suggesting that the VG vortices remain close to the wing surface until at least x/c = 0.95.

Three-dimensional corner flow is also apparent at the top (see arrow #5) and bottom (see arrow #6) of the right figure where the fences are attached to the wing. The top region appears larger for two reasons; a) because gravity drags the oil mix downwards at regions of low velocity and b) because the top VG pair distance to the respective fence is greater than the lower one by 1cm. As a result separation at the corner is controlled better at the lower corner than at the top one.

9.2.2 Mean flow

Figure 123 compares normalized streamwise velocity profiles at chordwise locations x/c = 0.6, x/c = 0.8 for both the controlled and the uncontrolled case. No data were available for the uncontrolled case on plane B. For the latter case, the profile at the centre of the wing span is plotted and negative streamwise velocity values are highlighted with blue circles. For the controlled case the spanwise average of the streamwise velocity $U_x(y)$ is plotted. The suppression of separation is confirmed by the PIV data. It is also apparent that the free stream outside the separated region is accelerated more in the uncontrolled case than in the case with the VGs as a result of different displacement flow flux.

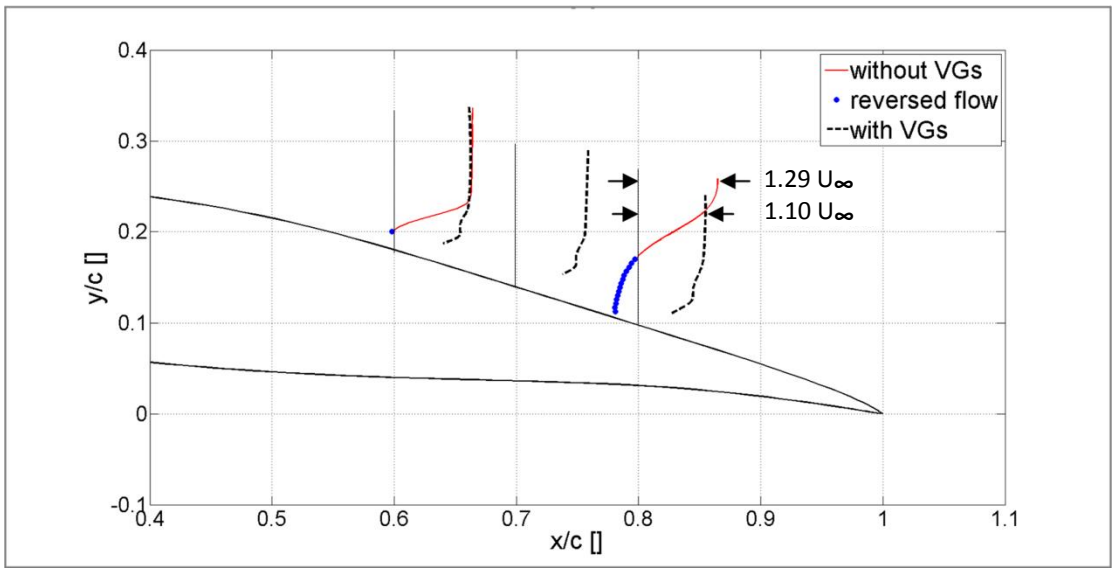

Figure 123: Normalized streamwise velocity profiles at streamwise locations x/c = 0.6, x/c = 0.7, x/c = 0.8. For the uncontrolled case the profile at the centre of the wing span is plotted and negative streamwise velocity values are shown with blue circles. For the controlled case the spanwise average of the streamwise velocity is plotted. No data for plane x/c = 0.7 were available from the uncontrolled case. The effective control of separation is clearly seen.

Using the triple decomposition, as suggested by (Stillfried et al., 2011), the total instantaneous velocity field $u_i(y,z,t)$ at constant x is decomposed into a mean velocity part $U_i(y)$, a fluctuating velocity part $u_i'(y,z,t)$ and a vortex velocity part $V_i(y,z)$.

$$u_i(y,z,t) = U_i(y) + u_i'(y,z,t) + V_i(y,z) \tag{22}$$

By time-averaging $u_i(y,z,t)$ the $u_{PIV}(y,z)$ field is obtained.

$$u_{PIV}(y,z) = \overline{u_i(y,z,t)} = U_i(y) + V_i(y,z) \quad (23)$$

For an array of counter rotating vortex generators the spanwise average of the vortex velocity field is zero, since $V_i(y,z)$ is symmetrical.

$$\langle \overline{u_{PIV}(y,z)} \rangle = \langle \overline{U_i(y) + V_i(y,z)} \rangle = U_i(y) \quad (24)$$

where $\langle \cdot \rangle$ denotes spanwise averaging in the z direction.

Thus the vortex velocity field can be obtained using:

$$V_i(y,z) = u_{PIV}(y,z) - \langle \overline{u_{PIV}(y,z)} \rangle \quad (25)$$

Figure 124, right, presents vorticity contours on planes A, B and C. The vectors superimposed on the velocity contours are the vortex field, $V_i(y,z)$ obtained as explained above. One out of every four vectors is plotted for clarity. Vorticity isolines are also drawn, for $\omega = \omega_{max}/2$, where ω_{max} is the peak vorticity value for each vortex on each plane. In the following, the vortex core is defined as the area inside the $\omega = \omega_{max}/2$ isolines.

The vortices in all planes appear to be above the BL. This is not surprising as the VG height was equal to the BL height and counter rotating vortices with common flow up are expected to lift each other as they progress downstream. The streamwise velocity shear layer has a distinct "omega" shape on plane A, which is subsequently diffused on planes B and C. Between the two vortices low momentum fluid is uplifted from closer to the surface due to the combined upwash. The vortices also bring flow of higher velocity towards the wall and the region between them. As discussed later this leads to a double peak in the streamwise velocity profile which is smoothened by diffusion on planes B and C.

Vorticity contours on plane A are stretched in the vertical direction due to the close proximity of the vortices. The vortex shape changes from plane A to plane B, indicating strong vortex interaction (Pauley & Eaton, 1988; Mehta & Bradshaw, 1988). The contour shapes on planes B and C are similar to each other suggesting that diffusion dominates over this part of the flow. The locations of peak vorticity (shown as black marks on the vorticity contours) are always at the lower part of the vorticity contours.

Vortex Path

The vortex centre on a YZ plane was defined as the location of peak vorticity. The vortex centre location for all measured planes is given in Figure 125 (left). In this graph the wing surface is at y/h = 0. With regard to their spanwise movement, it is observed that, for the planes examined, the vortices move away from each other.

On plane A (x/c = 0.6 or 27.2 heights downstream of the VG TE) the vortex centre is at 1.6h above the wing, see Figure 125 (left), indicating small vortex displacement in the vertical direction since their formation. At x/c = 0.8 (plane C or 47.2 heights downstream) the vorticity peak region is elongated compared to its shape on plane A, compare black marks in Figure 124. The vortex centre is now almost at double the distance from the wing surface.

This cannot be attributed to vortex core growth since, as explained later, the vortex core radius has only grown 20% over the same distance. Displacement can be attributed on one hand to surface curvature and on the other to the mutual induction/upwash that forces the vortex cores to move away from the solid surface.

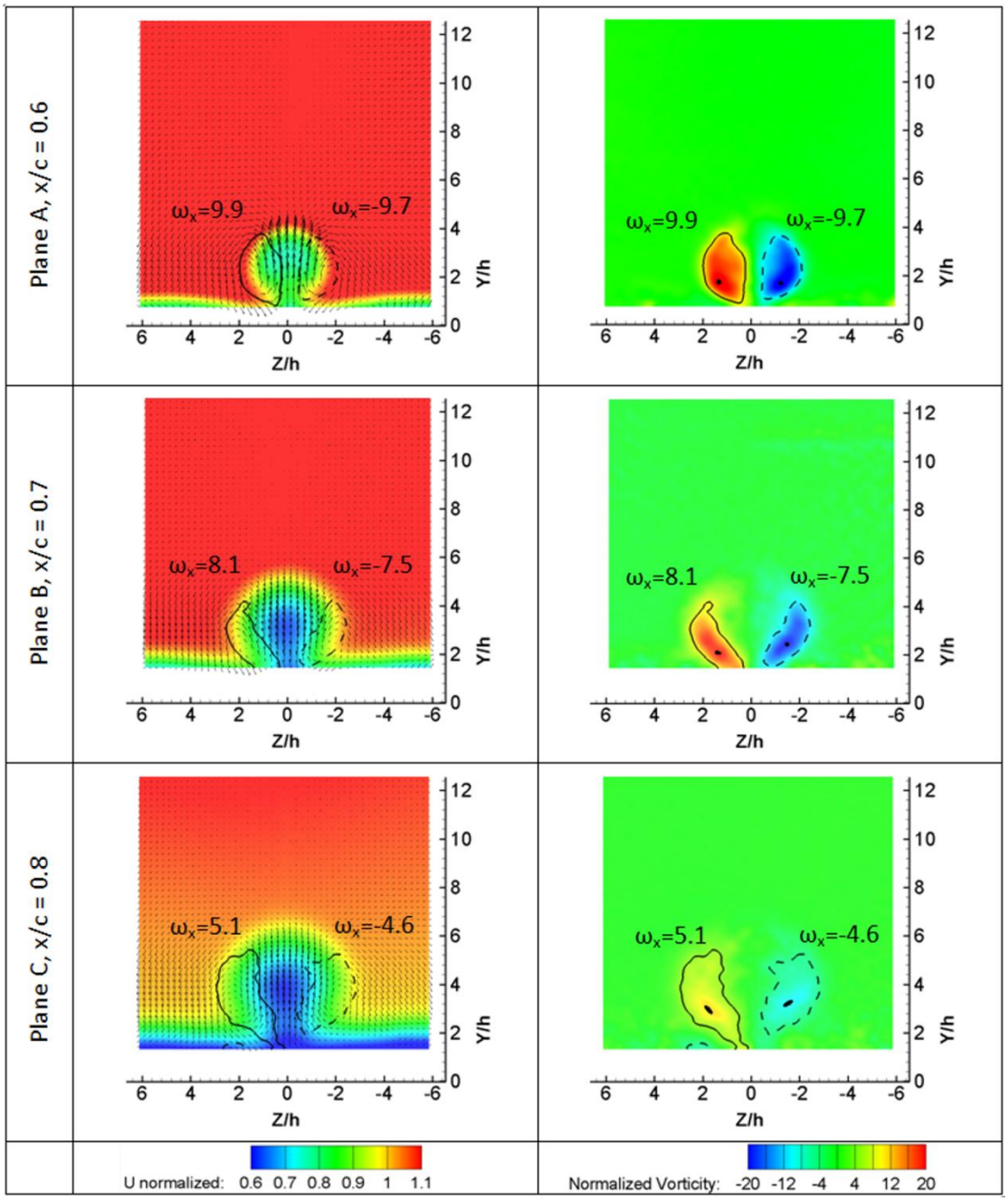

Figure 124: (Left Column) Normalized streamwise velocity contours and vectors of the in plane vortex velocity field. One out of every four vectors is plotted for clarity. (Right Column) Normalized vorticity contours. Vorticity isolines for ω = ω_{max}/2 for each vortex are also plotted. Top, middle and bottom row correspond to plane A (x/c = 0.6, Δx = 27.2h), B (x/c = 0.7, Δx = 37.2h) and plane C (x/c = 0.8, Δx = 47.2h), respectively. Vorticity peak locations are indicated by black marks. The wing surface is always at y/h = 0 and z/h = 0 is the centreline between the two VGs.

The right vortex centre appears to be higher than the left vortex centre on planes B and C. This could be attributed to vortex interaction, since the left vortex is stronger (see vorticity

isolines in Figure 124) and pushes the right one upwards more than the opposite. The difference in vortex strength is attributed to inaccuracies in the VG construction. The right hand side VG was measured to be 0.5mm shorter and at ~1° lower angle with respect to the free stream than the left VG.

Vortex Size

The "half-life" radius $R_{0.5}$ was used to examine the evolution of the vortex size, in a way similar to (Yao et al., 2002). $R_{0.5}$ is defined as the radial distance from the centre of the vortex core to the point where local vorticity is equal to half the peak vorticity. Since the vortex shape is not exactly circular, the area where vorticity was higher than half of the peak vorticity, $A_{0.5}$, was initially computed and then $R_{0.5}$ was found using

$$R_{0.5} = \sqrt{A_{0.5}/\pi} \tag{26}$$

Figure 125 (right) shows the $R_{0.5}$ values for both vortices and for the three measurement planes. $R_{0.5}$ remains stable from plane A to plane B and then it grows by ~20% on plane C, conceivably due to viscous diffusion, in agreement with (Mehta & Bradshaw, 1988). Attention is drawn to the fact that, although vortex half radius does not change from plane A to plane B, the vortex shape is different due to stretching, see Figure 124.

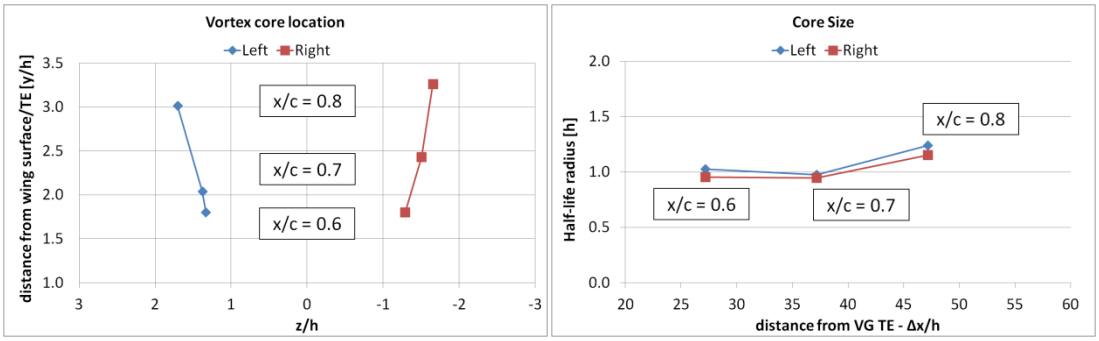

Figure 125: Vortex centre location on the XZ plane (left) and vortex half radius (right) at the three measurement planes.

Vortex Strength

Vortex circulation and peak vorticity for all measurement planes and both vortices are plotted in Figure 126. Both quantities are normalized with their respective values on plane A, in order to examine their decay as the vortices continue downstream. Circulation is computed as the surface integral of vorticity inside the vortex core. From plane A to plane B both circulation and vorticity drop significantly. From plane B to plane C circulation remains constant, whereas vorticity still drops confirming vortex diffusion.

A combined conclusion from Figure 124, Figure 125 and Figure 126 is that between plane A and plane B vortex interaction is still strong whereas between plane B and plane C diffusion dominates the vortex evolution.

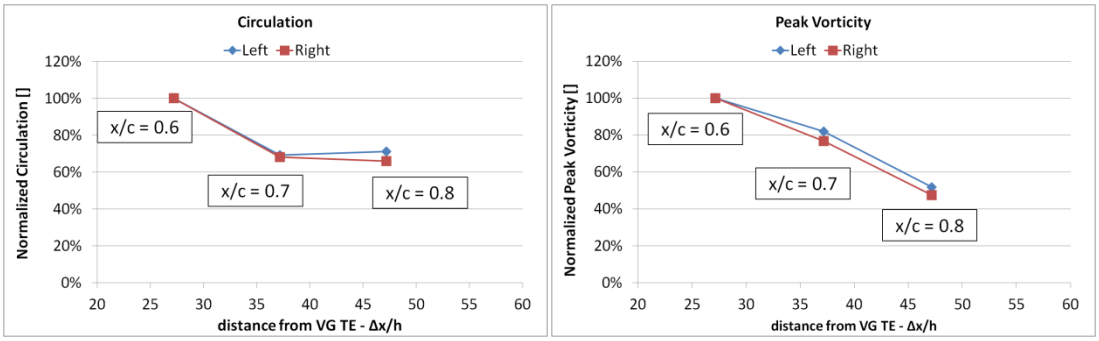

Figure 126: Vortex circulation (left) and peak vorticity (right) at the three measurement planes. Absolute peak vorticity is plotted for the negatively rotating right vortex.

9.2.3 Turbulence characteristics

In this section the measured Re stresses $\overline{u_i' u_j'}$ (negative sign not included unless otherwise stated) are presented along with computed Re stress production terms and Turbulent Kinetic Energy (TKE). Figure 127 and Figure 128 show the contours of the Re stresses on all planes while the remaining figures discuss their correlation with production.

The discussion indentifies the following mechanisms, in accordance with previous investigations. Downstream of the VGs, initially strong turbulent momentum transpot takes place across the "omega" shaped U shear layer (signified by high values of $\partial U/\partial y$ and $\partial U/\partial z$) and in between the vortices. Further downstream diffusion takes over in which the distributions of the various turbulence quantities get smoother by broadening and reducing their peak values, while keeping their shape. Regions of high normal stresses in all directions are related to velocity grandients. However, excessively high values of the $\overline{v'v'}$ between the two vortices are attributed to vortex wandering which adds to turbulence production.

Reynolds Stresses distribution

Figure 127 shows contours of $\overline{u_i' u_i'}$ on planes A (x/c = 0.6), B (x/c = 0.7), and C (x/c = 0.8). The ω = ω_{max}/2 vorticity isoline for each vortex is also plotted. Starting with plane A, regions of high $\overline{u'u'}$ values unsurprisingly follow the shape of the streamwise velocity shear layer, (see also Figure 124). An area of high $\overline{v'v'}$ is formed at the top region, between the two vortices, with values higher than those of the other normal stresses. Symmetric peaks on the two sides of the z = 0 plane are observed in the $\overline{w'w'}$ contour in agreement with (Mehta & Bradshaw, 1988; Angele & Grewe, 2007). In (Angele & Grewe, 2007) these peaks were linked to vortex wandering.

Indication in this respect was found in the snapshots from the measurements. They confirm that the vortices move in the spanwise direction at times independently towards and away from each other, and at times as a pair in the positive or negative z direction. When the two vortices approach each other the combined upwash between them becomes strong, whereas it is weakened when they move away from each other. Such a movement could give rise to high $\overline{v'v'}$ values at the top region. The $\overline{v'v'}$ peak above the two vortices at the region of outflow was also observed, at a plane closer to the VGs, by (Angele & Muhammad-Klingmann, 2005) who examined counter rotating vortices in an adverse pressure gradient BL flow. Otherwise the regions of high $\overline{u'u'}$ can be connected to the corresponding shear layer defined by $\partial U/\partial y$ and $\partial U/\partial z$ (see discussion on shear stresses).

On plane B, at x/c = 0.7, the shape of $\overline{u'u'}$ and $\overline{v'v'}$ distributions remains the same in form, but peak values are now reduced and their spatial distribution diffused. Values of $\overline{v'v'}$ are no longer the highest amongst the normal Re stresses which are now comparable in magnitude. Unlike the other normal stresses, $\overline{w'w'}$ distribution has changed: the two symmetric peaks give place to a smaller peak in the region of upwash in between the two vortices. As shown latter this is not due to production of $\overline{w'w'}$, which remains small. It is conceivable to attribute the appearance of high $\overline{w'w'}$ values without previous indication, to convection.

On plane C, at x/c = 0.8, normal Re stress distributions are similar to that of plane B, supporting the view that in that region diffusion takes over as the main mechanism. On the contrary the difference in Re stress distributions on plane A and B suggests that vortex interaction and turbulent transport of momentum between the vortices and the underlying flow is still strong in that region.

Contours of the shear Re stresses for all planes are given in Figure 128. Vorticity isolines for $\omega = \omega_{max}/2$ for each vortex are also plotted. The levels of the shear stresses are one order of magnitude smaller as compared to the normal stresses.

Starting again with plane A, negative $\overline{u'v'}$ values follow the top part of the U shear layer while along the outer part of the "omega" shaped shear layer u'w' takes over. Positive $\overline{u'v'}$ values at approximately z/h = ±1, also follow the shape of the shear layer, however, change sign due to its orientation. Both $\overline{u'w'}$ and $\overline{v'w'}$ have antisymmetric distributions, as expected. The overall structure is similar to the results presented in (Mehta & Bradshaw, 1988).

On plane B the region of negative $\overline{u'v'}$ that bridges the two vortices has grown while positive values are hardly visible, as the streamwise velocity shear layer is now smoothed. Also $\overline{u'w'}$ and $\overline{v'w'}$, appear significantly diffused. Regions of high $\overline{v'w'}$ values are now concentrated inside the vortices indicating the end of strong turbulent transport across the outer shear of the vortex pair. Contours on plane C are very similar to those on plane B, only more diffused.

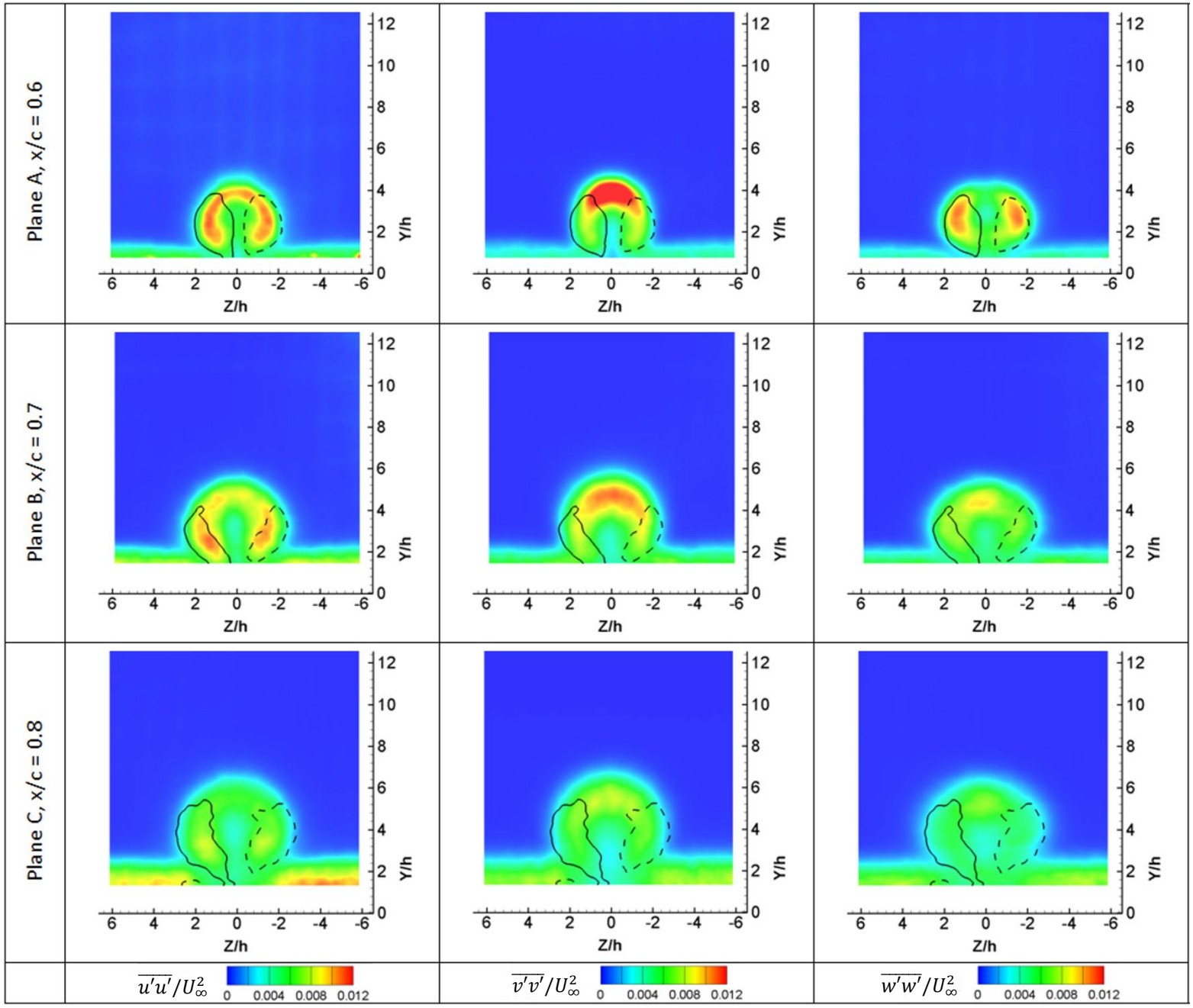

Figure 127: Normal Re stresses contours. Vorticity isolines for $\omega = \omega_{max}/2$ for each vortex are also plotted. The wing surface is always at y/h = 0 and z/h = 0 is the centreline between the two VGs.

Left Column: $\overline{u'u'}/U_\infty^2$ contours;

Central Column: $\overline{v'v'}/U_\infty^2$ contours;

Right Column: $\overline{w'w'}/U_\infty^2$ contours;

Top row: Plane A, x/c = 0.6 or Δx = 27.2h;

Middle row: Plane B, x/c = 0.7 or Δx = 37.2h;

Bottom row: Plane C, x/c = 0.8 or Δx = 47.2h;

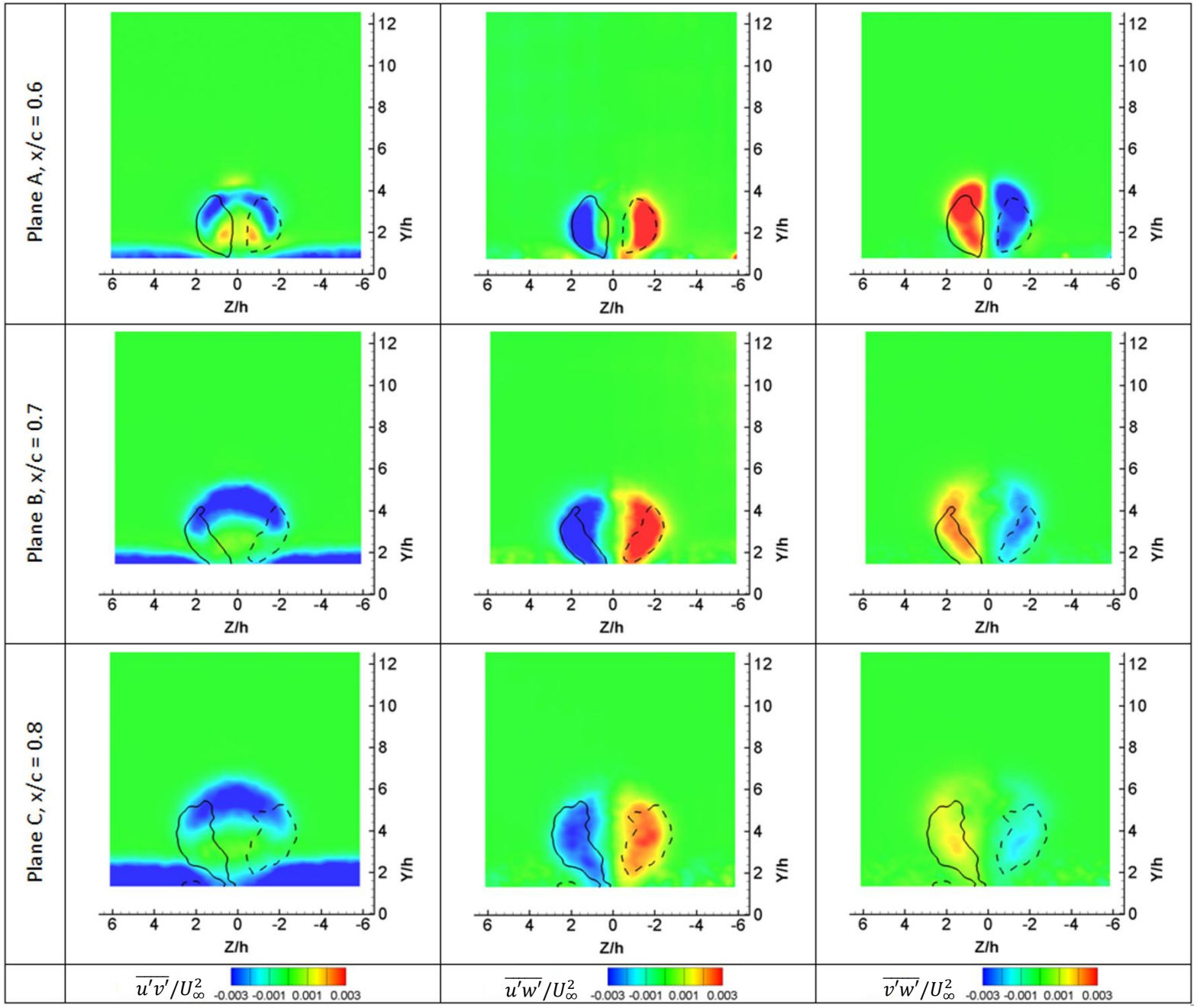

Figure 128: Shear Re stresses contours. Vorticity isolines for $\omega = \omega_{max}/2$ for each vortex are also plotted. The wing surface is always at y/h = 0 and z/h = 0 is the centreline between the two VGs.

Left Column: $\overline{u'v'}/U_\infty^2$ contours;

Central Column: $\overline{u'w'}/U_\infty^2$ contours;

Right Column: $\overline{v'w'}/U_\infty^2$ contours;

Top row: Plane A, x/c = 0.6 or Δx = 27.2h;

Middle row: Plane B, x/c = 0.7 or Δx = 37.2h;

Bottom row: Plane C, x/c = 0.8 or Δx = 47.2h;

Relation to mean flow gradients

In order to examine the relation between the mean flow gradients, Re stress production and Re stresses, their variation along vertical and horizontal lines is presented and discussed. The lines are shown graphically in Figure 129 and their exact positions are given in Table 9, below. Figure 129 also shows contours of the vertical (V) and spanwise (W) mean flow components for reference. Figure 130 to Figure 132 refer to the vertical lines j1, j2, j3 while Figure 133 to Figure 135 refer to the horizontal lines i1, i2, i3. The vertical lines are all taken on the left hand side (LHS) of the measurement planes, as conclusions from both sides are the same. All figures give the U profile along with $\partial U/\partial y$ and $\partial U/\partial z$ side by side with the TKE, normal and shear Re stresses and their production terms $P_{u_i'u_j'}$:

$$P_{u_iu_j} = -\overline{u_i'u_k'}\frac{\partial U_j}{\partial x_k} - \overline{u_j'u_k'}\frac{\partial U_i}{\partial x_k} \qquad (27)$$

In $P_{u_iu_j}$, the x derivatives of the mean flow are considered small in comparison with the vertical and spanwise variations of the flow and are omitted.

Plane		A	B	C
Chordwise position (x/c)		0.6	0.7	0.8
Distance form VG TE ((x-x_{VG})/h)		27.2	37.2	47.2
Vertical lines spanwise location (z/h)	j1, *"between the two vortices"*	0.0	0.0	0.0
	j2, "*through the vortex centres*"	1.3	1.5	1.7
	j3, "*left of the LHS vortex*"	2.6	3.0	3.4
Horizontal lines distance from the wing surface (y/h)	i1, "*top part of the BL*"	1.0	1.8	2.4
	i2, "*through the vortices*"	1.8	2.3	3.1
	i3, "*top part of the vortex pair*"	3.9	5.0	6.4

Table 9: Details of the lines along which data are plotted in Figure 130 to Figure 135.

Starting with line j1 (between the two vortices, Figure 130), the U profile is found to have double peaks, on all planes. This is due to the high velocity fluid entrained by the vortices inside the boundary layer. The upper part of the flow, i.e. higher than the first U peak, is dominated by the strong peak in $\partial U/\partial y$ which is present in all three planes. TKE, P_{vv}, P_{uv}, $\overline{v'v'}$ and $\overline{u'v'}$ also peak at max $\partial U/\partial y$ in agreement with the results of (Angele & Muhammad-Klingmann, 2005) where the effect of streamwise vortices on a separating BL was studied.

In plane A, P_{vv} is the highest normal stress production term, due to vortex wandering as explained earlier. In planes B and C, on the other hand, where diffusion is dominant P_{uu} and P_{vv} are comparable. In the region of peak $\partial U/\partial y$, negative P_{ww} is connected to local positive $\partial W/\partial z$ (not shown here for the sake of readability of the plots) which is due to VG model asymmetry. $\partial U/\partial z$ remains small and deviations from zero are attributed to model imperfections and remain present in all planes.

As the curved wing surface is approached on plane A, i.e. lower than the first U peak, not only $\overline{v'v'}$ but also $\overline{u'u'}$ tend to zero faster than $\overline{w'w'}$ while in the other two planes a rather balanced distribution is seen. Relatively high values of $\overline{w'w'}$ in the lower part of the BL show

activity, while the relevant production and the gradients of W (not shown here) in this region remain negligible. Therefore, this activity could be attributed to convection. Negative P_{vv} on plane A is connected to the inflection point in the U profile.

Along the line through the vortex centre (line j2, Figure 131), both of the U gradients are important. P_{vv} and P_{uv} and the corresponding Re stresses remain correlated to $\partial U/\partial y$ as Figure 131 shows for all measured planes. This is in agreement with (Liu et al., 1996) where the mean velocity deficit was found to have an important effect on the distribution of $\overline{u'v'}$ in the vortex core. TKE, $\overline{u'u'}$ and $\overline{w'w'}$ appear to correlate with $\partial U/\partial z$ at this station, in agreement with (Angele & Muhammad-Klingmann, 2005). P_{vw} and $\overline{v'w'}$ follow the variation of $\partial V/\partial z$ (not shown here). An indication on the variation of V and W on all planes can be drawn from Figure 129 contours.

At the left side of the LHS vortex (line j3, Figure 132), the flow is less affected by the three-dimensionality of the vortical flow and the Re stress distribution resembles that of a turbulent BL (Pope, 2000). There is small indication of the presence of the VG vortices in the U profile which is associated to the small bump in the k distribution, indicated by vectors in Figure 132. All activity is at y/h < 3. $\partial U/\partial y$ is strong and combined with strong but balanced normal Re stresses and negative $\overline{u'v'}$ Re stress. The variation in $\partial U/\partial z$ remains small and the same holds for the corresponding stresses and production terms.

Figure 133 shows the variation of the turbulence quantities along the horizontal line i1, inside the BL. The position of line i1 is defined by the height at which the local streamwise velocity, at the region outside the "omega" shape of the vortex pair, is approximately 0.8 times the local free stream velocity. The graphs show that outside the area that is affected by the vortices, P_{uv} is negative and P_{ww} is practically zero, as expected in a turbulent BL. P_{vv} on the other hand, takes positive values due to surface curvature. P_{vv} is reduced in the vortex region due to an increase in $\partial V/\partial y$ (not shown here) and P_{uv} tends to zero as $\partial U/\partial y$ decreases. The normal stresses peak at the location of the strongest velocity shear of their respective mean velocity components in agreement with (LöGdberg et al., 2009) while they remain comparable in magnitude. On all planes, $\overline{u'w'}$ and P_{uw} show strong negative correlation with $\partial U/\partial z$, in agreement with (Angele & Muhammad-Klingmann, 2005). In comparison to the profiles at a greater distance from the wing surface (line i2, Figure 134 and line i3, Figure 135), data from inside the BL are more noisy and the effect from the vortices is not as pronounced.

Moving higher from the wing surface (line i2, Figure 134), along the horizontal line passing through the vortex centres, the correlation between P_{uu}, P_{uw} and the respective Re stresses with $\partial U/\partial z$ is still strong. Also P_{uv} negatively correlates with $\partial U/\partial y$ notably on plane A. By comparing the shear stress distributions amongst the three planes, it follows that changes in shape are found between the first two planes while between planes B and C the distribution is basically smoothened indicating the dominance of diffusion.

Just on top of the vortex pair (line i3, Figure 135), on plane A, production is dominated by high values of P_{vv} and P_{uv}, both correlated to $\partial U/\partial y$. P_{vv} is indeed very strong and so is $\overline{v'v'}$. This is attributed to the spanwise movement of the vortices as already discussed while

the negative correlation of $\partial U/\partial y$ with $\overline{u'v'}$ is related to turbulent transport through the U shear layer. On plane B, P_{vv} and P_{uu} get even and the contribution of the normal stresses in TKE is more balanced. On all three planes, P_{uw} follows $\partial U/\partial z$ while P_{vw} follows $\partial V/\partial z$ (not shown here). As in the previous horizontal lines, passage from plane B to C is dominated by diffusion.

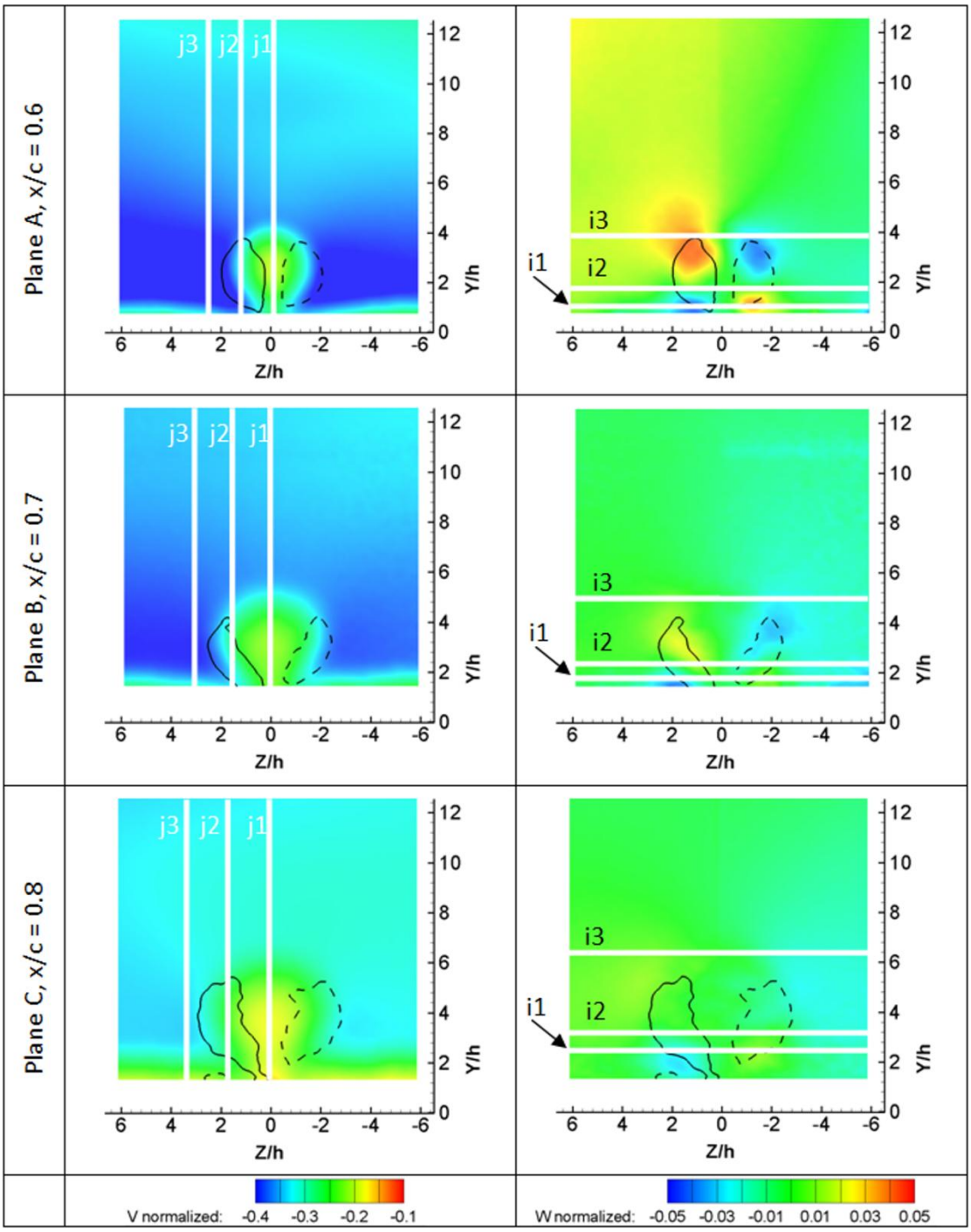

Figure 129: (Left Column) Normalized vertical velocity (V) contours. (Right Column) Normalized spanwise velocity (W) contours. Vorticity isolines for ω = ω_{max}/2 for each vortex are also plotted. Top, middle and bottom row correspond to plane A (x/c = 0.6 or Δx = 27.2h), B (x/c = 0.7 or Δx = 37.2h) and plane C (x/c = 0.8 or Δx = 47.2h), respectively. The wing surface is always at y/h = 0 and z/h = 0 is the centreline between the two VGs. Thick white cuts indicate the lines along which data are plotted in Figure 130 to Figure 135. The exact positions of the lines/cuts are given in Table 9.

Between the two vortices (centre of the VG pair)

Plane A, x/c = 0.6

Plane B, x/c = 0.7

Plane C, x/c = 0.8

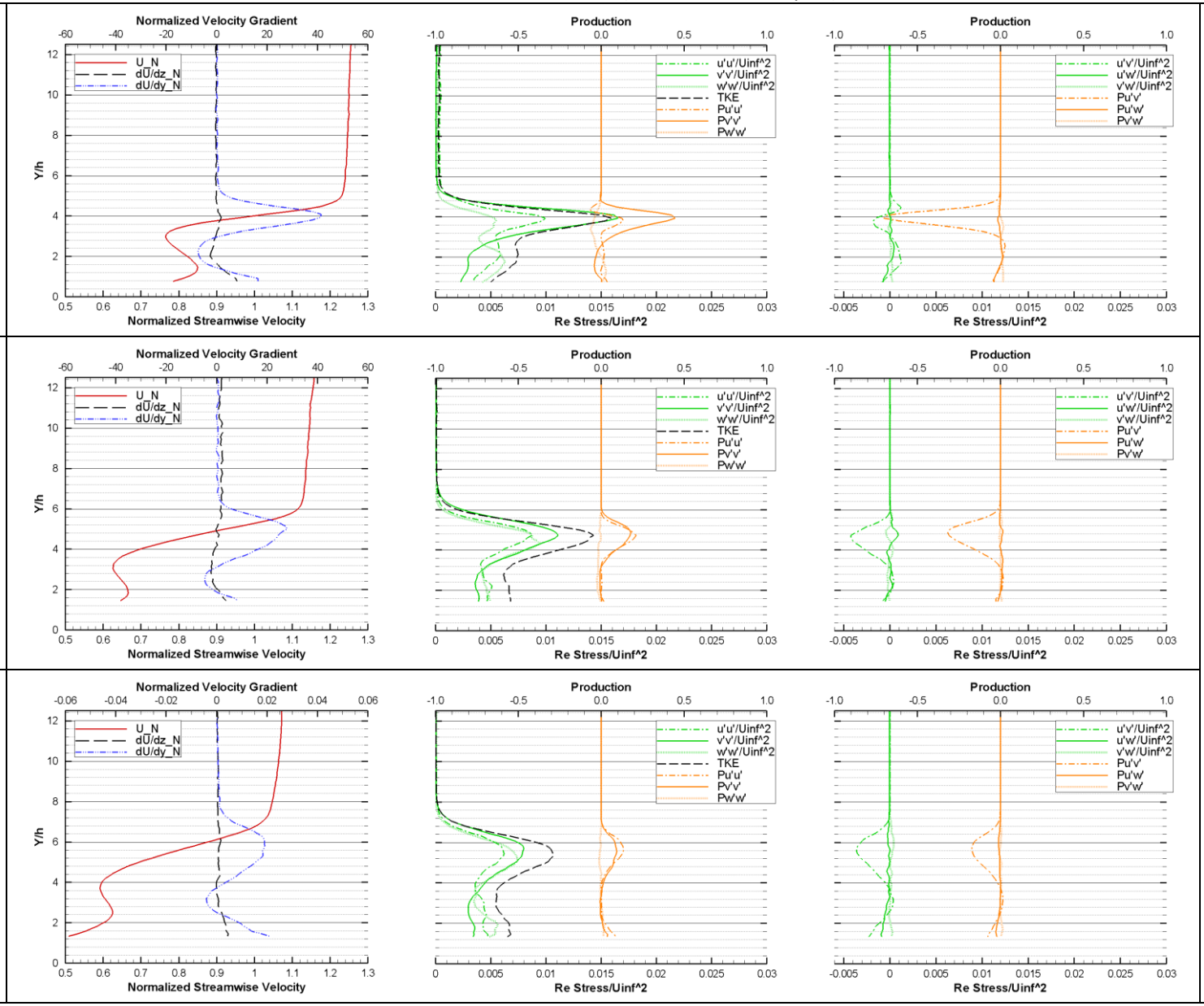

Figure 130: Profiles along line j1, defined in Figure 129.

Top row: Plane A, x/c = 0.6 or Δx = 27.2h;

Middle row: Plane B, x/c = 0.7 or Δx = 37.2h;

Bottom row: Plane C, x/c = 0.8 or Δx = 47.2h;

Left Column: Normalized streamwise velocity, ∂U/∂y and ∂U/∂z;

Central Column: TKE, normal Re stresses and production terms;

Right Column: Shear Re stresses and production terms.

Through the LHS vortex centre

Plane A, x/c = 0.6

Plane B, x/c = 0.7

Plane C, x/c = 0.8

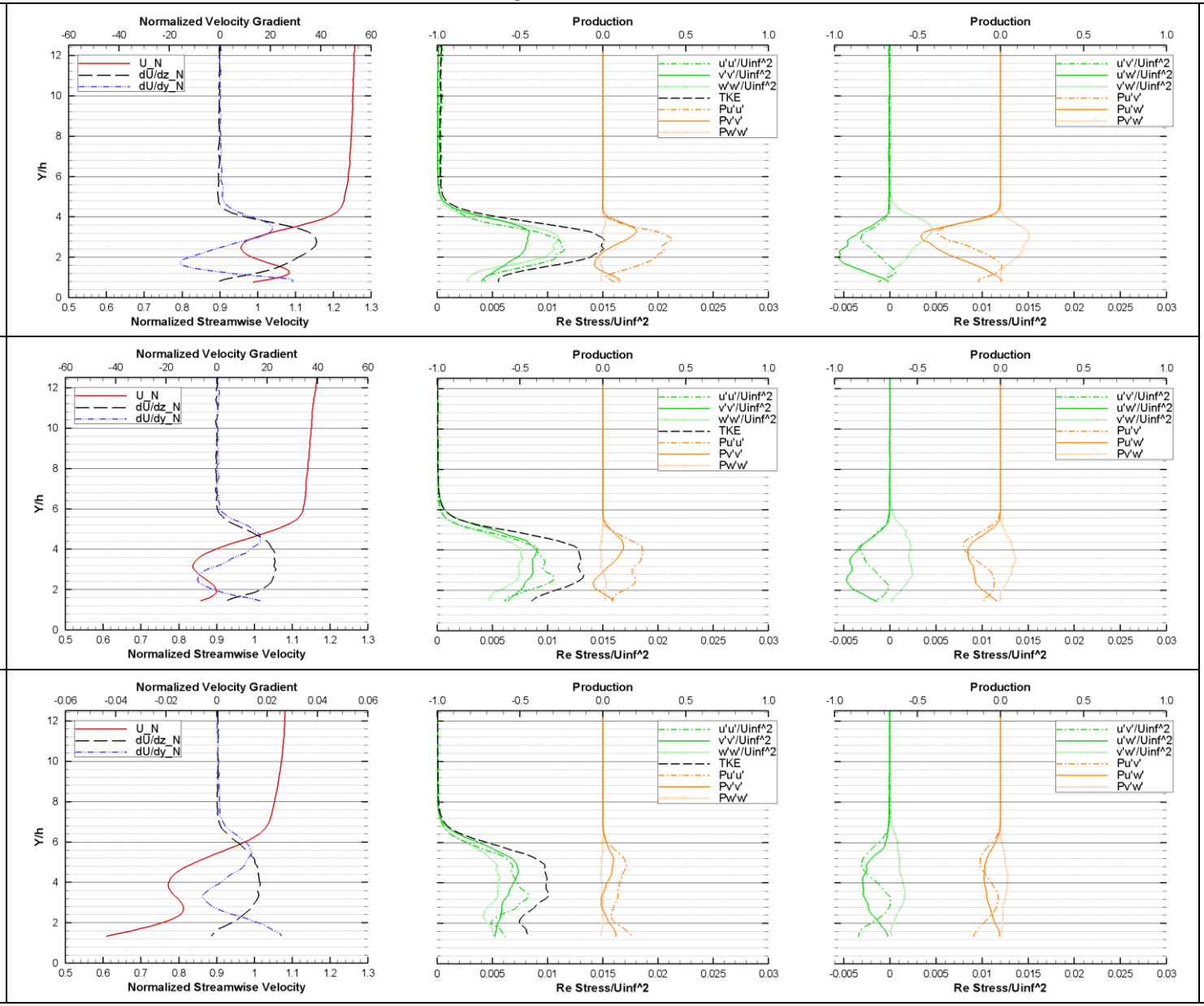

Figure 131: Profiles along line j2, defined in Figure 129.

Top row: Plane A, x/c = 0.6 or Δx = 27.2h;

Middle row: Plane B, x/c = 0.7 or Δx = 37.2h;

Bottom row: Plane C, x/c = 0.8 or Δx = 47.2h;

Left Column: Normalized streamwise velocity, ∂U/∂y and ∂U/∂z;

Central Column: TKE, normal Re stresses and production terms;

Right Column: Shear Re stresses and production terms.

At the side of the LHS vortex

Plane A, x/c = 0.6

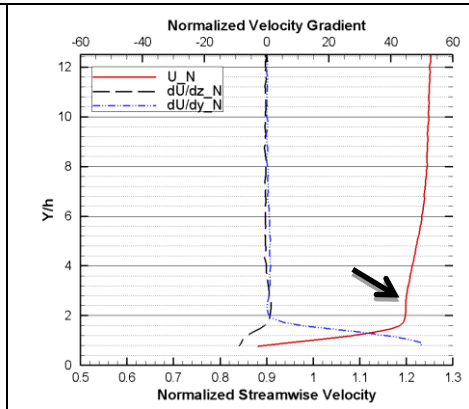

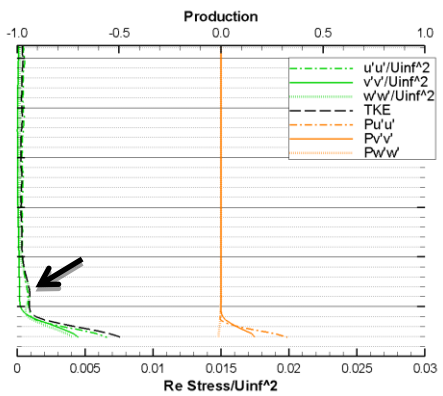

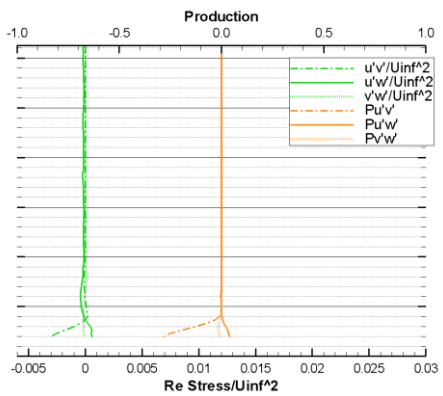

Plane B, x/c = 0.7

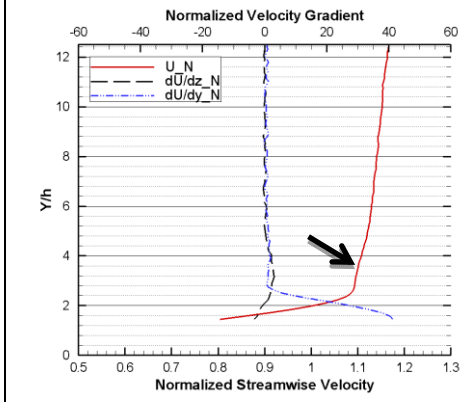

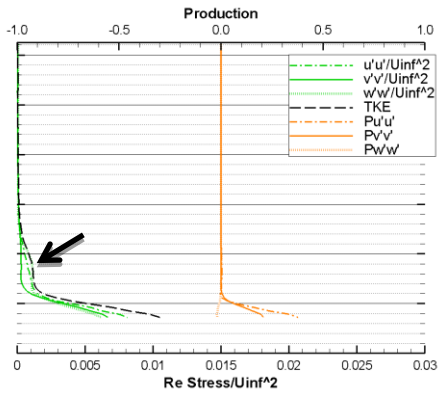

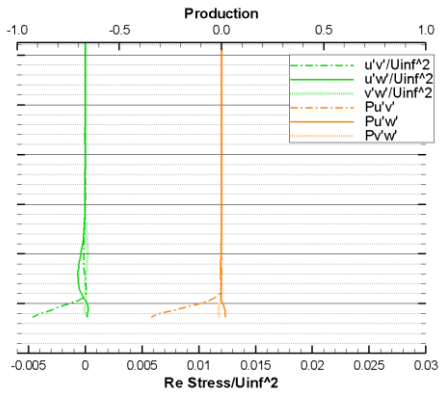

Plane C, x/c = 0.8

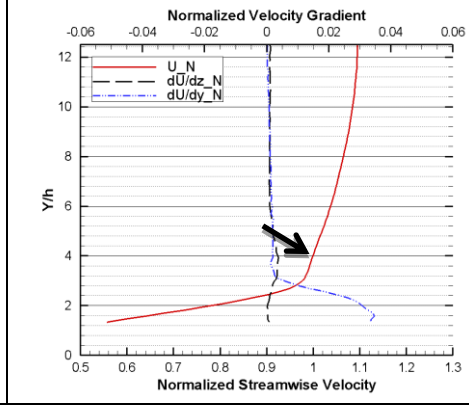

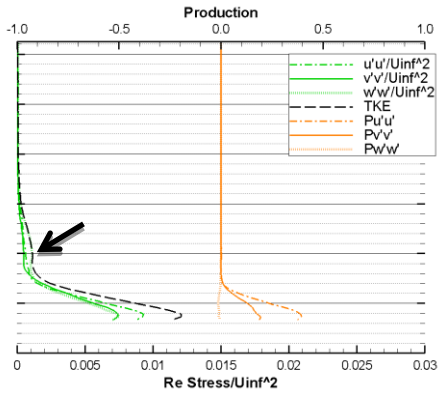

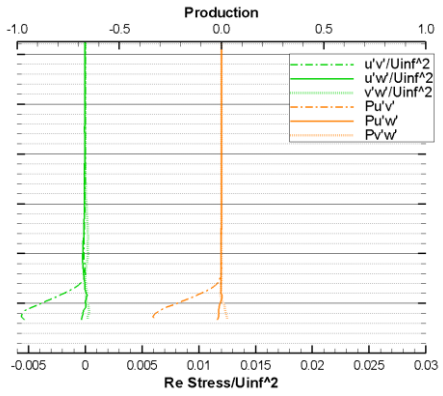

Figure 132: Profiles along line j3, defined in Figure 129.

Top row: Plane A, x/c = 0.6 or Δx = 27.2h;

Middle row: Plane B, x/c = 0.7 or Δx = 37.2h;

Bottom row: Plane C, x/c = 0.8 or Δx = 47.2h;

Left Column: Normalized streamwise velocity, ∂U/∂y and ∂U/∂z;

Central Column: TKE, normal Re stresses and production terms;

Right Column: Shear Re stresses and production terms.

Vectors indicate a "kick" in the profiles, sign of the vortex effect.

	Top part of the BL	
Plane A, x/c = 0.6	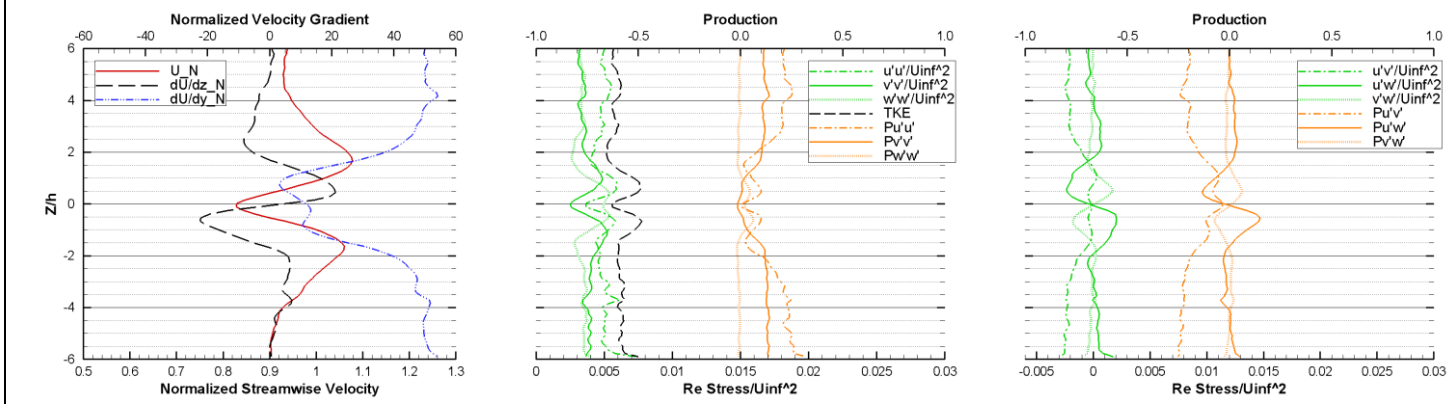	**Figure 133: Profiles along line i1, defined in Figure 129.** **Top row: Plane A, x/c = 0.6 or Δx = 27.2h;** **Middle row: Plane B, x/c = 0.7 or Δx = 37.2h;** **Bottom row: Plane C, x/c = 0.8 or Δx = 47.2h;** **Left Column: Normalized streamwise velocity, ∂U/∂y and ∂U/∂z;** **Central Column: TKE, normal Re stresses and production terms;** **Right Column: Shear Re stresses and production terms**
Plane B, x/c = 0.7	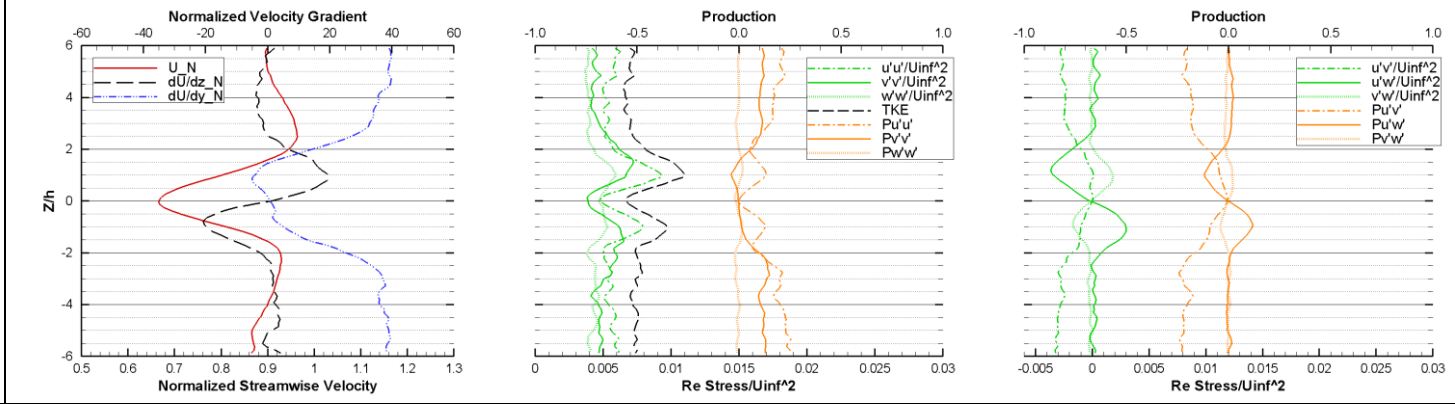	
Plane C, x/c = 0.8	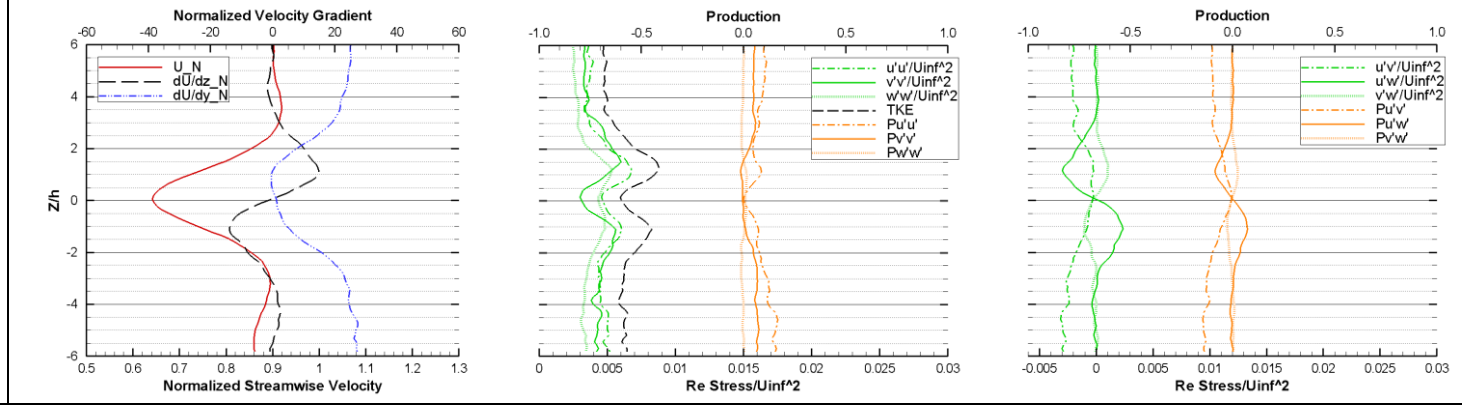	

Through the vortex centres

Plane A, x/c = 0.6

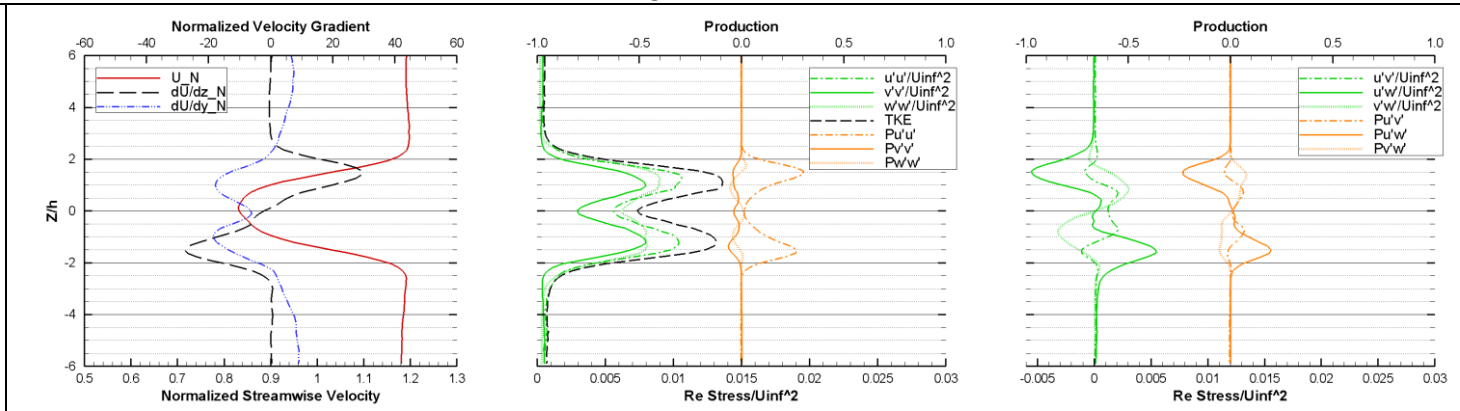

Plane B, x/c = 0.7

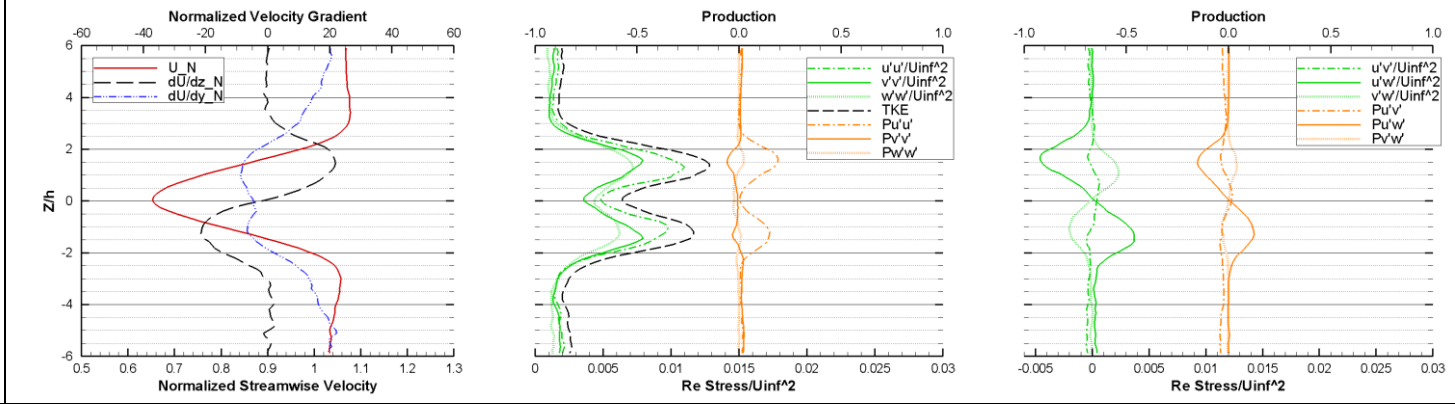

Plane C, x/c = 0.8

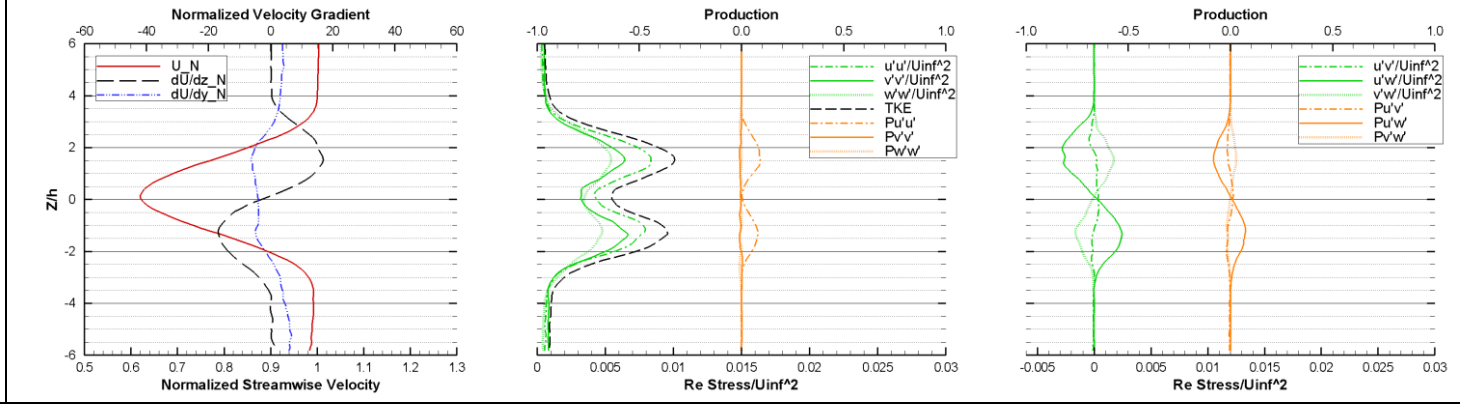

Figure 134: Profiles along line i2, defined in Figure 129.

Top row: Plane A, x/c = 0.6 or Δx = 27.2h;

Middle row: Plane B, x/c = 0.7 or Δx = 37.2h;

Bottom row: Plane C, x/c = 0.8 or Δx = 47.2h;

Left Column: Normalized streamwise velocity, ∂U/∂y and ∂U/∂z;

Central Column: TKE, normal Re stresses and production terms;

Right Column: Shear Re stresses and production terms.

Top part of the vortex pair

Plane A, x/c = 0.6

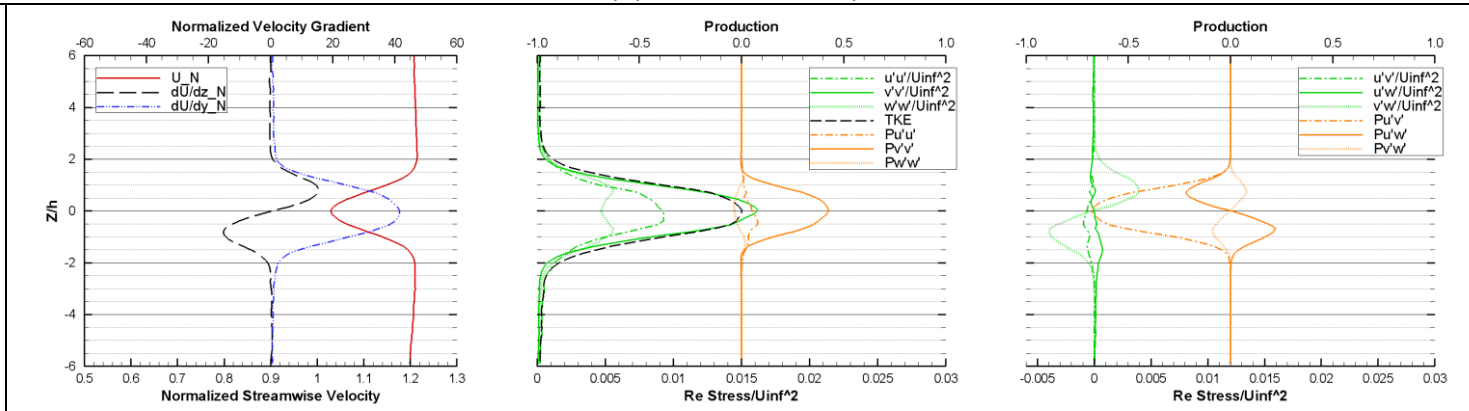

Plane B, x/c = 0.7

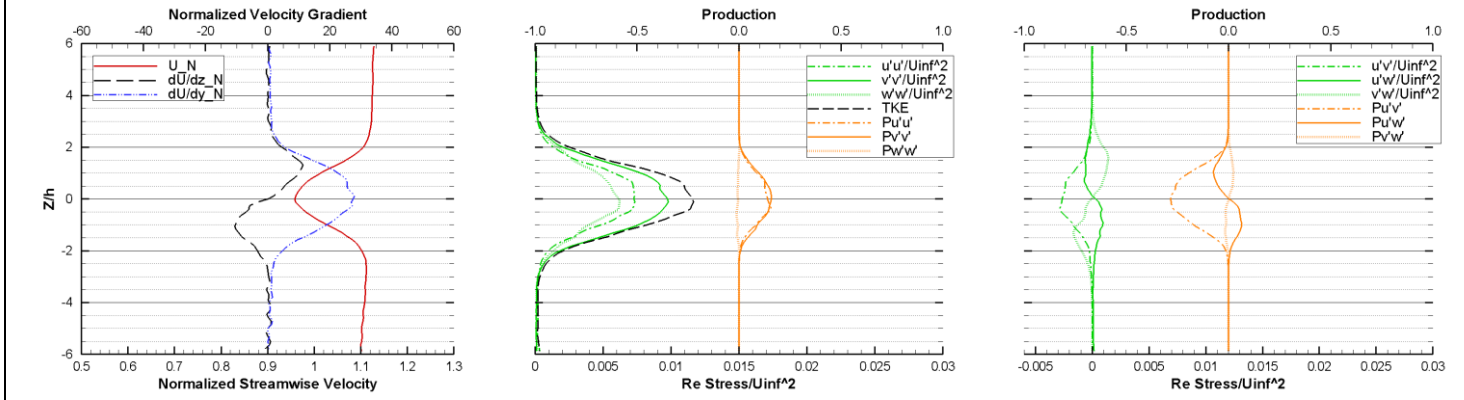

Plane C, x/c = 0.8

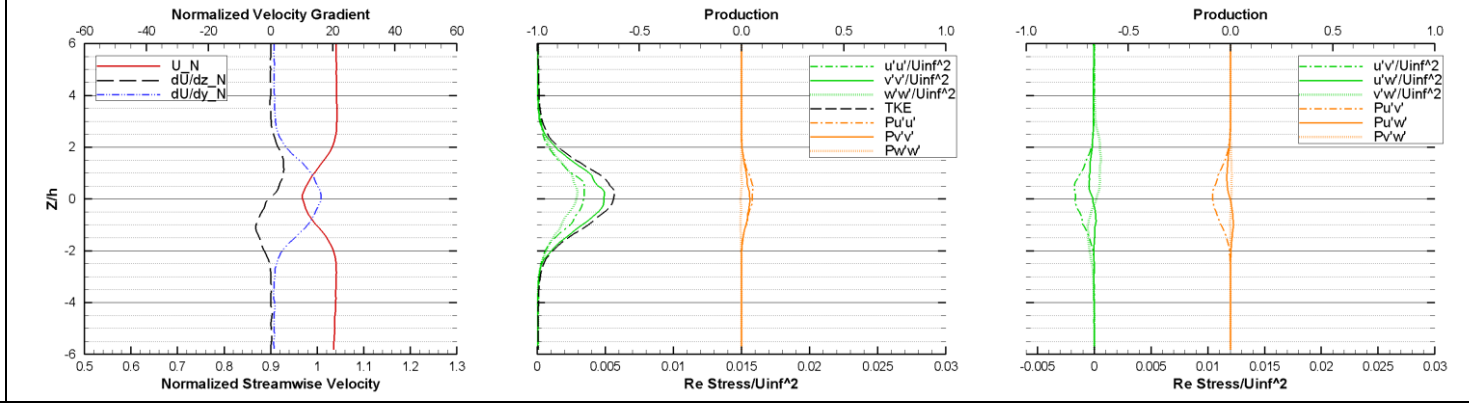

Figure 135: Profiles along line i3, defined in Figure 129.

Top row: Plane A, x/c = 0.6 or Δx = 27.2h;

Middle row: Plane B, x/c = 0.7 or Δx = 37.2h;

Bottom row: Plane C, x/c = 0.8 or Δx = 47.2h;

Left Column: Normalized streamwise velocity, ∂U/∂y and ∂U/∂z;

Central Column: TKE, normal Re stresses and production terms;

Right Column: Shear Re stresses and production terms.

9.2.4 Comparison with CFD data

It is widely accepted (Lin, 2002; Yao et al., 2002; Allan et al., 2002) that RANS simulations using eddy viscosity models are not expected to accurately predict the highly 3D anisotropic flow downstream of the VGs. Simulations tend to overpredict vortex diffusion and circulation decay. The results presented in this paragraph agree with these observations.

Figure 136 shows streamwise velocity (left) and vorticity (right) contours on planes A, B and C from the Stereo PIV data presented in the present chapter side by side with CFD data from the computations presented in the previous chapter. Vorticity isolines are also drawn, for $\omega = \omega_{max}/2$, where ω_{max} is the peak vorticity value for each vortex on each plane. Although there is good qualitative agreement as far as the vortex evolution is concerned, quantitative differences in the flow details are observed.

In simulations, as expected, the tip vortices have consistently smaller peak vorticity while the vortices appear wider and decay faster than in the experiments. Underestimation of peak vorticity has important effects on the evolution of the flow; in particular the upwash is weaker so the region of retarded streamwise velocity is smaller and the deficit itself is not as pronounced in the measurements. In this respect it could be added that fully resolving the VG would not significantly improve the accuracy of the simulation (Dudek, 2011; Chrisokentis, 2013). So, regarding CFD simulations, the essential inadequacy of eddy viscosity modelling in reproducing the details of this type of flow is reconfirmed.

9.3 Summary

The effect of passive vortex generators on the performance of a wing exhibiting three-dimensional separation of the “stall-cell” type was investigated on the basis of wind tunnel measurements. Counter-rotating triangular vanes with common flow up have been used. The reported data are Stereo PIV measurements at three chordwise stations positioned at 27.2, 37.2 and 47.2 VG heights downstream of the VG TE.

In general terms, the interpretation of the flow structure on the basis of Stereo PIV data is in agreement with previous studies conducted on flat plates with or without pressure gradient. For the space range considered, the averaged data show that the VG vortices grow in size and move away from each other and the wing surface as they move downstream. The mean streamwise velocity profile has a double peak due to the high velocity flow being entrained by the VG vortices close to the wing surface.

Mean flow velocity gradients are well correlated to regions of intense turbulent transport as denoted by high Re stresses and supported by the examination of the corresponding production terms. Regions of high normal Re stresses are well correlated to regions of high mean flow shear, while excessively strong $\overline{v'v'}$ indicates spanwise wandering of the vortices (the history of snapshots favours such an interpretation). Shear stresses are concentrated in regions of intense turbulent transport across the shear layers.

The combined conclusion (from vortex strength, vorticity contours and turbulence profiles) is that at the most upstream measurement plane, turbulent transport between the VG vortices and the underlying flow is strong, while from the second plane to the third diffusion becomes the main mechanism that governs the flow.

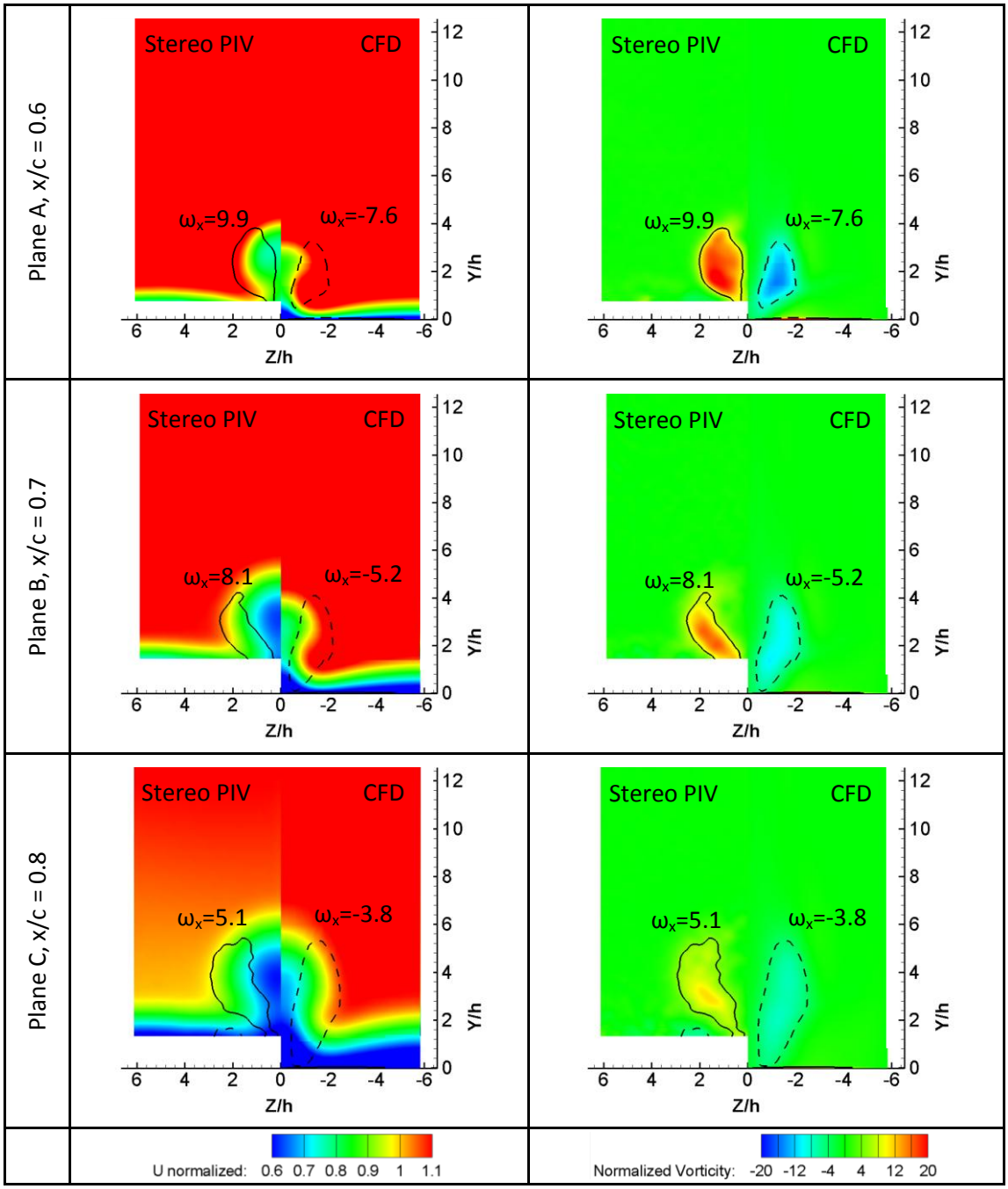

Figure 136: (Left Column) Normalized streamwise velocity contours. (Right Column) Normalized vorticity contours. Vorticity isolines for ω = ω_{max}/2 for each vortex are also plotted. Top, middle and bottom row correspond to plane A (x/c = 0.6, Δx = 27.2h), B (x/c = 0.7, Δx = 37.2h) and plane C (x/c = 0.8, Δx = 47.2h), respectively. The wing surface is always at y/h = 0 and z/h = 0 is the centreline between the two VGs. Positive z values show Stereo PIV data while negative z values show CFD data.

Part IV.

Conclusions

10 Conclusions and suggestions for future work

10.1 Conclusions

In the course of the present study 3D separation of the Stall Cell type on a rectangular wing was studied. In addition, the possibility of separation control using passive vortex generators was examined and the resulting flow was investigated.

Tuft flow visualization experiments confirmed the dynamic nature of the SCs. For the Reynolds numbers considered SCs move in the spanwise direction and can form/disappear in a seemingly random manner. The inherently unstable flow can be stabilized by means of a localized disturbance in the form of a ZZ tape located at the centre of the wing span. The resulting single stable SC has the same amount of separated flow for high enough angles of attack and for Re numbers ranging from $0.5x10^6$ to $1.5x10^6$. This stabilized SC was further investigated.

A computational study of the phenomenon using RANS simulations produced results in good qualitative agreement with the experimental data. The CFD data revealed the complex vortical structure of the time averaged flow inside a Stall Cell. Three different types of vortices exist which strongly interact with each other:

a. The two counter rotating SC vortices that start normal to the wing surface within the separation line and extend downstream.
b. The Separation Line Vortex that runs along the wing span. This vortex grows at the centre of the SC due to its interaction with the SC vortices and extends at the sides of the SC parallel to the wing TE.
c. The Trailing Edge Line Vortex that also grows inside the SC and runs parallel to the wing TE outside of it, but has vorticity of opposite sign compared to the SLV.

The turbulence characteristics of the flow inside the SC are highly anisotropic as the Stereo PIV study of the flow shows. The fact that computational results obtained using an eddy viscosity model provide a correct qualitative description of the Re averaged flow implies that turbulence detailed characteristics do not define the development of the averaged flow, once a SC is formed, and that SC formation is mainly affected by vorticity transport and deformation in scales larger than those characterizing turbulence. Based on the combined results a SC generation mechanism is suggested.

RANS simulations and experiments were combined to optimize a passive vortex generator configuration for 3D separation control. Counter rotating triangular vanes were used and experiments show the formation of SCs is delayed for 5° and Cl_{max} is increased by 44% when VGs are located at x/c = 0.3. A flow bifurcation is detected at α = 16° where the flow alternates between a mostly attached and a highly separated state. Flow hysteresis is observed when the VGs are located at x/c = 0.4 and the SC engulfs the VGs at higher angles of attack.

Stereo PIV study of the vortex generator induced flow revealed that the VG vortices grow in size and move away from each other and the wing surface as they move downstream. Regions of high normal Reynolds stresses are well correlated to regions of high mean flow

shear, while excessively strong $\overline{v'v'}$ is linked to spanwise vortex wandering. Turbulent interaction between the VG vortices and the underlying flow is strong closer to the VGs while further downstream diffusion becomes the main mechanism that governs the flow.

The present investigation comes in support of previous studies (e.g. (Fuglsang & Bove, 2008)) that highlighted the need to be cautious when using wind tunnel data, especially in the post stall region. The widely used assumption of 2D flow over a 2D airfoil set up is not valid when Stall Cells form. For the correct interpretation of experimental data it is vital to know how the tests were carried and what state of the flow was actually measured. Furthermore, the three-dimensionality of the separated flow should be taken into account when it comes to separation control.

10.2 Suggestions for future work

Many fields remain open regarding our understanding of three-dimensional separation and specifically Stall Cells. For example the vortical structure of a single Stall Cell is now better understood, however, the interaction between adjacent Stall Cells remains unclear. Furthermore, it is not yet clear whether a Stall Cell would form or how it would behave on a rotating wing. The Stall Cell formation hypothesis suggested in the present report also remains to be confirmed.

With regard to separation control the mechanisms that lead to flow bifurcation and hysteresis should be further investigated. It would also be interesting to examine the flow both closer to the vortex generators, where vortex interaction appears stronger, and further downstream, beyond the wing trailing edge, where the vortices leave the wing surface and meet the wake shear layer.

As far as the means to conduct further investigations are concerned, different methods could be used in addition to the ones already applied. Time resolved PIV combined with simultaneous pressure and force measurements could reveal a lot about the unstable features of both Stall Cells and vortex generator induced flow. Also volumetric PIV could increase our confidence regarding the description of vortical structures and their interaction.

The computational approach to the issue of 3D separation and separation control could be expanded to methods that are less simplifying than eddy viscosity RANS computations, such as Detached Eddy Simulations or Large Eddy Simulations. The unsteady flow features of the phenomenon could then be better investigated. It is also possible that a 3D vortex particle simulation could reveal more about the Stall Cell vortex interaction and formation mechanism.

References

Aider, J.-L., Beaudoin, J.-F., & Wesfreid, J. E. (2009). Drag and lift reduction of a 3D bluff-body using active vortex generators. *Experiments in Fluids, 48*(5), 771-789. doi: 10.1007/s00348-009-0770-y

Allan, B. G., Yao, C.-S., & Lin, J. C. (2002). Numerical simulations of vortex generator vanes and jets on a flat plate. *AIAA Paper, 3160*.

Angele, K. P., & Grewe, F. (2007). Instantaneous Behavior of Streamwise Vortices for Turbulent Boundary Layer Separation Control. *Journal of Fluids Engineering, 129*(2). doi: 10.1115/1.2409327

Angele, K. P., & Muhammad-Klingmann, B. (2005). The effect of streamwise vortices on the turbulence structure of a separating boundary layer. *European Journal of Mechanics - B/Fluids, 24*(5), 539-554. doi: 10.1016/j.euromechflu.2005.01.005

Ashill, P. R., Fulker, J. L., & Hackett, K. C. (2001). Research at DERA on sub-boundary layer vortexgenerator s (SBVGs). *AIAA Paper, 887*.

Barlow, J. B., Rae, W. H., & Pope, A. (1999). *Low-speed wind tunnel testing*. New York: John Wiley & Sons.

Bender, E. E., Anderson, B. H., & Yagle, P. J. (1999). Vortex generator modeling for Navier-Stokes codes. *ASME Paper FEDSM99-6919*.

Bertagnolio, F., Sørensen, N., & Rasmussen, F. (2005). New Insight Into the Flow Around a Wind Turbine Airfoil Section. *Journal of Solar Energy Engineering, 127*(2). doi: 10.1115/1.1861927

Bertagnolio, F., Sørensen, N. N., & Johansen, J. (2006). Profile catalogue for airfoil sections based on 3D computations. *Risø-R-1581*.

Bian, S., Ceccio, S. L., & Driscoll, J. F. (2009). A dual-camera cinematographic PIV measurement system at kilohertz frame rate for high-speed, unsteady flows. *Experiments in Fluids, 48*(3), 487-495. doi: 10.1007/s00348-009-0753-z

Boermans, L. (2006). Research on sailplane aerodynamics at Delft University of Technology. Recent and present developments. *Netherlands Association of Aeronautical Engineers NVvL, 1*.

Bragg, M. B., & Gregorek, G. M. (1987). Experimental study of airfoil performance with vortex generators. *Journal of Aircraft, 24*(5), 305-309. doi: 10.2514/3.45445

Braslow, A., & Knox, E. (1958). Simplified Method for Determination of Critical Height of Distributed Roughness Particles for Boundary-Layer Transition at Mach Numbers from 0 to 5. Washington: NACA.

Bremner, D. M., Hutcheson, F. V., & Stead, D. J. (2005). Methodology for the Elimination of Reflection and System Vibration Effects in Particle Image Velocimetry Data processing. *NASA/TM-2005-213257; L-19028*

Broeren, A. P., & Bragg, M. B. (2001). Spanwise Variation in the Unsteady Stalling Flowfields of Two-Dimensional Airfoil Models. *AIAA Journal, 39*(9), 1451-1461.

Chang, P. K. (1976). *Control of flow separation: Energy conservation, operational efficiency, and safety*. Washington D. C.: Hemisphere Publishing Corp.

Chrisokentis, G. (2013). *Analysis of the aerodynamic behavior of vortex generators using computational fluid dynamics methods.* Mechanical Engineering Graduate Thesis, National Technical University of Athens, Athens.

Christensen, K. T. (2004). The influence of peak-locking errors on turbulence statistics computed from PIV ensembles. *Experiments in Fluids, 36*(3), 484-497. doi: 10.1007/s00348-003-0754-2

Coles, D., & Wadcock, A. J. (1979). Flying-hot-wire study of flow past an NACA 4412 airfoil at maximum lift. *AIAA Journal, 17*(4), 321-329.

Crow, S. C. (1970). Stability theory for a pair of trailing vortices. *AIAA Journal, 8*(12), 2172-2179. doi: 10.2514/3.6083

DiOttavio, J., Watson, K., Cormey, J., Komerath, N., & Kondor, S. (2008). *Discrete structures in the radial flow over a rotor blade in dynamic stall.* Paper presented at the Proceedings of the 26th applied aerodynamics conference, AIAA, Honolulu, Hawaii, USA.

Dossing, M. (2008). High frequency microphone measurements for transition detection on airfoils. *Risø-R-1645*.

Drela, M. (1989). XFOIL: An Analysis and Design System for Low Reynolds Number Airfoils. In T. J. Mueller (Ed.), *Low Reynolds Number Aerodynamics* (Vol. 54, pp. 1-12). NY, US: Springer-Verlag.

Dropkin, A., Custodio, D., Henoch, C. W., & Johari, H. (2012). Computation of Flow Field Around an Airfoil with Leading-Edge Protuberances. *Journal of Aircraft, 49*(5), 1345-1355. doi: 10.2514/1.c031675

Dudek, J. C. (2006). Empirical Model for Vane-Type Vortex Generators in a Navier-Stokes Code. *AIAA Journal, 44*(8), 1779-1789. doi: 10.2514/1.20141

Dudek, J. C. (2011). Modeling vortex generators in a Navier-Stokes code. *AIAA Journal, 49*(4), 748-759.

Elimelech, Y., Arieli, R., & Iosilevskii, G. (2012). The three-dimensional transition stages over the NACA-0009 airfoil at Reynolds numbers of several ten thousand. *Physics of Fluids, 24*(2). doi: 10.1063/1.3682377

Elsinga, G. E., & Westerweel, J. (2011). Tomographic-PIV measurement of the flow around a zigzag boundary layer trip. *Experiments in Fluids, 52*(4), 865-876. doi: 10.1007/s00348-011-1153-8

Fish, F. E., & Battle, J. M. (1995). Hydrodynamic design of the humpback whale flipper. *Journal of Morphology, 225*(1), 51-60. doi: 10.1002/jmor.1052250105

Flynn, G. A., Morrison, J. F., & Mabey, D. G. (2001). Buffet Alleviation on Swept and Unswept Wings at High Incidence. *Journal of Aircraft, 38*(2), 368-378. doi: 10.2514/2.2771

Foucaut, J. M., Miliat, B., Perenne, N., & Stanislas, M. (2004). Characterization of different PIV algorithms using the EUROPIV synthetic image generator and real images from a turbulent boundary layer *Particle Image Velocimetry: Recent Improvements* (pp. 163-185): Springer.

Fuglsang, P., Antoniou, I., Dahl, K. S., & Aagaard Madsen, H. (1998). Wind tunnel tests of the FFA-W3-241, FFA-W3-301 and NACA 63-430 airfoils. *Risø-R 1041*.

Fuglsang, P., Bak, C., Gaunaa, M., & Antoniou, I. (2003). Wind tunnel tests of Risø-B1-18 and Risø-B1-24. *Risø-R-1375*.

Fuglsang, P., & Bove, S. (2008). *Wind Tunnel Testing Of Airfoils Involves More Than Just Wall Corrections.* Paper presented at the European Wind Energy Conference.

Gad-el-Hak, M., & Bushnell, D. M. (1991). Separation Control: Review. *Journal of Fluids Engineering, 113*(1). doi: 10.1115/1.2926497

Gleyzes, C., & Capbern, P. (2003). Experimental study of two AIRBUS/ONERA airfoils in near stall conditions. Part I: Boundary layers. *Aerospace Science and Technology, 7*(6), 439-449. doi: 10.1016/s1270-9638(03)00045-2

Godard, G., & Stanislas, M. (2006). Control of a decelerating boundary layer. Part 1: Optimization of passive vortex generators. *Aerospace Science and Technology, 10*(3), 181-191. doi: 10.1016/j.ast.2005.11.007

Goett, H. J. (1939). Experimental Investigation of the Momentum Method for Determining Profile Drag. *NACA T.R. - 660*.

Gregory, N., & O'Reilly, C. L. (1970). Low-speed aerodynamic characteristics of NACA 0012 aerofoil section, including the effects of upper-surface roughness simulating hoar frost *Research & Memoranda - 3726*: Aeronautical Research Council.

Gregory, N., Quincey, V. G., O'Reilly, C. L., & Hall, D. J. (1971). Progress Report on Observations of Three-Dimensional Flow Patterns obtained during Stall

Development on Aerofoils, and on the Problem of Measuring Two-Dimensional Characteristics. *C.P. 1146*: Aeronautical Research Council.

Gresham, N., Wang, Z., & Gursul, I. (2010). Vortex dynamics of free-to-roll slender and nonslender delta wings. *Journal of Aircraft, 47*(1), 292-302.

Hahn, D., Scholz, P., & Radespiel, R. (2010). *Experimental evaluation of the stall characteristics of a two-element high-lift airfoil*.

Heine, B., Mulleners, K., Joubert, G., & Raffel, M. (2011). *Dynamic stall control by passive disturbance generators.* Paper presented at the 29th AIAA Applied Aerodynamics Conference, Honolulu (Hawai), USA.

Holmes, A. E., Hickey, P. K., Murphy, W. R., & Hilton, D. A. (1987). The application of sub-boundary layer vortex generators to reduce canopy "Mach rumble" interior noise on the Gulfstream III. *AIAA Paper, 87-0084*.

Hunt, J. C. R., Abell, C., Peterka, J., & Woo, H. (1978). Kinematical studies of the flows around free or surface-mounted obstacles; applying topology to flow visualization. *Journal of Fluid Mechanics, 86*(01), 179-200.

Hunt, J. C. R., Wray, A. A., & Moin, P. (1988, 1988). *Eddies, streams, and convergence zones in turbulent flows.* Paper presented at the Studying Turbulence Using Numerical Simulation Databases, 2.

Jacobs, E. N., & Sherman, A. (1937). *Airfoil section characteristics as affected by variations of the Reynolds number*: National Advisory Committee for Aeronautics.

Janiszewska, J. M. (2004). *Three dimensional aerodynamics of a simple wing in oscillation including effects of vortex generators.* PhD, The Ohio State University.

Jeong, J., & Hussain, F. (1995). On the identification of a vortex. *Journal of Fluid Mechanics, 285*(-1), 69-94. doi: 10.1017/s0022112095000462

Jirasek, A. (2005). Vortex-Generator Model and Its Application to Flow Control. *Journal of Aircraft, 42*(6), 1486-1491. doi: 10.2514/1.12220

Joubert, G., Le Pape, A., & Huberson, S. (2011). *Numerical study of flow separation control over a OA209 Airfoil using Deployable Vortex Generator.* Paper presented at the 49th AIAA Aerospace Sciences Meeting.

Kang, D. H., Longo, J., Marquardt, M., & Stern, F. (2008, 2008). *Solid/free-surface juncture boundary layer and wake with waves.* Paper presented at the 27th Symposium on Naval Hydrodynamics.

Kerho, M., Hutcherson, S., Blackwelder, R. F., & Liebeck, R. H. (1993). Vortex generators used to control laminar separation bubbles. *Journal of Aircraft, 30*(3), 315-319.

Kerho, M., Kramer, B., & Torrance, C. A. (2003). Enhanced airfoil design incorporating boundary layer mixing devices. *AIAA Paper, 2003-211*.

Klausmeyer, S. M., Papadakis, M., & Lin, J. C. (1996). A flow physics study of vortex generators on a multi-element airfoil. *AIAA Paper*(96-0548).

Kolář, V. (2007). Vortex identification: New requirements and limitations. *International Journal of Heat and Fluid Flow, 28*(4), 638-652. doi: 10.1016/j.ijheatfluidflow.2007.03.004

Komerath, N. M., Raghav, V., & DiOttavio, J. (2009). Diagnostics of Flow Suppression on Rotor Blades: Final Report: Georgia Tech Research Corporation.

Krothapalli, A., Venkatakrishnan, L., Lourenco, L., Greska, B., & Elavarasan, R. (2003). Turbulence and noise suppression of a high-speed jet by water injection. *Journal of Fluid Mechanics, 491*, 131-159. doi: 10.1017/s0022112003005226

Kubin, R. F., & Fletcher, A. N. (1982). Fluorescence quantum yields of some rhodamine dyes. *Journal of Luminescence, 27*(4), 455-462. doi: 10.1016/0022-2313(82)90045-x

Kunik, W. G. (1986). *Application of a computational model for vortex generators in subsonic internal flows.* Paper presented at the 22nd Joint Propulsion Conference.

Langan, K. J., & Samuels, J. J. (1995). Experimental Investigations of Maneuver Performance Enhancements on an Advanced Fighter/Attack Aircraft. *AIAA Paper, 95-442*.

Lighthill, M. J. (1963). Attachment and separation in three-dimensional flow. In L. Rosenhead (Ed.), *Laminar Boundary Layers*: Oxford Univeristy Press.

Lin, J. C. (1999). Control of turbulent boundary-layer separation using micro-vortex generators. *AIAA Paper*(99-993404).

Lin, J. C. (2002). Review of research on low-profile vortex generators to control boundary-layer separation. *Progress in Aerospace Sciences, 38*(4-5), 389-420. doi: 10.1016/s0376-0421(02)00010-6

Lin, J. C., Robinson, S. K., McGhee, R. J., & Valarezo, W. O. (1994). Separation control on high-lift airfoils via micro-vortex generators. *Journal of Aircraft, 31*(6), 1317-1323.

Lin, J. C., Selby, G. V., & Howard, F. G. (1991). Exploratory study of vortex-generating devices for turbulent flow separation control. *AIAA Paper*(91-0042).

Liu, J., Piomelli, U., & Spalart, P. R. (1996). Interaction between a spatially growing turbulent boundary layer and embedded streamwise vortices. *Journal of Fluid Mechanics, 326*(-1). doi: 10.1017/s0022112096008270

Lockman, W. K., & Seegmiller, H. L. (1983). An experimental investigation of the subcritical and supercritical flow about a swept semispan wing: DTIC Document.

LöGdberg, O., Fransson, J. H. M., & Alfredsson, P. H. (2009). Streamwise evolution of longitudinal vortices in a turbulent boundary layer. *Journal of Fluid Mechanics, 623*. doi: 10.1017/s0022112008004825

Lowson, M. (1964). Some experiments with vortex breakdown(Water tunnel flow visualization on slender delta wings reveal vortex breakdown formation to be a nonaxisymmetric stability). *ROYAL AERONAUTICAL SOCIETY, JOURNAL, 68*, 343-346.

Lu, F. K., Li, Q., Shih, Y., Pierce, A. J., & Liu, C. (2011). *Review of Micro Vortex Generators in High-Speed Flow.* Paper presented at the 49th AIAA Aerospace Sciences Meeting.

Lyon, C. A., Selig, M. S., & Broeren, A. P. (1997, 1997/01//). *Boundary Layer Trips on Airfoils at Low Reynolds Numbers.* Paper presented at the 35th Aerospace Sciences Meeting.

Manolesos, M., & Voutsinas, S. G. (2011, 2011/07/27/15:51:13). 3D flow separation on plane wing, from http://www.aerolab.mech.ntua.gr/3D_flow_separation_on_plane_wing_1.html

Martin, P. B., Leishman, J., Pugliese, G. J., & Anderson, S. L. (2000). *Stereoscopic PIV measurements in the wake of a hovering rotor.* Paper presented at the AHS International, Annual Forum, 56 th, Virginia Beach, VA.

May, N. (2001, 2001). *A new vortex generator model for use in complex configuration CFD solvers.* Paper presented at the 19th AIAA Applied Aerodynamics Conference.

McCurdy, W. J. (1948). Investigation of Boundary Layer Control of an NACA 16-325 Airfoil by Means of Vortex Generators. *United Aircraft Corp., Research Department, Rept. M-15038-3*.

Mehta, R. D., & Bradshaw, P. (1988). Longitudinal vortices imbedded in turbulent boundary layers Part 2. Vortex pair with 'common flow' upwards. *Journal of Fluid Mechanics, 188*(-1). doi: 10.1017/s0022112088000837

Menter, F. R. (1993). Zonal two-equation k-w turbulence model for aerodynamic flows. *AIAA Paper, 1993 - 2906*.

Moss, G. F., & Murdin, P. M. (1971). *Two-Dimensional Low-Speed Tunnel Tests on the NACA 0012 Section Including Measurements Made During Pitching Oscillations at the Stall* (1st ed.). London: H.M. Stationery Office.

Mourikis, D., Riziotis, V., & Voutsinas, S. (2005). Optimum aerodynamic design of 52m blade for a prototype 5MW WEC *TR-01*. Athens: National Technical University of Athens.

Mulleners, K., Kindler, K., & Raffel, M. (2012). Dynamic stall on a fully equipped helicopter model. *Aerospace Science and Technology, 19*(1), 72-76. doi: 10.1016/j.ast.2011.03.013

Murri, D., & Jordan, F. (1987). Wind-tunnel investigation of a full-scale general aviation airplane equipped with an advanced natural laminar flow wing *NASA-TP-2772*.

Nikolaou, I. G., Politis, E. S., & Chaviaropoulos, P. K. (2005). Modelling the Flow Around Airfoils Equipped with Vortex Generators Using a Modified 2D Navier–Stokes Solver. *Journal of Solar Energy Engineering, 127*(2). doi: 10.1115/1.1850486

Øye, S. (1995). *The effect of vortex generators on the performance of the Elkraft 1000 kW turbine.* Paper presented at the 9th IEA Symposium on Aerodynamics of Wind Turbines.

Papadakis, G. (2011). Formulation of a cell-centered (U)RANS compressible solver *PhD Progress Report*. Athens: National Technical University of Athens.

Pape, A. L., Costes, M., Joubert, G., David, F., & Deluc, J. M. (2012). Dynamic Stall Control Using Deployable Leading-Edge Vortex Generators. *AIAA Journal, 50*(10), 2135-2145.

Pauley, W. R., & Eaton, J. K. (1988). Experimental study of the development of longitudinal vortex pairs embedded in a turbulent boundary layer. *AIAA Journal, 26*(7), 816-823. doi: 10.2514/3.9974

Pearcey, H. H. (1961). Shock induced separation and its prevention by design and boundary layer control. In G. V. Lachmann (Ed.), *Boundary Layer and Flow Control* (Vol. 2, pp. 1166-1344): Pergamon Press.

Pope, S. B. (2000). *Turbulent flows*. Cambridge ; New York: Cambridge University Press.

Raffel, M., Kompenhans, J., & Willert, C. E. (1998). *Particle image velocimetry : a practical guide*. Berlin: Springer.

Raghav, V., Richards, P., Komerath, N., & Smith, M. (2009). *Three-Dimensional Features of the Stalled Flow Field of a Rotor Blade in Forward Flight*. Paper presented at the 2nd International Forum on Rotorcraft Multidisciplinary Technology

Ramasamy, M., & Leishman, J. G. (2006). *Benchmarking PIV with LDV for Rotor Wake Vortex Flows.* Paper presented at the 24 th AIAA Applied Aerodynamics Conference.

Ramasamy, M., Paetzel, R., & Bhagwat, M. J. (2011). Aperiodicity correction for rotor tip vortex measurements *DTIC Document*.

Rao, D. M., & Kariya, T. T. (1988). *Boundary-layer submerged vortex generators for separation control - An exploratory study.* Paper presented at the 1st National Fluid Dynamics Congress.

Rodríguez, D., & Theofilis, V. (2010). On the birth of stall cells on airfoils. *Theoretical and Computational Fluid Dynamics, 25*(1-4), 105-117. doi: 10.1007/s00162-010-0193-7

Ross, H. M., & Perkins, J. N. (1994). Tailoring stall characteristics using leading edge droop modification. *Journal of Aircraft, 31*(4), 767-772. doi: 10.2514/3.46559

Rubinstein, R., Rumsey, C. L., Salas, M. D., & Thomas, J. L. (2001). Turbulence Modeling Workshop *NASA/CR 2001-210841*.

Schewe, G. (2001). Reynolds-number effects in flow around more-or-less bluff bodies. *Journal of Wind Engineering and Industrial Aerodynamics, 89*, 1267-1289. doi: 10.1016/s0167-6105(01)00158-1

Schubauer, G. B., & Spangenberg, W. G. (1959). Forced mixing in boundary layers. *Journal of Fluid Mechanics, 8*(01). doi: 10.1017/s0022112060000372

Seshagiri, A., Cooper, E., & Traub, L. W. (2009). Effects of vortex generators on an airfoil at low Reynolds numbers. *Journal of Aircraft, 46*(1), 116-122.

Smith, F. T. (1994). Theoretical prediction and design for vortex generators in turbulent boundary layers. *Journal of Fluid Mechanics, 270*(1), 91-132.

Sørensen, N. N., & Schreck, S. (2012). Computation of the National Renewable Energy Laboratory Phase-VI rotor in pitch motion during standstill. *Wind Energy, 15*(3), 425-442. doi: 10.1002/we.480

Spalart, P. R., & Allmaras, S. R. (1992,). *A one-equation turbulence model for aerodynamic flows.* Paper presented at the 30th Aerospace Sciences Meeting and Exhibit.

Stillfried, F. V., Wallin, S., & Johansson, A. V. (2011). Evaluation of a Vortex Generator Model in Adverse Pressure Gradient Boundary Layers. *AIAA Journal, 49*(5), 982-993. doi: 10.2514/1.j050680

Stillfried, F. V., Wallin, S., & Johansson, A. V. (2012). Vortex-Generator Models for Zero- and Adverse-Pressure-Gradient Flows. *AIAA Journal, 50*(4), 855-866. doi: 10.2514/1.j051169

Storms, B. L., & Jang, C. S. (1994). Lift enhancement of an airfoil using a Gurney flap and vortex generators. *Journal of Aircraft, 31*(3), 542-547.

Supamusdisukul, J. (2008). *Experimental investigation of wing-fuselage interaction geometries including CFD analyses.* MSc Thesis, University of Maryland, Maryland, US.

Swalwell, K. E., Sheridan, J., & Melbourne, W. H. (2004). *The effect of turbulence intensity on performance of a NACA 4421 airfoil section.* Paper presented at the 42nd AIAA Aerospace Sciences Meeting and Exhibit, Reno, Nevada.

Taira, K., & Colonius, T. (2009). Three-dimensional flows around low-aspect-ratio flat-plate wings at low Reynolds numbers. *Journal of Fluid Mechanics, 623*. doi: 10.1017/s0022112008005314

Tangler, J. L. (2002). The nebulous art of using wind tunnel aerofoil data for predicting rotor performance. *Wind Energy, 5*(2-3), 245-257.

Taylor, H. D. (1950). Summary report on vortex generators *Technical Report No. R-05280-9*: United Aircraft Corporation. Research Dept.

Theofilis, V., Hein, S., & Dallmann, U. (2000). On the origins of unsteadiness and three-dimensionality in a laminar separation bubble. *Philosophical Transactions of the Royal Society A: Mathematical, Physical and Engineering Sciences, 358*(1777), 3229-3246. doi: 10.1098/rsta.2000.0706

Timmer, W. A., & Van Rooij, R. P. J. O. M. (2003). Summary of the Delft University Wind Turbine Dedicated Airfoils. *Journal of Solar Energy Engineering, 125*(4), 488-496. doi: 10.1115/1.1626129

Tobak, M., & Peake, D. J. (1982). Topology of three-dimensional separated flows. *Annual Review of Fluid Mechanics, 14*(1), 61-85.

Van Raemdonck, G. M. R., & Van Tooren, M. J. L. (2008, 2008//20/20/07). *Time averaged phenomenological investigation of a wake behind a bluff body.* Paper presented at the BBAA VI International Colloquium on: Bluff Bodies Aerodynamics & Applications.

Van Rooij, R. P. J. O. M., & Timmer, W. A. (2003). Roughness sensitivity considerations for thick rotor blade airfoils. *Journal of Solar Energy Engineering, 125*(4), 22-31. doi: 10.1115/wind2003-350

Velte, C. M. (2013). Vortex Generator Flow Model Based on Self-Similarity. *AIAA Journal, 51*(2), 526-529. doi: 10.2514/1.j051865

Velte, C. M., & Hansen, M. O. L. (2012). Investigation of flow behind vortex generators by stereo particle image velocimetry on a thick airfoil near stall. *Wind Energy*. doi: 10.1002/we.1541

Velte, C. M., & Manolesos, M. (2011). [Wind Tunnel Tests - Personal Communication].

Waithe, K. A. (2004a). *Source Term Model for an Array of Vortex Generator Vanes.* Paper presented at the 42nd AIAA Aerospace Sciences Meeting and Exhibit AIAA-2004-1236.

Waithe, K. A. (2004b). *Source Term Model for Vortex Generator Vanes in a Navier-Stokes Computer Code.* Paper presented at the 42nd AIAA Aerospace Sciences Meeting and Exhibit.

Waldman, R. M., & Breuer, K. S. (2012). Accurate measurement of streamwise vortices using dual-plane PIV. *Experiments in Fluids, 53*(5), 1487-1500. doi: 10.1007/s00348-012-1368-3

Weihs, D., & Katz, J. (1983). Cellular patterns in poststall flow over unswept wings. *AIAA Journal, 21*(12), 1757-1759. doi: 10.2514/3.8321

Wendt, B. (1996). *The modelling of symmetric airfoil vortex generators.* Paper presented at the 34th Aerospace Sciences Meeting and Exhibit.

Wendt, B. (2004). Parametric Study of Vortices Shed from Airfoil Vortex Generators. *AIAA Journal, 42*(11), 2185-2195.

Wendt, B., Reichert, B. A., & Foster, J. D. (1995). The decay of longitudinal vortices shed from airfoil vortex generators.

Westerweel, J. (2000). Theoretical analysis of the measurement precision in particle image velocimetry. *Experiments in Fluids, 29*(1), S003-S012.

Willert, C. (1997). Stereoscopic digital particle image velocimetry for application in wind tunnel flows. *Measurement Science and Technology, 8*(12), 1465-1479. doi: 10.1088/0957-0233/8/12/010

Winkelmann, A. E. (1981). An experimental study of separated flow on a finite wing. *AIAA Paper* (81-1882).

Winkelmann, A. E. (1982). An experimental study of mushroom shaped stall cells. *AIAA Paper* (82-0942).

Winkelmann, A. E., & Barlow, J. B. (1980). Flowfield Model for a Rectangular Planform Wing beyond Stall. *AIAA Journal, 18*(08), 1006-1008.

Wokoeck, R., Krimmelbein, N., Ortmanns, J., Ciobaca, V., Radespiel, R., & Krumbein, A. (2006). *RANS simulation and experiments on the stall behaviour of an airfoil with laminar separation bubbles.* Paper presented at the 44th AIAA aerospace sciences meeting and exhibit, Reno, AIAA-2006-244.

Yao, C. S., Lin, J. C., & Brian, A. G. (2002, 2002). *Flow-Field Measurement of Device-Induced Embedded Streamwise Vortex on a Flat Plate.* Paper presented at the 1st AIAA Flow Control Conference.

Yon, S. A., & Katz, J. (1998). Study of the Unsteady Flow Features on a Stalled Wing. *AIAA Journal, 36*(3), 305-312.

Yoshida, K., & Noguchi, M. (2000). *Adverse Reynolds Number Effect on Maximum Lift of Two Dimensional Airfoils.* Paper presented at the ICAS.

Zarutskaya, T., & Arieli, R. (2005). *On vortical flow structures at wing stall and beyond.* Paper presented at the 35th AIAA Fluid Dynamics Conference and Exhibit.

Zhang, L., Yang, K., Xu, J., & Zhang, M. (2011). Modeling of delta-wing type vortex generators. *Science China Technological Sciences, 54*(2), 277-285. doi: 10.1007/s11431-010-4284-x

Part V.

Appendices

Appendix A

Tuft flow Visualization

The pictures below are snapshots from various set-ups, all of them with the localized disturbance. On each picture the SC area is outlined. Even though the snapshots presented here are representative, one should bear in mind that the SC area was measured based on the videos (some are available in (Manolesos & Voutsinas, 2011)) and not on these snapshots.

A.1 Angle of attack effect

Figure 137: AR = 2.0, Re = 1.0x10^6, α = 8.0°, case with ZZ tape. Outlined is the area shown in Figure 139 (left).

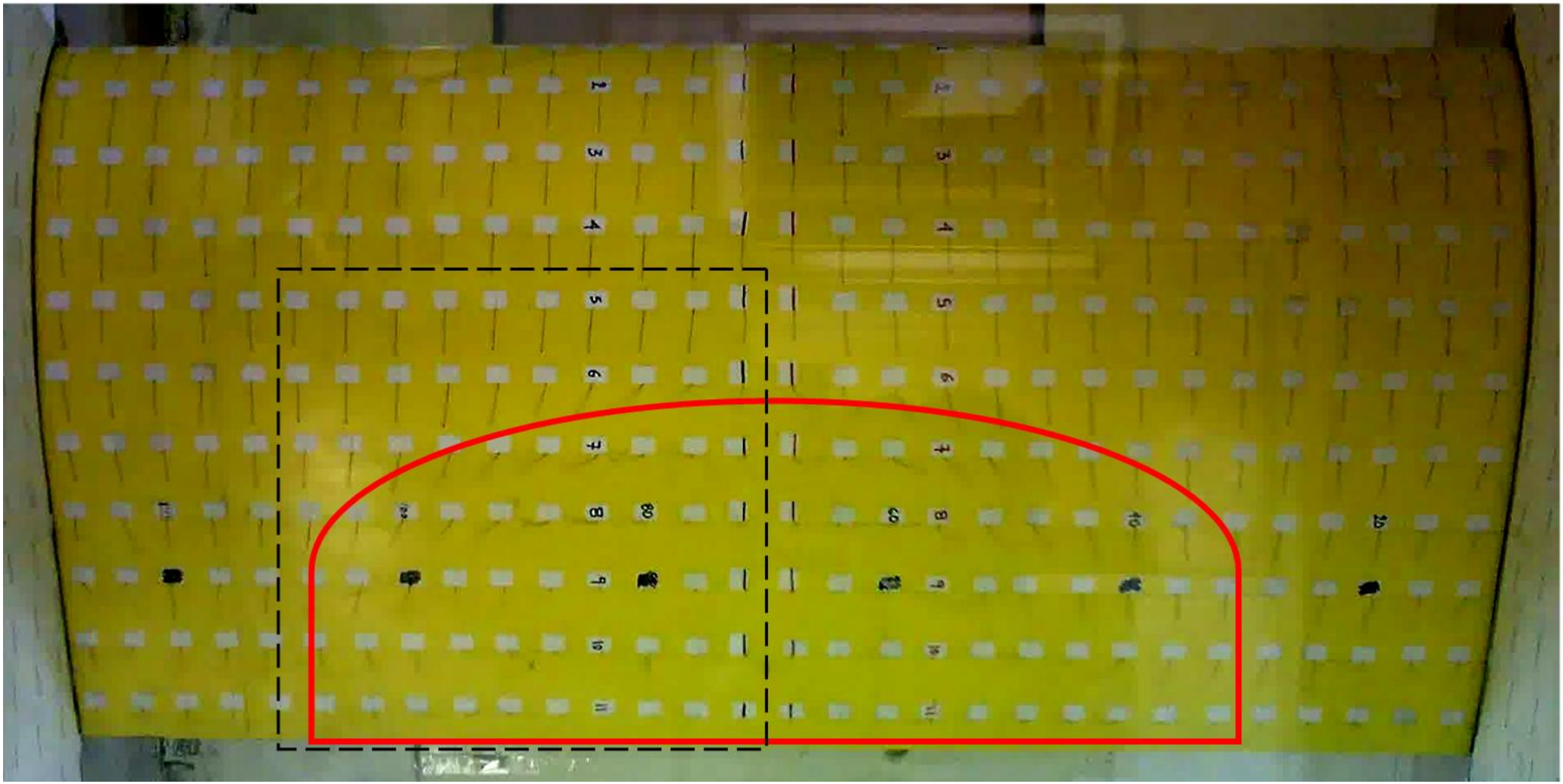

Figure 138: AR = 2.0, Re = 1.0x10^{6}, α = 9.0°, case with ZZ tape. Outlined is the detail area shown in Figure 139 (right).

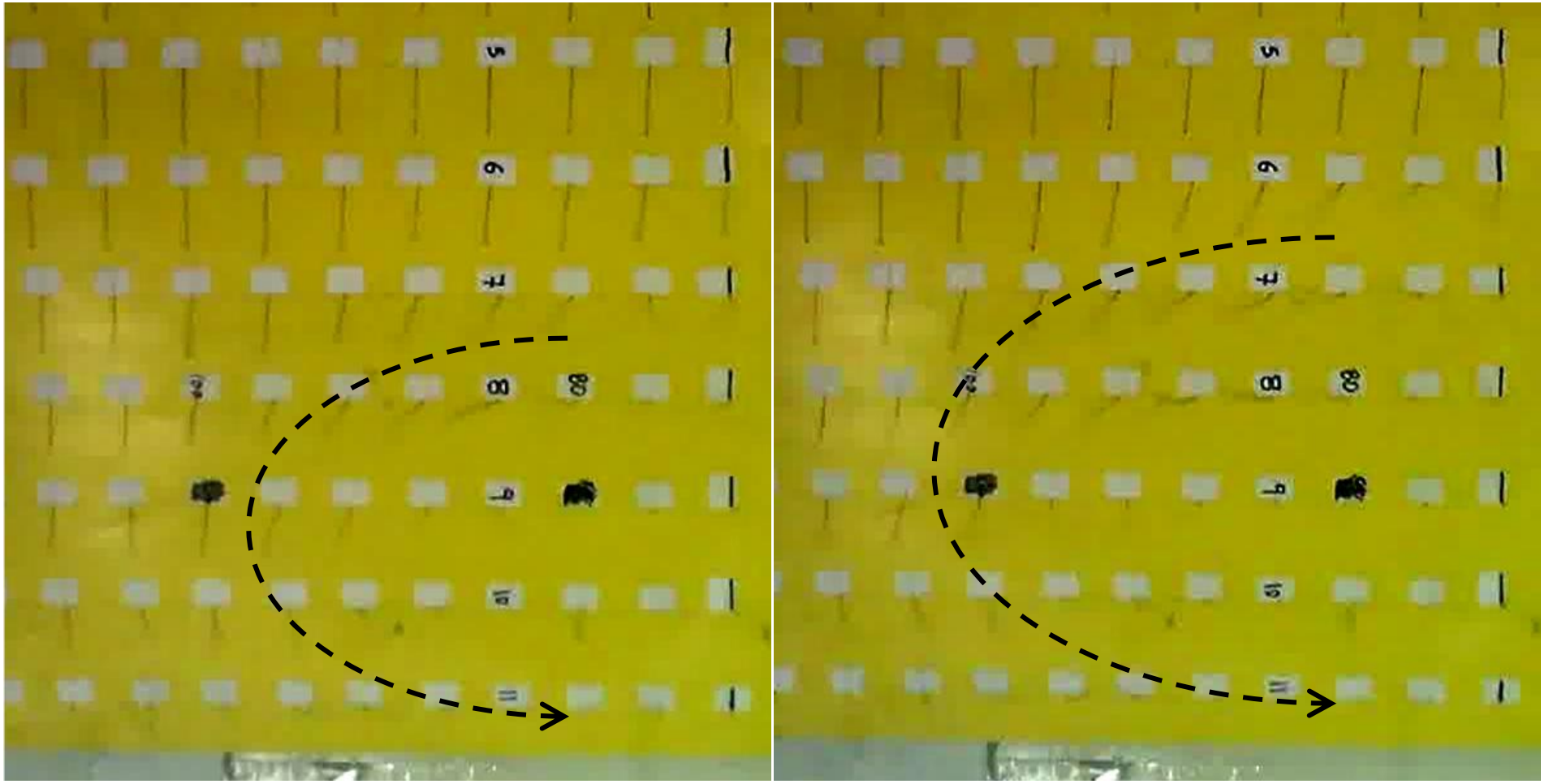

Figure 139: AR = 2.0, Re = 1.0x10^{6}, case with ZZ tape. The growth of a SC vortex for an increase of one degree in angle of attack is shown. α = 8.0° (left), α = 9.0° (right).

A.2 AR effect

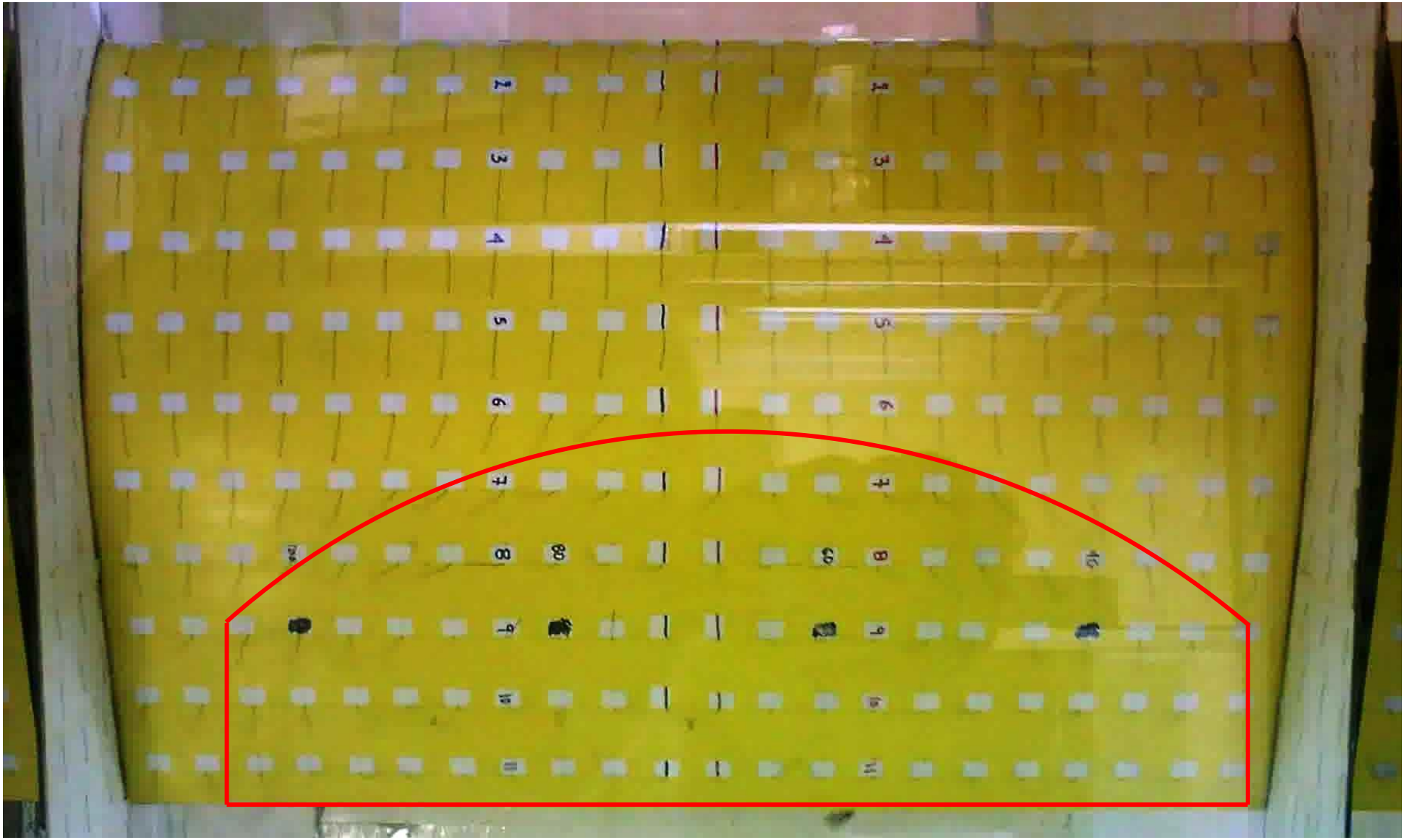

Figure 140: AR = 1.5, Re = 0.5x10^6, α = 11.0°, case with ZZ tape. Compare SC size with Figure 141.

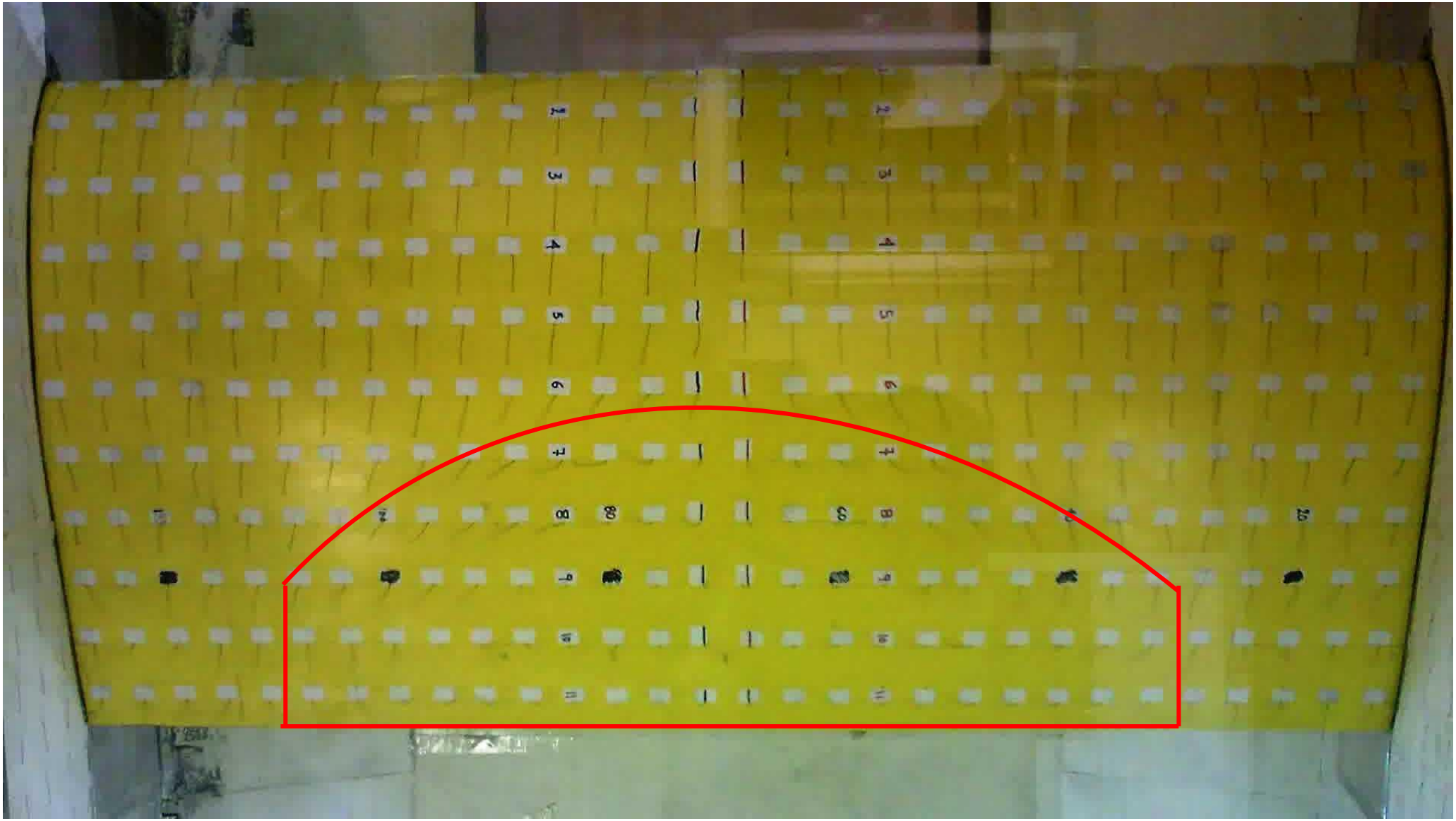

Figure 141: AR = 2.0, Re = 0.5x10^6, α = 11.0°, case with ZZ tape. Compare SC size with Figure 140.

A.3 Re number effect

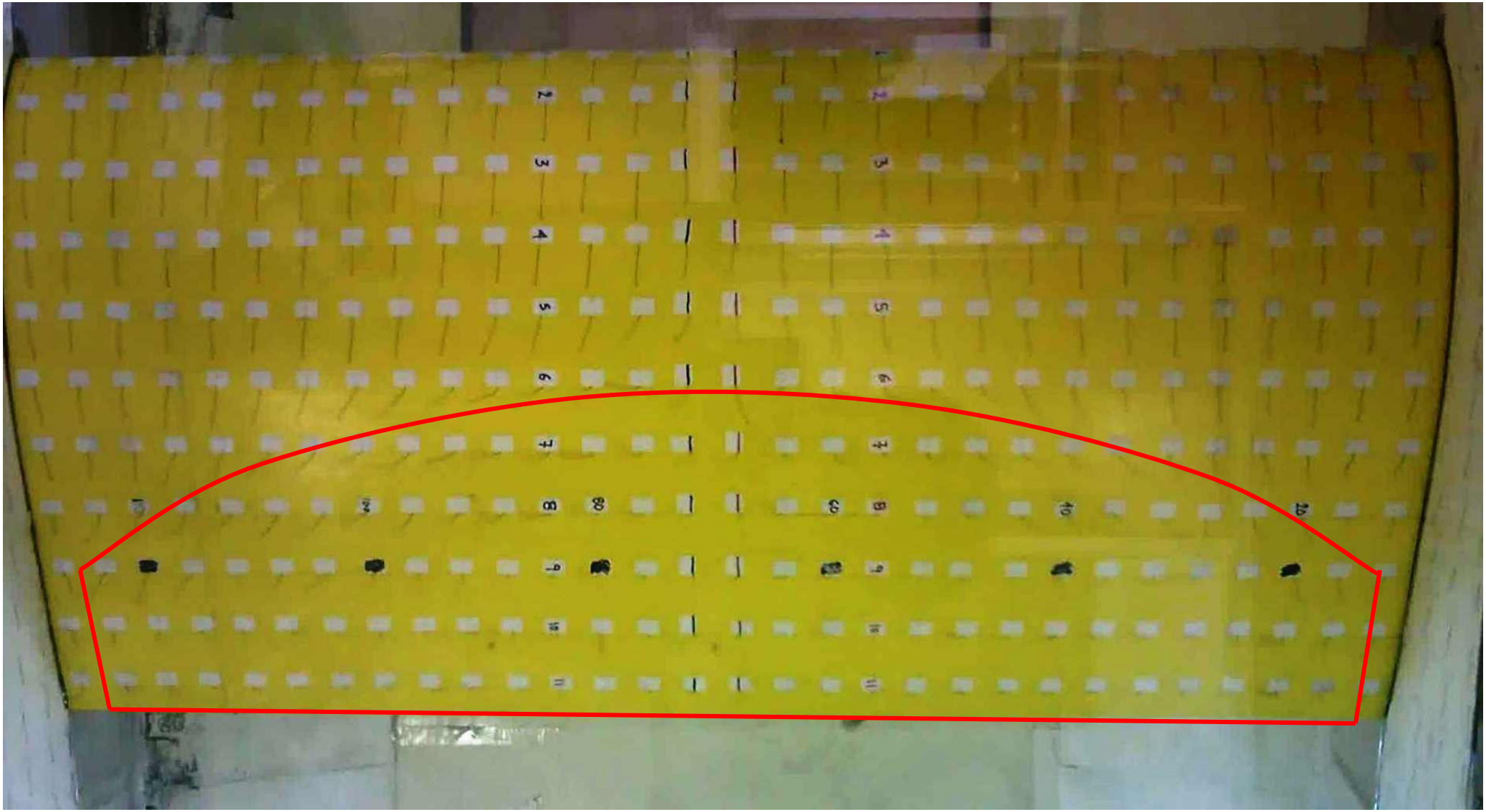

Figure 142: AR = 2.0, Re = 0.5x10^6, α = 14.0°, case with ZZ tape. Compare SC size with Figure 143 and Figure 144.

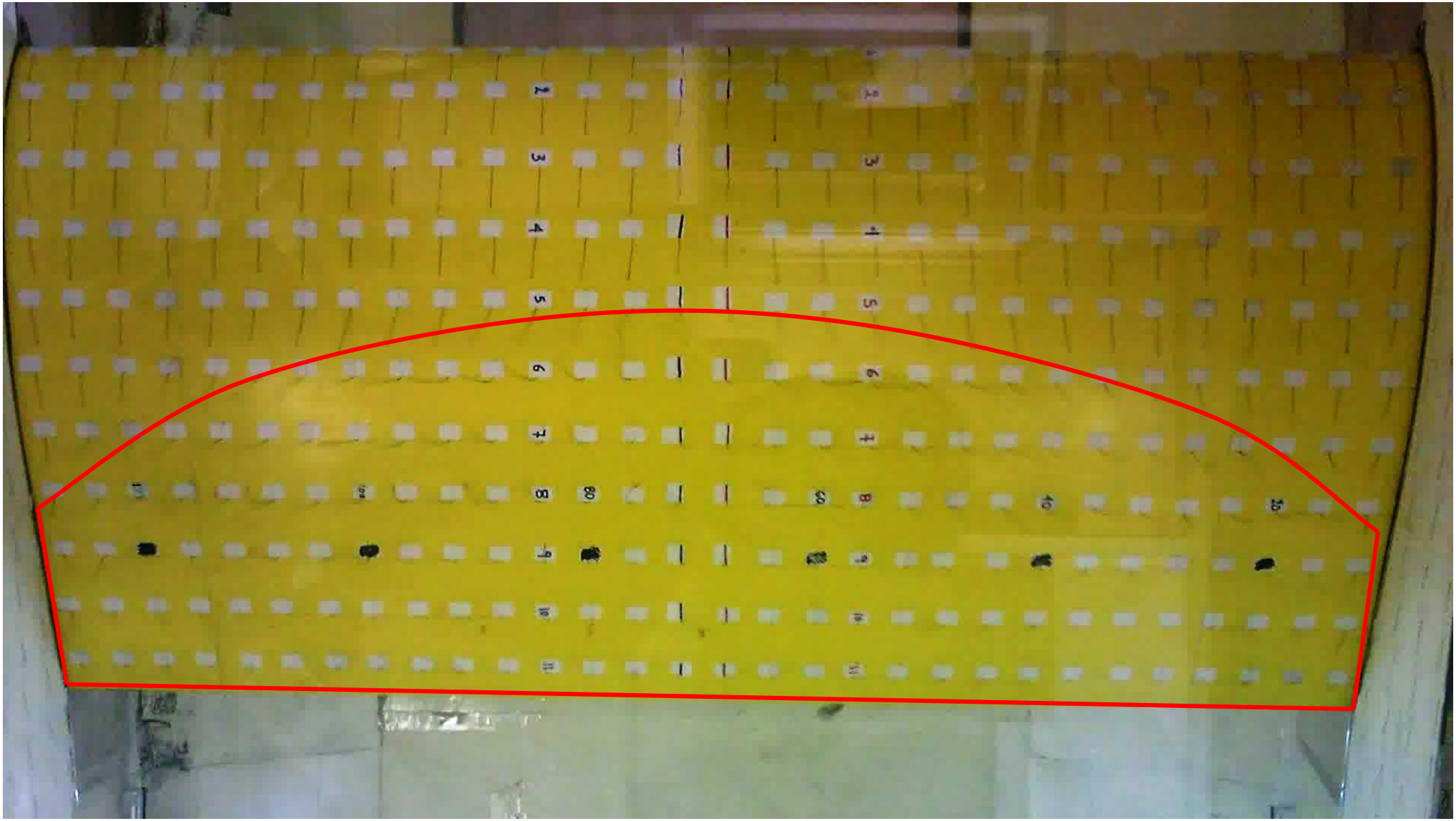

Figure 143: AR = 2.0, Re = 1.0x10^6, α = 14.0°, case with ZZ tape. Compare SC size with Figure 142 and Figure 144.

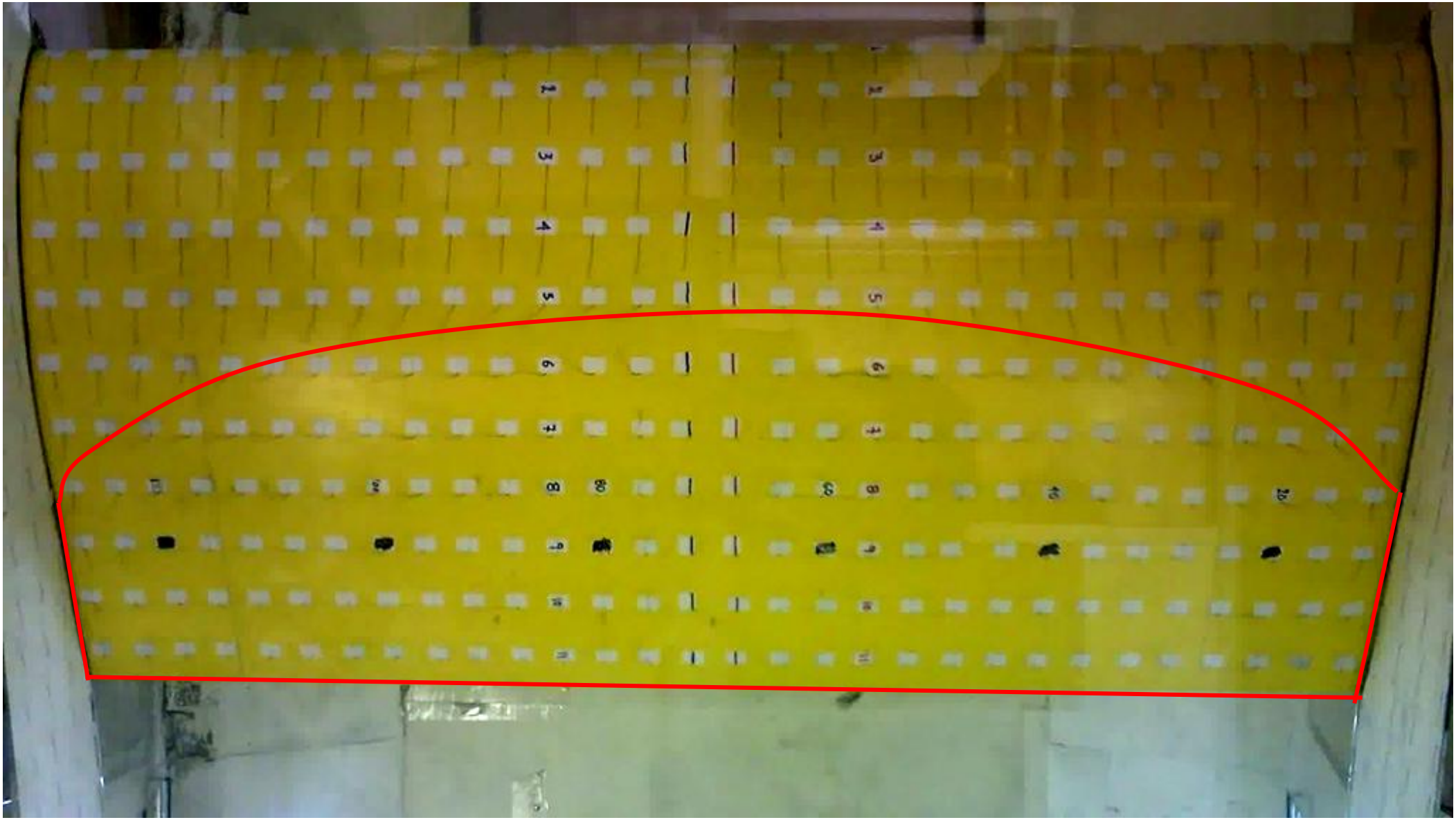

Figure 144: AR = 2.0, Re = 1.5x10^{6}, α = 14.0°, case with ZZ tape. Compare SC size with Figure 142 and Figure 143.

Appendix B

Zigzag tape height computation

Regarding the minimum height for tripping a laminar boundary layer, (Braslow & Knox, 1958) provide an empirical relation that includes the Reynolds number, Re_k, based on the flow velocity at the trip height and the trip height. According to (Barlow et al., 1999) its value should be 600 for Reynolds numbers greater than $1.0x10^4$ based on the free stream and distance from the LE to the trip strip, Re_x. For very low Re_x a value of 1000 is suggested. (Van Rooij & Timmer, 2003) propose a value of 200 for ZZ tapes as the latter are more effective than grit roughness in tripping the flow. However, they make no reference for low Re_x. Using the value of 200 for high Re_x and 330 for low Re_x (a third of the value suggested for grit roughness), the critical height for a ZZ tape located at 0.02c for a chord Reynolds number of $0.5x10^6$ is 0.29mm (accordingly: 0.14mm for Re = $1.0x10^6$ and 0.09mm for Re = $1.5x10^6$).

It was decided to use an oversized ZZ tape even for the lowest Re number so that the trip tape would be oversized throughout the range of Re numbers considered in this report. A 0.4mm thick zigzag tape with 60^o angle was used. Of course the effect is not entirely the same given the Re number and angle of attack range, however, under all circumstances the ZZ tape is met by laminar flow and exceeds height requirements for transition.

Besides, this is not the first time an oversized ZZ tape is used. A ZZ tape of the same height at the same chordwise position had been used by (Dossing, 2008) in his transition study who reported that it tripped the flow immediately, at Re 1.6million and higher. Also, ZZ tapes of height similar to the one used in the paper have been used to examine the performance of wind turbine airfoils under increased LE roughness conditions for a Re numbers from $1.0x10^6$ to $3.0x10^6$ (Van Rooij & Timmer, 2003).

Finally, pressure data confirm that the ZZ tape did trip the flow even at the lowest Re number, e.g. see Figure 145 where pressure distribution at the wing mid span with and without the 10% span ZZ tape (case: AR = 2.0, Re = $0.5x10^6$, $\alpha = 0^o$). Clearly the transition step is missing from the case with the ZZ tape.

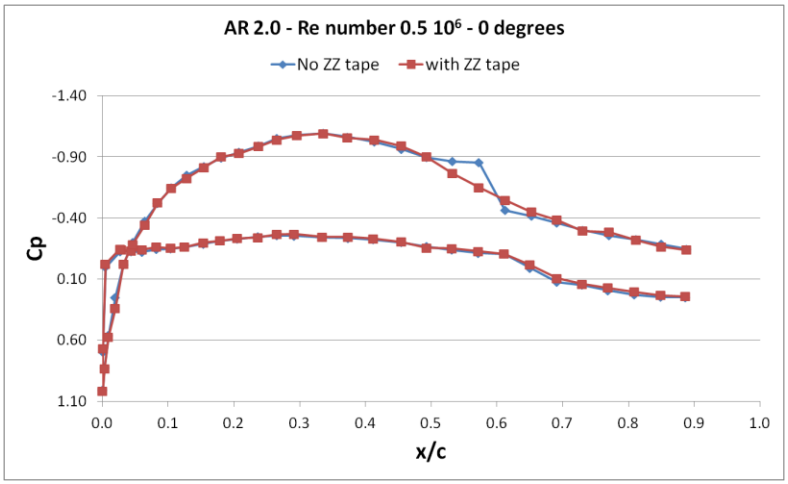

Figure 145: Pressure distribution at the wing mid span with and without the 10% span ZZ tape. AR = 2.0, Re = $0.5x10^6$, $\alpha = 0^o$.

Appendix C

Airfoil coordinates

#	X	Y			
1	1.000000	0.0000000	41	0.786298	-0.0050599
2	0.998006	0.0000518	42	0.780472	-0.0057056
3	0.993837	0.0001627	43	0.774643	-0.0063706
4	0.989430	0.0002838	44	0.768803	-0.0070549
5	0.984788	0.0004154	45	0.762946	-0.0077583
6	0.979928	0.0005569	46	0.757067	-0.0084803
7	0.974874	0.0007069	47	0.751164	-0.0092201
8	0.969660	0.0008635	48	0.745235	-0.0099770
9	0.964322	0.0010243	49	0.739282	-0.0107488
10	0.958895	0.0011867	50	0.733308	-0.0115315
11	0.953407	0.0013484	51	0.727320	-0.0123204
12	0.947877	0.0015065	52	0.721327	-0.0131101
13	0.942321	0.0016569	53	0.715344	-0.0138952
14	0.936750	0.0017953	54	0.709386	-0.0146762
15	0.931178	0.0019173	55	0.703462	-0.0154573
16	0.925616	0.0020189	56	0.697578	-0.0162435
17	0.920074	0.0020963	57	0.691734	-0.0170403
18	0.914559	0.0021466	58	0.685924	-0.0178525
19	0.909072	0.0021677	59	0.680139	-0.0186759
20	0.903608	0.0021574	60	0.674369	-0.0195029
21	0.898157	0.0021133	61	0.668602	-0.0203259
22	0.892700	0.0020328	62	0.662827	-0.0211377
23	0.887219	0.0019147	63	0.657032	-0.0219310
24	0.881694	0.0017625	64	0.651206	-0.0227073
25	0.876119	0.0015803	65	0.645342	-0.0234753
26	0.870499	0.0013729	66	0.639437	-0.0242436
27	0.864853	0.0011461	67	0.633496	-0.0250201
28	0.859214	0.0009061	68	0.627525	-0.0258071
29	0.853619	0.0006515	69	0.621535	-0.0266025
30	0.848087	0.0003741	70	0.615546	-0.0274030
31	0.842614	0.0000654	71	0.609577	-0.0282052
32	0.837178	-0.0002839	72	0.603656	-0.0290046
33	0.831744	-0.0006785	73	0.597809	-0.0297953
34	0.826276	-0.0011162	74	0.592054	-0.0305659
35	0.820752	-0.0015942	75	0.586394	-0.0313062
36	0.815154	-0.0021090	76	0.580818	-0.0320085
37	0.809479	-0.0026562	77	0.575305	-0.0326680
38	0.803733	-0.0032293	78	0.569830	-0.0332934
39	0.797939	-0.0038220	79	0.564376	-0.0339046
40	0.792122	-0.0044323	80	0.558935	-0.0345202

81	0.553510	-0.0351574	125	0.313344	-0.0496982
82	0.548106	-0.0358203	126	0.307627	-0.0496482
83	0.542723	-0.0364957	127	0.301879	-0.0495843
84	0.537357	-0.0371704	128	0.296118	-0.0495086
85	0.531995	-0.0378324	129	0.290369	-0.0494239
86	0.526618	-0.0384702	130	0.284665	-0.0493329
87	0.521200	-0.0390741	131	0.279041	-0.0492373
88	0.515715	-0.0396485	132	0.273524	-0.0491303
89	0.510148	-0.0402039	133	0.268122	-0.0490026
90	0.504498	-0.0407505	134	0.262824	-0.0488461
91	0.498779	-0.0412974	135	0.257610	-0.0486596
92	0.493027	-0.0418494	136	0.252466	-0.0484606
93	0.487278	-0.0423993	137	0.247397	-0.0482687
94	0.481560	-0.0429382	138	0.242420	-0.0481016
95	0.475889	-0.0434589	139	0.237561	-0.0479571
96	0.470272	-0.0439554	140	0.232829	-0.0478081
97	0.464704	-0.0444229	141	0.228209	-0.0476290
98	0.459174	-0.0448589	142	0.223675	-0.0473964
99	0.453674	-0.0452635	143	0.219185	-0.0470927
100	0.448196	-0.0456367	144	0.214700	-0.0467339
101	0.442736	-0.0459782	145	0.210198	-0.0463508
102	0.437293	-0.0462874	146	0.205677	-0.0459762
103	0.431868	-0.0465644	147	0.201153	-0.0456343
104	0.426465	-0.0468098	148	0.196652	-0.0453108
105	0.421089	-0.0470240	149	0.192185	-0.0449826
106	0.415748	-0.0472114	150	0.187751	-0.0446265
107	0.410447	-0.0473873	151	0.183338	-0.0442199
108	0.405190	-0.0475681	152	0.178925	-0.0437688
109	0.399977	-0.0477696	153	0.174506	-0.0433134
110	0.394808	-0.0480064	154	0.170092	-0.0428852
111	0.389676	-0.0482746	155	0.165707	-0.0424772
112	0.384565	-0.0485469	156	0.161368	-0.0420740
113	0.379452	-0.0487957	157	0.157085	-0.0416608
114	0.374300	-0.0489954	158	0.152862	-0.0412233
115	0.369069	-0.0491453	159	0.148695	-0.0407485
116	0.363733	-0.0492588	160	0.144580	-0.0402414
117	0.358280	-0.0493504	161	0.140516	-0.0397238
118	0.352728	-0.0494358	162	0.136514	-0.0392179
119	0.347119	-0.0495247	163	0.132589	-0.0387429
120	0.341494	-0.0496093	164	0.128760	-0.0382890
121	0.335878	-0.0496795	165	0.125039	-0.0378239
122	0.330273	-0.0497254	166	0.121421	-0.0373250
123	0.324661	-0.0497414	167	0.117897	-0.0368097
124	0.319022	-0.0497308	168	0.114457	-0.0363056

169	0.111095	-0.0358371	213	0.017330	-0.0179566
170	0.107809	-0.0354241	214	0.016314	-0.0176323
171	0.104599	-0.0350520	215	0.015335	-0.0172872
172	0.101468	-0.0346725	216	0.014392	-0.0169154
173	0.098410	-0.0342447	217	0.013483	-0.0165173
174	0.095412	-0.0337709	218	0.012606	-0.0160976
175	0.092465	-0.0332757	219	0.011757	-0.0156605
176	0.089561	-0.0327823	220	0.010936	-0.0152100
177	0.086698	-0.0323125	221	0.010140	-0.0147496
178	0.083874	-0.0318863	222	0.009369	-0.0142827
179	0.081092	-0.0315136	223	0.008622	-0.0138103
180	0.078360	-0.0311732	224	0.007901	-0.0133311
181	0.075679	-0.0308388	225	0.007205	-0.0128439
182	0.073050	-0.0304867	226	0.006534	-0.0123476
183	0.070471	-0.0300953	227	0.005888	-0.0118411
184	0.067937	-0.0296520	228	0.005270	-0.0113230
185	0.065440	-0.0291742	229	0.004681	-0.0107917
186	0.062977	-0.0286857	230	0.004125	-0.0102455
187	0.060550	-0.0282096	231	0.003604	-0.0096833
188	0.058164	-0.0277615	232	0.003119	-0.0091036
189	0.055830	-0.0273317	233	0.002673	-0.0085055
190	0.053553	-0.0269047	234	0.002274	-0.0078893
191	0.051338	-0.0264669	235	0.001926	-0.0072544
192	0.049183	-0.0260106	236	0.001629	-0.0066025
193	0.047086	-0.0255438	237	0.001371	-0.0059390
194	0.045048	-0.0250763	238	0.001139	-0.0052706
195	0.043068	-0.0246172	239	0.000922	-0.0046038
196	0.041149	-0.0241720	240	0.000719	-0.0039412
197	0.039293	-0.0237417	241	0.000538	-0.0032820
198	0.037503	-0.0233265	242	0.000386	-0.0026245
199	0.035777	-0.0229265	243	0.000270	-0.0019664
200	0.034117	-0.0225416	244	0.000191	-0.0013061
201	0.032522	-0.0221686	245	0.000144	-0.0006434
202	0.030990	-0.0218015	246	0.000127	0.0000220
203	0.029519	-0.0214352	247	0.000136	0.0006903
204	0.028107	-0.0210655	248	0.000166	0.0013616
205	0.026749	-0.0206891	249	0.000216	0.0020359
206	0.025440	-0.0203091	250	0.000281	0.0027133
207	0.024174	-0.0199330	251	0.000365	0.0033943
208	0.022948	-0.0195672	252	0.000468	0.0040793
209	0.021757	-0.0192171	253	0.000592	0.0047685
210	0.020599	-0.0188871	254	0.000740	0.0054619
211	0.019474	-0.0185744	255	0.000914	0.0061592
212	0.018384	-0.0182676	256	0.001116	0.0068600

257	0.001345	0.0075648	301	0.036171	0.0462468
258	0.001596	0.0082755	302	0.037771	0.0473170
259	0.001861	0.0089941	303	0.039419	0.0484153
260	0.002136	0.0097226	304	0.041106	0.0495561
261	0.002413	0.0104622	305	0.042821	0.0507515
262	0.002700	0.0112089	306	0.044573	0.0519867
263	0.003007	0.0119566	307	0.046382	0.0532340
264	0.003348	0.0126992	308	0.048273	0.0544705
265	0.003736	0.0134313	309	0.050255	0.0557029
266	0.004171	0.0141548	310	0.052332	0.0569470
267	0.004642	0.0148777	311	0.054501	0.0582197
268	0.005136	0.0156087	312	0.056755	0.0595391
269	0.005638	0.0163564	313	0.059080	0.0609196
270	0.006141	0.0171236	314	0.061468	0.0623504
271	0.006651	0.0179063	315	0.063925	0.0638106
272	0.007176	0.0187001	316	0.066463	0.0652806
273	0.007723	0.0195002	317	0.069108	0.0667443
274	0.008302	0.0203021	318	0.071883	0.0682067
275	0.008918	0.0211048	319	0.074806	0.0696848
276	0.009570	0.0219116	320	0.077885	0.0711943
277	0.010255	0.0227259	321	0.081113	0.0727469
278	0.010973	0.0235513	322	0.084459	0.0743413
279	0.011720	0.0243916	323	0.087893	0.0759507
280	0.012492	0.0252505	324	0.091408	0.0775495
281	0.013283	0.0261316	325	0.095026	0.0791257
282	0.014094	0.0270337	326	0.098782	0.0806952
283	0.014926	0.0279529	327	0.102692	0.0822832
284	0.015783	0.0288846	328	0.106732	0.0839044
285	0.016672	0.0298245	329	0.110847	0.0855432
286	0.017596	0.0307683	330	0.114997	0.0871672
287	0.018565	0.0317126	331	0.119179	0.0887565
288	0.019579	0.0326599	332	0.123421	0.0903112
289	0.020638	0.0336162	333	0.127736	0.0918511
290	0.021739	0.0345876	334	0.132091	0.0933829
291	0.022878	0.0355804	335	0.136427	0.0948833
292	0.024048	0.0366009	336	0.140710	0.0963236
293	0.025244	0.0376512	337	0.144936	0.0976875
294	0.026467	0.0387244	338	0.149131	0.0989689
295	0.027719	0.0398118	339	0.153338	0.1001723
296	0.029005	0.0409049	340	0.157595	0.1013306
297	0.030331	0.0419951	341	0.161920	0.1024808
298	0.031705	0.0430744	342	0.166300	0.1036552
299	0.033135	0.0441374	343	0.170704	0.1048637
300	0.034625	0.0451910	344	0.175113	0.1060738

345	0.179538	0.1072535	389	0.397436	0.1301838
346	0.184019	0.1083824	390	0.402758	0.1300529
347	0.188597	0.1094731	391	0.408023	0.1299024
348	0.193298	0.1105472	392	0.413232	0.1297204
349	0.198117	0.1116219	393	0.418407	0.1294952
350	0.203017	0.1127089	394	0.423586	0.1292192
351	0.207936	0.1137959	395	0.428806	0.1288957
352	0.212842	0.1148530	396	0.434089	0.1285298
353	0.217746	0.1158608	397	0.439437	0.1281279
354	0.222683	0.1168225	398	0.444833	0.1276985
355	0.227678	0.1177499	399	0.450239	0.1272485
356	0.232739	0.1186516	400	0.455619	0.1267754
357	0.237855	0.1195334	401	0.460957	0.1262739
358	0.242995	0.1203955	402	0.466257	0.1257373
359	0.248127	0.1212286	403	0.471538	0.1251583
360	0.253229	0.1220243	404	0.476827	0.1245352
361	0.258298	0.1227770	405	0.482144	0.1238690
362	0.263337	0.1234852	406	0.487498	0.1231618
363	0.268353	0.1241502	407	0.492888	0.1224171
364	0.273354	0.1247730	408	0.498299	0.1216395
365	0.278348	0.1253550	409	0.503718	0.1208298
366	0.283341	0.1259032	410	0.509140	0.1199870
367	0.288325	0.1264330	411	0.514569	0.1191078
368	0.293278	0.1269583	412	0.520025	0.1181874
369	0.298164	0.1274910	413	0.525533	0.1172250
370	0.302944	0.1280240	414	0.531110	0.1162276
371	0.307607	0.1285249	415	0.536754	0.1152068
372	0.312180	0.1289660	416	0.542442	0.1141781
373	0.316711	0.1293247	417	0.548133	0.1131491
374	0.321265	0.1295978	418	0.553797	0.1121183
375	0.325898	0.1298029	419	0.559416	0.1110812
376	0.330652	0.1299572	420	0.564991	0.1100309
377	0.335549	0.1300782	421	0.570533	0.1089581
378	0.340588	0.1301860	422	0.576069	0.1078538
379	0.345727	0.1303013	423	0.581625	0.1067179
380	0.350898	0.1304230	424	0.587222	0.1055535
381	0.356049	0.1305362	425	0.592870	0.1043662
382	0.361155	0.1306268	426	0.598570	0.1031639
383	0.366218	0.1306821	427	0.604309	0.1019578
384	0.371265	0.1306900	428	0.610064	0.1007557
385	0.376344	0.1306424	429	0.615813	0.0995535
386	0.381501	0.1305506	430	0.621551	0.0983422
387	0.386754	0.1304321	431	0.627288	0.0971101
388	0.392085	0.1303068	432	0.633044	0.0958506

433	0.638838	0.0945634	477	0.897252	0.0351376
434	0.644683	0.0932503	478	0.902813	0.0337433
435	0.650580	0.0919154	479	0.908237	0.0323674
436	0.656524	0.0905647	480	0.913529	0.0310022
437	0.662497	0.0892067	481	0.918707	0.0296370
438	0.668476	0.0878460	482	0.923802	0.0282581
439	0.674444	0.0864840	483	0.928853	0.0268521
440	0.680388	0.0851206	484	0.933888	0.0254163
441	0.686305	0.0837550	485	0.938909	0.0239573
442	0.692196	0.0823898	486	0.943889	0.0224902
443	0.698063	0.0810290	487	0.948776	0.0210374
444	0.703912	0.0796765	488	0.953503	0.0196254
445	0.709748	0.0783357	489	0.958009	0.0182699
446	0.715578	0.0770095	490	0.962265	0.0169506
447	0.721409	0.0756998	491	0.966287	0.0156372
448	0.727246	0.0744011	492	0.970116	0.0142988
449	0.733093	0.0731060	493	0.973801	0.0129036
450	0.738951	0.0718077	494	0.977394	0.0114324
451	0.744816	0.0704997	495	0.980934	0.0098812
452	0.750688	0.0691798	496	0.984445	0.0082500
453	0.756564	0.0678532	497	0.987938	0.0065427
454	0.762443	0.0665259	498	0.991413	0.0047629
455	0.768327	0.0652038	499	0.994866	0.0029111
456	0.774215	0.0638914	500	0.998295	0.0009880
457	0.780107	0.0625870	501	1.000000	0.0000000
458	0.786003	0.0612869			
459	0.791901	0.0599875			
460	0.797800	0.0586851			
461	0.803700	0.0573761			
462	0.809598	0.0560571			
463	0.815494	0.0547267			
464	0.821386	0.0533849			
465	0.827274	0.0520319			
466	0.833157	0.0506681			
467	0.839032	0.0492937			
468	0.844898	0.0479095			
469	0.850757	0.0465161			
470	0.856609	0.0451140			
471	0.862457	0.0437030			
472	0.868305	0.0422829			
473	0.874153	0.0408542			
474	0.879994	0.0394192			
475	0.885809	0.0379831			
476	0.891573	0.0365529			

Υπολογιστική και πειραματική μελέτη της τρισδιάστατης αποκόλλησης σε αεροτομές και έλεγχος αυτής με χρήση στροβιλογεννητριών

Σύνοψη

Η συγκεκριμένη διδακτορική διατριβή ασχολείται με την τρισδιάστατη αποκόλληση σε αεροτομές και συγκεκριμένα με την αποκόλληση όπου εμφανίζονται κυψέλες ανακυκλοφορίας (Stall Cells - SCs). Μελετάται τόσο η φύση της αποκόλλησης όσο και η δυνατότητα ελέγχου αυτής με παθητικές γεννήτριες στροβιλότητας (passive Vortex Generators - VGs).

Το πρόβλημα προσεγγίστηκε τόσο πειραματικά όσο και υπολογιστικά. Στην αεροσήραγγα του ΕΜΠ εκτελέστηκαν πειράματα οπτικοποίησης της ροής, μετρήσεις πιέσεων και μετρήσεις Stereo Particle Image Velocimetry (SPIV) ενώ, υπολογιστικά, χρησιμοποιήθηκε ο κώδικας MaPFlow, ένας επιλύτης των μη μόνιμων Reynolds Averaged εξισώσεων Navier-Stokes.

Ο ασταθής χαρακτήρας των Stall Cells επιβεβαιώθηκε μέσω πειραμάτων με νημάτια (tufts) και βρέθηκε ότι η εγγενής αστάθεια των δομών αυτών μπορεί να κατασταλεί με χρήση αρκετά μεγάλων μόνιμων διαταραχών κατά το εκπέτασμα της πτέρυγας. Τα υπολογιστικά αποτελέσματα αποκάλυψαν μία σύνθετη δομή στροβίλων στο εσωτερικό των Stall Cells, μία δομή η οποία επιβεβαιώθηκε από τις πειραματικές μετρήσεις.

Συγκεκριμένα, ένα Stall Cell αποτελείται από στροβίλους τριών διαφορετικών τύπων:

- Τους Stall Cell στροβίλους που αρχικά ξεκινούν κάθετα από την επιφάνεια της πτέρυγας στην περιοχή ανακυκλοφορίας και στη συνέχεια εκτείνονται στον ομόρρου, παράλληλα με την ελεύθερη ροή.
- Τον στρόβιλο της γραμμής αποκόλλησης που εκτείνεται παράλληλα με το εκπέτασμα της πτέρυγας.
- Τον στρόβιλο της ακμής εκφυγής που επίσης εκτείνεται παράλληλα με το εκπέτασμα της πτέρυγας, αλλά έχει περιστροφή από τον στρόβιλο της γραμμής αποκόλλησης.

Η μελέτη των χαρακτηριστικών της τύρβης της ροής δείχνει πως η ροή στο εσωτερικό ενός Stall Cell είναι έντονα ανισότροπη. Το γεγονός πως τα υπολογιστικά αποτελέσματα προβλέπουν τη ροή ποιοτικά σωστά, παρ' όλο που αδυνατούν να προλέξουν ορθά τις λεπτομέρειες της τύρβης, αποδίδεται στο γεγονός ότι το ισότροπο μοντέλο τύρβης που χρησιμοποιήθηκε δίνει ποιοτικά σωστά τις διατμητικές τάσεις. Τέλος, ένας μηχανισμός δημιουργίας των Stall Cells προτείνεται βασισμένος στην συνολική έρευνα.

Σχετικά με τον έλεγχο της τρισδιάστατης αποκόλλησης βρέθηκε ότι αύτη μπορεί να κατασταλεί με χρήση τριγωνικών passive Vortex Generators (VGs). Παρατηρήθηκε ακόμα ότι ανάλογα με τη γωνία πρόσπτωσης της πτέρυγας και με τη θέση των VGs είναι δυνατόν να εμφανιστούν φαινόμενα αστάθειας της ροής. Επίσης, αποδείχθηκε ότι υπολογισμοί σε πτέρυγες με πολύ χαμηλό λόγο επιμήκους αδυνατούν να προλέξουν την εμφάνιση των Stall Cells και δίνουν παραπλανητικά αποτελέσματα όσον αφορά την απόδοση των VGs. Οι μετρήσεις SPIV έδειξαν ότι κοντά στα VGs είναι έντονη η τυρβώδης αλληλεπίδραση μεταξύ των στροβίλων ενώ σε μεγαλύτερη απόσταση η εξέλιξη της ροής κυριαρχείται από την διάχυση .

Συνολικά, η έρευνα αυτή έρχεται σε συνέχεια προηγουμένων που σημείωναν την ανάγκη προσεκτικής καταγραφής και χρήσης των πειραματικών δεδομένων, ειδικά στην περίπτωση της αποκολλημένης ροής. Η συνήθης υπόθεση της δισδιάστατης ροής γύρω από αεροτομή δεν ισχύει στην περίπτωση που δημιουργούνται Stall Cells. Επιπλέον, το τρισδιάστατο της αποκολλημένης ροής θα πρέπει να λαμβάνεται υπ' όψιν σε σχέση με τον έλεγχο της ροής.

Περιεχόμενα

1 Εισαγωγή

1.1 Κίνητρο

Η τρισδιάστατη αποκόλληση τύπου κυψελών αποκόλλησης (Stall Cells - SCs) απαντάται σε πλήθος εφαρμογών εξωτερικής ροής, όπως π.χ. η αποκολλημένη ροή σε επίπεδες πλάκες, κυλίνδρους (Winkelmann, 1982), σε διαφόρους τύπους πτερύγων (Lockman & Seegmiller, 1983; Murri & Jordan, 1987; Ross & Perkins, 1994; Flynn et al., 2001; Supamusdisukul, 2008; Hahn et al., 2010; Dropkin et al., 2012), σε αποκόλληση πίσω από κύμα κρούσης ή σε πτέρυγες που προσομοιάζουν το προφίλ πτερυγίου φάλαινας.

Παρά τη συχνότητα εμφάνισής τους, ωστόσο, η γνώση γύρω από τα SCs παραμένει περιορισμένη. Μέχρι πρόσφατα, στην δημοσιευμένη βιβλιογραφία, τα μοντέλα αεροτομών που εμφάνιζαν SCs είτε δεν χρησιμοποιούνταν (Fuglsang & Bove, 2008) είτε μελετούνταν μόνο μέχρι την εμφάνιση των SCs (Gleyzes & Capbern, 2003). Εξάλλου, από πολύ νωρίς (Gregory & O'Reilly, 1970) είχαν διατυπωθεί ενστάσεις σχετικά με την αξιοπιστία πειραμάτων δισδιάστατων μοντέλων αεροτομών στην περίπτωση δημιουργίας SCs.

Πέρα από το δεδομένο κενό γνώσης γύρω από την τρισδιάστατη αποκόλληση, τα SCs είναι ιδιαίτερης σημασίας για την βιομηχανία αιολικής ενέργειας για τους παρακάτω λόγους:

1. Εμφανίζονται σε ανεμογεννήτριες εν στάσει (Sorensen and Schreck, 2010)
2. Εμφανίζονται σε πειραματικά μοντέλα αεροτομών που έχουν σχεδιαστεί ή χρησιμοποιούνται σε πτερύγια ανεμογεννητριών (NACA 6 series, DU family airfoils)
3. Εκτιμάται (Tangler, 2002) ότι η μεγαλύτερη πηγή σφάλματος στον υπολογισμό της απόδοσης ανεμογεννητριών είναι η ακρίβεια στη πειραματικά δεδομένα αεροτομών.

Το πρώτο μέρος της παρούσας έρευνας αφιερώθηκε τόσο στη βασική μελέτη των SCs αλλά και ειδικότερα σε συνάρτηση με την ακρίβεια των πειραματικών μετρήσεων μοντέλων αεροτομών. Το δεύτερο μέρος αφορούσε την μελέτη της δυνατότητας ελέγχου της δημιουργίας SCs με τη χρήση παθητικών γεννητριών στροβιλότητας (passive Vortex Generators - VGs).

Υπάρχουν πολλοί διαφορετικοί τύποι VGs, αλλά ο τρόπος λειτουργίας είναι κοινός: δημιουργούν διαμήκεις στροβίλους οι οποίοι ενεργοποιούν το οριακό στρώμα μεταφέροντας ρευστό υψηλής ορμής προς το τοίχωμα. Με το τρόπο αυτό καθυστερεί την αποκόλληση ως προς την γωνία πρόσπτωσης. Στα πλεονεκτήματα των VGs ως μεθόδου ελέγχου της αποκόλλησης περιλαμβάνονται το μικρό βάρος, η αξιοπιστία τους και ο εξαιρετικά εύκολος τρόπος κατασκευής και τοποθέτησης. Επιπρόσθετα, έχουν αποδειχθεί αποτελεσματικά σε πλήθος διαφορετικών εφαρμογών (αεροπορική βιομηχανία (Ashill et al., 2001; Seshagiri et al., 2009), αιολική ενέργεια (Øye, 1995), αυτοκινητοβιομηχανία (Aider et al., 2009), εσωτερικές ροές (Wendt et al., 1995), μείωση θορύβου (Holmes et al., 1987) κ.ά..

Αν και η πρώτη χρήση VGs για έλεγχο της αποκόλλησης χρονολογείται ήδη από 1950 (Taylor, 1950), ο μηχανισμός ελέγχου της ροής δεν έχει κατανοηθεί πλήρως και ο αριθμός των λεπτομερών πειραματικών μελετών είναι περιορισμένος.

1.2 Στόχος

Οι στόχος της συγκεκριμένης εργασίας ήταν να πραγματοποιηθούν πειραματικές μετρήσεις και προσομοιώσεις που από τη μία να οδηγήσουν σε βαθύτερη κατανόηση της τρισδιάστατης αποκόλλησης σε αεροτομές και από την άλλη να εξετάσουν τη δυνατότητα ελέγχου της με χρήση παθητικών γεννητριών στροβιλότητας. Ειδικότερα, ενδιάμεσοι στόχοι-ορόσημα κατά τη διάρκεια της μελέτης ήταν οι ακόλουθοι:

- Η μελέτη της δυναμικής φύσης των SCs.
- Η πιστοποίηση των υπολογιστικών προσομοιώσεων με βάση τα πειραματικά αποτελέσματα.
- Η πειραματική μελέτη των SCs.
- Η βελτιστοποίηση της διάταξη των VGs
- Η πειραματική μελέτη των στροβίλων που παράγονται από τα VGs.

1.3 Εργαλεία

1.3.1 Πειραματική διάταξη

Όλα τα πειράματα πραγματοποιήθηκαν στο μικρό τμήμα δοκιμών της αεροσήραγγας του Ε.Μ.Π.. Η μορφή της αεροτομής που χρησιμοποιήθηκε έχει βελτιστοποιηθεί για χρήση σε ανεμογεννήτριες μεταβλητής ταχύτητας και πολλών MW (Mourikis et al., 2005). Για τον περιορισμό της επίδρασης του οριακού στρώματος χρησιμοποιήθηκαν διαμήκεις φραγμοί (fences) οι οποίοι παρουσιάζονται στο Σχήμα 1, αριστερά. Μία σχηματική απεικόνιση της πειραματικής διάταξης δίνεται στο δεξί μέρος στο Σχήμα 1.

Ο υπολογισμός του συντελεστή άνωσης (Cl) της αεροτομής έγινε με ολοκλήρωση της πίεσης γύρω από την αεροτομή. Η πίεση μετρήθηκε μέσω οπών στο κεντρικό τμήμα της πτέρυγας. Ο συντελεστής αντίστασης (Cd) υπολογίστηκε από την πίεση στον ομόρρου της πτέρυγας η οποία μετρήθηκε με τη χρήση ενός wake rake.

Για της μετρήσεις Stereo Particle Image Velocimetry (SPIV) χρησιμοποιήθηκαν δύο 4MP κάμερες τοποθετημένες στο εσωτερικό του τμήματος δοκιμών, όπως φαίνεται στο Σχήμα 2. Οι κάμερες είχαν περιορισμένη ταλάντωση με το εξ αυτής σφάλμα να είναι μία τάξη μεγέθους μικρότερο της ελάχιστης μετρούμενης ταχύτητας από το σύστημα SPIV, και κατά συνέπεια αμελητέο.

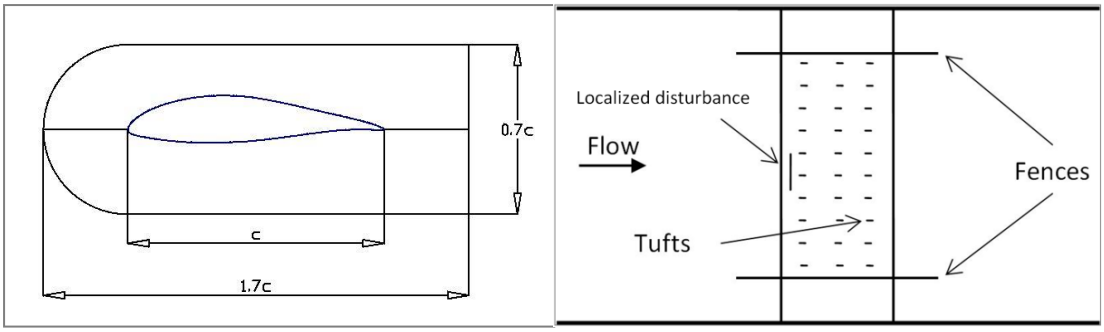

Σχήμα 1: Σχήμα των fences (αριστερά) και σχηματική απεικόνιση της πειραματικής διάταξης με fences και νημάτια (tufts).

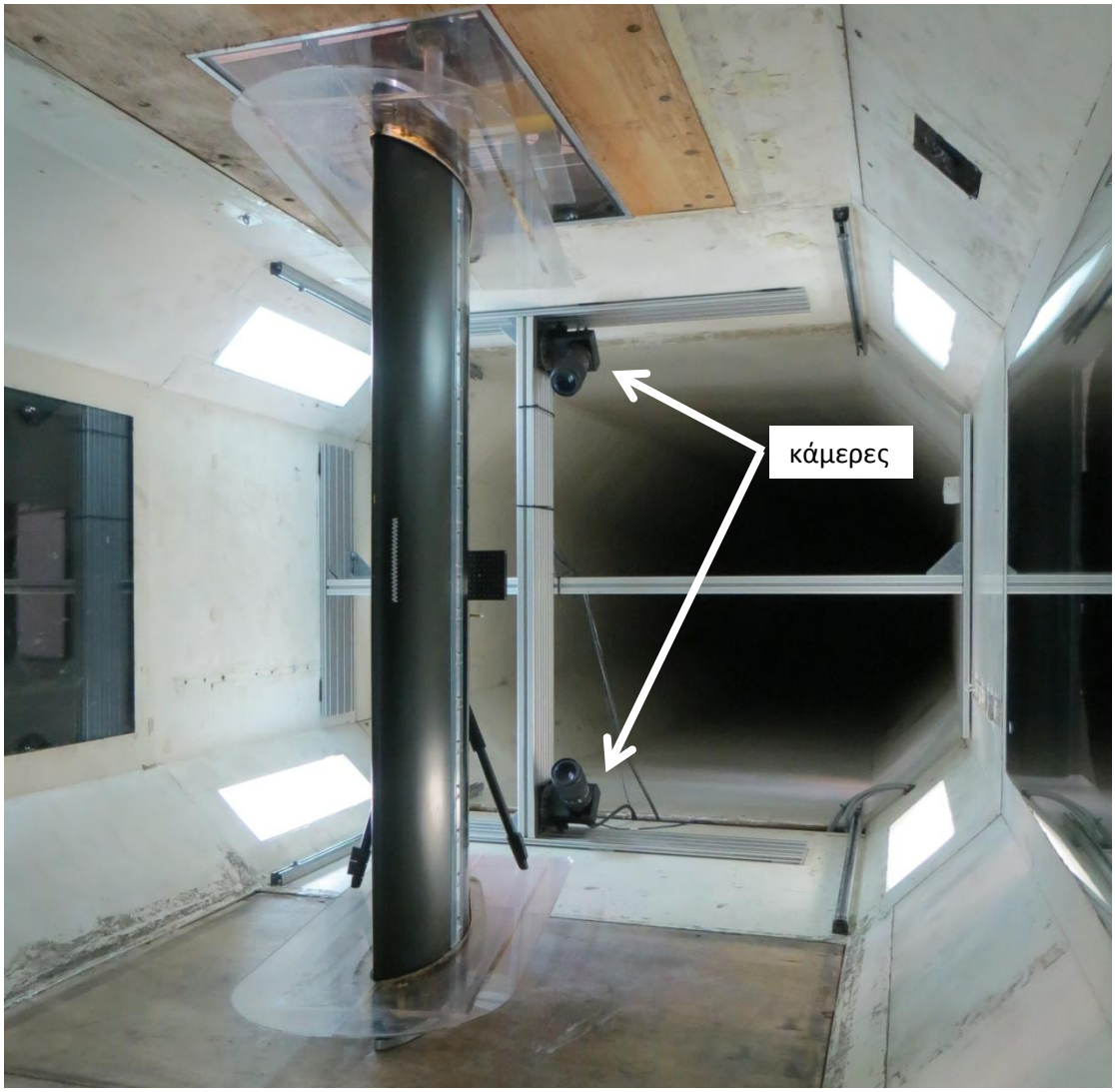

Σχήμα 2: Άποψη του τμήματος δοκιμών με τις SPIV κάμερες.

1.3.2 Υπολογιστικά εργαλεία

Για την υπολογιστική προσομοίωση της ροής χρησιμοποιήθηκε ο κώδικας MaPFlow (Papadakis, 2011) που έχει αναπτυχθεί από το εργαστήριο αεροδυναμικής. Πρόκειται για έναν επιλύτη των μη μόνιμων Reynolds Averaged Navier-Stokes εξισώσεων. Σε όλα τα αποτελέσματα που περιέχονται σε αυτό το κείμενο χρησιμοποιήθηκε το μοντέλο τύρβης των Spalart & Allmaras (Spalart & Allmaras, 1992).

Για την μοντελοποίηση των VGs χρησιμοποιήθηκε το μοντέλο BAY (Bender et al., 1999). Σύμφωνα με αυτό ένα VG αναπαρίσταται από έναν όρο πηγής στις εξισώσεις ορμής και ενέργειας. Ο όρος αυτός προσομοιώνει την δύναμη άνωσης που ασκείται από το VG στο ρευστό και έχει ως αποτέλεσμα να ευθυγραμμίζει τοπικά τη ροή με τη επιφάνεια του VG.

2 Γεωμετρικός χαρακτηρισμός των Stall Cells

2.1 Σταθεροποίηση των SCs

Τα πειράματα οπτικοποίησης της ροής με νημάτια επιβεβαίωσαν τον ασταθή χαρακτήρα των SCs. Σαν παράδειγμα το Σχήμα 3 δείχνει ότι περισσότερες από μία καταστάσεις είναι πιθανές όταν εμφανίζονται SCs. Συγκεκριμένα τα SCs μπορεί να ταξιδεύουν κατά το εκπέτασμα της πτέρυγας και να σχηματίζονται ή καταστρέφονται με τυχαίο τρόπο. Ούτε στην παρούσα έρευνα ούτε στη βιβλιογραφία έχει βρεθεί κάποια συσχέτιση της ασταθούς αυτής συμπεριφοράς με τον αριθμό Reynolds, την γωνία πρόσπτωσης ή το λόγο επιμήκους της πτέρυγας. Η αστάθεια αυτή ωστόσο μειώνει την επαναληψιμότητα του πειράματος και δυσχεραίνει εξαιρετικά την αξιόπιστη μελέτη των SCs.

Βρέθηκε ότι είναι δυνατόν να σταθεροποιηθεί η αποκολλημένη ροή σε μία θέση με τη χρήση μιας τοπικής διαταραχής (localized disturbance) με τη μορφή μιας ταινίας μετάβασης (zigzag tape - ZZ tape). Η ταινία μετάβασης τοποθετήθηκε στο 2% της χορδής και μόνο για 10% του εκπετάσματος της πτέρυγας. Στο Σχήμα 4, αριστερά, φαίνεται η γεωμετρία της ταινίας και, δεξιά, η ροή στην πτέρυγα με την ταινία μετάβασης.

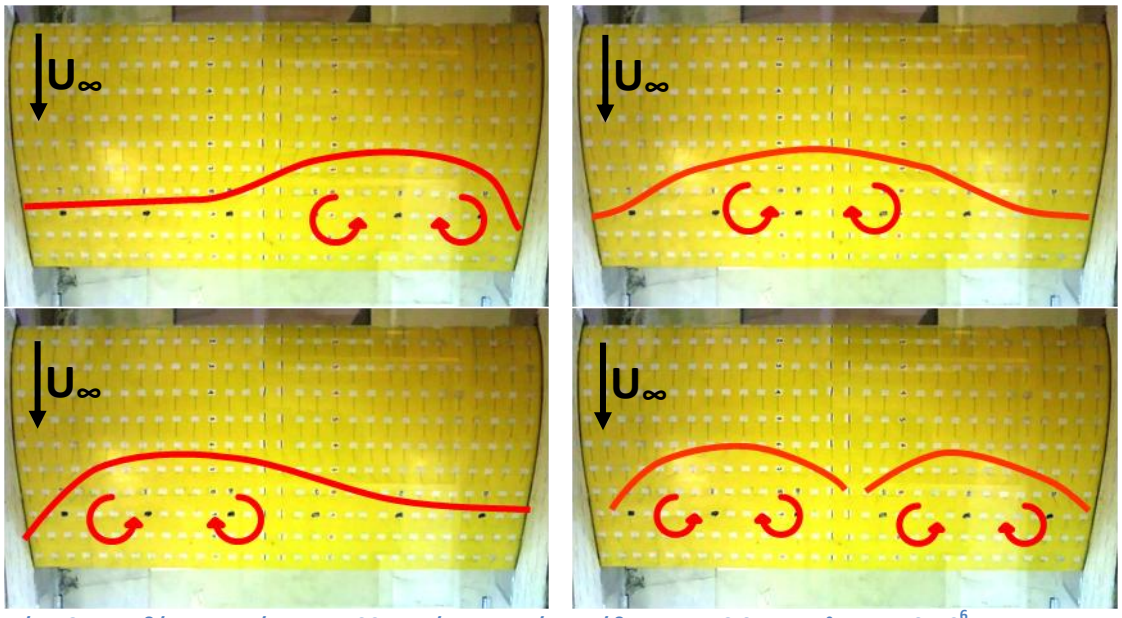

Σχήμα 3: Ασταθής χαρακτήρας των SCs χωρίς την ταινία μετάβασης. AR 2.0, α = 11°, Re = 1.0x10^6

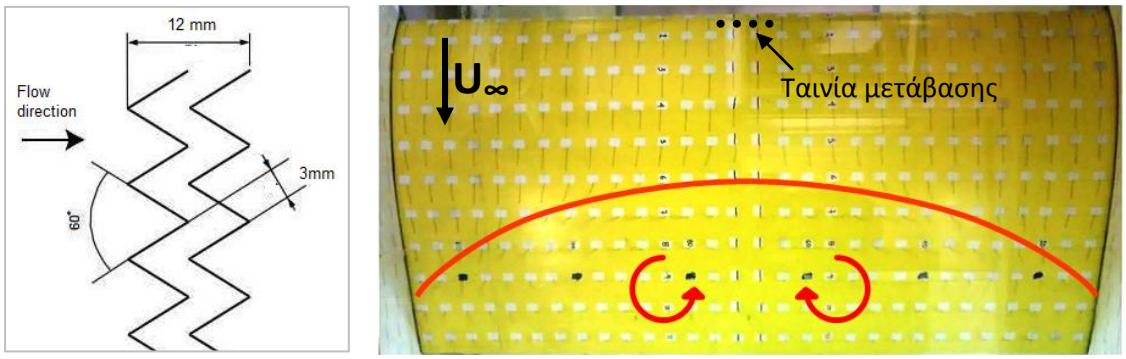

Σχήμα 4: Γεωμετρία της ταινίας μετάβασης (αριστερά) και η ροή στην πτέρυγα με την ταινία μετάβασης. AR 2.0, α = 11°, Re = 1.0x10^6

2.2 Επίδραση της ταινίας μετάβασης

Η επίδραση της ταινίας μετάβασης μελετήθηκε με βάση τα ακόλουθα μεγέθη:

- Το πλέον ανάντη σημείο αποκολλημένης ροής (earliest point of separation), όπως αυτό φαίνεται με κόκκινο βέλος στο Σχήμα 5.
- Την επιφάνεια του SC (κόκκινη κλειστή καμπύλη στο Σχήμα 6) σαν ποσοστό της συνολικής επιφάνειας της πτέρυγας (μπλε περίγραμμα στο Σχήμα 6).

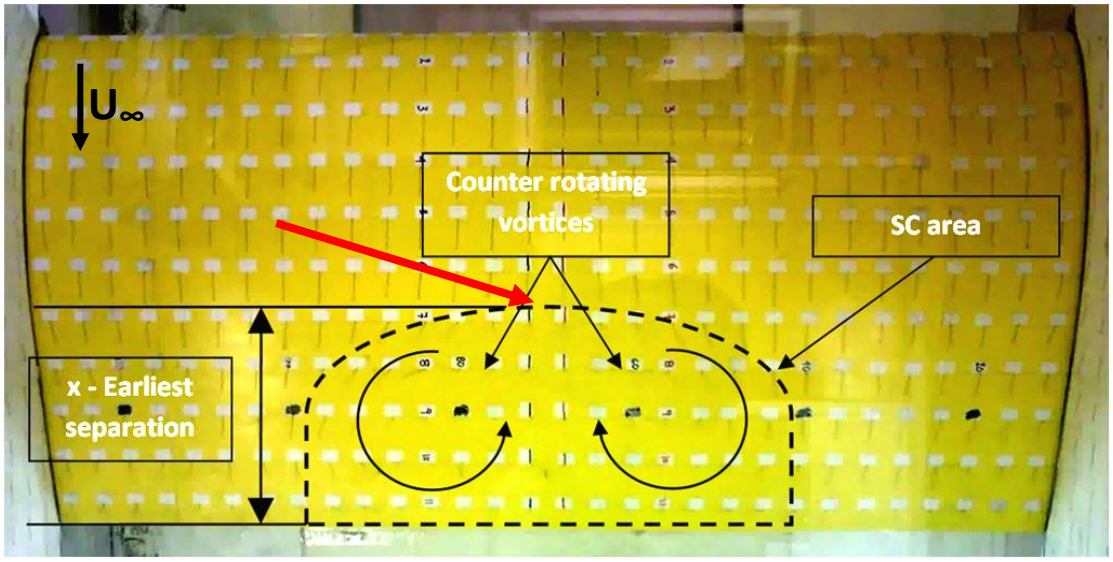

Σχήμα 5: Ορισμός του πλέον ανάντη σημείου αποκολλημένης ροής.

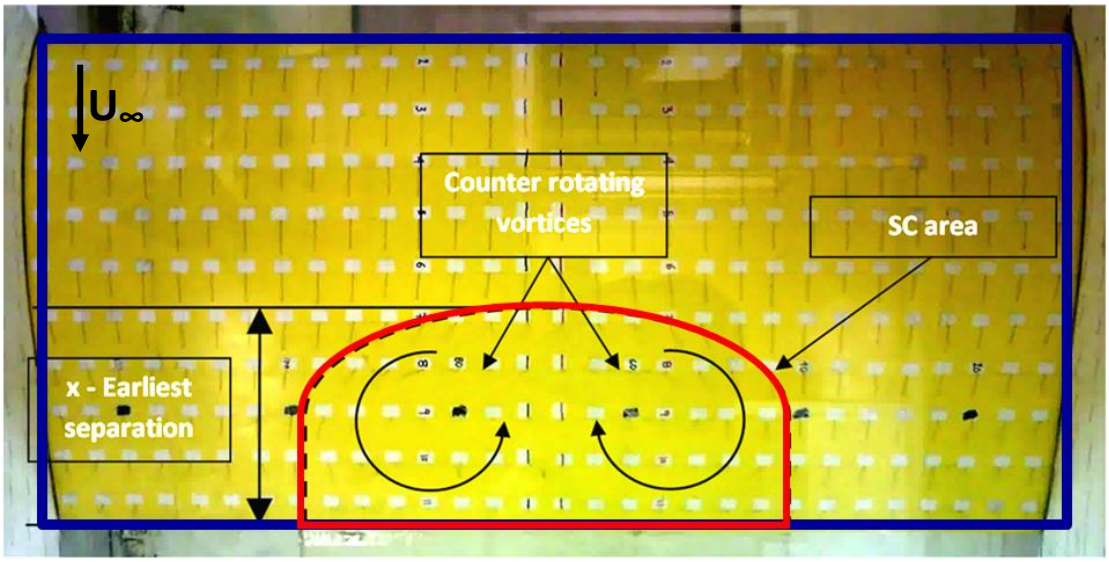

Σχήμα 6: Η επιφάνεια του SC σε σχέση με τη συνολική επιφάνεια της πτέρυγας.

Τα αποτελέσματα δείχνουν ότι η χρήση της ταινίας μετάβασης οδηγεί σε δημιουργία του SC σε χαμηλότερη γωνία προσβολής, αλλά δεν επηρεάζει σημαντικά την σχετική επιφάνεια του SC ή το σημείο αποκόλλησης σε μεγαλύτερες γωνίες, όπως δείχνουν το Σχήμα 7 και το Σχήμα 8. Εάν δεν αναφέρεται κάτι διαφορετικό, στο υπόλοιπο της εργασίας τα αποτελέσματα θα αναφέρονται στην περίπτωση με ταινία μετάβασης.

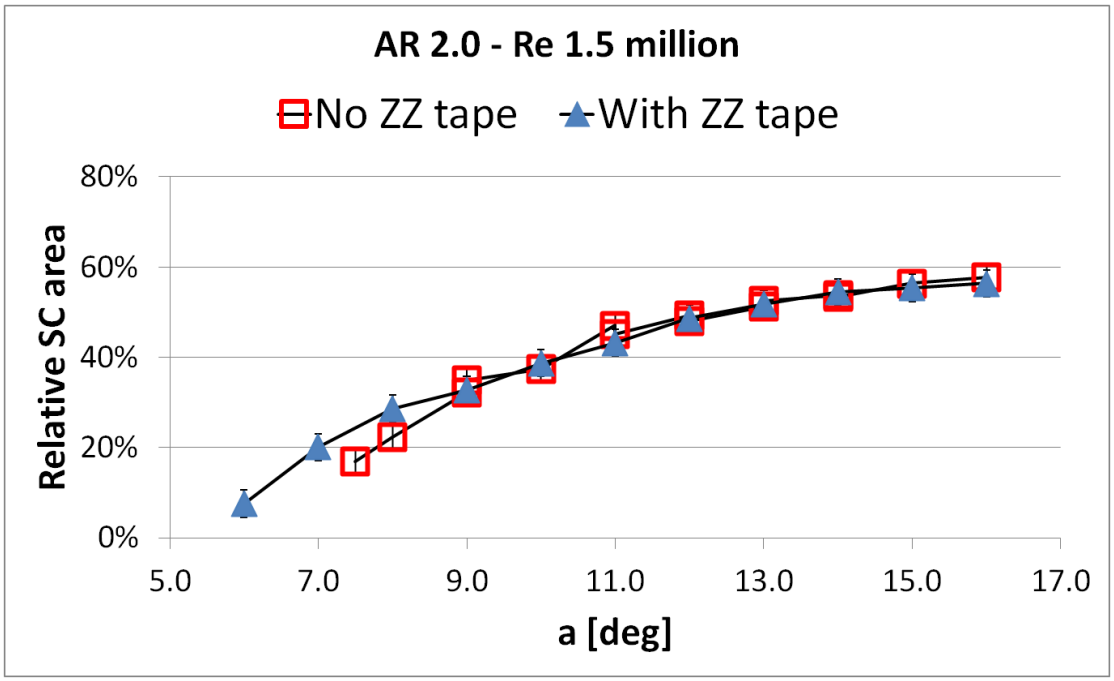

Σχήμα 7: Μεταβολή της σχετικής επιφάνειας του SC με τη γωνία πρόσπτωσης για τις περιπτώσεις με και χωρίς ταινία μετάβασης. AR 2.0, Re = 1.5×10^6.

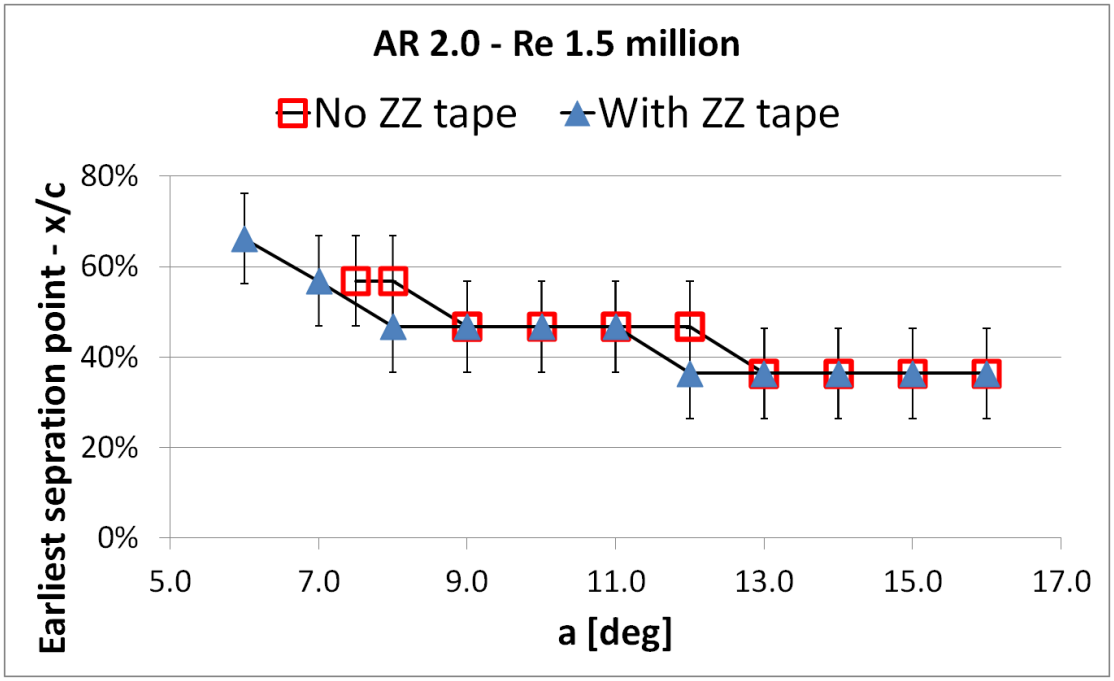

Σχήμα 8: Μεταβολή του πλέον ανάντη σημείου αποκολλημένης ροής με τη γωνία πρόσπτωσης για τις περιπτώσεις με και χωρίς ταινία μετάβασης. AR 2.0, Re = 1.5×10^6.

3 Πιστοποίηση του υπολογιστικού κώδικα

Η σύγκριση του πειραματικού συντελεστή άνωσης και αντίστασης με το συντελεστή άνωσης για δισδιάστατους και τρισδιάστατους υπολογισμούς δίνεται στο Σχήμα 9 και το Σχήμα 10, αντίστοιχα. Ειδικά για το Cl, στο γραμμικό κομμάτι της καμπύλης υπάρχει συμφωνία μεταξύ των τριών τιμών, ενώ σε μεγαλύτερες γωνίες προσβολής μόνο οι τρισδιάστατοι υπολογισμοί δίνουν ποιοτικά σωστά αποτελέσματα.

Πιο αναλυτικά, στο Σχήμα 11 γίνεται σύγκριση της κατανομής πίεσης κατά μήκος της αεροτομής για α=7°, όπου υπάρχει πολύ καλή συμφωνία μεταξύ μετρήσεων και 2Δ και 3Δ υπολογισμών. Το Σχήμα 12 δείχνει την ίδια κατανομή πιέσεων, αλλά για α=10°. Πλέον οι διαφορές μεταξύ των τριών καμπυλών είναι σημαντικές. Στο πείραμα το SC είναι σημαντικά ανεπτυγμένο, με την αποκόλληση να φτάνει στο x=0.5c και σχετικά μειωμένη μέγιστη υποπίεση. Στους 3Δ υπολογισμούς το SC έχει δημιουργηθεί, αλλά με 3° διαφορά (καθυστέρηση) σε σχέση με το πείραμα γεγονός που οδηγεί σε αισθητά μικρότερο μέγεθος. Στην 2Δ προσομοίωση η αποκόλληση είναι πολύ περιορισμένη και η κατανομή της πίεσης διαφέρει σημαντικά, από την πειραματική. Στις 16° (Σχήμα 13) η συμφωνία των 3Δ υπολογισμών με το πείραμα είναι ακόμα καλύτερη, ενώ τα 2Δ αποτελέσματα αποτυγχάνουν να προβλέψουν σωστά τόσο το μέγεθος της αποκολλημένης περιοχής όσο και τη μέγιστη υποπίεση.

Με βάση τα αποτελέσματα αυτά κρίνεται πως οι 3Δ υπολογισμοί μπορούν να δώσουν ποιοτικά σωστά αποτελέσματα στην περιοχή γωνιών πρόσπτωσης μετά τη μέγιστη τιμή του Cl. Αντίθετα, η 2Δ προσομοίωση μίας εγγενώς 3Δ ροής δίνει, όπως ήταν αναμενόμενο, παραπλανητικά αποτελέσματα.

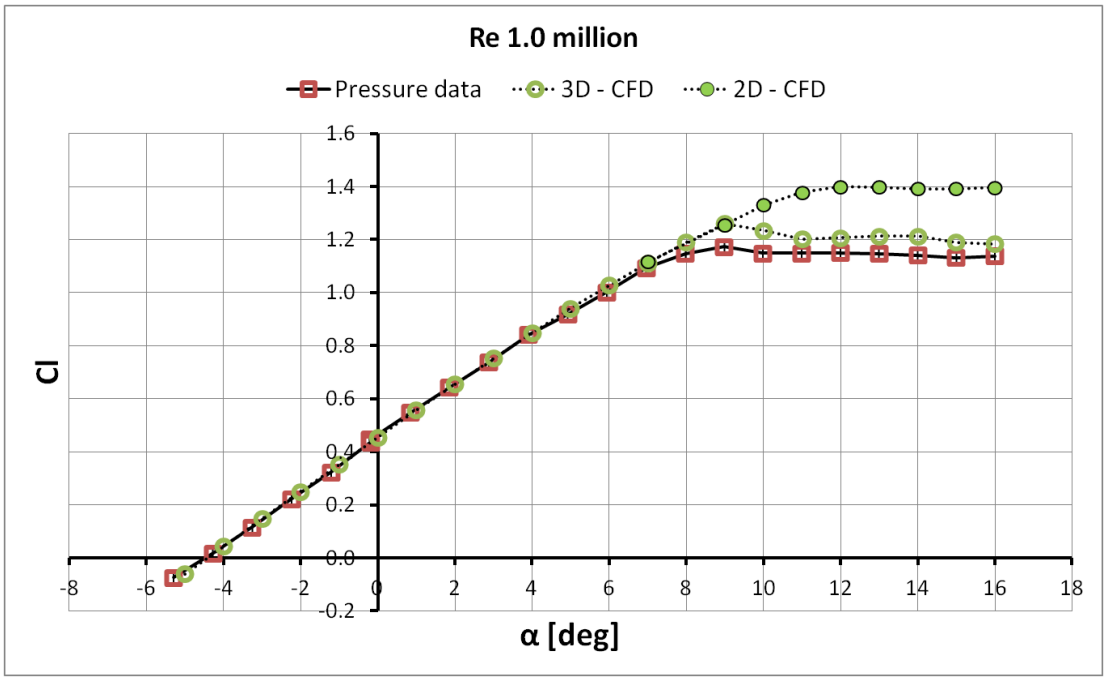

Σχήμα 9: Μεταβολή του Cl με τη γωνία προσβολής. AR = 2.0, Re = 1.0x10^6.

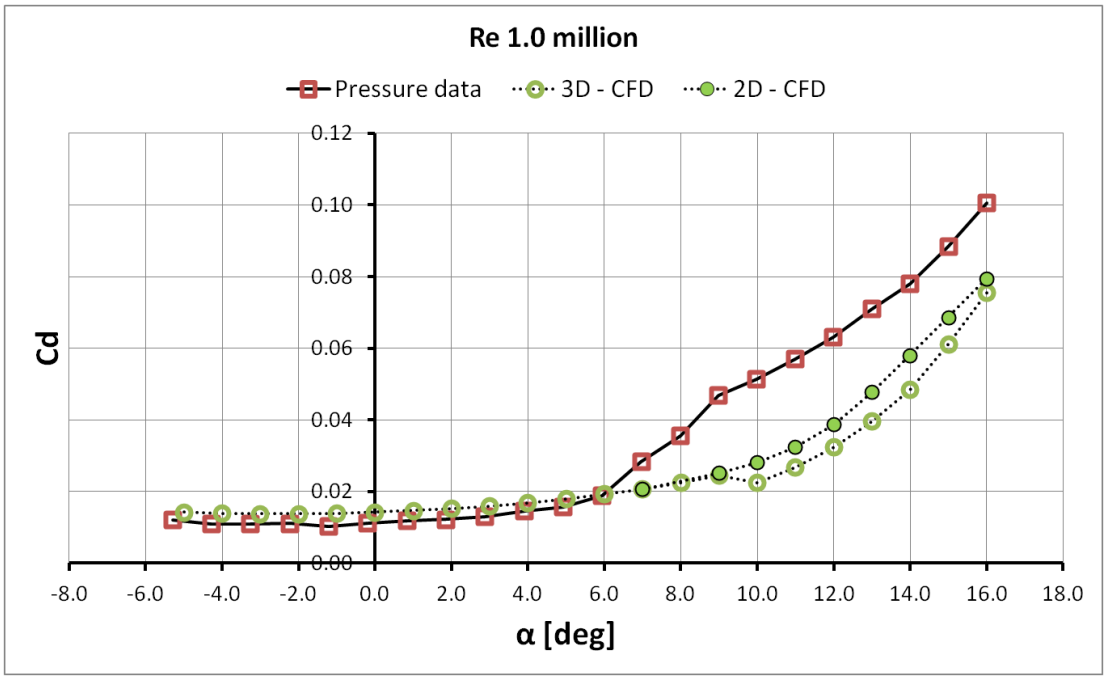

Σχήμα 10: Μεταβολή του Cd με τη γωνία προσβολής. AR = 2.0, Re = 1.0×10^6.

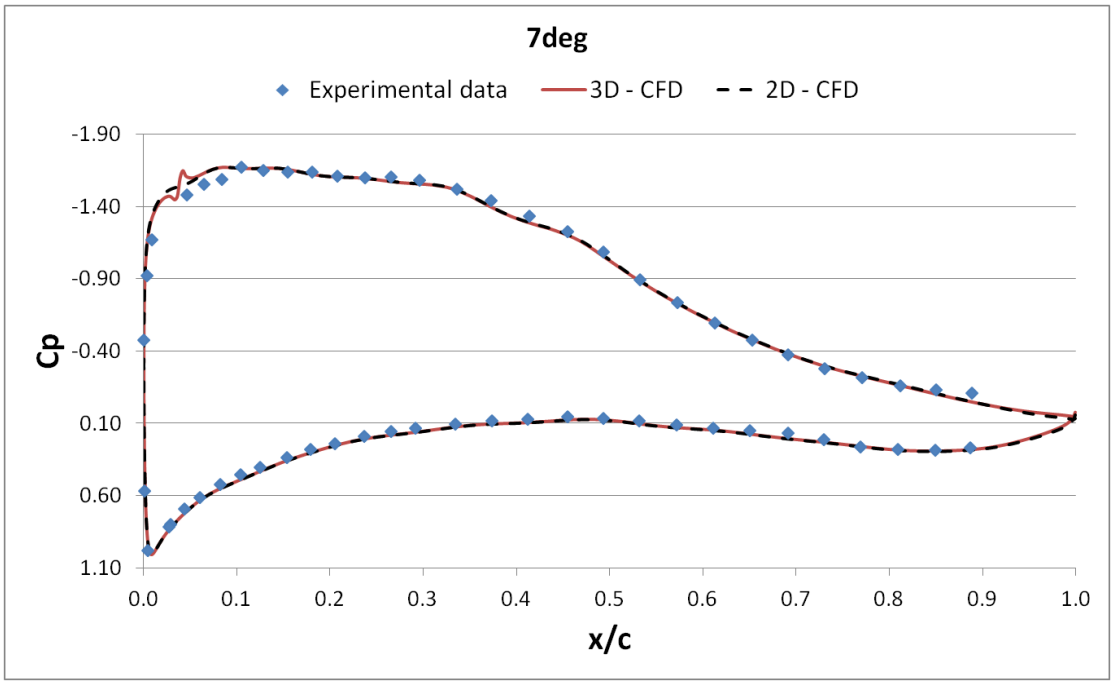

Σχήμα 11: Κατανομή του συντελεστή πίεσης για AR = 2.0, Re = 1.0×10^6, α = 7^o.

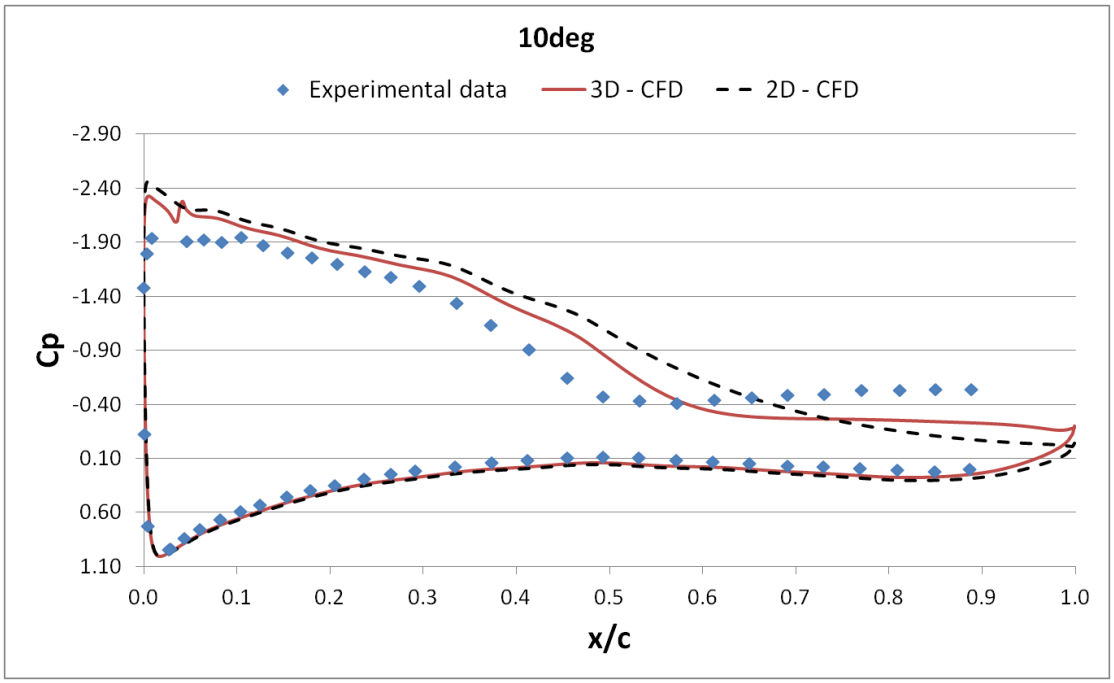

Σχήμα 12: Κατανομή του συντελεστή πίεσης για AR = 2.0, Re = 1.0×10^6, α = 10^o.

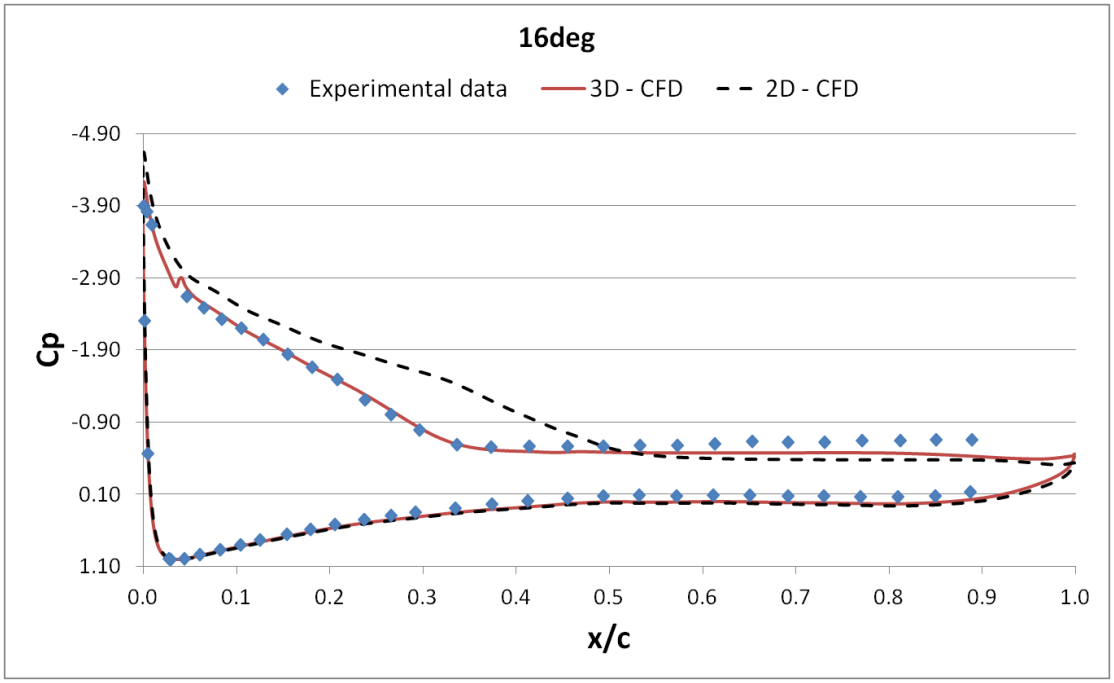

Σχήμα 13: Κατανομή του συντελεστή πίεσης για AR = 2.0, Re = 1.0×10^6, α = 16^o.

4 Η δομή στο εσωτερικό ενός SC

Με βάση τους 3Δ υπολογισμούς γίνεται μια ποιοτική ανάλυση των στροβίλων στο εσωτερικό ενός SC. Στο Σχήμα 14, στις επιφανειακές γραμμές ροής, εμφανίζεται το κέντρο του SC στροβίλου στην πλευρά υποπίεσης της αεροτομής. Επιπρόσθετα, στο επίπεδο συμμετρίας εμφανίζονται δύο ακόμα κέντρα στροβίλων, ένα του στροβίλου της γραμμής αποκόλλησης (Separation Line Vortex - SLV) και ένα του στροβίλου της ακμής εκφυγής (Trailing Edge Line Vortex - TELV).

Η πλάγια όψη του χείλους εκφυγής με 2Δ γραμμές ροής παρουσιάζεται στο Σχήμα 15. Είναι σαφές ότι το κέντρο του SLV κινείται ανάντη και ψηλότερα προς το κέντρο του SC. Αντίστοιχα το κέντρο του TELV κινείται κατάντη και ψηλότερα στο κέντρο του SC. Επίσης, ο TELV είναι ασθενέστερος στα άκρα του SC καθώς οι γραμμές ροής δεν είναι κυκλικές.

Όπως φαίνεται στο Σχήμα 16, ο SC στρόβιλος που ξεκινά από την επιφάνεια της πτέρυγας μέχρι να φτάσει στο χείλος εκφυγής έχει μετατοπιστεί προς το εσωτερικό του SC και έχει πλέον σημαντική συνιστώσα στροβιλότητας παράλληλη με τη διεύθυνση X. Στον ομόρρου, όπως δείχνει το Σχήμα 17, το κέντρο του SC στροβίλου παραμένει σταθερό στην διεύθυνση Z.

Οπτικοποίηση των στροβίλων που συνθέτουν το SC δίνεται στο Σχήμα 18 όπου οι στρόβιλοι οπτικοποιούνται στο χώρο με τη βοήθεια ισοεπιφάνειας του κριτηρίου Q (Hunt et al., 1988). Παρατηρούνται τρεις συνεχείς επιφάνειες:

1. Μία που αντιστοιχεί στον TELV
2. Μία που εμπεριέχει τον SLV και το αρχικό τμήμα του SC στροβίλου
3. Μία που αντιστοιχεί στη συνέχεια του SC στροβίλου στον ομόρρου

Είναι πιθανόν το κενό κατά μήκος του SC στροβίλου να οφείλεται στην αδυναμία του κριτηρίου Q να ανιχνεύσει δομές στροβιλότητας σε περιοχές ισχυρής διάτμησης (Jeong & Hussain, 1995).

Ως προς τις υπόλοιπες επιδράσεις των στροβίλων: Ο SC στρόβιλος ξεκινά κάθετα στην επιφάνεια υποπίεσης της αεροτομής και κάτω από την επίδρασή του η γραμμή αποκόλλησης μεγαλώνει στο εσωτερικό του SC και μαζί της ο SLV. Αντίστοιχα μεγαλώνει και ο TELV στο εσωτερικό του SC. Υπό την επίδραση του SLV ο SC στρόβιλος κάμπτεται προς το εσωτερικό του SC και γίνεται παράλληλος με την ελεύθερη ροή.

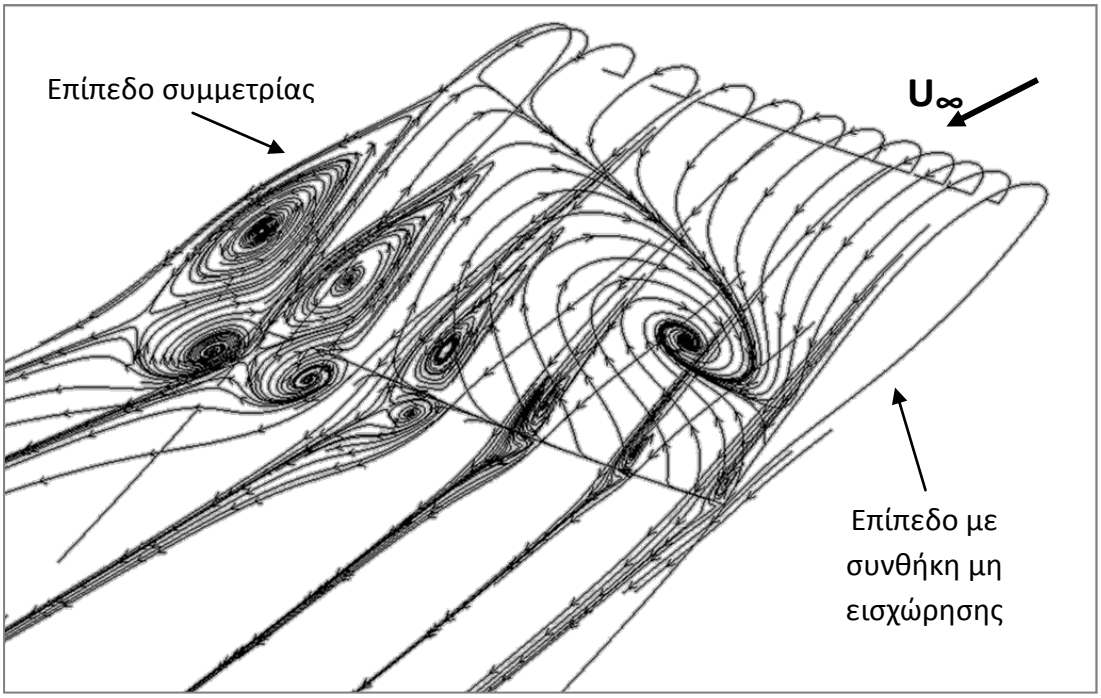

Σχήμα 14: Επιφανειακές γραμμές ροής και 2Δ γραμμές ροής στα επίπεδα z/S = 0% (επίπεδο συμμετρίας), z/S = 10%, z/S = 20%, z/S = 30%, z/S = 40%, z/S = 50% (ακροπτερύγιο, επίπεδο με συνθήκη μη εισχώρησης). AR = 2.0, Re = 1.0x10^6, α = 16°.

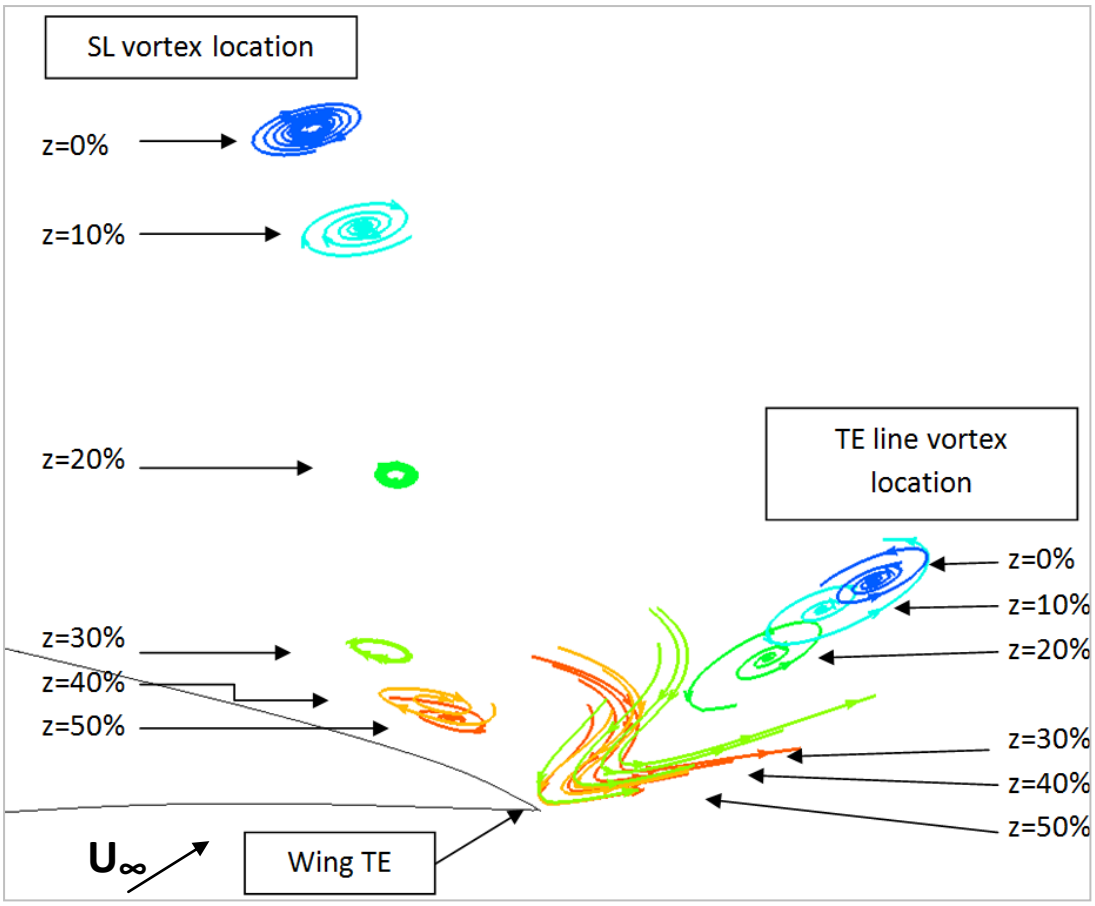

Σχήμα 15: Πλάγια όψη του χείλους εκφυγής. 2Δ γραμμές ροής χρωματισμένες με βάση την κατά το εκπέτασμα θέση, στα ίδια επίπεδα με το Σχήμα 14.. AR = 2.0, Re = 1.0x10^6, α = 16°.

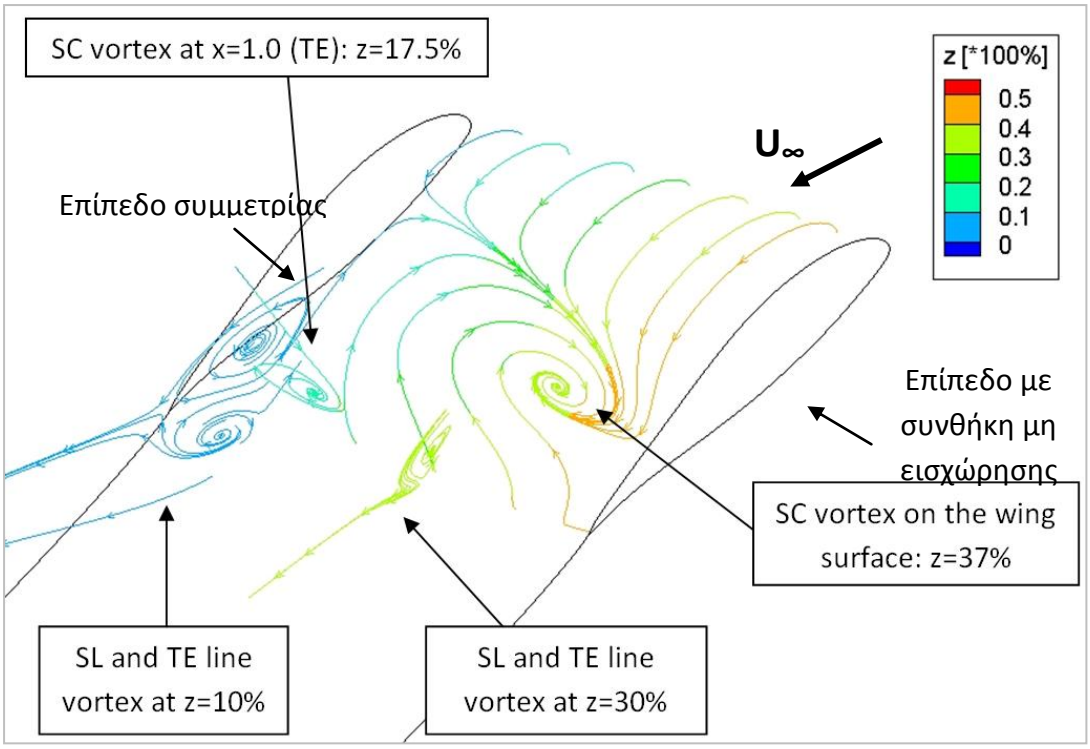

Σχήμα 16: Επιφανειακές γραμμές ροής και 2Δ γραμμές ροής στα επίπεδα z/S = 10%, z/S = 30%, x/c = 1.0. Οι γραμμές ροής είναι χρωματισμένες με βάση την κατά το εκπέτασμα θέση. AR = 2.0, Re = 1.0x10^6, α = 16°.

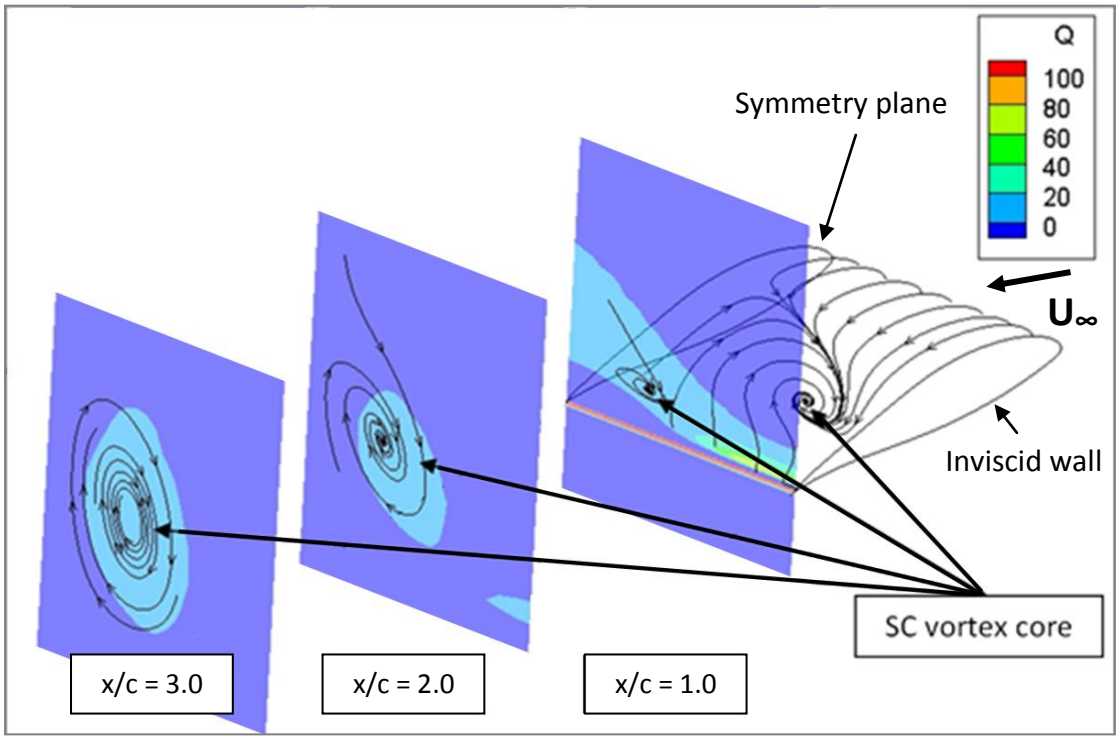

Σχήμα 17: Επιφανειακές γραμμές ροής και 2Δ γραμμές ροής και διαγράμματα Q στα επίπεδα at x/c = 1.0 (χείλος εκφυγής), x/c = 2.0 and x/c = 3.0. Το κέντρο του SC στροβίλου βρίσκεται στο z/S = 37% στην επιφάνεια της πτέρυγας και στο z ≈ 17.5% στα κατάντη επίπεδα. AR = 2.0, Re = 1.0x10^6, α = 16°.

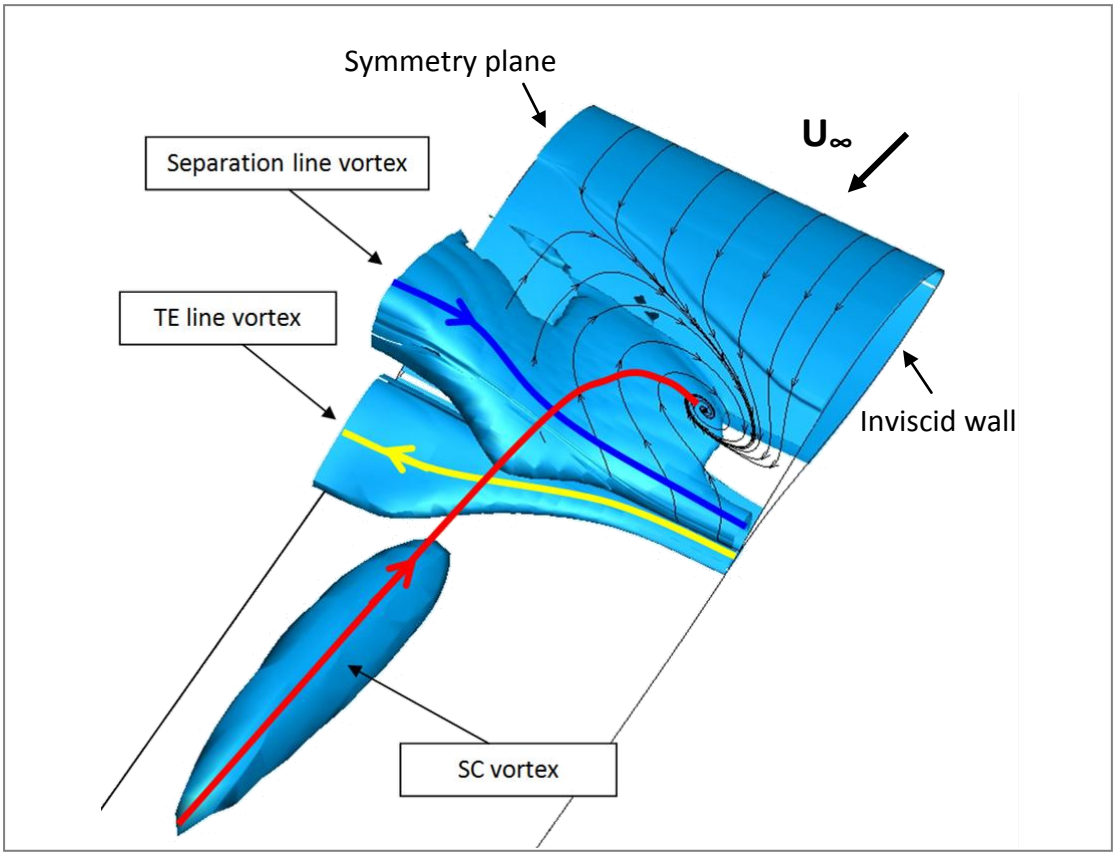

Σχήμα 18: Επιφανειακές γραμμές ροής, ισοεπιφάνεια Q=1 και ποιοτικές γραμμές στροβιλότητας για κάθε στρόβιλο.

5 Πειραματική μελέτη των SCs

5.1 Επίπεδα μέτρησης SPIV

Το Σχήμα 19 δείχνει τα επίπεδα μέτρησης με SPIV, τόσο κάθετα στην ελεύθερη ροή όσο και κάθετα στο εκπέτασμα της πτέρυγας. Το Σχήμα 20 παρουσιάζει μια σχηματική αναπαράσταση της πειραματικής διάταξης SPIV μαζί με τα επίπεδα μέτρησης. Στο Σχήμα 21 οι θέσεις των επιπέδων μέτρησης δίνονται σε συνδυασμό με αποτελέσματα οπτικοποίησης της ροής με λάδι. Τα επίπεδα A και B είναι ανάντη των κέντρων των SC στροβίλων, ενώ τα επίπεδα α και ε βρίσκονται ακριβώς κατάντη αυτών. Τα επίπεδα β, γ, δ βρίσκονται στο εσωτερικό του SC.

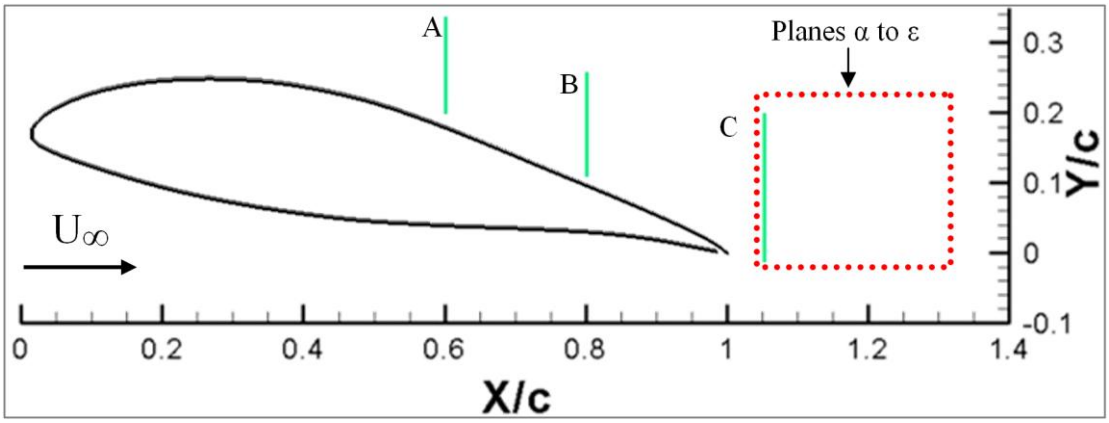

Σχήμα 19: Επίπεδα μέτρησης SPIV για α = 10°. Τα επίπεδα A, B, C είναι κάθετα στην ελεύθερη ροή στις θέσεις x/c = 0.6, 0.8 και 1.06, αντίστοιχα. Τα επίπεδα α έως ε είναι κάθετα στο εκπέτασμα της πτέρυγας στις θέσεις z/S = ±0.067, z/S = ±0.133, z/S = 0.0.

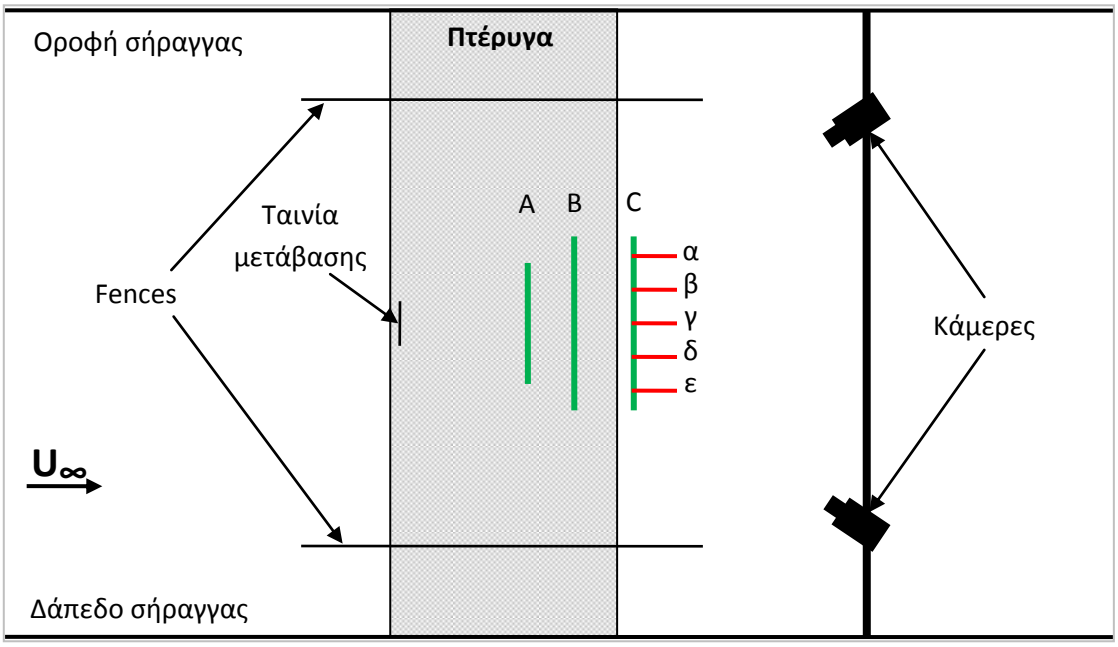

Σχήμα 20: Σχηματική αναπαράσταση της πειραματικής διάταξης SPIV.

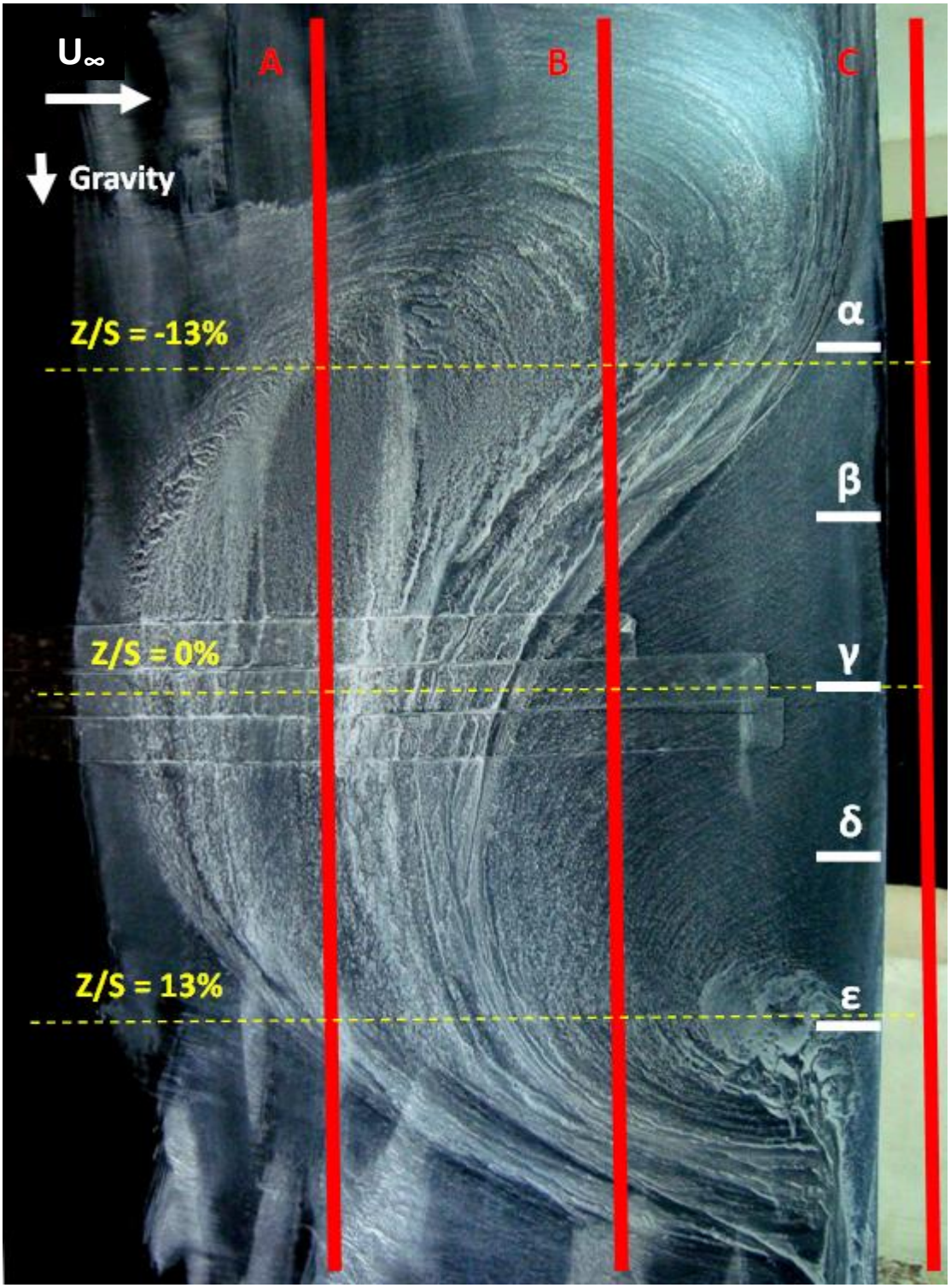

Σχήμα 21: Οπτικοποίηση της ροής με λάδι, AR = 2.0, α = 10°, Re = 0.87x10^6. Η ελεύθερη ροή είναι από αριστερά προς τα δεξιά. Λόγω της κατακόρυφης τοποθέτησης της πτέρυγας η τελική μορφή της εικόνας επηρεάζεται από την βαρύτητα. Οι κόκκινες και οι λευκές συνεχείς γραμμές δείχνουν τη θέση των επιπέδων κάθετα στην ελεύθερη ροή (A, B, C) και κάθετα στο εκπέτασμα της πτέρυγας, αντίστοιχα. Οι κίτρινες διακεκομμένες γραμμές υποδεικνύουν το κέντρο της πτέρυγας (z/S = 0.0%) και την θέση των SC στροβίλων.

5.2 Αποτελέσματα

Το Σχήμα 22 και το Σχήμα 23 παρουσιάζουν τα περιγράμματα ταχύτητας και στροβιλότητας στη διεύθυνση του άξονα X για τα επίπεδα κάθετα στην ελεύθερη ροή. Στην κατανομή στροβιλότητας στο επίπεδο C (Σχήμα 23) με βέλη σημειώνονται τέσσερις περιοχές υψηλής στροβιλότητας, όλες εκτός της περιοχής ανακυκλοφορίας.

Εντός των περιοχών αυτών εμφανίζονται τέσσερις περιοχές υψηλού Q (Σχήμα 24-α). Οι δυο μεγαλύτερες (βέλη 1 και 2 στο Σχήμα 24-α) αντιστοιχούν στους SC στροβίλους. Οι δύο μικρότερες αντιστοιχούν στον TELV ο οποίος κινείται κατάντη στο εσωτερικό του SC, όπως είδαμε και στο προηγούμενο κεφάλαιο. Εάν υποθέσουμε ότι $\omega_z = \frac{\partial V}{\partial x} - \frac{\partial U}{\partial y} \approx -\frac{\partial U}{\partial y}$, οι ισογραμμές $\partial u / \partial y = \pm 4$ στο Σχήμα 24 (β) αντιστοιχούν στο στρώμα διάτμησης της αποκόλλησης και του χείλους εκφυγής. Παρατηρούμε ότι τόσο οι SC στρόβιλοι όσο και ο SLV εμπεριέχονται στο στρώμα διάτμησης της αποκόλλησης και του χείλους εκφυγής αντίστοιχα.

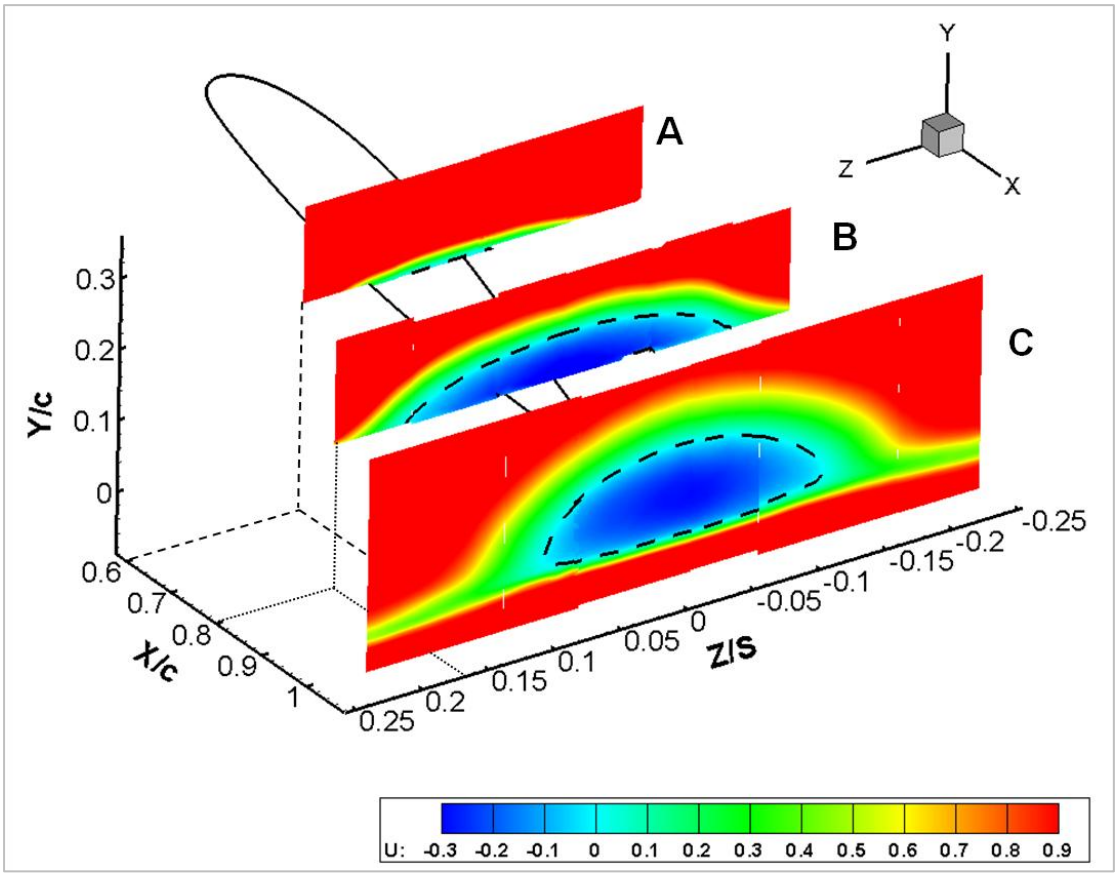

Σχήμα 22: Κατανομή ταχύτητας στις θέσεις x/c = 0.6, 0.8 και 1.06. Η διακεκομμένη μαύρη γραμμή αντιστοιχεί σε ταχύτητα U = 0. AR = 2.0, α = 10°, Re = 0.87×106.

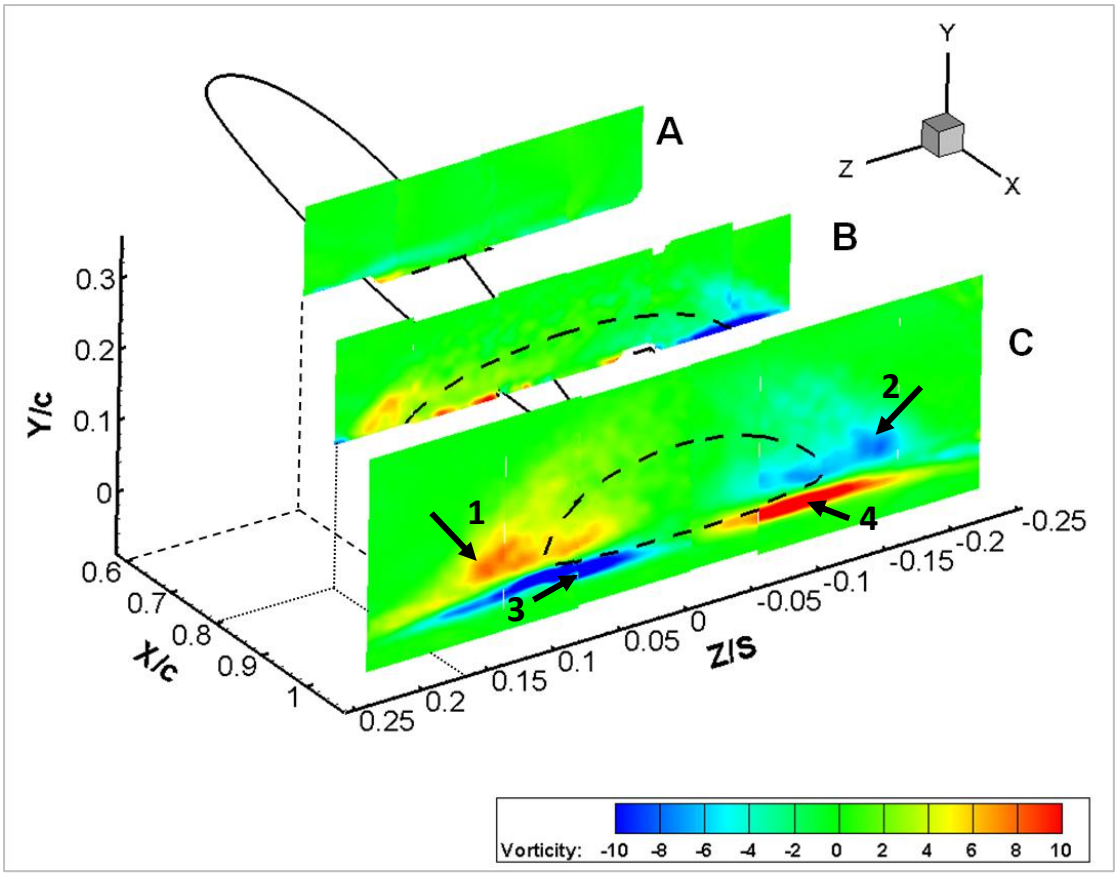

Σχήμα 23: Κατανομή στροβιλότητας στις θέσεις x/c = 0.6, 0.8 και 1.06. Η διακεκομμένη μαύρη γραμμή αντιστοιχεί σε ταχύτητα U = 0. AR = 2.0, α = 10°, Re = 0.87×106.

Το Σχήμα 25 δείχνει ότι ο SLV και ο TELV είναι μεγαλύτεροι και ισχυρότεροι στο εσωτερικό του SC (επίπεδα β, γ, δ), σε συμφωνία με την πρόβλεψη από τις προσομοιώσεις που παρουσιάστηκαν στο προηγούμενο κεφάλαιο. Οι κατανομές της ταχύτητας στον άξονα Z που παρουσιάζονται στο Σχήμα 26 δείχνουν ότι κάτω από την αλληλεπίδραση των SC στροβίλων ο ομόρους της πτέρυγας ωθείται προς τα επάνω.

Η ποιοτική συμφωνία μεταξύ πειραματικών αποτελεσμάτων και προσομοιώσεων είναι πολύ καλή, όπως δείχνει το Σχήμα 27. Αυτό πιθανότατα οφείλεται στην ποιοτικά σωστή πρόβλεψη των διατμητικών τάσεων, όπως δείχνει το Σχήμα 28. Η πρόλεξη των ορθών τάσεων αντίθετα είναι λανθασμένη, ωστόσο οι ορθές τάσεις είναι τάξεις μεγέθους μικρότερες από τους όρους πίεσης και για αυτό λιγότερο σημαντικοί.

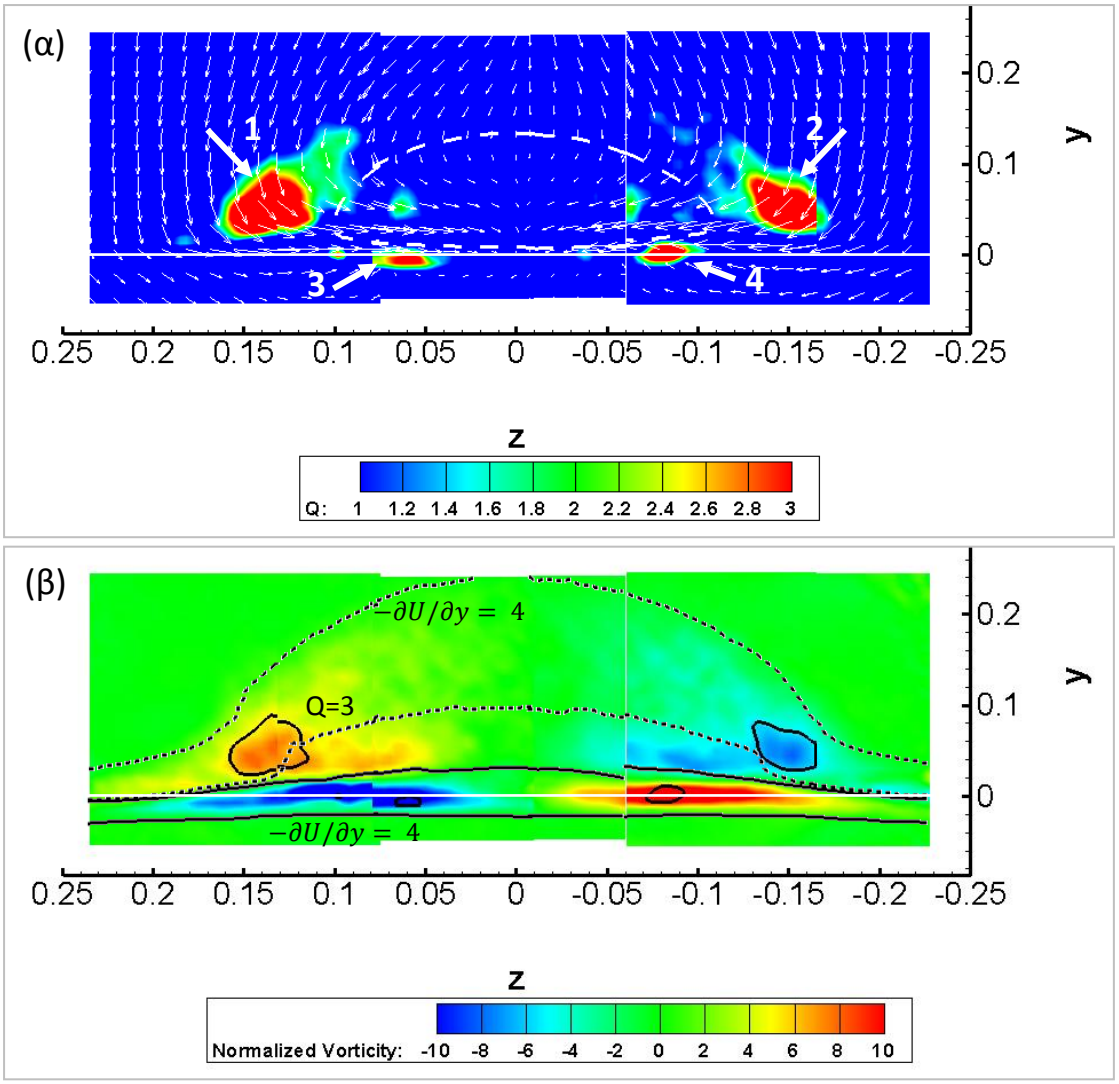

Σχήμα 24: Επίπεδο C. (α) Κατανομή του κριτηρίου Q με 2Δ διανύσματα ταχύτητας και ισογραμμή για U = 0. (β) Κατανομή στροβιλότητας και ισογραμμές για Q = 3 και $\partial u/\partial y = \pm 4$. Το χείλος εκφυγής είναι στη θέση Y = 0 και σημειώνεται με μια λευκή οριζόντια γραμμή. AR = 2.0, α = 10°, Re = 0.87×106.

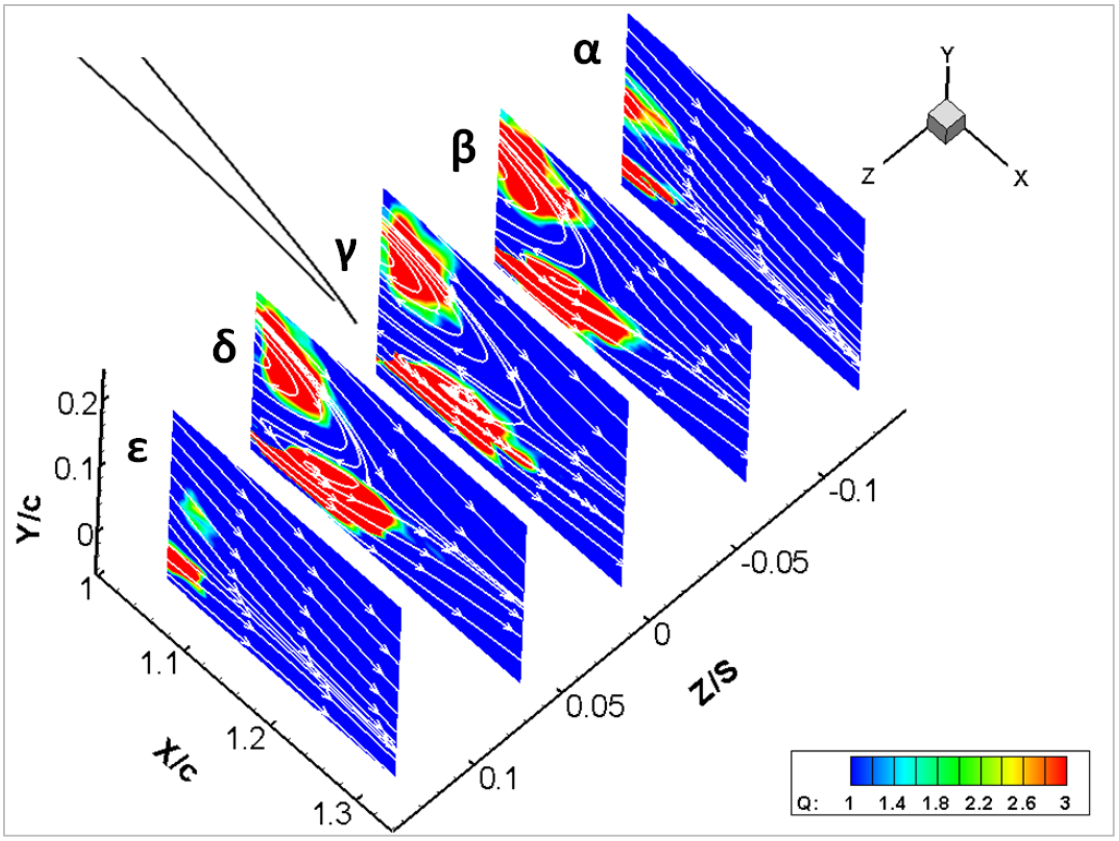

Σχήμα 25: Κατανομή του κριτηρίου Q με 2Δ γραμμές ροής στις θέσεις z/S = 0.0, z/S = ±0.067 και z/S = ±0.133. AR = 2.0, α = 10°, Re = 0.87×106.

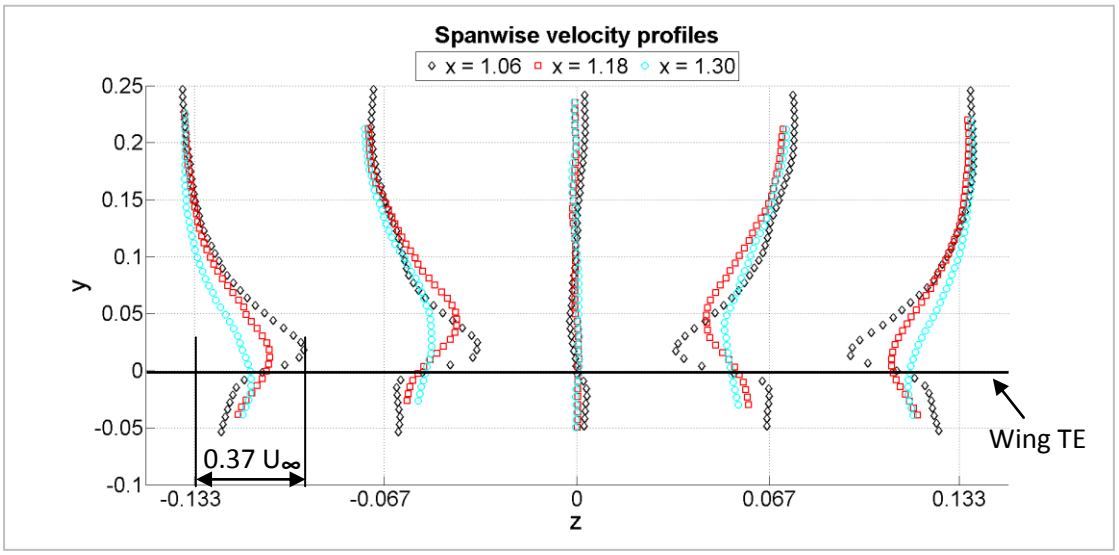

Σχήμα 26: Κατανομή ταχύτητας W στις θέσεις z/S = 0.0, z/S = ±0.067, z/S = ±0.133. Ο μαύροι ρόμβοι αντιστοιχούν στη θέση x/c = 1.06, τα κόκκινα τετράγωνα στη θέση x/c = 1.18 και οι γαλάζιοι κύκλοι στη θέση x/c = 1.30. Η μαύρη οριζόντια γραμμή υποδηλώνει τη θέση του χείλους εκφυγής. AR = 2.0, α = 10°, Re = 0.87×106.

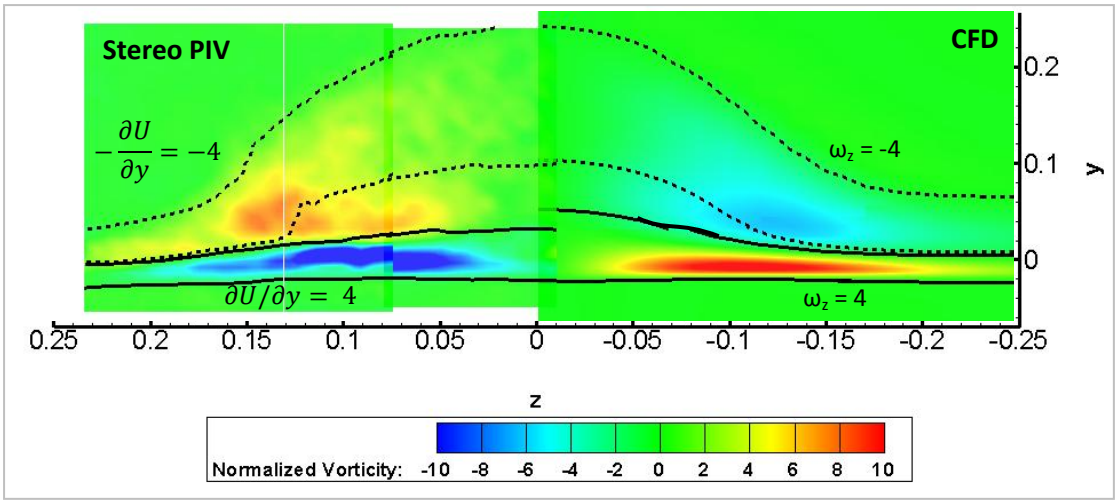

Σχήμα 27: Κατανομή στροβιλότητας στο επίπεδο C. SPIV αποτελέσματα αριστερά (με ισογραμμές $\partial u/\partial y = \pm 4$) και υπολογιστικά αποτελέσματα δεξιά (με ισογραμμές ω_z=±4). AR = 2.0, α = 10°, Re = 0.87×106.

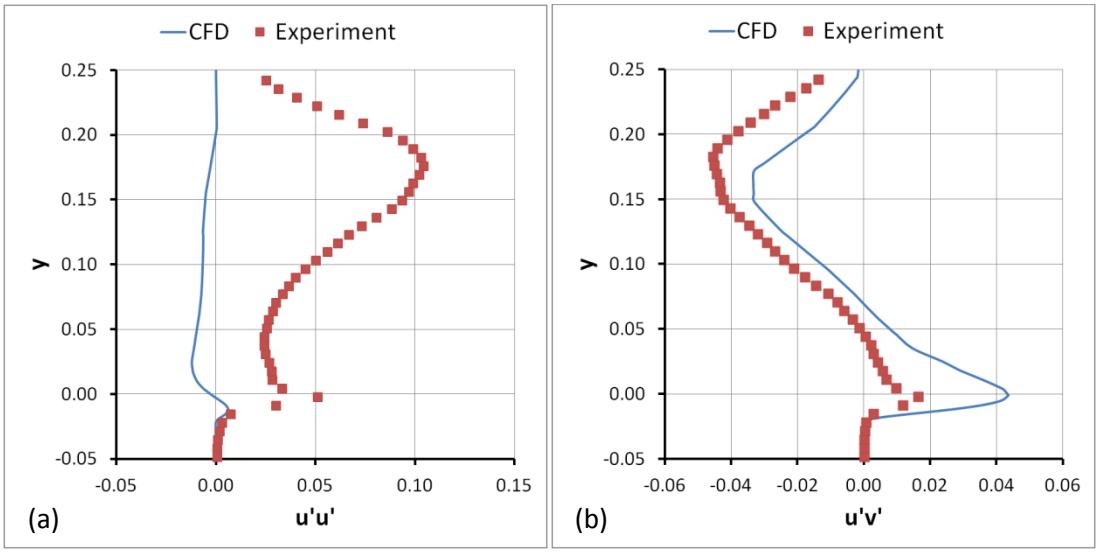

Σχήμα 28: (α) u'u' και (β) u'v' μεταβολή στη θέση z/S = 0, σύμφωνα με τα πειραματικά δεδομένα και υπολογισμούς με χρήση του μοντέλου τύρβης Spalart Allmaras. AR = 2.0, α = 10°, Re = 0.87×106.

Τα χαρακτηριστικά της τύρβης της ροής στο εσωτερικό του SC παρουσιάζονται στη συνέχεια, από το Σχήμα 29 μέχρι το Σχήμα 34. Συνοπτικά, οι κύριες παρατηρήσεις είναι οι εξής:

- Έντονη ανισοτροπία των ορθών τάσεων.
- Η υψηλή συγκέντρωση u'u' υποδηλώνει ταλαντωτική κίνηση του στρώματος διάτμησης της αποκόλλησης.
- Η υψηλή συγκέντρωση v'v' και w'w' φανερώνει κίνηση των SC στροβίλων κατά την οριζόντια και την κατακόρυφη διεύθυνση, αντίστοιχα. Η κατανομή των v'v' τάσεων δείχνει ακόμα πως οι SC στρόβιλοι συγκλίνουν προς το κέντρο του SC μετά το τέλος της περιοχής ανακυκλοφορίας.
- Από τις διατμητικές τάσεις ισχυρότερη είναι η u'v', στις περιοχές των στρωμάτων διάτμησης.
- Οι τάσεις v'w' επίσης φανερώνουν την προς τα μέσα κίνηση των SC στροβίλων

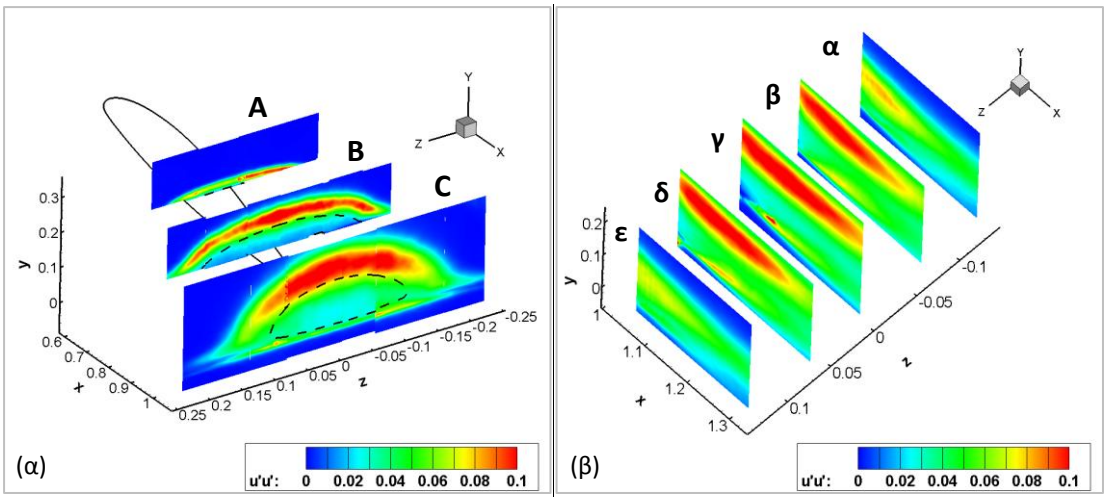

Σχήμα 29: Κατανομή των τάσεων u'u' (α) στις θέσεις x/c = 0.6, 0.8 και 1.06; (β) στις θέσεις z/S = 0.0, ±0.067 και ±0.133. AR = 2.0, α = 10°, Re = 0.87×106.

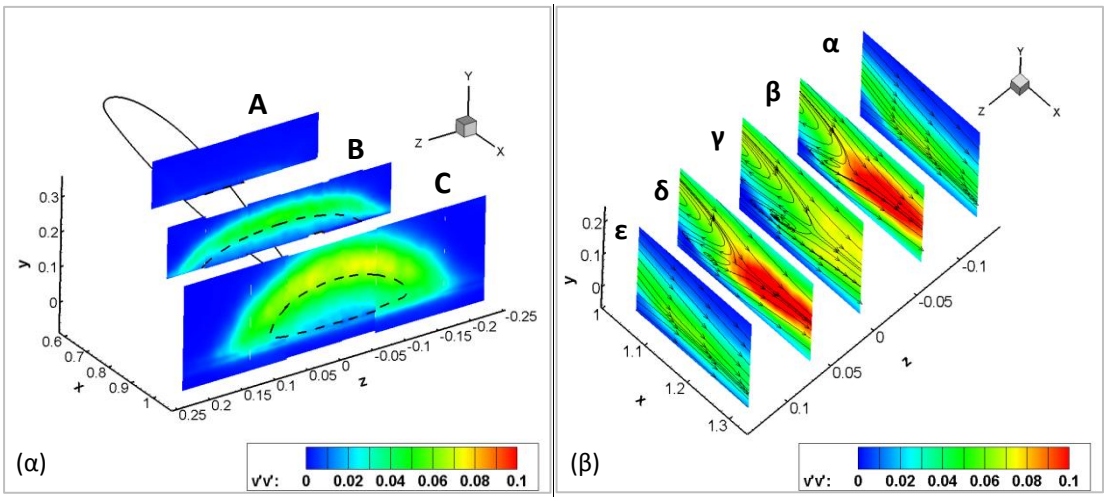

Σχήμα 30: Κατανομή των τάσεων v'v' (α) στις θέσεις x/c = 0.6, 0.8 και 1.06; (β) στις θέσεις z/S = 0.0, ±0.067 και ±0.133. AR = 2.0, α = 10°, Re = 0.87×106.

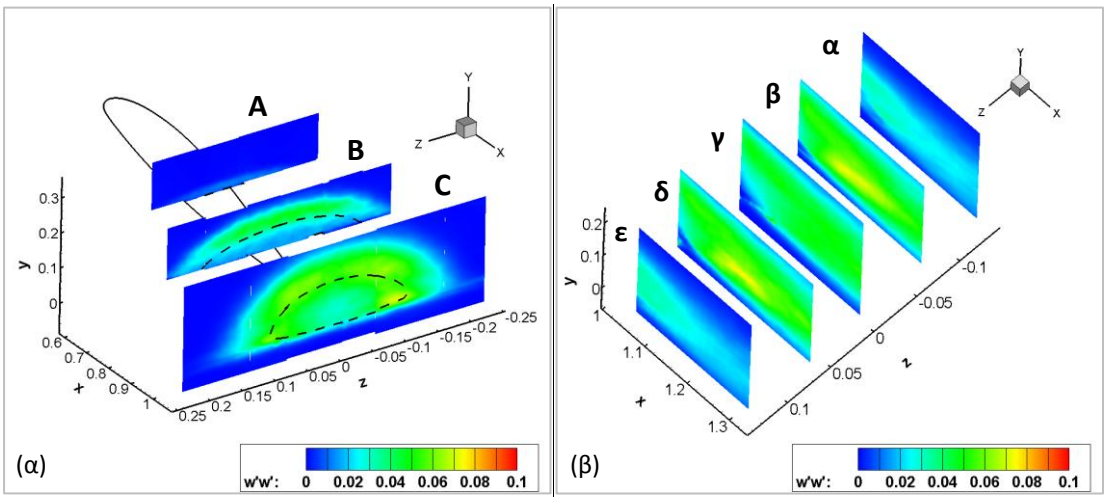

Σχήμα 31: Κατανομή των τάσεων w'w' (α) στις θέσεις x/c = 0.6, 0.8 και 1.06; (β) στις θέσεις z/S = 0.0, ±0.067 και ±0.133. AR = 2.0, α = 10°, Re = 0.87×106.

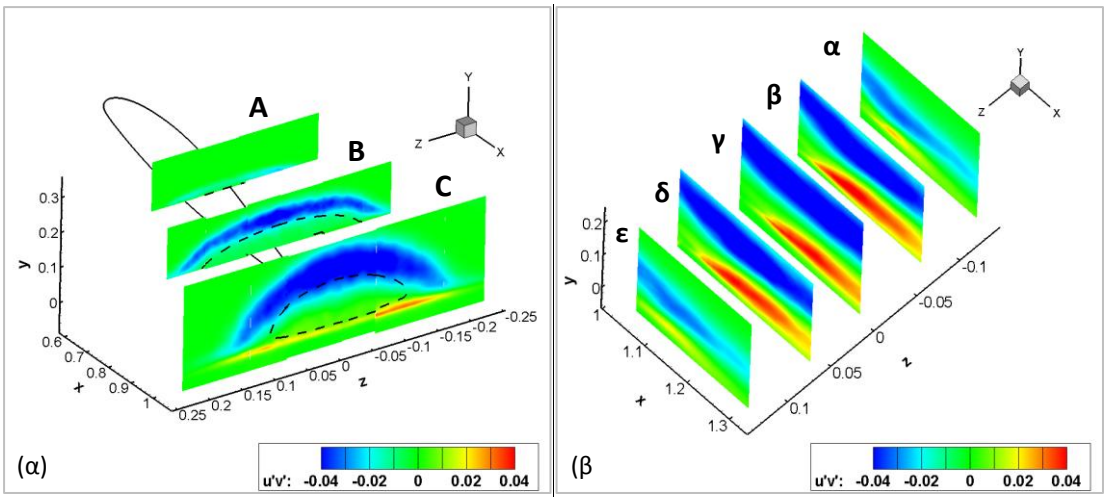

Σχήμα 32: Κατανομή των τάσεων u'v' (α) στις θέσεις x/c = 0.6, 0.8 και 1.06; (β) στις θέσεις z/S = 0.0, ±0.067 και ±0.133. AR = 2.0, α = 10°, Re = 0.87×106.

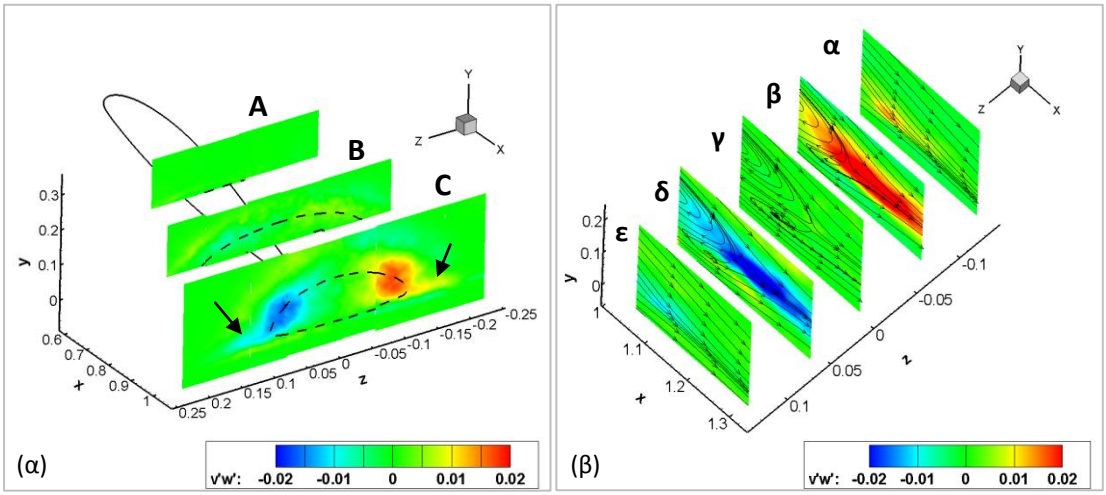

Σχήμα 33: Κατανομή των τάσεων v'w' (α) στις θέσεις x/c = 0.6, 0.8 και 1.06; (β) στις θέσεις z/S = 0.0, ±0.067 και ±0.133 (α = 10°, Re = 0.87×10^6).

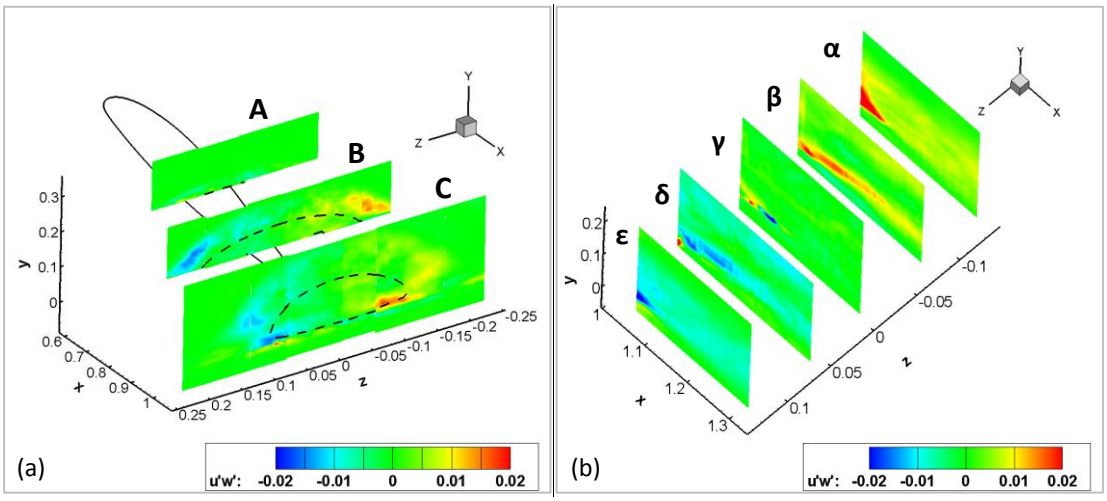

Σχήμα 34: Κατανομή των τάσεων u'w' (α) στις θέσεις x/c = 0.6, 0.8 και 1.06; (β) στις θέσεις z/S = 0.0, ±0.067 και ±0.133. AR = 2.0, α = 10°, Re = 0.87×106.

6 Βελτιστοποίηση της διάταξης των VGs

6.1 Υπολογιστική παραμετρική μελέτη

Η βελτιστοποίηση της διάταξης των VGs έγινε μέσω υπολογιστικής παραμετρικής μελέτης. Οι παράμετροι που εξετάστηκαν παρουσιάζονται στο Σχήμα 35 και ήταν οι ακόλουθες:

x : Θέση των VGs κατά τον X άξονα
h : Ύψος των VGs
l : Μήκος των VGs
D : Απόσταση μεταξύ δύο ζυγαριών VGs
β : VG angle to the free stream flow
d : spanwise distance between the LE of two VGs of the same pair

Βρέθηκε ότι οι δύο διατάξεις που έδιναν τα καλύτερα αποτελέσματα αύξησης του λόγου άνωσης αντίστασης είναι αυτές που παρουσιάζει ο Πίνακας 1. Η διαφορά μεταξύ τους ήταν η θέση των VGs κατά τον X άξονα.

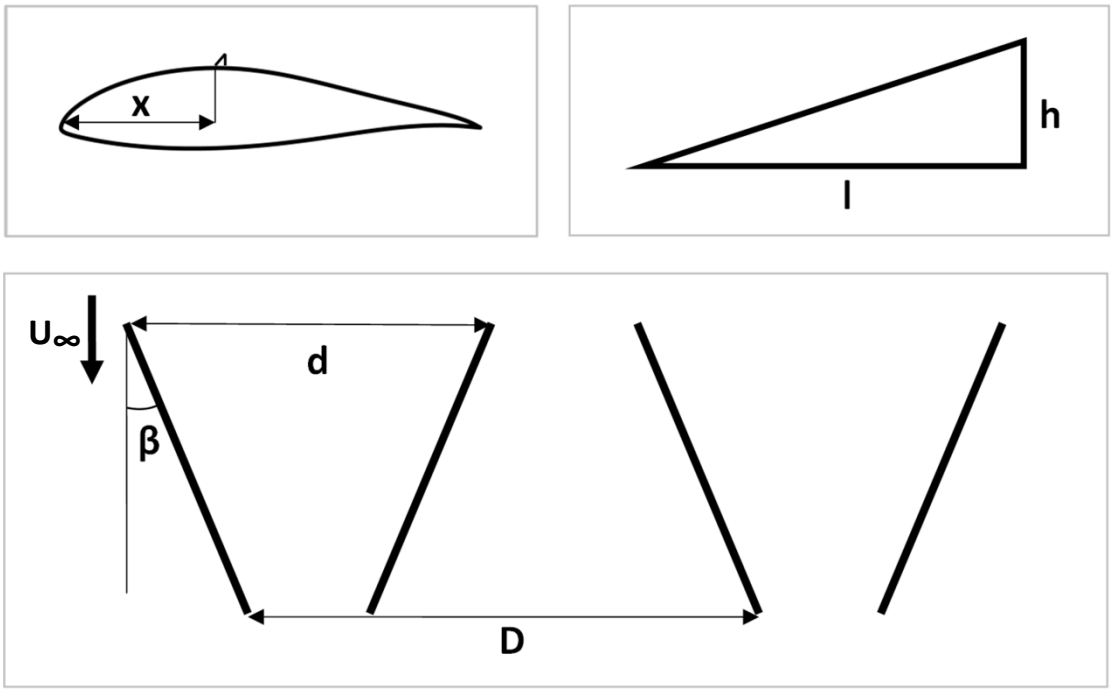

Σχήμα 35: Παράμετροι σχεδιασμού των VGs.

Case	β [deg]	height (h/δ)	length (l/h)	Distance between VGs (d/h)	Chordwise position (x/c)	VG pair distance (D/h)	Cl	Cd	L/D
K	20	1.0	3.0	3.7	0.3	11.7	1.711	0.032	53.0
K-0.4	20	1.0	3.0	3.7	0.4	11.7	1.734	0.032	54.3
2D	-	-	-	-	-	-	1.576	0.036	43.7

Πίνακας 1: Γεωμετρικές λεπτομέρειες για τις δύο διατάξεις VGs με την καλύτερη απόδοση και η απόδοση της αεροτομής χωρίς VGs.

6.2 Πειραματικά αποτελέσματα

Στο Σχήμα 36 και στο Σχήμα 37 βλέπουμε την μεταβολή του Cl με τη γωνία πρόσπτωσης για την πτέρυγα με τα VGs στη θέση x/c = 0.3 και 0.4 αντίστοιχα. Και στις δύο περιπτώσεις η βελτίωση σε σχέση με την περίπτωση χωρίς έλεγχο της ροής είναι εμφανής. Για την περίπτωση με VGs στη θέση x/c = 0.4 εμφανίζεται υστέρηση της ροής γύρω από τις 12°. Για την περίπτωση με τα VGs στη θέση x/c = 0.3 παρατηρήθηκε αστάθεια της ροής στις 16°, όπου η ροή εναλλασσόταν μεταξύ δύο καταστάσεων, μίας "συχνής" όπου η ροή παραμένει κατά κύριο λόγο προσκολλημένη στην πτέρυγα και μία περισσότερο "σπάνια", όπου ένα μεγάλο SC δημιουργείται και το σημείο αποκόλλησης φτάνει μέχρι τα VGs. Η περίπτωση με τα VGs στην πιο ανάντη θέση προτιμήθηκε για περαιτέρω έρευνα, λόγω της μεγαλύτερης αύξησης του Cl.

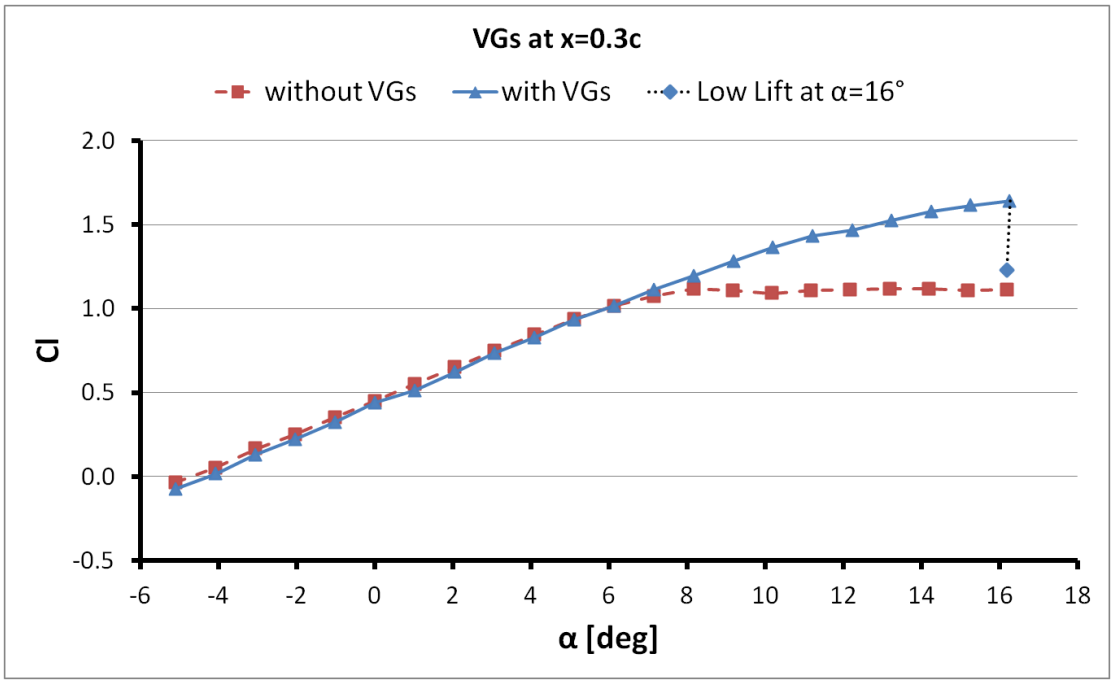

Σχήμα 36: Μεταβολή του Cl με τη γωνία πρόσπτωσης για την πτέρυγα με τα VGs στη θέση x/c = 0.3 και χωρίς VGs. AR = 2.0, Re = 0.87x10^6.

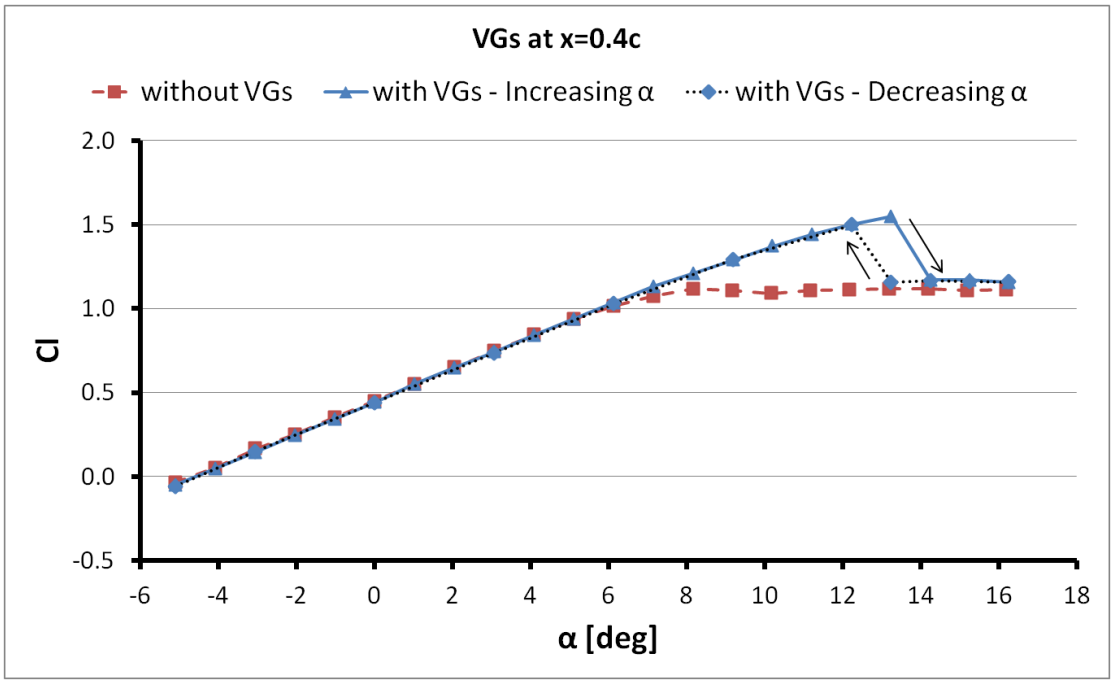

Σχήμα 37: Μεταβολή του Cl με τη γωνία πρόσπτωσης για την πτέρυγα με τα VGs στη θέση x/c = 0.4 και χωρίς VGs. AR = 2.0, Re = 0.87×10^6.

7 Πειραματική μελέτη της ροής κατάντη των VGs

7.1 Μέσες τιμές μεγεθών

Τα επίπεδα μέτρησης με SPIV φαίνονται στο Σχήμα 38 και είναι κάθετα στην ελεύθερη ροή στις θέσεις x/c = 0.6, 0.7 και 0.8 ή αντίστοιχα 27.2h, 37.2h και 47.2η κατάντη του χείλους εκφυγής των VGs. Οι κατανομές της ταχύτητας επιβεβαιώνουν ότι η αποκόλληση στις 10° καταπολεμάται αποτελεσματικά (Σχήμα 39) και έχουν ένα διπλό μέγιστο, γεγονός που οφείλεται στην επίδραση των VGs.

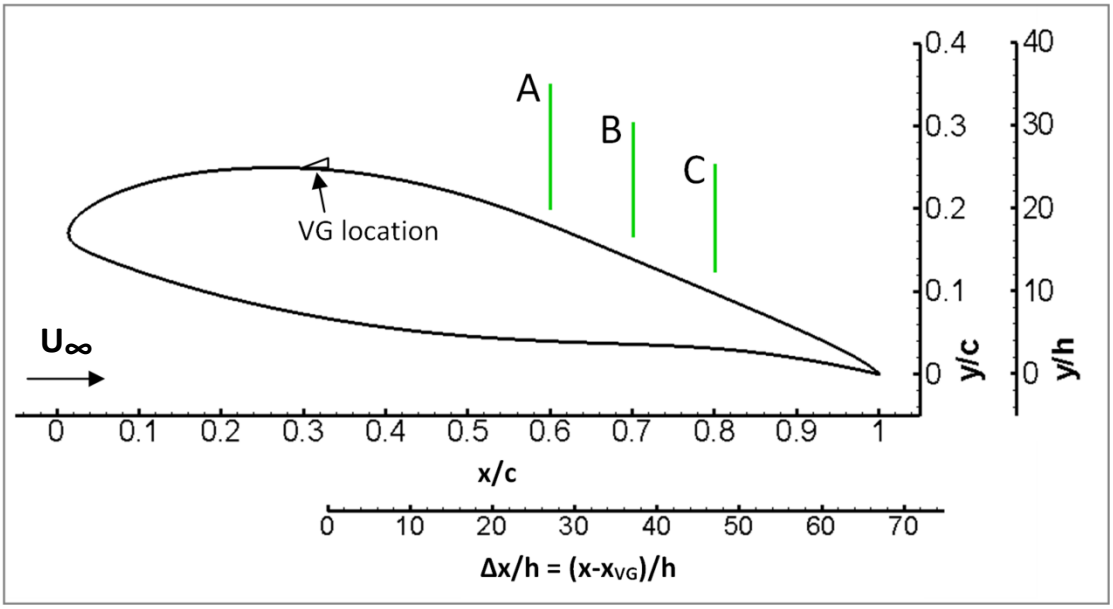

Σχήμα 38: Επίπεδα μέτρησης SPIV για την περίπτωση με VGs και α=10°. Οι άξονες X και Y έχουν αδιαστατοποιηθεί δύο φορές, μία με το μήκος της χορδής, c, και μία με το ύψος των VGs, h. Στη δεύτερη περίπτωση αρχή των αξόνων θεωρείται το χείλος εκφυγής των VGs.

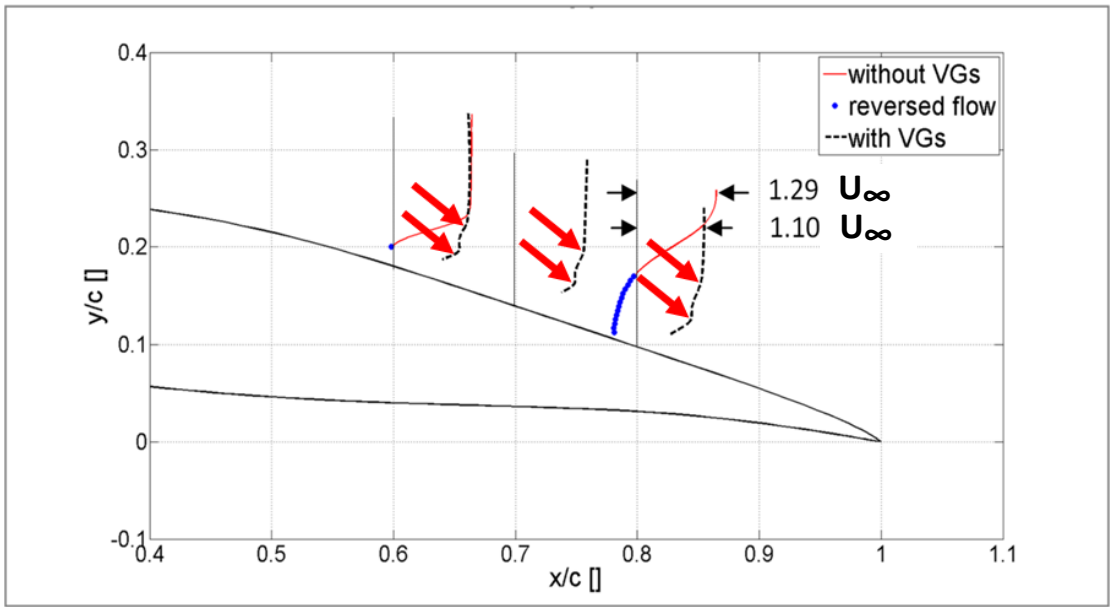

Σχήμα 39: Σύγκριση της κατανομής της ταχύτητας στο κέντρο της πτέρυγας για την περίπτωση χωρίς VGs με την κατανομή της ταχύτητας με VGs (μέση τιμή κατά το εκπέτασμα). AR = 2.0, α = 10°, Re = 0.87×10^6.

Το Σχήμα 40 δείχνει την κατανομή της ταχύτητας και της στροβιλότητας στα τρία επίπεδα μέτρησης μαζί με ισογραμμές στροβιλότητας για ω = $\omega_{max}/2$. Το σχήμα των στροβίλων αλλάζει από το επίπεδο Α στο επίπεδο Β, ενώ από το επίπεδο Β στο επίπεδο C το σχήμα του στροβίλου διατηρείται και οι στρόβιλοι έχουν αυξημένο μέγεθος λόγω διάχυσης. Λόγω της αλληλεπίδρασης των στροβίλων τα κέντρα τους απομακρύνονται από την επιφάνεια της πτέρυγας καθώς προχωρούν κατάντη (Σχήμα 41 - αριστερά).

Ως κέντρο του στροβίλου ορίστηκε το σημείο μέγιστης στροβιλότητας και η ημιακτίνα του, $R_{0.5}$, σύμφωνα με την εξίσωση

$$R_{0.5} = \sqrt{A_{0.5}/\pi} \tag{28}$$

Όπου $A_{0.5}$ είναι το εμβαδό της περιοχής που εσωκλείεται από την ισογραμμή στροβιλότητας για ω = $\omega_{max}/2$.

Στο Σχήμα 41 - δεξιά παρατηρούμε ότι η ημιακτίνα των στροβίλων παραμένει σταθερή από το επίπεδο Α στο επίπεδο Β, ενώ μεγαλώνει αισθητά από το επίπεδο Β στο επίπεδο C, σε συμφωνία και με τους (Mehta & Bradshaw, 1988).

Η σημαντική πτώση της κυκλοφορίας μεταξύ των δύο πρώτων επιπέδων (Σχήμα 42) ενδεχομένως να οφείλεται στην έντονη αλληλεπίδραση των στροβίλων στο αρχικό στάδιο, ενώ στη συνέχεια, όταν η διάχυση κυριαρχεί, η κυκλοφορίας παραμένει σταθερή. Η μεγίστη στροβιλότητα μειώνεται καθώς οι στρόβιλοι κινούνται κατάντη.

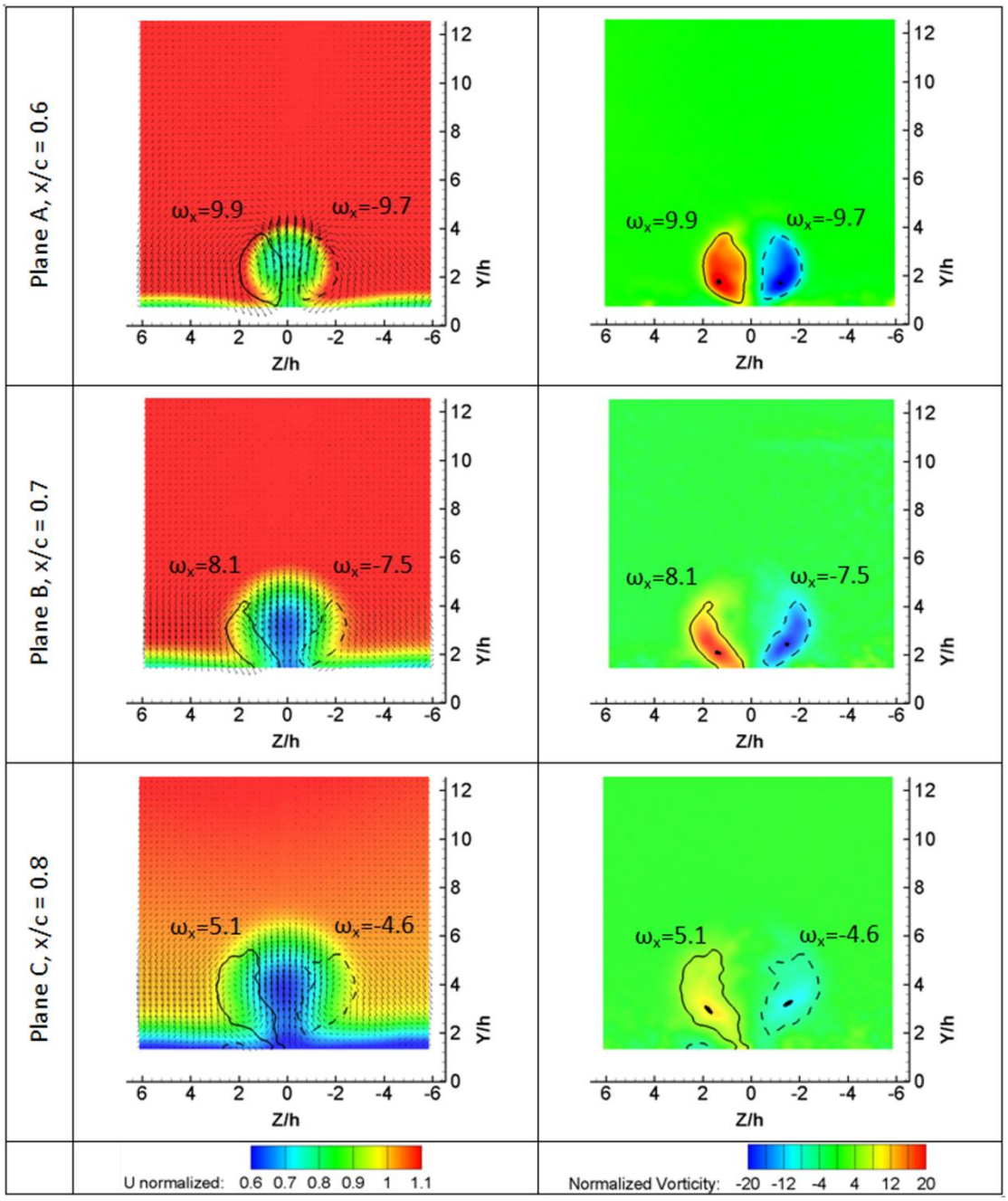

Σχήμα 40: Κατανομή της παράλληλης στην ελεύθερη ροή ταχύτητας και διανύσματα του πεδίου ταχύτητας των στροβίλων (αριστερή στήλη) και της στροβιλότητας (δεξιά στήλη) στις θέσεις x/c = 0.6, 0.7, 0.8. Ισογραμμές στροβιλότητας για ω = ω_{max}/2 έχουν επίσης σχεδιαστεί. Η επιφάνεια της αεροτομής είναι πάντα στο y/h = 0 και στη θέση z/h = 0 είναι το κέντρο του ζεύγους των VGs. AR = 2.0, α = 10°, Re = 0.87×10^6.

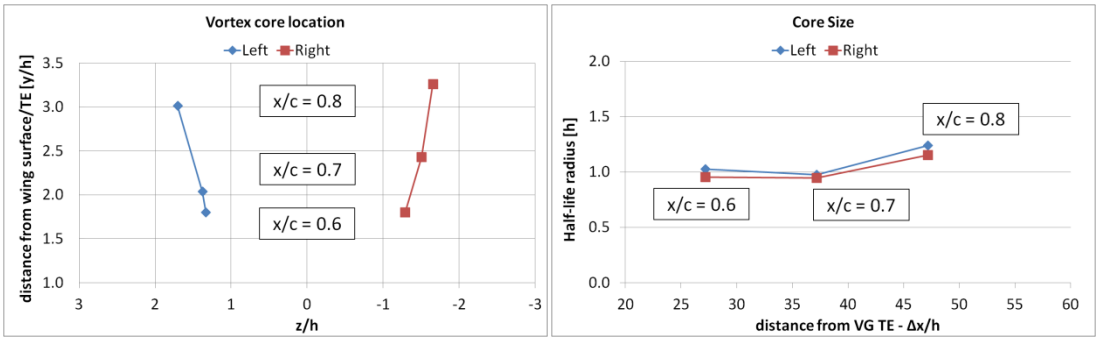

Σχήμα 41: Θέση του κέντρου των στροβίλων (αριστερά) και μεταβολή της ημιακτίνας τους (δεξιά) με την απόσταση από το χείλος εκφυγής των VGs. AR = 2.0, α = 10°, Re = 0.87×10^6.

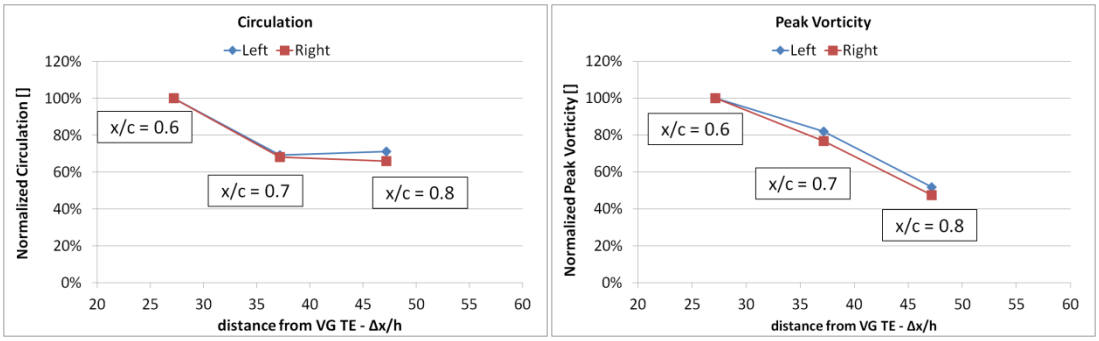

Σχήμα 42: Μεταβολή της κυκλοφορίας (αριστερά) και της μέγιστης στροβιλότητας (δεξιά) με την απόσταση από το χείλος εκφυγής των VGs. AR = 2.0, α = 10°, Re = 0.87×10^6.

7.2 Χαρακτηριστικά της τύρβης στη ροή

Οι κατανομές των ορθών και διατμητικών τάσεων Reynolds σε όλα τα επίπεδα δίνονται στο Σχήμα 43 και το Σχήμα 44, αντίστοιχα. Οι κύριες παρατηρήσεις είναι οι εξής:

- Οι υψηλές τιμές $\overline{v'v'}$ στο επάνω μέρος, ανάμεσα στους δύο στροβίλους αποδίδεται στην άτακτη κίνηση των τελευταίων, οι οποίοι όταν πλησιάζουν δημιουργούν τοπικά έντονη ροή προς τα επάνω.
- Σε συμφωνία με τους (Mehta & Bradshaw, 1988; Angele & Grewe, 2007) παρατηρούνται υψηλές τιμές $\overline{w'w'}$ κοντά στο κέντρο των στροβίλων, που αποδίδεται στην οριζόντια κίνηση τους.
- Στα επίπεδα B και C οι μέγιστες τιμές $\overline{w'w'}$ στο επάνω μέρος, ανάμεσα στους δύο στροβίλους, πιθανώς προκύπτουν λόγω μεταφοράς.
- Από το επίπεδο A στο επίπεδο B υπάρχει έντονη αλληλεπίδραση μεταξύ των στροβίλων και του οριακού στρώματος, ενώ από το επίπεδο B στο επίπεδο C φαίνεται η διάχυση να είναι ο κυρίαρχος μηχανισμός.
- Οι τιμές του $\overline{u'v'}$ ακολουθούν τα στρώματα διάτμησης, ενώ οι συγκεντρώσεις των $\overline{u'w'}$ και $\overline{v'w'}$ είναι αντισυμμετρικές όπως αναμενόταν (Mehta & Bradshaw, 1988).

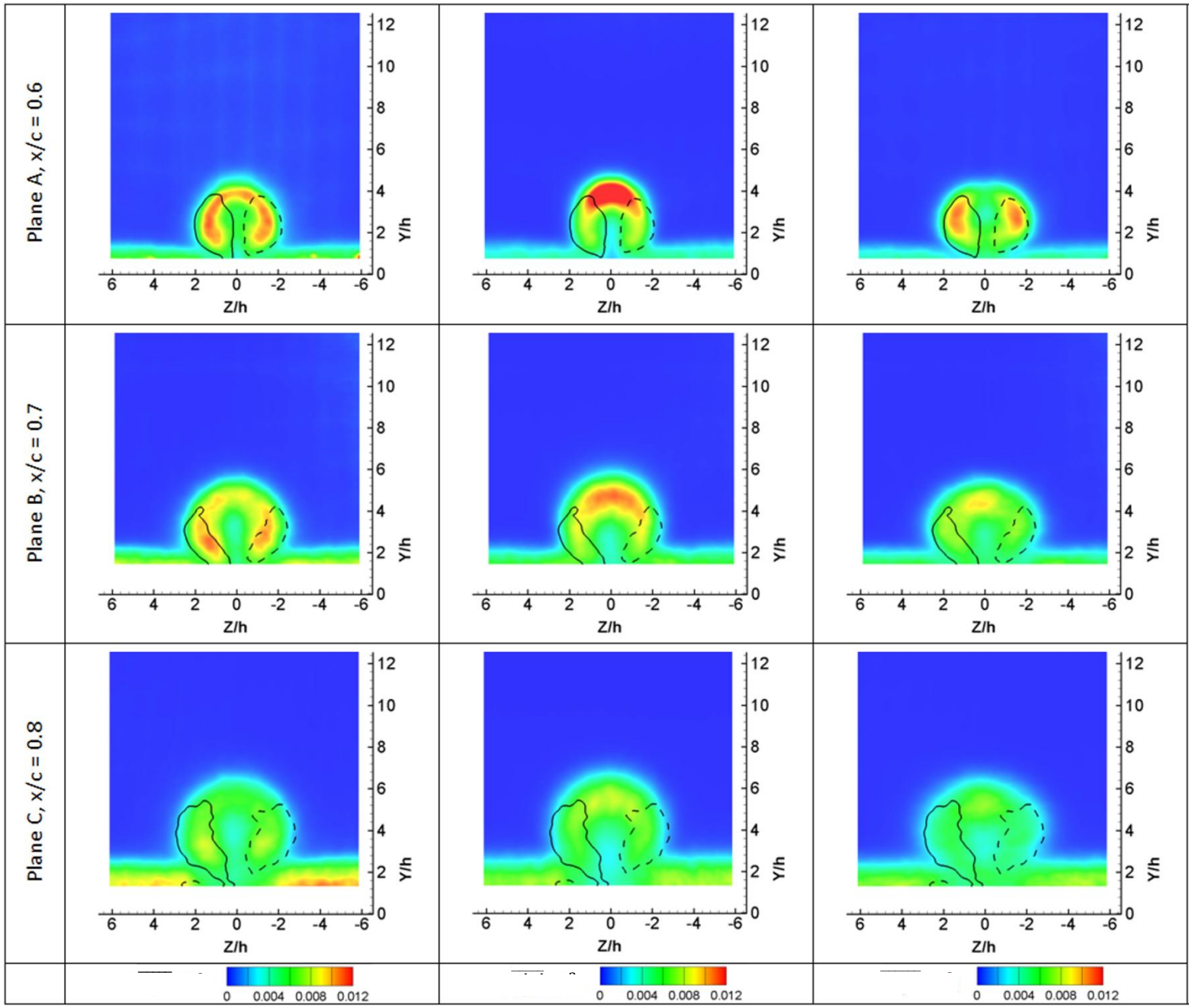

Σχήμα 43: Κατανομή ορθών τάσεων Reynolds. Ισογραμμές στροβιλότητας για ω = $\omega_{max}/2$ έχουν επίσης σχεδιαστεί. Η επιφάνεια της αεροτομής είναι πάντα στο y/h = 0 και στη θέση z/h = 0 είναι το κέντρο του ζεύγους των VGs. AR = 2.0, α = 10°, Re = 0.87×10^6.

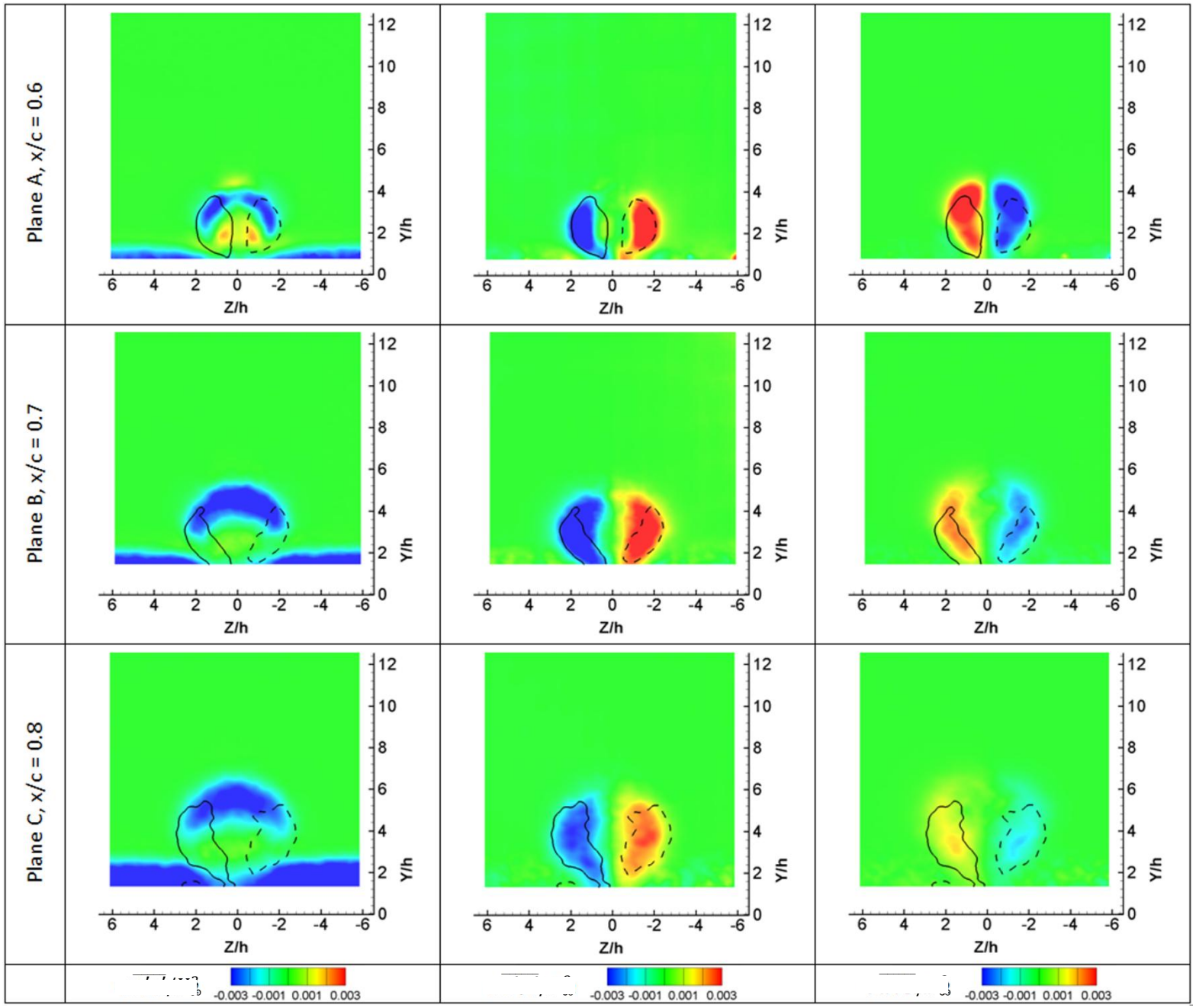

Σχήμα 44: Κατανομή ορθών τάσεων Reynolds. Ισογραμμές στροβιλότητας για ω = $\omega_{max}/2$ έχουν επίσης σχεδιαστεί. Η επιφάνεια της αεροτομής είναι πάντα στο y/h = 0 και στη θέση z/h = 0 είναι το κέντρο του ζεύγους των VGs. AR = 2.0, α = 10°, Re = 0.87×10^6.

Για να μελετηθεί λεπτομερέστερα η σχέση μεταξύ των κλίσεων ταχύτητας, των τάσεων Reynolds και των όρων παραγωγής τους,. εξετάστηκε η μεταβολή τους κατά μήκος οριζόντιων και κάθετων γραμμών, οι οποίες παρουσιάζονται στο Σχήμα 45. Οι όροι παραγωγής υπολογίστηκαν με βάση την εξίσωση:

$$P_{u_i u_j} = -\overline{u_i{}' u_k{}'} \frac{\partial U_j}{\partial x_k} - \overline{u_j{}' u_k{}'} \frac{\partial U_i}{\partial x_k} \quad (29)$$

Με βάση τα δεδομένα που παρουσιάζονται στη συνέχεια (από το Σχήμα 46 έως το Σχήμα 51) ενισχύεται η άποψη ότι από το επίπεδο B στο επίπεδο C η διάχυση είναι ο κυρίαρχος μηχανισμός στη ροή. Πιο ειδικά συμπεράσματα συνοψίζονται παρακάτω:

Κατακόρυφη Γραμμή J1: Ανάμεσα στους στροβίλους

- Η κατανομή της ταχύτητας εμφανίζει διπλό μέγιστο σαν αποτέλεσμα της επίδρασης των στροβίλων.
- Υπάρχει ισχυρή συσχέτιση μεταξύ των ∂U/∂y, των τάσεων Reynolds και των όρων παραγωγής τους.

Κατακόρυφη Γραμμή J2: Δια μέσου του αριστερού στροβίλου

- Η κατανομή της ταχύτητας εμφανίζει διπλό μέγιστο σαν αποτέλεσμα της επίδρασης των στροβίλων.
- Υπάρχει ισχυρή συσχέτιση μεταξύ των ∂U/∂y και P_{uu}, P_{vv}, P_{uv}, ενώ ο όρος P_{uw} συσχετίζεται με την κλίση ∂U/∂z.

Κατακόρυφη Γραμμή J3: Αριστερά του αριστερού στροβίλου

- Έντονη κλίση της U με μία "γωνία" στην κατανομή, λόγω της επίδρασης των στροβίλων.
- Υπάρχει ισχυρή συσχέτιση μεταξύ των ∂U/∂y, των τάσεων Reynolds και των όρων παραγωγής τους.
- Τα χαρακτηριστικά της τύρβης μοιάζουν με αυτά ενός τυρβώδους οριακού στρώματος.

Οριζόντια Γραμμή I1: Στο εσωτερικό του οριακού στρώματος

- Εκτός της περιοχής που επηρεάζεται από τους στροβίλους ο όρος P_{uv} είναι αρνητικός και ο όρος P_{ww} είναι πρακτικά μηδενικός, όπως στα τυρβώδη οριακά στρώματα. Ο όρος P_{vv} από την άλλη είναι θετικός λογω της καμπυλότητας της στερεής επιφάνειας.
- Υπάρχει αρνητική συσχέτιση μεταξύ των $\overline{u'w'}$ και P_{uw} με την κλίση ∂U/∂z, σε συμφωνία με τους (Angele & Muhammad-Klingmann, 2005).

Οριζόντια Γραμμή I2: Δια μέσου των στροβίλων

- Υπάρχει ισχυρή συσχέτιση μεταξύ των όρων P_{uu}, P_{uw}, των αντίστοιχων τάσεων και της κλίσης ∂U/∂z.
- Υπάρχει αρνητική συσχέτιση μεταξύ των P_{uv} και ∂U/∂y.

Οριζόντια Γραμμή I2: Ψηλότερα από το κέντρο των στροβίλων

- Υπάρχει ισχυρή συσχέτιση μεταξύ των όρων P_{vv} και P_{uv}, που έχουν υψηλή συσχέτιση με την κλίση ∂U/∂y.
- Στο επίπεδο A οι υψηλές τιμές P_{vv} και $\overline{v'v'}$ σχετίζονται με την κίνηση των στροβίλων όπως εξηγήθηκε προηγουμένως.
- Υπάρχει ισχυρή συσχέτιση μεταξύ P_{uw} και ∂U/∂z.

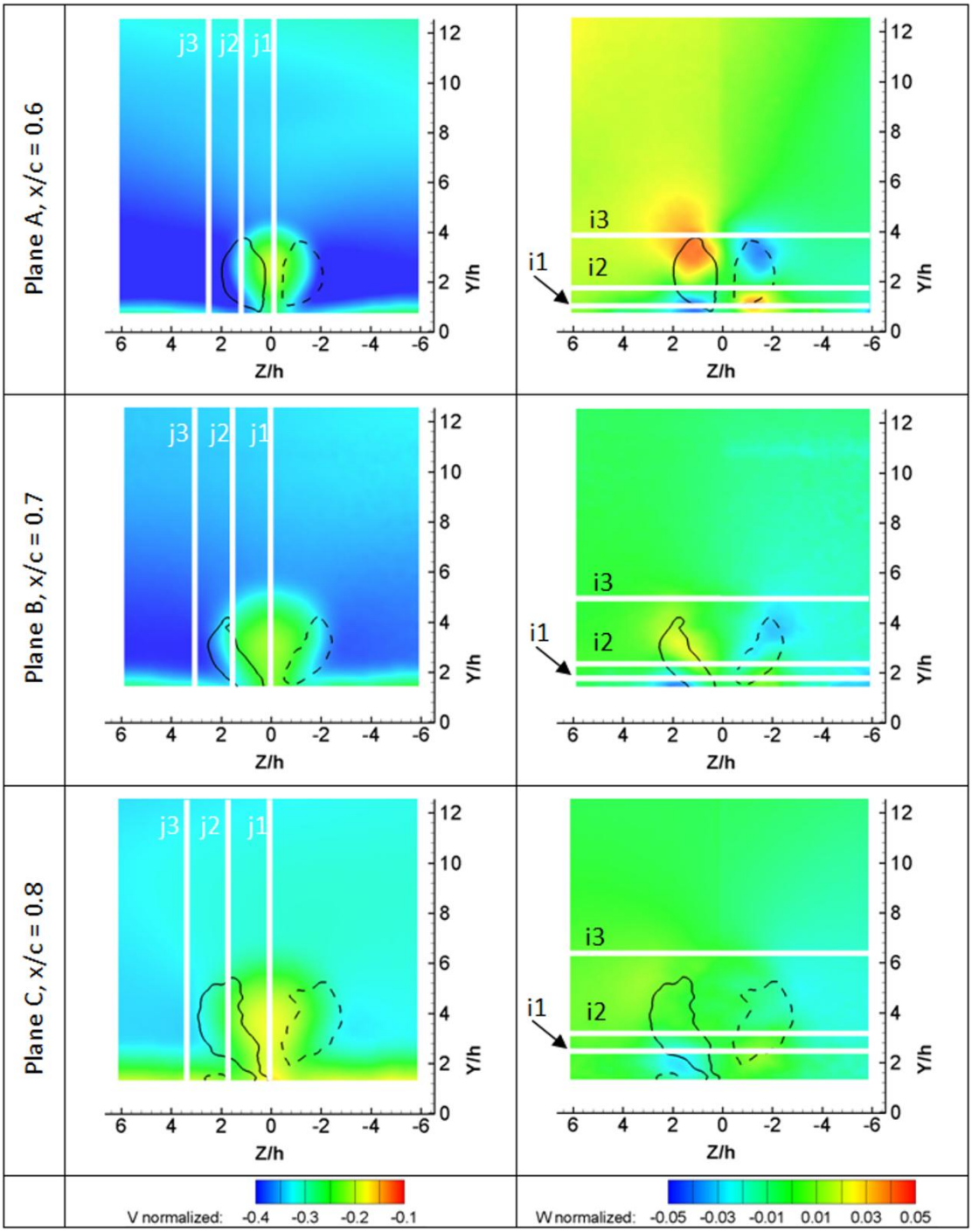

Σχήμα 45: Κατανομή κατακόρυφης (αριστερά) και οριζόντιας (δεξιά) ταχύτητας. Οι λευκές οριζόντιες και κάθετες γραμμές δείχνουν τις θέσεις στις οποίες εξετάζονται οι τάσεις Reynolds στη συνέχεια (από το Σχήμα 46 έως το Σχήμα 51). Ισογραμμές στροβιλότητας για ω = ω_{max}/2 έχουν επίσης σχεδιαστεί. Η επιφάνεια της αεροτομής είναι πάντα στο y/h = 0 και στη θέση z/h = 0 είναι το κέντρο του ζεύγους των VGs. AR = 2.0, α = 10°, Re = 0.87×10^6.

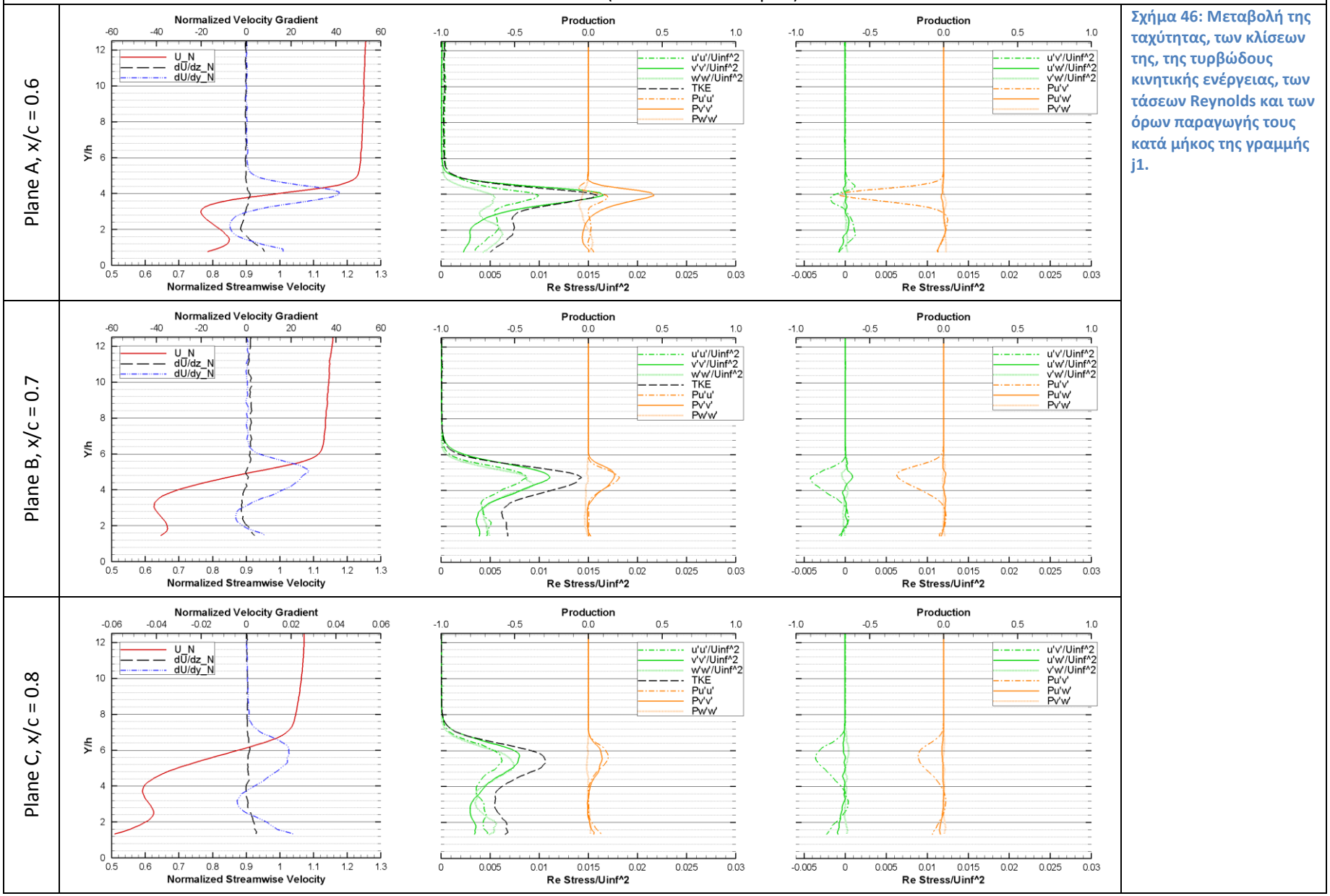

Σχήμα 46: Μεταβολή της ταχύτητας, των κλίσεων της, της τυρβώδους κινητικής ενέργειας, των τάσεων Reynolds και των όρων παραγωγής τους κατά μήκος της γραμμής j1.

Through the LHS vortex centre

Plane A, x/c = 0.6

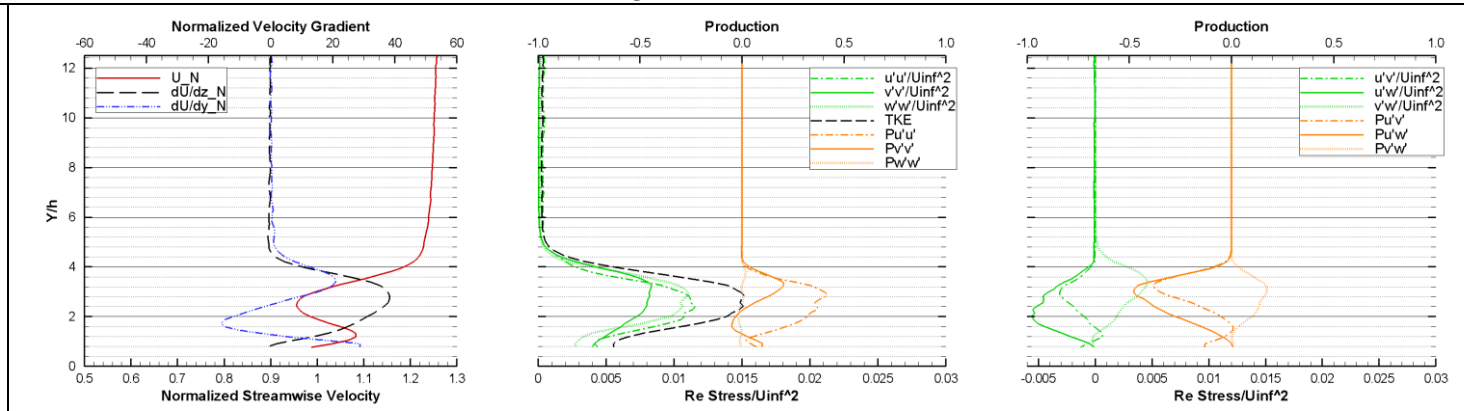

Plane B, x/c = 0.7

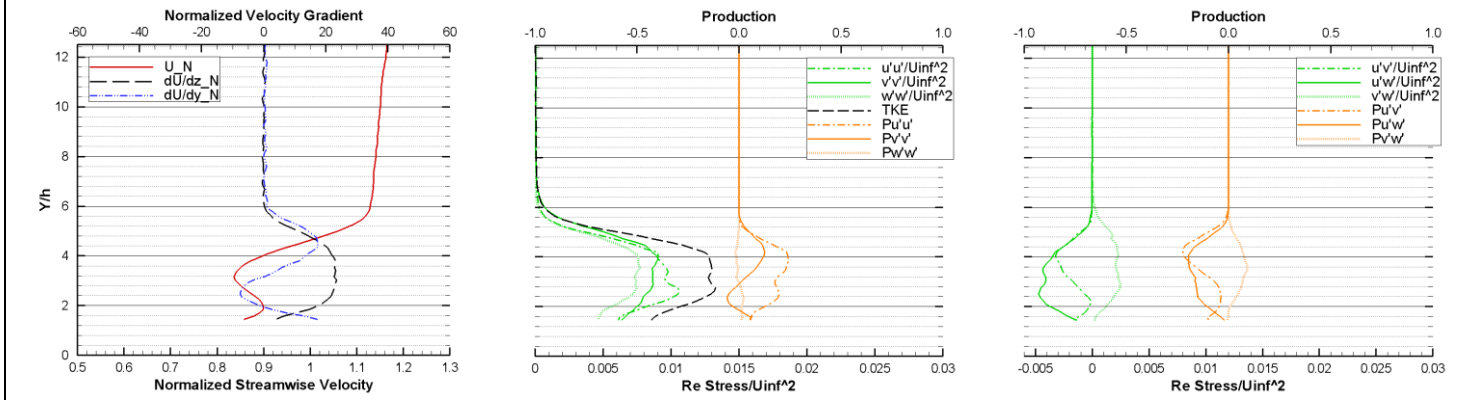

Plane C, x/c = 0.8

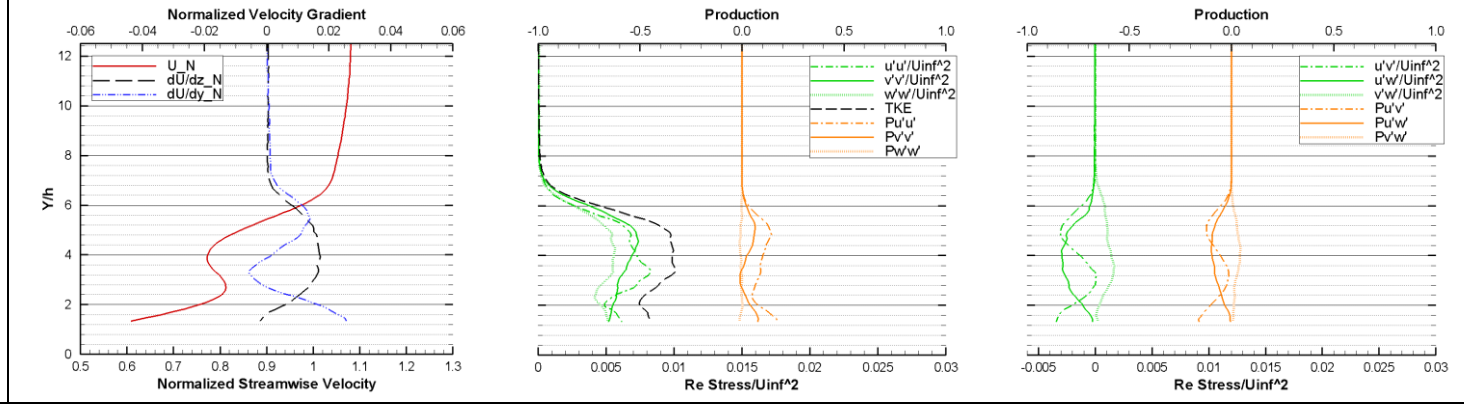

Σχήμα 47: Μεταβολή της ταχύτητας, των κλίσεων της, της τυρβώδους κινητικής ενέργειας, των τάσεων Reynolds και των όρων παραγωγής τους κατά μήκος της γραμμής j2.

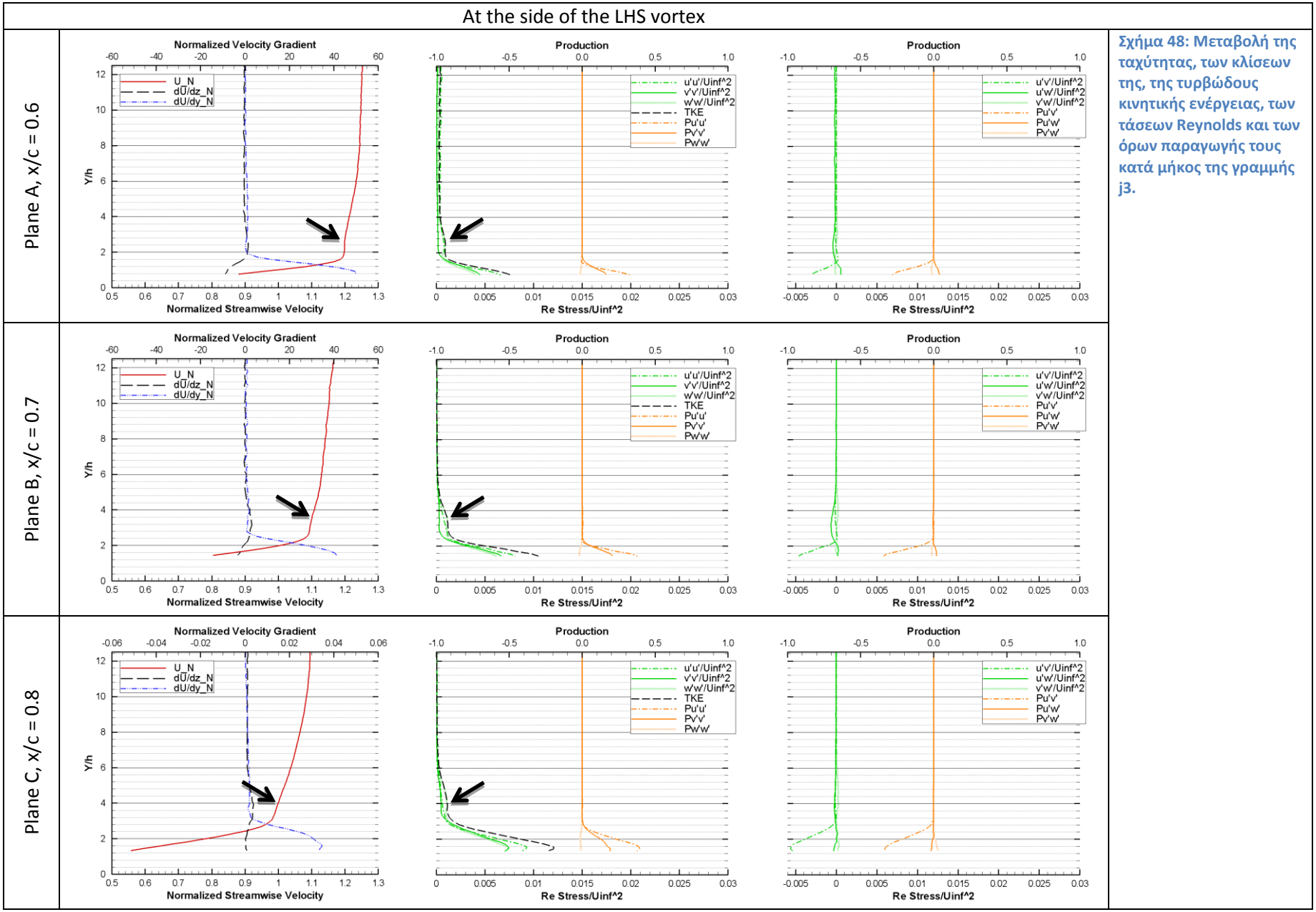

Σχήμα 48: Μεταβολή της ταχύτητας, των κλίσεων της, της τυρβώδους κινητικής ενέργειας, των τάσεων Reynolds και των όρων παραγωγής τους κατά μήκος της γραμμής j3.

	Top part of the BL	
Plane A, x/c = 0.6	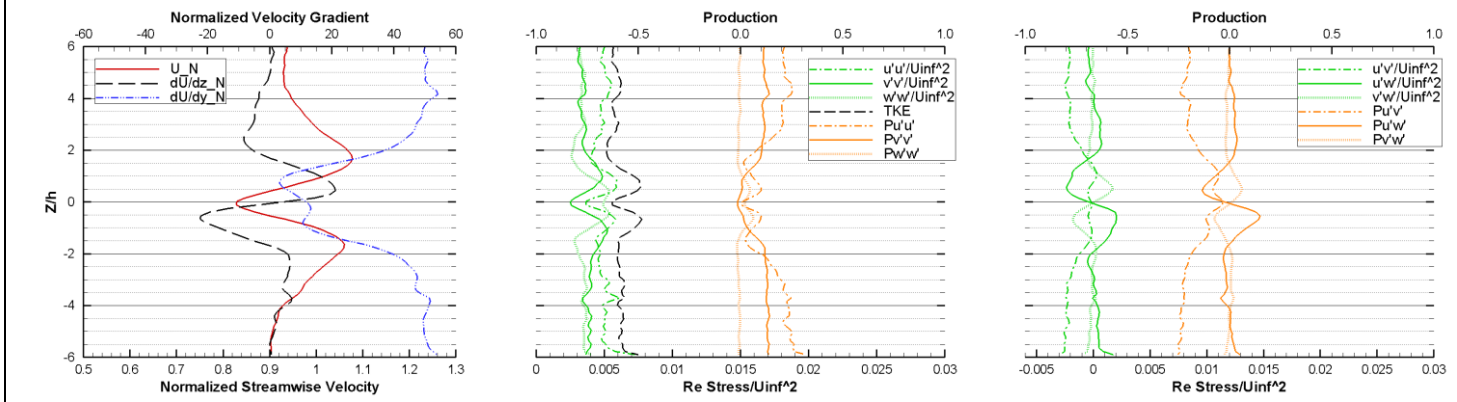	**Σχήμα 49: Μεταβολή της ταχύτητας, των κλίσεων της, της τυρβώδους κινητικής ενέργειας, των τάσεων Reynolds και των όρων παραγωγής τους κατά μήκος της γραμμής i1.**
Plane B, x/c = 0.7	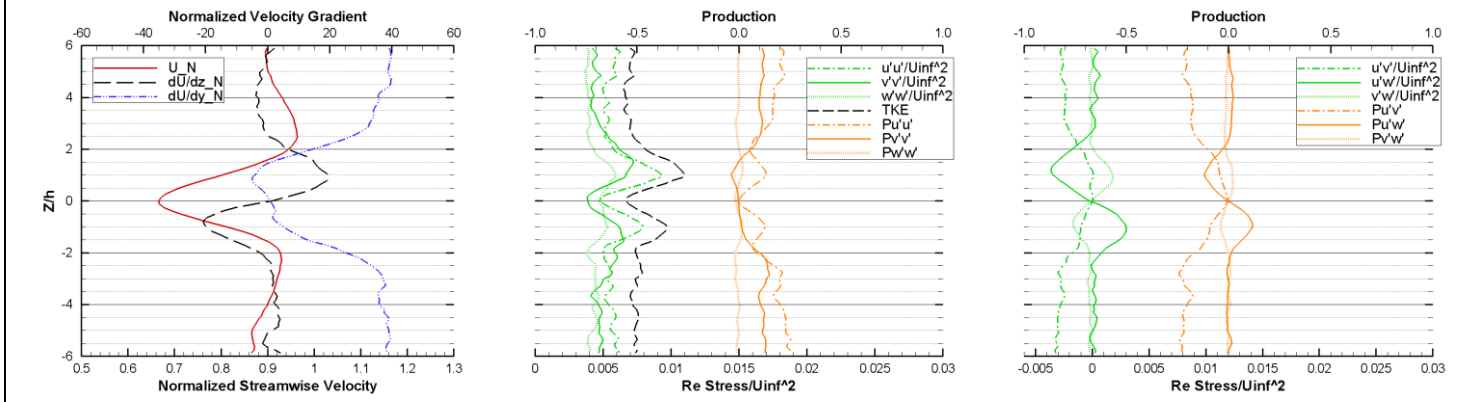	
Plane C, x/c = 0.8	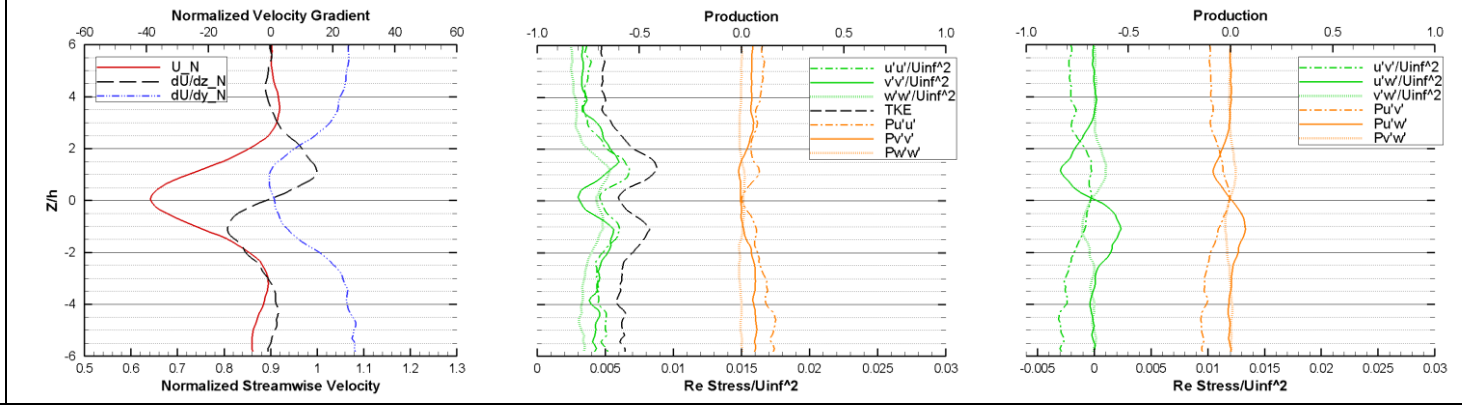	

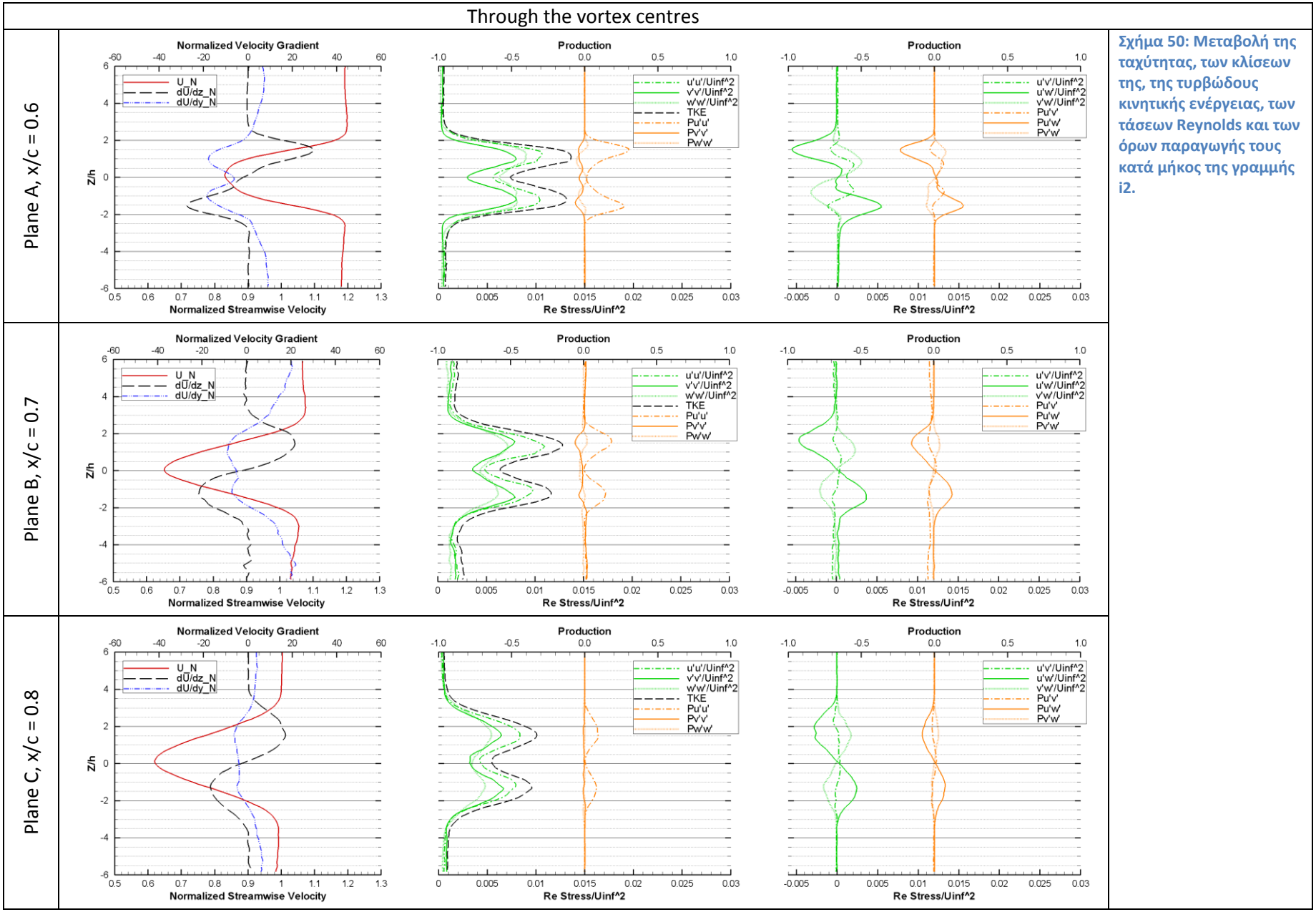

Σχήμα 50: Μεταβολή της ταχύτητας, των κλίσεων της, της τυρβώδους κινητικής ενέργειας, των τάσεων Reynolds και των όρων παραγωγής τους κατά μήκος της γραμμής i2.

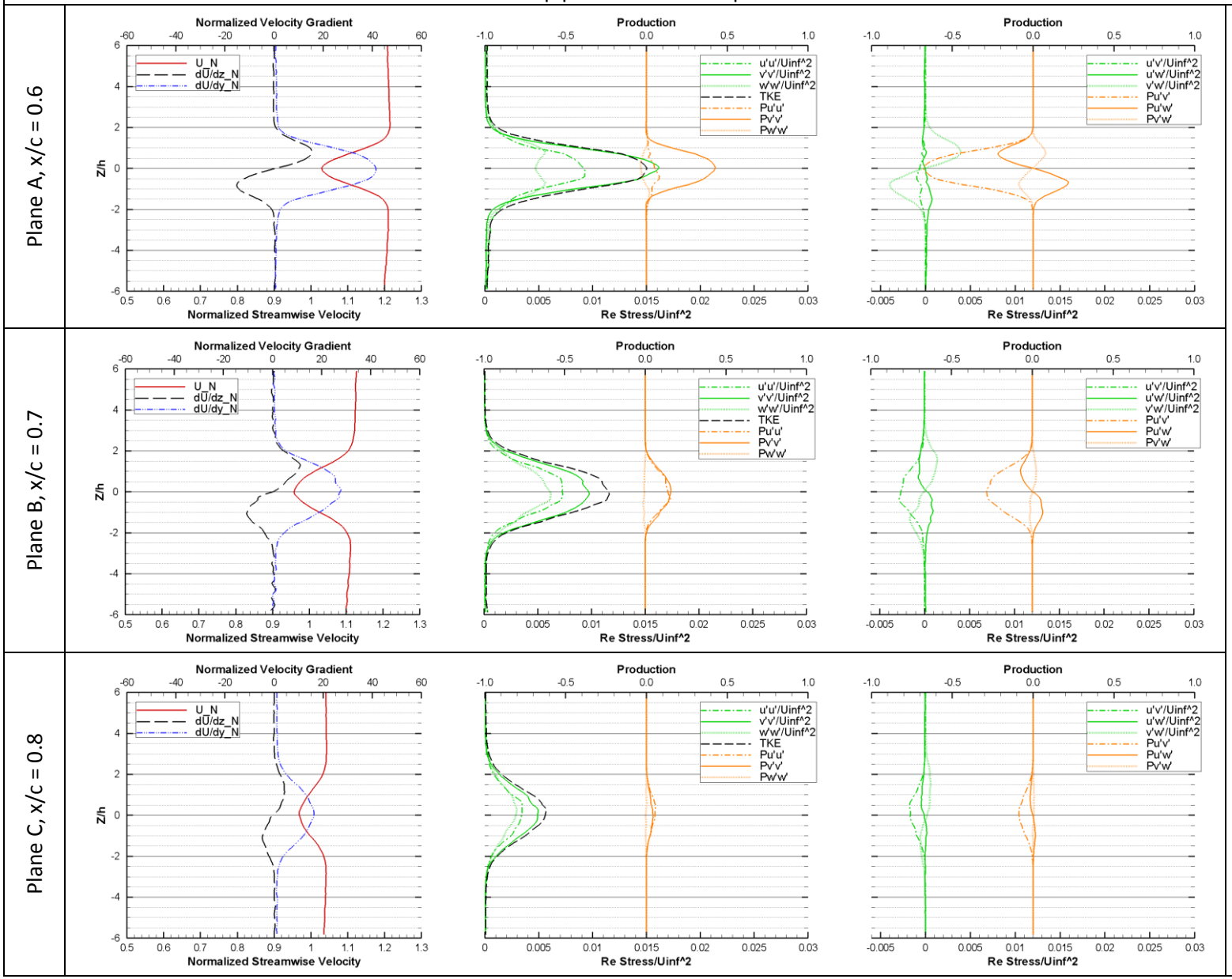

Σχήμα 51: Μεταβολή της ταχύτητας, των κλίσεων της, της τυρβώδους κινητικής ενέργειας, των τάσεων Reynolds και των όρων παραγωγής τους κατά μήκος της γραμμής i3.

8 Συμπεράσματα

Στο πλαίσιο της παρούσας διδακτορικής διατριβής μελετήθηκε πειραματικά και υπολογιστικά η τρισδιάστατη αποκόλληση σε αεροτομές (τύπου SCs) και εξετάστηκε η δυνατότητα έλεγχου αυτής με χρήση VGs. Τα βασικά συμπεράσματα συνοψίζονται ως εξής:

- Κατανοήθηκε η δομή και η αλληλεπίδραση των στροβίλων στο εσωτερικό ενός SC.
- Τα χαρακτηριστικά της τύρβης στο εσωτερικό ενός SC είναι έντονα ανισόρροπα
- Η χρήση VGs καθυστερεί την δημιουργία SC κατά 5° και οδηγεί σε αύξηση του μέγιστου συντελεστή άνωσης κατά 44%.
- Βρέθηκε ισχυρή συσχέτιση μεταξύ των κλίσεων του πεδίου ταχύτητας, των τάσεων Reynolds και των όρων παράγωγης τους
- Η αλληλεπίδραση των VG στροβίλων είναι ισχυρή μέχρι και 40h κατάντη των VGs ενώ στη συνέχεια η διάχυση είναι ο βασικός μηχανισμός στη ροή.

Βιβλιογραφία

Aider, J.-L., Beaudoin, J.-F., & Wesfreid, J. E. (2009). Drag and lift reduction of a 3D bluff-body using active vortex generators. *Experiments in Fluids, 48*(5), 771-789. doi: 10.1007/s00348-009-0770-y

Allan, B. G., Yao, C.-S., & Lin, J. C. (2002). Numerical simulations of vortex generator vanes and jets on a flat plate. *AIAA Paper, 3160*.

Angele, K. P., & Grewe, F. (2007). Instantaneous Behavior of Streamwise Vortices for Turbulent Boundary Layer Separation Control. *Journal of Fluids Engineering, 129*(2). doi: 10.1115/1.2409327

Angele, K. P., & Muhammad-Klingmann, B. (2005). The effect of streamwise vortices on the turbulence structure of a separating boundary layer. *European Journal of Mechanics - B/Fluids, 24*(5), 539-554. doi: 10.1016/j.euromechflu.2005.01.005

Ashill, P. R., Fulker, J. L., & Hackett, K. C. (2001). Research at DERA on sub-boundary layer vortexgenerator s (SBVGs). *AIAA Paper, 887*.

Barlow, J. B., Rae, W. H., & Pope, A. (1999). *Low-speed wind tunnel testing*. New York: John Wiley & Sons.

Bender, E. E., Anderson, B. H., & Yagle, P. J. (1999). Vortex generator modeling for Navier-Stokes codes. *ASME Paper FEDSM99-6919*.

Bertagnolio, F., Sørensen, N., & Rasmussen, F. (2005). New Insight Into the Flow Around a Wind Turbine Airfoil Section. *Journal of Solar Energy Engineering, 127*(2). doi: 10.1115/1.1861927

Bertagnolio, F., Sørensen, N. N., & Johansen, J. (2006). Profile catalogue for airfoil sections based on 3D computations. *Risø-R-1581*.

Bian, S., Ceccio, S. L., & Driscoll, J. F. (2009). A dual-camera cinematographic PIV measurement system at kilohertz frame rate for high-speed, unsteady flows. *Experiments in Fluids, 48*(3), 487-495. doi: 10.1007/s00348-009-0753-z

Boermans, L. (2006). Research on sailplane aerodynamics at Delft University of Technology. Recent and present developments. *Netherlands Association of Aeronautical Engineers NVvL, 1*.

Bragg, M. B., & Gregorek, G. M. (1987). Experimental study of airfoil performance with vortex generators. *Journal of Aircraft, 24*(5), 305-309. doi: 10.2514/3.45445

Braslow, A., & Knox, E. (1958). Simplified Method for Determination of Critical Height of Distributed Roughness Particles for Boundary-Layer Transition at Mach Numbers from 0 to 5. Washington: NACA.

Bremner, D. M., Hutcheson, F. V., & Stead, D. J. (2005). Methodology for the Elimination of Reflection and System Vibration Effects in Particle Image Velocimetry Data processing. *NASA/TM-2005-213257; L-19028*

Broeren, A. P., & Bragg, M. B. (2001). Spanwise Variation in the Unsteady Stalling Flowfields of Two-Dimensional Airfoil Models. *AIAA Journal, 39*(9), 1451-1461.

Chang, P. K. (1976). *Control of flow separation: Energy conservation, operational efficiency, and safety*. Washington D. C.: Hemisphere Publishing Corp.

Chrisokentis, G. (2013). *Analysis of the aerodynamic behavior of vortex generators using computational fluid dynamics methods.* Mechanical Engineering Graduate Thesis, National Technical University of Athens, Athens.

Christensen, K. T. (2004). The influence of peak-locking errors on turbulence statistics computed from PIV ensembles. *Experiments in Fluids, 36*(3), 484-497. doi: 10.1007/s00348-003-0754-2

Coles, D., & Wadcock, A. J. (1979). Flying-hot-wire study of flow past an NACA 4412 airfoil at maximum lift. *AIAA Journal, 17*(4), 321-329.

Crow, S. C. (1970). Stability theory for a pair of trailing vortices. *AIAA Journal, 8*(12), 2172-2179. doi: 10.2514/3.6083

DiOttavio, J., Watson, K., Cormey, J., Komerath, N., & Kondor, S. (2008). *Discrete structures in the radial flow over a rotor blade in dynamic stall.* Paper presented at the Proceedings of the 26th applied aerodynamics conference, AIAA, Honolulu, Hawaii, USA.

Dossing, M. (2008). High frequency microphone measurements for transition detection on airfoils. *Risø-R-1645*.

Drela, M. (1989). XFOIL: An Analysis and Design System for Low Reynolds Number Airfoils. In T. J. Mueller (Ed.), *Low Reynolds Number Aerodynamics* (Vol. 54, pp. 1-12). NY, US: Springer-Verlag.

Dropkin, A., Custodio, D., Henoch, C. W., & Johari, H. (2012). Computation of Flow Field Around an Airfoil with Leading-Edge Protuberances. *Journal of Aircraft, 49*(5), 1345-1355. doi: 10.2514/1.c031675

Dudek, J. C. (2006). Empirical Model for Vane-Type Vortex Generators in a Navier-Stokes Code. *AIAA Journal, 44*(8), 1779-1789. doi: 10.2514/1.20141

Dudek, J. C. (2011). Modeling vortex generators in a Navier-Stokes code. *AIAA Journal, 49*(4), 748-759.

Elimelech, Y., Arieli, R., & Iosilevskii, G. (2012). The three-dimensional transition stages over the NACA-0009 airfoil at Reynolds numbers of several ten thousand. *Physics of Fluids, 24*(2). doi: 10.1063/1.3682377

Elsinga, G. E., & Westerweel, J. (2011). Tomographic-PIV measurement of the flow around a zigzag boundary layer trip. *Experiments in Fluids, 52*(4), 865-876. doi: 10.1007/s00348-011-1153-8

Fish, F. E., & Battle, J. M. (1995). Hydrodynamic design of the humpback whale flipper. *Journal of Morphology, 225*(1), 51-60. doi: 10.1002/jmor.1052250105

Flynn, G. A., Morrison, J. F., & Mabey, D. G. (2001). Buffet Alleviation on Swept and Unswept Wings at High Incidence. *Journal of Aircraft, 38*(2), 368-378. doi: 10.2514/2.2771

Foucaut, J. M., Miliat, B., Perenne, N., & Stanislas, M. (2004). Characterization of different PIV algorithms using the EUROPIV synthetic image generator and real images from a turbulent boundary layer *Particle Image Velocimetry: Recent Improvements* (pp. 163-185): Springer.

Fuglsang, P., Antoniou, I., Dahl, K. S., & Aagaard Madsen, H. (1998). Wind tunnel tests of the FFA-W3-241, FFA-W3-301 and NACA 63-430 airfoils. *Risø-R 1041*.

Fuglsang, P., Bak, C., Gaunaa, M., & Antoniou, I. (2003). Wind tunnel tests of Risø-B1-18 and Risø-B1-24. *Risø-R-1375*.

Fuglsang, P., & Bove, S. (2008). *Wind Tunnel Testing Of Airfoils Involves More Than Just Wall Corrections.* Paper presented at the European Wind Energy Conference.

Gad-el-Hak, M., & Bushnell, D. M. (1991). Separation Control: Review. *Journal of Fluids Engineering, 113*(1). doi: 10.1115/1.2926497

Gleyzes, C., & Capbern, P. (2003). Experimental study of two AIRBUS/ONERA airfoils in near stall conditions. Part I: Boundary layers. *Aerospace Science and Technology, 7*(6), 439-449. doi: 10.1016/s1270-9638(03)00045-2

Godard, G., & Stanislas, M. (2006). Control of a decelerating boundary layer. Part 1: Optimization of passive vortex generators. *Aerospace Science and Technology, 10*(3), 181-191. doi: 10.1016/j.ast.2005.11.007

Goett, H. J. (1939). Experimental Investigation of the Momentum Method for Determining Profile Drag. *NACA T.R. - 660*.

Gregory, N., & O'Reilly, C. L. (1970). Low-speed aerodynamic characteristics of NACA 0012 aerofoil section, including the effects of upper-surface roughness simulating hoar frost *Research & Memoranda - 3726*: Aeronautical Research Council.

Gregory, N., Quincey, V. G., O'Reilly, C. L., & Hall, D. J. (1971). Progress Report on Observations of Three-Dimensional Flow Patterns obtained during Stall Development on Aerofoils, and on the Problem of Measuring Two-Dimensional Characteristics. *C.P. 1146*: Aeronautical Research Council.

Gresham, N., Wang, Z., & Gursul, I. (2010). Vortex dynamics of free-to-roll slender and nonslender delta wings. *Journal of Aircraft, 47*(1), 292-302.

Hahn, D., Scholz, P., & Radespiel, R. (2010). *Experimental evaluation of the stall characteristics of a two-element high-lift airfoil*.

Heine, B., Mulleners, K., Joubert, G., & Raffel, M. (2011). *Dynamic stall control by passive disturbance generators.* Paper presented at the 29th AIAA Applied Aerodynamics Conference, Honolulu (Hawai), USA.

Holmes, A. E., Hickey, P. K., Murphy, W. R., & Hilton, D. A. (1987). The application of sub-boundary layer vortex generators to reduce canopy "Mach rumble" interior noise on the Gulfstream III. *AIAA Paper, 87-0084*.

Hunt, J. C. R., Abell, C., Peterka, J., & Woo, H. (1978). Kinematical studies of the flows around free or surface-mounted obstacles; applying topology to flow visualization. *Journal of Fluid Mechanics, 86*(01), 179-200.

Hunt, J. C. R., Wray, A. A., & Moin, P. (1988, 1988). *Eddies, streams, and convergence zones in turbulent flows.* Paper presented at the Studying Turbulence Using Numerical Simulation Databases, 2.

Jacobs, E. N., & Sherman, A. (1937). *Airfoil section characteristics as affected by variations of the Reynolds number*: National Advisory Committee for Aeronautics.

Janiszewska, J. M. (2004). *Three dimensional aerodynamics of a simple wing in oscillation including effects of vortex generators.* PhD, The Ohio State University.

Jeong, J., & Hussain, F. (1995). On the identification of a vortex. *Journal of Fluid Mechanics, 285*(-1), 69-94. doi: 10.1017/s0022112095000462

Jirasek, A. (2005). Vortex-Generator Model and Its Application to Flow Control. *Journal of Aircraft, 42*(6), 1486-1491. doi: 10.2514/1.12220

Joubert, G., Le Pape, A., & Huberson, S. (2011). *Numerical study of flow separation control over a OA209 Airfoil using Deployable Vortex Generator.* Paper presented at the 49th AIAA Aerospace Sciences Meeting.

Kang, D. H., Longo, J., Marquardt, M., & Stern, F. (2008, 2008). *Solid/free-surface juncture boundary layer and wake with waves.* Paper presented at the 27th Symposium on Naval Hydrodynamics.

Kerho, M., Hutcherson, S., Blackwelder, R. F., & Liebeck, R. H. (1993). Vortex generators used to control laminar separation bubbles. *Journal of Aircraft, 30*(3), 315-319.

Kerho, M., Kramer, B., & Torrance, C. A. (2003). Enhanced airfoil design incorporating boundary layer mixing devices. *AIAA Paper, 2003-211*.

Klausmeyer, S. M., Papadakis, M., & Lin, J. C. (1996). A flow physics study of vortex generators on a multi-element airfoil. *AIAA Paper*(96-0548).

Kolář, V. (2007). Vortex identification: New requirements and limitations. *International Journal of Heat and Fluid Flow, 28*(4), 638-652. doi: 10.1016/j.ijheatfluidflow.2007.03.004

Komerath, N. M., Raghav, V., & DiOttavio, J. (2009). Diagnostics of Flow Suppression on Rotor Blades: Final Report: Georgia Tech Research Corporation.

Krothapalli, A., Venkatakrishnan, L., Lourenco, L., Greska, B., & Elavarasan, R. (2003). Turbulence and noise suppression of a high-speed jet by water injection. *Journal of Fluid Mechanics, 491*, 131-159. doi: 10.1017/s0022112003005226

Kubin, R. F., & Fletcher, A. N. (1982). Fluorescence quantum yields of some rhodamine dyes. *Journal of Luminescence, 27*(4), 455-462. doi: 10.1016/0022-2313(82)90045-x

Kunik, W. G. (1986). *Application of a computational model for vortex generators in subsonic internal flows.* Paper presented at the 22nd Joint Propulsion Conference.

Langan, K. J., & Samuels, J. J. (1995). Experimental Investigations of Maneuver Performance Enhancements on an Advanced Fighter/Attack Aircraft. *AIAA Paper, 95-442*.

Lighthill, M. J. (1963). Attachment and separation in three-dimensional flow. In L. Rosenhead (Ed.), *Laminar Boundary Layers*: Oxford Univeristy Press.

Lin, J. C. (1999). Control of turbulent boundary-layer separation using micro-vortex generators. *AIAA Paper*(99-993404).

Lin, J. C. (2002). Review of research on low-profile vortex generators to control boundary-layer separation. *Progress in Aerospace Sciences, 38*(4-5), 389-420. doi: 10.1016/s0376-0421(02)00010-6

Lin, J. C., Robinson, S. K., McGhee, R. J., & Valarezo, W. O. (1994). Separation control on high-lift airfoils via micro-vortex generators. *Journal of Aircraft, 31*(6), 1317-1323.

Lin, J. C., Selby, G. V., & Howard, F. G. (1991). Exploratory study of vortex-generating devices for turbulent flow separation control. *AIAA Paper*(91-0042).

Liu, J., Piomelli, U., & Spalart, P. R. (1996). Interaction between a spatially growing turbulent boundary layer and embedded streamwise vortices. *Journal of Fluid Mechanics, 326*(-1). doi: 10.1017/s0022112096008270

Lockman, W. K., & Seegmiller, H. L. (1983). An experimental investigation of the subcritical and supercritical flow about a swept semispan wing: DTIC Document.

LöGdberg, O., Fransson, J. H. M., & Alfredsson, P. H. (2009). Streamwise evolution of longitudinal vortices in a turbulent boundary layer. *Journal of Fluid Mechanics, 623*. doi: 10.1017/s0022112008004825

Lowson, M. (1964). Some experiments with vortex breakdown(Water tunnel flow visualization on slender delta wings reveal vortex breakdown formation to be a nonaxisymmetric stability). *ROYAL AERONAUTICAL SOCIETY, JOURNAL, 68*, 343-346.

Lu, F. K., Li, Q., Shih, Y., Pierce, A. J., & Liu, C. (2011). *Review of Micro Vortex Generators in High-Speed Flow.* Paper presented at the 49th AIAA Aerospace Sciences Meeting.

Lyon, C. A., Selig, M. S., & Broeren, A. P. (1997, 1997/01//). *Boundary Layer Trips on Airfoils at Low Reynolds Numbers.* Paper presented at the 35th Aerospace Sciences Meeting.

Manolesos, M., & Voutsinas, S. G. (2011, 2011/07/27/15:51:13). 3D flow separation on plane wing, from http://www.aerolab.mech.ntua.gr/3D_flow_separation_on_plane_wing_1.html

Martin, P. B., Leishman, J., Pugliese, G. J., & Anderson, S. L. (2000). *Stereoscopic PIV measurements in the wake of a hovering rotor.* Paper presented at the AHS International, Annual Forum, 56 th, Virginia Beach, VA.

May, N. (2001, 2001). *A new vortex generator model for use in complex configuration CFD solvers.* Paper presented at the 19th AIAA Applied Aerodynamics Conference.

McCurdy, W. J. (1948). Investigation of Boundary Layer Control of an NACA 16-325 Airfoil by Means of Vortex Generators. *United Aircraft Corp., Research Department, Rept. M-15038-3*.

Mehta, R. D., & Bradshaw, P. (1988). Longitudinal vortices imbedded in turbulent boundary layers Part 2. Vortex pair with 'common flow' upwards. *Journal of Fluid Mechanics, 188*(-1). doi: 10.1017/s0022112088000837

Menter, F. R. (1993). Zonal two-equation k-w turbulence model for aerodynamic flows. *AIAA Paper, 1993 - 2906*.

Moss, G. F., & Murdin, P. M. (1971). *Two-Dimensional Low-Speed Tunnel Tests on the NACA 0012 Section Including Measurements Made During Pitching Oscillations at the Stall* (1st ed.). London: H.M. Stationery Office.

Mourikis, D., Riziotis, V., & Voutsinas, S. (2005). Optimum aerodynamic design of 52m blade for a prototype 5MW WEC *TR-01*. Athens: NTUA.

Mulleners, K., Kindler, K., & Raffel, M. (2012). Dynamic stall on a fully equipped helicopter model. *Aerospace Science and Technology, 19*(1), 72-76. doi: 10.1016/j.ast.2011.03.013

Murri, D., & Jordan, F. (1987). Wind-tunnel investigation of a full-scale general aviation airplane equipped with an advanced natural laminar flow wing *NASA-TP-2772*.

Nikolaou, I. G., Politis, E. S., & Chaviaropoulos, P. K. (2005). Modelling the Flow Around Airfoils Equipped with Vortex Generators Using a Modified 2D Navier–Stokes Solver. *Journal of Solar Energy Engineering, 127*(2). doi: 10.1115/1.1850486

Øye, S. (1995). *The effect of vortex generators on the performance of the Elkraft 1000 kW turbine.* Paper presented at the 9th IEA Symposium on Aerodynamics of Wind Turbines.

Papadakis, G. (2011). Formulation of a cell-centered (U)RANS compressible solver *PhD Progress Report*. Athens: National Technical University of Athens.

Pape, A. L., Costes, M., Joubert, G., David, F., & Deluc, J. M. (2012). Dynamic Stall Control Using Deployable Leading-Edge Vortex Generators. *AIAA Journal, 50*(10), 2135-2145.

Pauley, W. R., & Eaton, J. K. (1988). Experimental study of the development of longitudinal vortex pairs embedded in a turbulent boundary layer. *AIAA Journal, 26*(7), 816-823. doi: 10.2514/3.9974

Pearcey, H. H. (1961). Shock induced separation and its prevention by design and boundary layer control. In G. V. Lachmann (Ed.), *Boundary Layer and Flow Control* (Vol. 2, pp. 1166-1344): Pergamon Press.

Pope, S. B. (2000). *Turbulent flows*. Cambridge ; New York: Cambridge University Press.

Raffel, M., Kompenhans, J., & Willert, C. E. (1998). *Particle image velocimetry: a practical guide*. Berlin: Springer.

Raghav, V., Richards, P., Komerath, N., & Smith, M. (2009). *Three-Dimensional Features of the Stalled Flow Field of a Rotor Blade in Forward Flight*. Paper presented at the 2nd International Forum on Rotorcraft Multidisciplinary Technology

Ramasamy, M., & Leishman, J. G. (2006). *Benchmarking PIV with LDV for Rotor Wake Vortex Flows.* Paper presented at the 24 th AIAA Applied Aerodynamics Conference.

Ramasamy, M., Paetzel, R., & Bhagwat, M. J. (2011). Aperiodicity correction for rotor tip vortex measurements *DTIC Document*.

Rao, D. M., & Kariya, T. T. (1988). *Boundary-layer submerged vortex generators for separation control - An exploratory study.* Paper presented at the 1st National Fluid Dynamics Congress.

Rodríguez, D., & Theofilis, V. (2010). On the birth of stall cells on airfoils. *Theoretical and Computational Fluid Dynamics, 25*(1-4), 105-117. doi: 10.1007/s00162-010-0193-7

Ross, H. M., & Perkins, J. N. (1994). Tailoring stall characteristics using leading edge droop modification. *Journal of Aircraft, 31*(4), 767-772. doi: 10.2514/3.46559

Rubinstein, R., Rumsey, C. L., Salas, M. D., & Thomas, J. L. (2001). Turbulence Modeling Workshop *NASA/CR 2001-210841*.

Schewe, G. (2001). Reynolds-number effects in flow around more-or-less bluff bodies. *Journal of Wind Engineering and Industrial Aerodynamics, 89*, 1267-1289. doi: 10.1016/s0167-6105(01)00158-1

Schubauer, G. B., & Spangenberg, W. G. (1959). Forced mixing in boundary layers. *Journal of Fluid Mechanics, 8*(01). doi: 10.1017/s0022112060000372

Seshagiri, A., Cooper, E., & Traub, L. W. (2009). Effects of vortex generators on an airfoil at low Reynolds numbers. *Journal of Aircraft, 46*(1), 116-122.

Smith, F. T. (1994). Theoretical prediction and design for vortex generators in turbulent boundary layers. *Journal of Fluid Mechanics, 270*(1), 91-132.

Sørensen, N. N., & Schreck, S. (2012). Computation of the National Renewable Energy Laboratory Phase-VI rotor in pitch motion during standstill. *Wind Energy, 15*(3), 425-442. doi: 10.1002/we.480

Spalart, P. R., & Allmaras, S. R. (1992,). *A one-equation turbulence model for aerodynamic flows.* Paper presented at the 30th Aerospace Sciences Meeting and Exhibit.

Stillfried, F. V., Wallin, S., & Johansson, A. V. (2011). Evaluation of a Vortex Generator Model in Adverse Pressure Gradient Boundary Layers. *AIAA Journal, 49*(5), 982-993. doi: 10.2514/1.j050680

Stillfried, F. V., Wallin, S., & Johansson, A. V. (2012). Vortex-Generator Models for Zero- and Adverse-Pressure-Gradient Flows. *AIAA Journal, 50*(4), 855-866. doi: 10.2514/1.j051169

Storms, B. L., & Jang, C. S. (1994). Lift enhancement of an airfoil using a Gurney flap and vortex generators. *Journal of Aircraft, 31*(3), 542-547.

Supamusdisukul, J. (2008). *Experimental investigation of wing-fuselage interaction geometries including CFD analyses.* MSc Thesis, University of Maryland, Maryland, US.

Swalwell, K. E., Sheridan, J., & Melbourne, W. H. (2004). *The effect of turbulence intensity on performance of a NACA 4421 airfoil section.* Paper presented at the 42nd AIAA Aerospace Sciences Meeting and Exhibit, Reno, Nevada.

Taira, K., & Colonius, T. (2009). Three-dimensional flows around low-aspect-ratio flat-plate wings at low Reynolds numbers. *Journal of Fluid Mechanics, 623*. doi: 10.1017/s0022112008005314

Tangler, J. L. (2002). The nebulous art of using wind tunnel aerofoil data for predicting rotor performance. *Wind Energy, 5*(2-3), 245-257.

Taylor, H. D. (1950). Summary report on vortex generators *Technical Report No. R-05280-9*: United Aircraft Corporation. Research Dept.

Theofilis, V., Hein, S., & Dallmann, U. (2000). On the origins of unsteadiness and three-dimensionality in a laminar separation bubble. *Philosophical Transactions of the Royal Society A: Mathematical, Physical and Engineering Sciences, 358*(1777), 3229-3246. doi: 10.1098/rsta.2000.0706

Timmer, W. A., & Van Rooij, R. P. J. O. M. (2003). Summary of the Delft University Wind Turbine Dedicated Airfoils. *Journal of Solar Energy Engineering, 125*(4), 488-496. doi: 10.1115/1.1626129

Tobak, M., & Peake, D. J. (1982). Topology of three-dimensional separated flows. *Annual Review of Fluid Mechanics, 14*(1), 61-85.

Van Raemdonck, G. M. R., & Van Tooren, M. J. L. (2008, 2008//20/20/07). *Time averaged phenomenological investigation of a wake behind a bluff body.* Paper presented at the BBAA VI International Colloquium on: Bluff Bodies Aerodynamics & Applications.

Van Rooij, R. P. J. O. M., & Timmer, W. A. (2003). Roughness sensitivity considerations for thick rotor blade airfoils. *Journal of Solar Energy Engineering, 125*(4), 22-31. doi: 10.1115/wind2003-350

Velte, C. M. (2013). Vortex Generator Flow Model Based on Self-Similarity. *AIAA Journal, 51*(2), 526-529. doi: 10.2514/1.j051865

Velte, C. M., & Hansen, M. O. L. (2012). Investigation of flow behind vortex generators by stereo particle image velocimetry on a thick airfoil near stall. *Wind Energy*. doi: 10.1002/we.1541

Velte, C. M., & Manolesos, M. (2011). [Wind Tunnel Tests - Personal Communication].

Waithe, K. A. (2004a). *Source Term Model for an Array of Vortex Generator Vanes.* Paper presented at the 42nd AIAA Aerospace Sciences Meeting and Exhibit AIAA-2004-1236.

Waithe, K. A. (2004b). *Source Term Model for Vortex Generator Vanes in a Navier-Stokes Computer Code.* Paper presented at the 42nd AIAA Aerospace Sciences Meeting and Exhibit.

Waldman, R. M., & Breuer, K. S. (2012). Accurate measurement of streamwise vortices using dual-plane PIV. *Experiments in Fluids, 53*(5), 1487-1500. doi: 10.1007/s00348-012-1368-3

Weihs, D., & Katz, J. (1983). Cellular patterns in poststall flow over unswept wings. *AIAA Journal, 21*(12), 1757-1759. doi: 10.2514/3.8321

Wendt, B. (1996). *The modelling of symmetric airfoil vortex generators.* Paper presented at the 34th Aerospace Sciences Meeting and Exhibit.

Wendt, B. (2004). Parametric Study of Vortices Shed from Airfoil Vortex Generators. *AIAA Journal, 42*(11), 2185-2195.

Wendt, B., Reichert, B. A., & Foster, J. D. (1995). The decay of longitudinal vortices shed from airfoil vortex generators.

Westerweel, J. (2000). Theoretical analysis of the measurement precision in particle image velocimetry. *Experiments in Fluids, 29*(1), S003-S012.

Willert, C. (1997). Stereoscopic digital particle image velocimetry for application in wind tunnel flows. *Measurement Science and Technology, 8*(12), 1465-1479. doi: 10.1088/0957-0233/8/12/010

Winkelmann, A. E. (1981). An experimental study of separated flow on a finite wing. *AIAA Paper* (81-1882).

Winkelmann, A. E. (1982). An experimental study of mushroom shaped stall cells. *AIAA Paper* (82-0942).

Winkelmann, A. E., & Barlow, J. B. (1980). Flowfield Model for a Rectangular Planform Wing beyond Stall. *AIAA Journal, 18*(08), 1006-1008.

Wokoeck, R., Krimmelbein, N., Ortmanns, J., Ciobaca, V., Radespiel, R., & Krumbein, A. (2006). *RANS simulation and experiments on the stall behaviour of an airfoil with laminar separation bubbles.* Paper presented at the 44th AIAA aerospace sciences meeting and exhibit, Reno, AIAA-2006-244.

Yao, C. S., Lin, J. C., & Brian, A. G. (2002, 2002). *Flow-Field Measurement of Device-Induced Embedded Streamwise Vortex on a Flat Plate.* Paper presented at the 1st AIAA Flow Control Conference.

Yon, S. A., & Katz, J. (1998). Study of the Unsteady Flow Features on a Stalled Wing. *AIAA Journal, 36*(3), 305-312.

Yoshida, K., & Noguchi, M. (2000). *Adverse Reynolds Number Effect on Maximum Lift of Two Dimensional Airfoils.* Paper presented at the ICAS.

Zarutskaya, T., & Arieli, R. (2005). *On vortical flow structures at wing stall and beyond.* Paper presented at the 35th AIAA Fluid Dynamics Conference and Exhibit.

Zhang, L., Yang, K., Xu, J., & Zhang, M. (2011). Modeling of delta-wing type vortex generators. *Science China Technological Sciences, 54*(2), 277-285. doi: 10.1007/s11431-010-4284-x